The 2010 Chesapeake Bay Eutrophication Model

A Report to the US Environmental Protection Agency Chesapeake Bay Program

and to

The US Army Engineer Baltimore District

December 2010

Carl F. Cerco
Sung-Chan Kim
Mark R. Noel

US Army Engineer Research and Development Center, Vicksburg MS
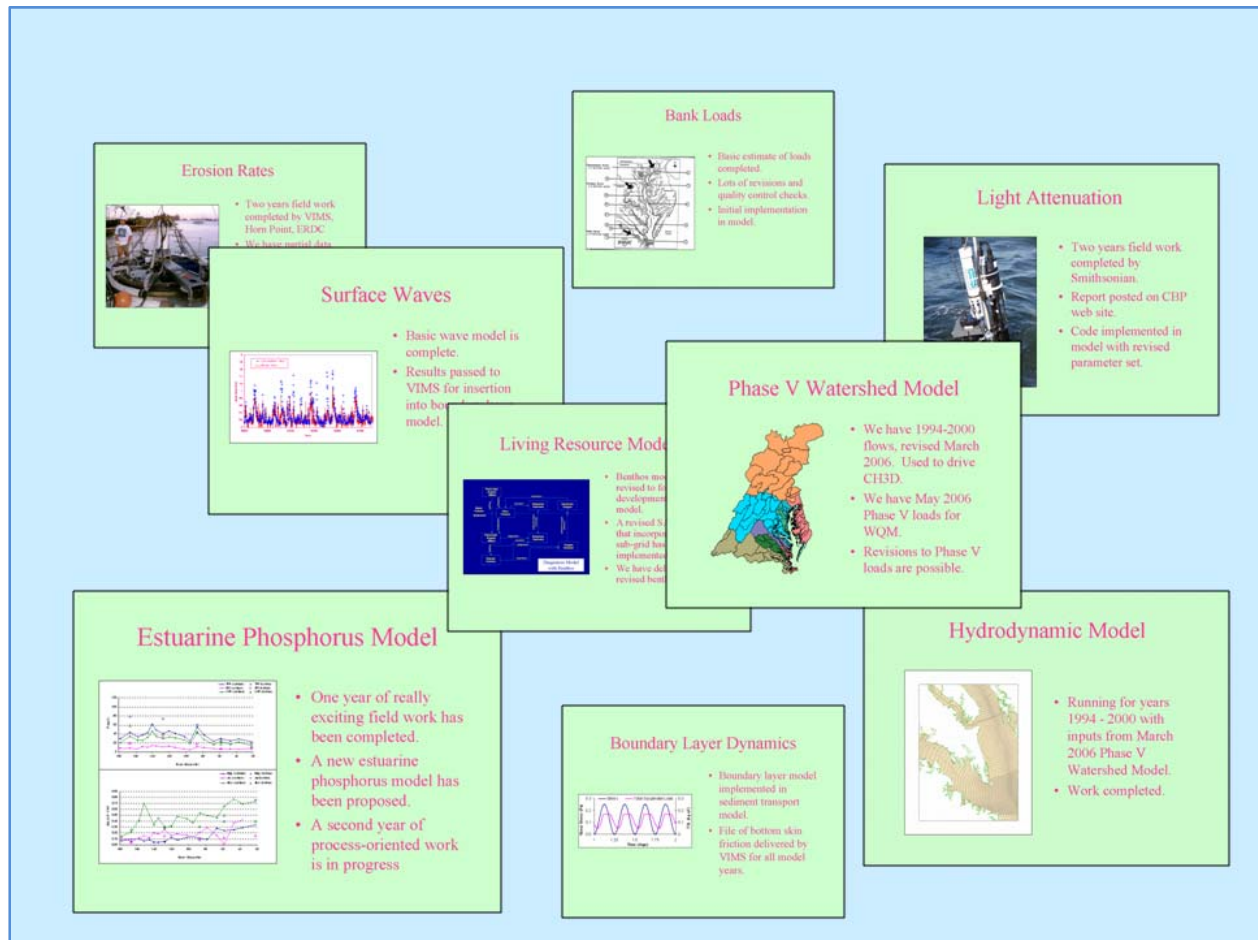
Preface

The Chesapeake Bay Environmental Model Package is a combination of interactive models. The Community Multi-Scale Air Quality Model and a set of regression models compute daily atmospheric nitrogen and phosphorus loads to the Chesapeake Bay watershed and to the water surface. The Watershed Model (WSM) provides daily computations of flow, solids loads, and nutrient loads at the heads of major tributaries and along the shoreline below the tributary inputs. Flows from the WSM are one set of inputs to the CH3D (Computational Hydrodynamics in Three Dimensions) hydrodynamic model. CH3D computes surface level, three-dimensional velocities, and vertical diffusion on a time scale measured in minutes. Loads from the WSM and transport processes from CH3D drive the CE-QUAL-ICM (Corps of Engineers Integrated Compartment Water Quality Model) eutrophication model. ICM computes, in three dimensions, physical properties, algal production, and elements of the aquatic carbon, nitrogen, phosphorus, silica, and oxygen cycles.

The basic modeling framework was established more than 20 years ago and has been subject to continuous revision since then. The present phase of the study originated with the US Army Engineer Baltimore District (NAB) as part of a Regional Sediment Management plan. In April 2004, a Feasibility Cost Sharing Agreement entitled "Evaluation of Suspended Solids Transport and of Living Resource Interactions in the Chesapeake Bay and Potomac River" was completed with the Metropolitan Washington Council of Governments and the Maryland Department of Environment in partnership with the US Environmental Protection Agency Chesapeake Bay Program (CBP). The agreement called for a combination of field measures, hydrodynamic modeling, and water quality modeling aimed at improving the understanding and quantification of suspended solids impacts on living resources, especially phytoplankton and submerged aquatic vegetation.

The "Chesapeake 2000" agreement committed the Chesapeake Bay Program partners to maintain previously-derived nutrient load reduction goals and to develop sediment load reductions. The commitment was reinforced by the requirement for CBP to develop, by May 2011, Total Maximum Daily Loads (TMDL's) for the bay which will remove water quality impairments. Removal of impairments in the bay focuses on three key measures:

- Dissolved Oxygen
- Water Clarity
- Chlorophyll

The CBP's interests overlap with NAB regarding sediment management but extend beyond the goals of the feasibility study, especially with regard to dissolved oxygen and chlorophyll. Consequently, CBP engaged in a separate agreement with the US Army Engineer Research and Development Center to supplement the tools developed during the Feasibility Study and to ensure the availability of technology to aid in determining the TMDL's.

The present report provides the primary documentation for the modeling activities conducted as part of the Feasibility Study and conducted for the CBP, with the exception of the pH – Alkalinity and Algal Species Modeling in the Potomac River. These are the subject of a separate report in preparation.

Acknowledgements

Point of Contact

Carl F. Cerco, PhD, PE
Research Hydrologist
US Army ERDC
3909 Halls Ferry Road
Vicksburg MS 39180
601-634-4207
Carl.F.Cerco@usace.army.mil

1 Introduction

The CBEMP

The Chesapeake Bay Environmental Model Package is a combination of interactive models. The Community Multi-Scale Air Quality Model (Dennis et al., 2010) and a set of regression models (Grimm and Lynch, 2004) compute daily atmospheric nitrogen and phosphorus loads to the Chesapeake Bay watershed and to the water surface. The Watershed Model (WSM, US EPA, 2010) provides daily computations of flow, solids loads, and nutrient loads at the heads of major tributaries and along the shoreline below the tributary inputs. Flows from the WSM are one set of inputs to the CH3D (Computational Hydrodynamics in Three Dimensions, Johnson et al., 1993) hydrodynamic model. CH3D computes surface level, three-dimensional velocities, and vertical diffusion on a time scale measured in minutes. Loads from the WSM and transport processes from CH3D drive the CE-QUAL-ICM (Corps of Engineers Integrated Compartment Water Quality Model) eutrophication model (Cerco and Cole, 1993). ICM computes, in three dimensions, physical properties, algal production, and elements of the aquatic carbon, nitrogen, phosphorus, silica, and oxygen cycles. These are computed on time scales of minutes although computations averaged up to longer time periods, hours to one day, are more representative of observations. ICM incorporates several sub-models including sediment diagenesis (DiToro, 2001), submerged aquatic vegetation (Cerco and Moore, 2001), and benthic invertebrates (Cerco and Meyers, 2000).

Previous Study Phases

The basic modeling framework was established more than 20 years ago and has been subject to continuous revision since then. Three major study phases preceded this one. The first phase (Cerco and Cole, 1994) provided modeling technology for the 1991 re-evaluation of the 1987 nutrient reduction goals. The second phase (Cerco et al., 2002) refined the computational grid to improve representation in the Virginia tributaries and introduced living resources into the computational framework. This phase provided computational tools for the Tributary Strategy management effort. The third phase (Cerco and Noel, 2004a) continued the grid refinements and extended the model into still smaller tributaries. Calibration of the model during this phase emphasized representation of primary production (Cerco and Noel, 2004b). Light attenuation was computed based on computed suspended solids (Cerco and Noel 2004c). This version of the model provided verification for a 2003 agreement to cap average annual nitrogen and phosphorus loads to the bay.

The January 2003 STAC Workshop

In January 2003, a workshop was conducted by the Chesapeake Bay Program Scientific and Technical Advisory Committee to review the computation of solids and light attenuation in the 2002 version of the CBEMP. Although the review was largely supportive, several weaknesses were identified. The foremost was absence of resuspension in the suspended solids model. The model used a representation in which settling to the bed was less than settling through the water column. This net settling velocity represented the long term difference between settling and resuspension. However, once a particle settled to the bed it stayed there permanently. Some workshop participants feared that this representation over-estimated the potential benefits of solids load reductions. They suspected that benefits from load reductions might be negated by continuous resuspension of particulate matter already in the bay.

A second weakness was identified in the quantification of solids loads from bank erosion. Bankloads were derived from the best-available, but sparse, information (USACE, 1990) and input to the model at a constant rate averaged over extensive lengths of shoreline.

Suspended Solids Transport and Living Resource Interactions in the Chesapeake Bay and Potomac River

The present phase of the study originated with the US Army Engineer Baltimore District (NAB) as part of a Regional Sediment Management plan. A Feasibility Cost Sharing Agreement (USACE, 2004) was completed with the Metropolitan Washington Council of Governments and the Maryland Department of Environment in partnership with the US Environmental Protection Agency Chesapeake Bay Program (CBP). Key tasks called for in the study included:

- Erosion Rate Measures – This task involves the measurement and analysis of sediment erosion rates in the Potomac and upper Chesapeake Bay. Most fieldwork will take place in the Potomac. The Bay data exists but must be analyzed and integrated into the model.

- Measures of Light Attenuation – This task involves fundamental measures of the effects of suspended solids on light attenuation. The data obtained must be incorporated into the model.

- Hydrodynamic Model – This task involves setting up and calibrating the CH3D hydrodynamic model on a revised grid suited for detailed sediment transport calculations.

- Surface Waves – This task involves selecting and implementing a surface wave model. Wind-driven wave action is a major force driving sediment resuspension in shallow water.

- Boundary Layer Dynamics – Sediment resuspension involves forces that act in a thin boundary layer, on the order or millimeters. Cells in the hydrodynamic model are over a meter thick. Algorithm development is required to reconcile the disparity in boundary layer and cell thickness.

- Bank Loads – Loads from shoreline erosion are a major component of the solids budget. These loads are presently poorly quantified. Spatially detailed estimates will be created for the upper bay and Potomac.

- Particle Settling Velocity – This task involves investigating interactions between phytoplankton and inorganic solids settling. The premise of the investigation is that plankton form complexes with solids and that the complexes settle at a different rate than solids alone. This task involves data analysis, laboratory investigation, and algorithm development.

- Linkage to Water Quality Model – Sediment transport must be computed in the water quality model in order to accommodate interactions with living resources represented in the water quality model. This will require major code development and testing.

- Living Resource Modeling – This task will involve direct modeling of interactions between suspended solids and living resources. Emphasis will be placed on benthos and submerged aquatic vegetation.

- pH – Alkalinity – Develop a mathematical modeling framework which would relate pH to nutrient loading, primary production, and other factors.

- Algal Species Modeling – The objective of this work is to refine and improve the representation of algal speciation, sources, dynamics, and food web interactions in the Potomac portion of the Bay model. Emphasis will be placed on better understanding and representation of the spring diatom bloom, species succession and *Microcystis* dynamics.

The "Chesapeake 2000" agreement committed the Chesapeake Bay Program partners to maintain previously derived nutrient load reduction goals and to develop sediment load reductions. The commitment was reinforced by the requirement for CBP to develop, by May 2011, Total Maximum Daily Loads (TMDL's) for the bay which will remove water quality impairments. Removal of impairments in the bay focuses on three key measures:

- Dissolved Oxygen
- Water Clarity
- Chlorophyll

The CBP's interests overlap with NAB regarding sediment management but extend beyond the goals of the feasibility study, especially with regard to dissolved oxygen and chlorophyll. Consequently, CBP engaged in a separate agreement with the US Army Engineer Research and Development Center to

supplement the tools developed during the Feasibility Study and to ensure the availability of technology to aid in determining the TMDL's.

The present report provides the primary documentation for the modeling activities conducted as part of the Feasibility Study and conducted for the CBP, with the exception of the pH – Alkalinity and Algal Species Modeling. These are the subject of a separate report in preparation.

References

Cerco, C., and Cole, T. (1993). "Three-dimensional eutrophication model of Chesapeake Bay," *Journal of Environmental Engineering*, 119(6), 1006-1025.

Cerco, C.F. and Cole, T. M. (1994). "Three-dimensional eutrophication model of Chesapeake Bay," Technical Report EL-94-4, U.S. Army Engineer Waterways Experiment Station, Vicksburg MS.

Cerco, C., and Meyers, M. (2000). "Tributary refinements to the Chesapeake Bay Model," *Journal of Environmental Engineering*, 126(2), 164-174.

Cerco, C., and Moore, K. (2001). "System-wide submerged aquatic vegetation model for Chesapeake Bay," *Estuaries*, 24(4), 522-534.

Cerco, C., Johnson, B., and Wang, H. (2002). "Tributary refinements to the Chesapeake Bay model," ERDC TR-02-4, US Army Engineer Research and Development Center, Vicksburg, MS.

Cerco, C., and Noel, M. (2004a). "The 2002 Chesapeake Bay eutrophication model," EPA 903-R-04-004, Chesapeake Bay Program Office, US Environmental Protection Agency, Annapolis MD. (available at http://www.chesapeakebay.net/modsc.htm)

Cerco, C., and Noel, M. (2004b). "Process-based primary production modeling in Chesapeake Bay," *Marine Ecology Progress Series*, 282, 45-58.

Cerco, C., and Noel, M. (2004c). "Managing for water clarity in Chesapeake Bay," *Journal of Environmental Engineering*, 130(6), 631-642.

Dennis, R.L., Mathur, R., Pleim, J., and Walker, J. (2010). "Fate and transport of ammonia at the local and regional scale as simulated by the Community Multiscale Air Quality Model," *Air Pollution Research,* submitted for publication.

DiToro, D. (2001). *Sediment Flux Modeling*, John Wiley and Sons, New York.

Johnson, B. H., Kim, K., Heath, R., Hsieh, B., Butler, L. (1993). "Validation of a three-dimensional hydrodynamic model of Chesapeake Bay," *Journal of Hydraulic Engineering*, 119, 2-20.

United States Army Corps of Engineers. (1990). "Chesapeake Bay shoreline erosion study," Feasibility Report October 1990, Baltimore District, Corps of Engineers, Baltimore MD.

United States Army Corps of Engineers. (2004). "Chesapeake Bay sediment budget, modeling, and regional sediment management," Feasibility Cost Sharing Agreement and Project Management Plan, Baltimore District, Corps of Engineers, Baltimore MD.

United States Environmental Protection Agency. (2010). "Chesapeake Bay Phase 5 Community Watershed Model," EPA XXX-X-XX-008, Chesapeake Bay Program Office, Annapolis MD. (in preparation, available from http://www.chesapeakebay.net/model_phase5.aspx?menuitem=26169)

2 The Hydrodynamic Model

CH3D Basics

CH3D (Computational Hydrodynamics in Three Dimensions) is a general-purpose hydrodynamic model for use in lakes, rivers, estuaries, and coastal waters. The model provides computations of surface level, velocity, vertical diffusion, temperature, and salinity. CH3D was developed for the US Army Engineer Waterways Experiment Station by Sheng (1986) and extensively modified thereafter (Johnson et al. 1991). The model operates by computing numerical solutions to the basic equations of continuity, motion, and mass conservation.

Continuity Equation

$$\frac{\partial u}{\partial x} + \frac{\partial v}{\partial y} + \frac{\partial w}{\partial z} = 0 \tag{1}$$

in which:

u, v, w = velocity in longitudinal, lateral, and vertical directions

Equations of Motion

$$\frac{\partial u}{\partial t} + \frac{\partial u^2}{\partial x} + \frac{\partial uv}{\partial y} + \frac{\partial uw}{\partial z} = fv - \frac{1}{\rho}\frac{\partial p}{\partial x} + \frac{\partial}{\partial x}\left(A_H \frac{\partial v}{\partial x}\right)$$
$$+ \frac{\partial}{\partial y}\left(A_H \frac{\partial u}{\partial y}\right) + \frac{\partial}{\partial z}\left(A_v \frac{\partial u}{\partial z}\right) \tag{2}$$

$$\frac{\partial v}{\partial t} + \frac{\partial uv}{\partial x} + \frac{\partial v^2}{\partial y} + \frac{\partial vw}{\partial z} = -fu - \frac{1}{\rho}\frac{\partial p}{\partial y} + \frac{\partial}{\partial x}\left(A_H \frac{\partial v}{\partial x}\right)$$
$$+ \frac{\partial}{\partial y}\left(A_H \frac{\partial v}{\partial y}\right) + \frac{\partial}{\partial z}\left(A_v \frac{\partial v}{\partial z}\right) \tag{3}$$

$$\frac{\partial p}{\partial z} = -\rho g \tag{4}$$

in which:

t = time

f = Coriolis parameter defined as $2\Omega \sin\phi$ where Ω is the
    rotational speed of the earth and ϕ = latitude

ρ = density

p = pressure

A_H = horizontal turbulent momentum diffusion coefficient

A_v = vertical turbulent momentum diffusion coefficient

g = gravitational acceleration

Equation 4 indicates that vertical acceleration is negligible and pressure is hydrostatic.

Mass Conservation Equations

$$\frac{\partial T}{\partial t} + \frac{\partial uT}{\partial x} + \frac{\partial vT}{\partial y} + \frac{\partial wT}{\partial z}$$
$$= \frac{\partial}{\partial x}\left(K_H \frac{\partial T}{\partial x}\right) + \frac{\partial}{\partial y}\left(K_H \frac{\partial T}{\partial y}\right) + \frac{\partial}{\partial z}\left(K_v \frac{\partial T}{\partial z}\right) \tag{5}$$

$$\frac{\partial S}{\partial t} + \frac{\partial uS}{\partial x} + \frac{\partial vS}{\partial y} + \frac{\partial wS}{\partial z}$$
$$= \frac{\partial}{\partial x}\left(K_H \frac{\partial S}{\partial x}\right) + \frac{\partial}{\partial y}\left(K_H \frac{\partial S}{\partial y}\right) + \frac{\partial}{\partial z}\left(K_v \frac{\partial S}{\partial z}\right) \tag{6}$$

$$\rho = \rho(T, S) \tag{7}$$

in which:

K_H = horizontal turbulent mass diffusion coefficient

K_v = vertical turbulent mass diffusion coefficient

T = temperature

S = salinity

Horizontal diffusion coefficients are specified by the user. Vertical diffusion coefficients are computed by a k-ε turbulence model (Rodi, 1980; Bloss, 1988). The governing equations are first non-dimensionalized and then solved on a discrete computational grid using the finite-difference method. Time step for numerical integration of the bay model is 30 seconds. Details of the solution scheme are provided by Johnson et al. (1991).

Computational Grid

The computational grid (Figures 1, 2) extends from the mouth of the bay to the heads of tide of the bay and major tributaries. The CH3D grid has several

distinct features. A curvilinear non-orthogonal coordinate system is used in the horizontal plane. In practical terms, this feature optimizes the fit of the grid to complicated geometries. A Z-plane coordinate system is used in the vertical in which the number of layers varies according to local depth (Figure 3). Thickness of all layers is constant except for the surface layer which varies according to tidal and wind forcing. The original CH3D used sigma coordinates in which the number of layers was the same everywhere and depth was represented by varying layer thickness. Experience with the initial application (Johnson et al., 1993) indicated the sigma coordinate system hampered computation of stratification on the original grid. Grid characteristics of the present grid include:

- 11,064 surface cells
- 56,920 total cells
- 1 to 19 layers in vertical
- average grid cell is 1,025 x 1,025 m in extent
- surface layer = 2.14 m thick at mean tide
- sub-surface layers = 1.53 m thick

Results

CH3D was initially applied to the years 1993 – 1999 in a continuous sequence. Various calibration parameters including bottom friction and vertical mixing were evaluated based on these years. The application was subsequently extended, by the Engineer Research and Development Center, to 1991 – 2000, to provide a ten-year sequence for the water quality model. A second extension to the years 1985 – 2001 was completed by personnel at the Chesapeake Bay Program (CBP). Results presented here are from the original 7-year application. Model calibration and validation were based largely on visual comparison of computed and observed salinity and on visual and harmonic analysis of computed and observed tides. Salinity is an integrator of multiple modeled processes. Comparison of computed and observed salinity along the longitudinal axis is indicative of computed circulation and stratification. Comparison of computed and observed salinity in vertical casts provides the most rigorous indication of vertical stratification. Computed and observed time series at individual stations indicate the reaction of the model to events such as storm flows. Comparison of computed and observed tides provides validation of tidal currents and indicates the response of the model to events such as the passage of storms.

The quantity of material produced during the validation is voluminous and cannot be presented here in total. This report samples salinity results in the bay and in the Potomac River, the largest tributary. Complete results are posted on the CBP web page. Since the Potomac is significant from a management perspective and is the subject of multiple studies, results of harmonic analysis of tides and currents and comparisons of computed and observed long-term circulation are also presented.

Chesapeake Bay Salinity

The CBP conducts baywide surveys at monthly intervals. For comparison with the model along the longitudinal axis, surface and bottom samples at each station were averaged into seasons for each year:

- January – March
- April – June
- July – September
- October – December

The seasonal averages for each year were averaged again into seasonal averages for the application period and compared to the model results averaged in the same fashion (Figures 4 – 7). These figures present a broad summary of the model's ability to represent axial circulation and vertical stratification. The figures indicate, in particular, that the surface-to-bottom salinity difference during the critical summer months is well represented (Figure 6).

Computed and observed vertical salinity casts are presented for Station CB5.3, located near the center of the bay, south of the Potomac River junction (Figure 8). These comparisons are most demanding since the observations represent an instant in time. To match the observations, the model must capture the surface salinity, the bottom salinity, and the difference between the two, as a function of depth, at the time of collection. Achievement of this goal is confounded since the forcing functions which create the vertical profiles are not known in detail at the exact time and location of the casts. Demands on the model are relaxed a bit by examining the model results over a day rather than at an instant in time. Comparisons (Figure 9) are presented for 1994, a year of "average" runoff in the Susquehanna River, the source of freshwater at the head of tide. The comparisons are difficult to summarize since there are a large number of casts and some comparisons are favorable while others are not. One overarching impression is that the observations of ten show a distinct surface mixed layer (e.g. Days 163, 254) while the modeled vertical salinity profile demonstrates a smooth, gradual variation from top to bottom.

Salinity time series are presented for three stations (Figure 8), one at the northern extent of the bay (CB2.2, Figure 10), one in the center of the bay (CB5.3, Figure 11) and one near the mouth (CB7.3, Figure 12). These figures indicate the model captures the range of salinity at the head of the bay from essentially freshwater, during flow events, to 15 ppt salinity. (Note that fall-line and distributed flows are provided by the CBP Watershed Model). At CB5.2, the range between minimum and maximum salinity is similar to the head of the bay (15 ppt) but the minimum is greater, 5 to 10 ppt. The computed surface salinity shows short-period oscillations associated with tidal currents while the variations near the bottom are of longer period. Near the mouth of the bay, tidal variation is present in computed surface and bottom salinity. The observations indicate higher salinity at the bottom than in the model, an effect which may reflect the specification of boundary conditions at the nearby bay mouth.

Potomac River Salinity

The format for presentation of Potomac River results is the same as for the bay. The longitudinal salinity comparisons (Figures 13 – 16) indicate the length of salinity intrusion up the river is well represented. Computed bottom

salinity is higher than observed in the lower estuary resulting in less vertical stratification in this portion of the estuary. Computed and observed vertical casts at Station LE2.2 (Figure 17) reinforce the perception that computed vertical stratification is less than observed although agreement between model and observations is, at times, excellent. Time series plots indicate the model correctly represents the occasional intrusion of salinity into tidal fresh water (TF2.4, Figure 18). The mid- (RET2.4, Figure 19) and lower-Potomac (LE2.2, Figure 20) stations reflect the mid-bay station; surface salinity shows tidal oscillations which are damped or absent at the bottom. Computed salinity in the river-estuary transition zone often exceeds observed, especially during 1996 when this portion of the estuary was freshwater. Generalizations are difficult to draw from the time series in the lower estuary although there are extended periods when the computed surface salinity exceeds the observed.

Potomac River Tidal Harmonics

The National Oceanographic and Atmospheric Administration (NOAA) maintains three tide stations on the Potomac River, at Colonial Beach, Lewisetta, and Washington DC (Figure 21). Tidal harmonics derived from observations at these stations are published on the NOAA web page (http://tidesandcurrents.noaa.gov). For comparison, model surface levels for the year 2000 were sampled at hourly intervals and subjected to harmonic analysis as per Pawlowicz et al. (2002). Overall, the model tides are damped relative to observed and lag the observed in phase (Table 1). For many harmonics, the amplitude error is less than the 95% confidence interval of the analysis although the tendency towards damped amplitude and delayed phase is present in the M2 tide which has the lowest relative error. Model performance is best at Lewisetta and Colonial Beach and shows the greatest difference from observed at Washington DC. The Washington station is located in a region of complex geometry close to the head of tide. Local non-linear effects which are not replicated in the model may be present in the observed record. For the preponderance of locations and harmonics, the model amplitude is with 2 cm of the observed and is within 7 cm of the observed for the M2 tide at Washington DC. The phase of the model harmonics is within 15° (1 hour) of the observed for most locations and harmonics and is within 28° (< 2 hours) at Washington DC.

Potomac River Tidal Currents

Long-term current meter stations are maintained at two locations in the Potomac River (Figure 21). The first is the NOAA Potomac River MidChannel Site. The second is the Potomac buoy of the Chesapeake Bay Interpretive Buoy System. Surface current speed and direction were retrieved from on-line data sources (http://tidesandcurrents.noaa.gov and http://www.buoybay.org) and subjected to harmonic analysis as per Pawlowicz et al. (2002). Comparable model values were retrieved at hourly intervals for the year 2000 and subjected to the same analysis. The amplitudes of the model harmonics are damped relative to the observations (Table 2). Both observations and model indicate the amplitude of the M2 component is an order of magnitude greater than the amplitude of each minor component although the principal model component is up to 10 cm/s less than the observed. The amplitude of the observed minor components is 2 to 5 cm/s and the model reflects these well. The major axes of

the observed components line up with 10° of each other. The model axes line up within this criterion for the most significant components (M2, S2, N2) but vary widely for the lesser components. Relatively large 95% confidence intervals, especially for K1 and O1 at CBIS, indicate the model representation of these two harmonics is difficult to isolate. The computed and observed phases for the most significant components at CB901 are within 10° (less than one hour) of each other although the differences are 20° to 50° (1.3 to 3.3 hours) for the most significant components at CBIS. These comparisons indicate, in part, the difficulty of comparing observed and computed currents in a region of complicated and constrained geometry. Currents are computed in model cells for which the orientation may not perfectly agree with the channel geometry. Differences between actual and model cross sectional area influence the magnitude of the currents. Overall, the model replicates the amplitude of the most significant tidal currents (M2, S2, N2), which are the determining factor for current-generated bottom shear stress, within 30%.

Potomac River Residual Currents

A one-year current meter mooring (Figure 21), at three depths, was maintained and analyzed by Elliott (1978). He reported that the mean flow at 3-meter depth was seaward while the mean flows at 7.6 m and 12.2 m were landward. Throughout the year, the daily-average flow at 3 meters reversed direction at intervals of four or five days. Daily-average flows at deeper depths were almost exclusively landward although occasional reversals occurred. Amplitude of the current fluctuations was $\approx$ 20 cm s^{-1}. Model residual currents for one year (1991) were obtained at the location and depths of Elliott's measures. Residuals were determined as the 25-hour moving average of the computed velocities. Results (Figure 22) compare well with Elliott's findings. Non-tidal currents near the surface reverse directions frequently while currents at greater depths are primarily landward but demonstrate occasional flow reversals. Currents at all depths fluctuate at periods of five to six days. Magnitude of the fluctuations is 10 to 20 cm s^{-1}.

References

Bloss, S., Lehfeldt, R., and Patterson, J. (1988). "Modeling turbulent transport in a stratified estuary," *Journal of Hydraulic Engineering,* 114(9), 1113-33.

Elliott, A. (1978). "Observations of the meteorologically induced circulation in the Potomac River estuary," *Estuarine and Coastal Marine Science* 6, 285-299.

Johnson, B., Heath, R., Hsieh, B., Kim, K., and Butler, L. (1991). "User's guide for a three-dimensional numerical hydrodynamic, salinity, and temperature model of Chesapeake Bay," Technical Report HL-91-20, Department of the Army Waterways Experiment Station, Vicksburg MS.

Johnson, B. H., Kim, K., Heath, R., Hsieh, B., Butler, L. (1993). "Validation of a three-dimensional hydrodynamic model of Chesapeake Bay," *Journal of Hydraulic Engineering*, 119, 2-20.

Pawlowicz, R., Beardsley, B., and Lentz, S. (2002). "Classical tidal harmonic analysis including error estimates in MATLAB using T_TIDE," *Computers & Geosciences* 28, 929-937.

Rodi, W. (1980). "Turbulence models and their application in hydraulics: A state of the art review," IAHR, Delft, The Netherlands.

Sheng, Y. P. (1986). "A three-dimensional mathematical model of coastal, estuarine, and lake currents using boundary-fitted grid," Report No. 585, A.R.A.P. Group of Titan Systems, Princeton, NJ.

Table 1
Potomac River Tidal Harmonics

Station	Tide	Observed Amplitude, m	Model Amplitude, m	95% Confidence Interval, m	Observed Phase, Degrees	Model Phase, Degrees	Confidence Interval, Degrees
Lewisetta, VA	M2	0.184	0.174	0.006	176.4	161.5	2.0
	S2	0.028	0.026	0.006	200.0	185.8	15.0
	N2	0.040	0.035	0.006	152.3	138.4	9.7
	K1	0.023	0.021	0.007	276.2	270.3	17.9
	O1	0.019	0.019	0.006	298.7	291.5	19.2
Colonial Beach, VA	M2	0.246	0.227	0.006	213.9	203.4	1.5
	S2	0.039	0.035	0.005	247.9	233.3	10.1
	N2	0.050	0.048	0.006	193.8	182.8	6.9
	K1	0.030	0.024	0.007	294.3	286.7	15.0
	O1	0.026	0.023	0.006	311.5	309.7	16.2
Washington, DC	M2	0.407	0.331	0.006	20.4	352.4	1.1
	S2	0.052	0.042	0.006	64.300	25.4	8.3
	N2	0.075	0.058	0.007	356.500	329.4	6.3
	K1	0.046	0.032	0.006	357.000	354.6	11.3
	O1	0.035	0.029	0.006	22.600	8.1	13.9

Table 2
Potomac River Current Harmonics

Station	Tide	Observed velocity along major axis, cm s-1	95% confidence interval, cm s-1	Model velocity along major axis, cms-1	95% confidence interval, cm s-1	Observed inclination of major axis, degrees	95% confidence interval, degrees	Model inclination along major axis, degrees	95% confidence interval, degrees	Observed phase, degrees	95% confidence interval, degrees	Model phase, degrees	95% confidence interval, degrees
CB0901	M2	20.58	0.24	17.63	1.14	139.94	0.59	136.58	4.56	153.01	0.82	164.24	3.85
	S2	3.91	0.24	3.09	1.15	144.57	2.96	137.57	25.51	193.38	3.89	182.19	19.57
	N2	4.90	0.24	3.56	0.95	136.63	2.34	145.60	23.37	129.74	2.92	132.74	14.22
	K1	2.79	0.22	2.52	1.49	138.48	4.28	129.16	30.38	233.33	4.79	197.74	26.37
	O1	2.56	0.24	2.13	1.46	130.25	4.05	129.88	34.20	248.35	5.28	272.65	39.11
CBIS	M2	33.74	0.95	23.22	0.57	124.60	0.84	154.65	0.62	166.95	1.74	120.46	1.51
	S2	5.92	0.90	3.61	0.63	122.83	5.47	156.36	3.43	177.15	9.79	153.10	10.78
	N2	7.17	0.95	4.70	0.63	126.85	4.50	157.96	2.68	147.31	7.86	91.68	7.61
	K1	3.53	0.82	1.72	0.29	139.87	15.27	56.90	23.74	75.78	22.11	243.36	10.34
	O1	4.69	0.79	1.11	0.50	135.29	5.75	7.97	66.38	105.52	10.47	326.69	84.39

Figure 1. Plan view of 50,000-cell CH3D Chesapeake Bay grid.

Figure 2. Rectilinear plan view of 50,000-cell CH3D Chesapeake Bay grid. In this view, all cells are represented as unit squares. This view emphasizes the number of cells in narrow reaches such as the tidal freshwater portions of the tributaries.
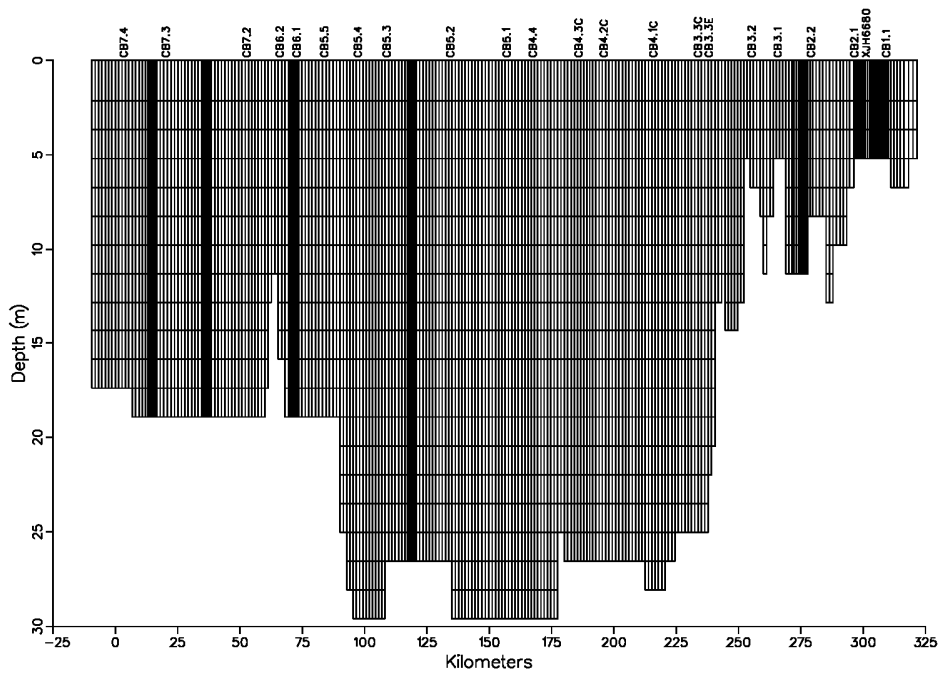
Figure 3. **Elevation view of grid along a transect from the mouth of the bay (km 0) to the head of tide (≈ km 320). Note that variations in depth are represented by variations in the number of cells in the vertical dimension.**
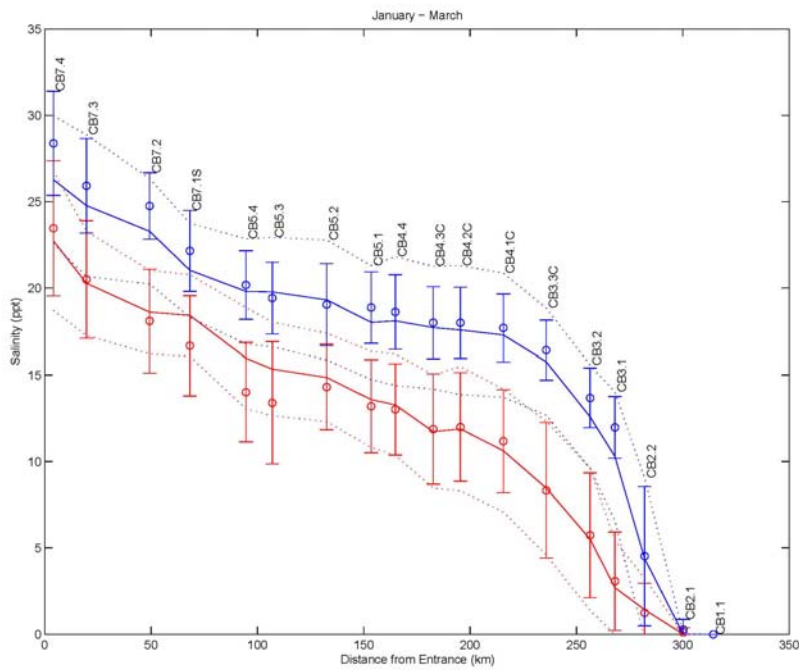
Figure 4. **Observed (circles and bars) and computed (solid and dotted lines) surface and bottom salinity (mean and range) along Chesapeake Bay axis January – March, 1993 – 1999.**
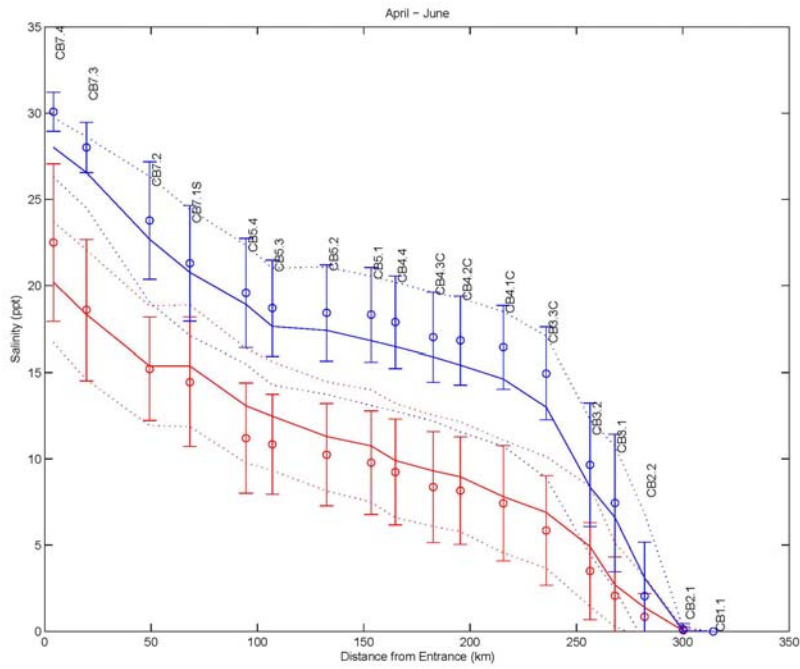
Figure 5. Observed (circles and bars) and computed (solid and dotted lines) surface and bottom salinity (mean and range) along Chesapeake Bay axis April – June, 1993 – 1999.
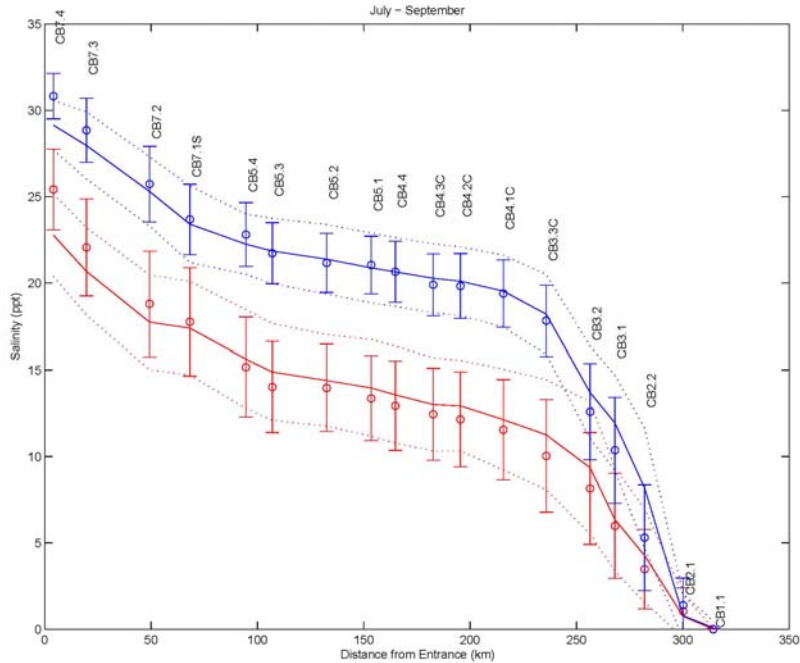

Figure 6. Observed (circles and bars) and computed (solid and dotted lines) surface and bottom salinity (mean and range) along Chesapeake Bay axis July – September, 1993 – 1999.

Figure 7. Observed (circles and bars) and computed (solid and dotted lines) surface and bottom salinity (mean and range) along Chesapeake Bay axis October – December, 1993 – 1999.
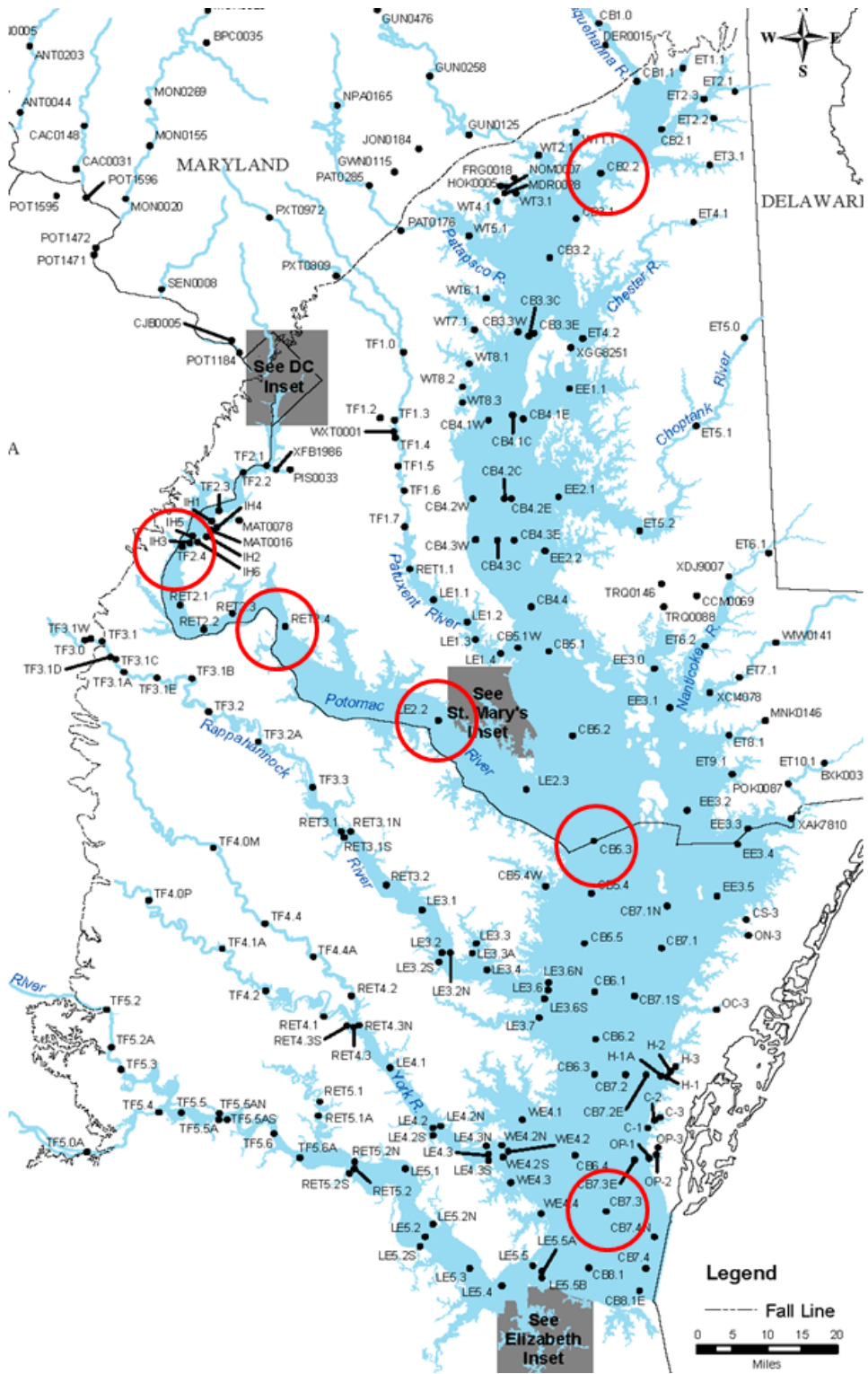
Figure 8. Stations for vertical casts and time series comparisons.
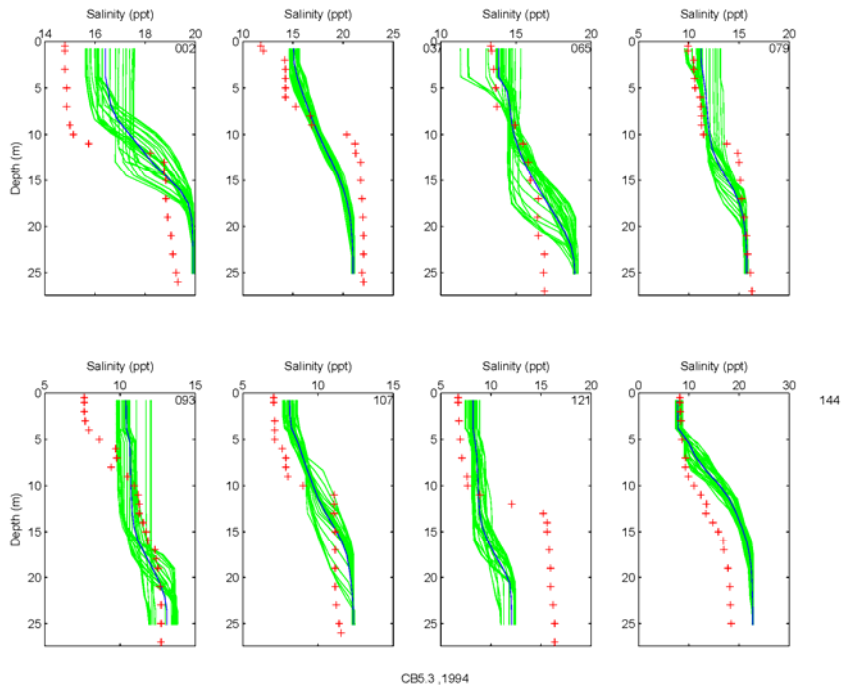
Figure 9. Observed (red crosses) and computed (solid lines) vertical salinity casts at Station CB5.3 for 1994. The green lines are hourly computations while the blue line is daily average on the day of the cast. Julian day is given in the upper right hand corner of each panel.
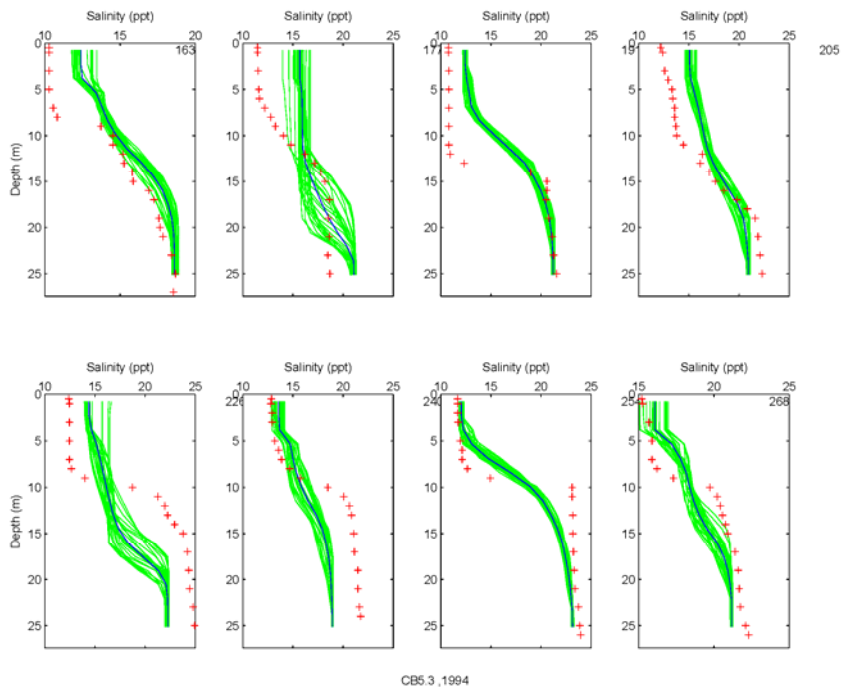
Figure 9 Continued.
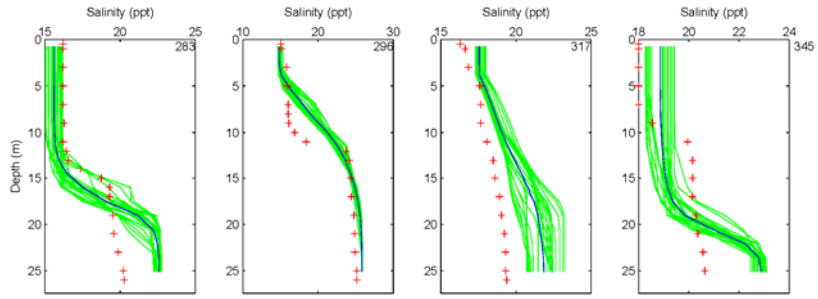
CB5.3 ,1994

Figure 9 Continued.
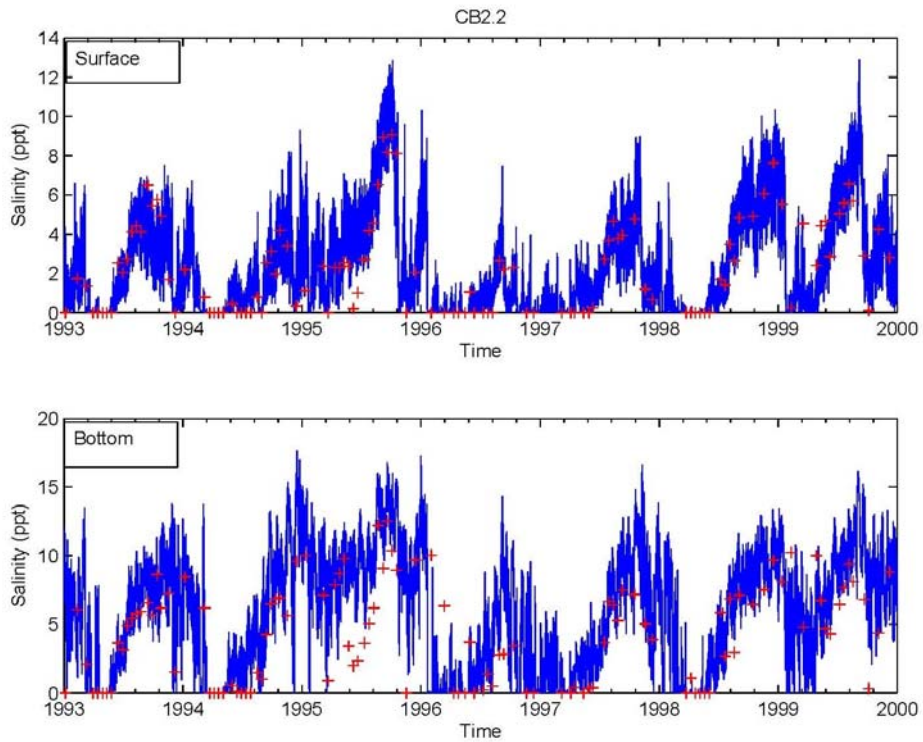
Figure 10. Observed and computed salinity time series (surface and bottom) at Station CB2.2.
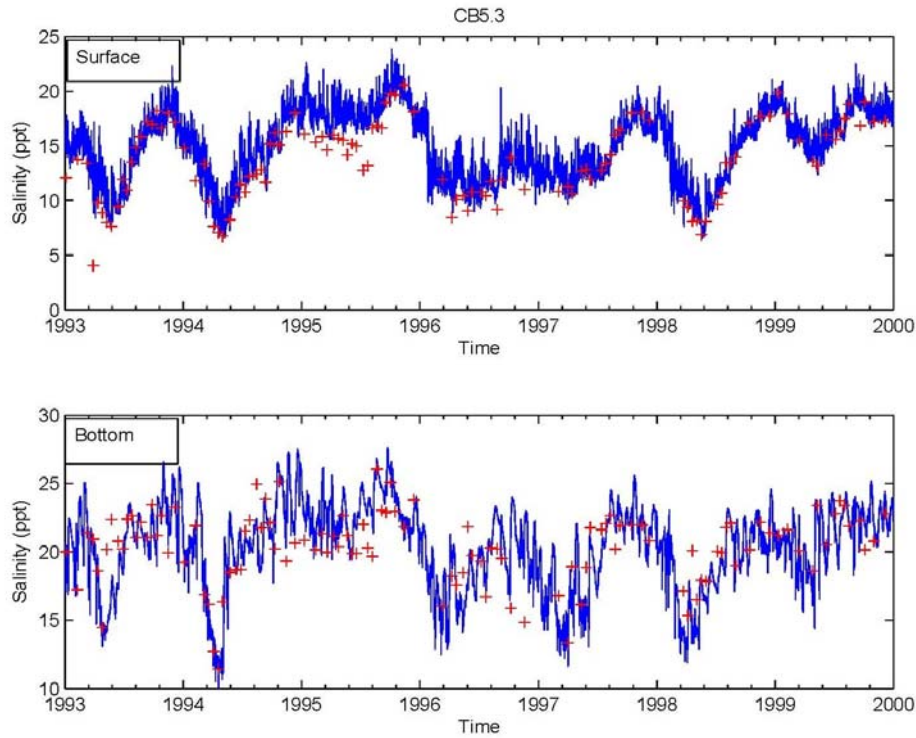
Figure 11. Observed and computed salinity time series (surface and bottom) at Station CB5.3.
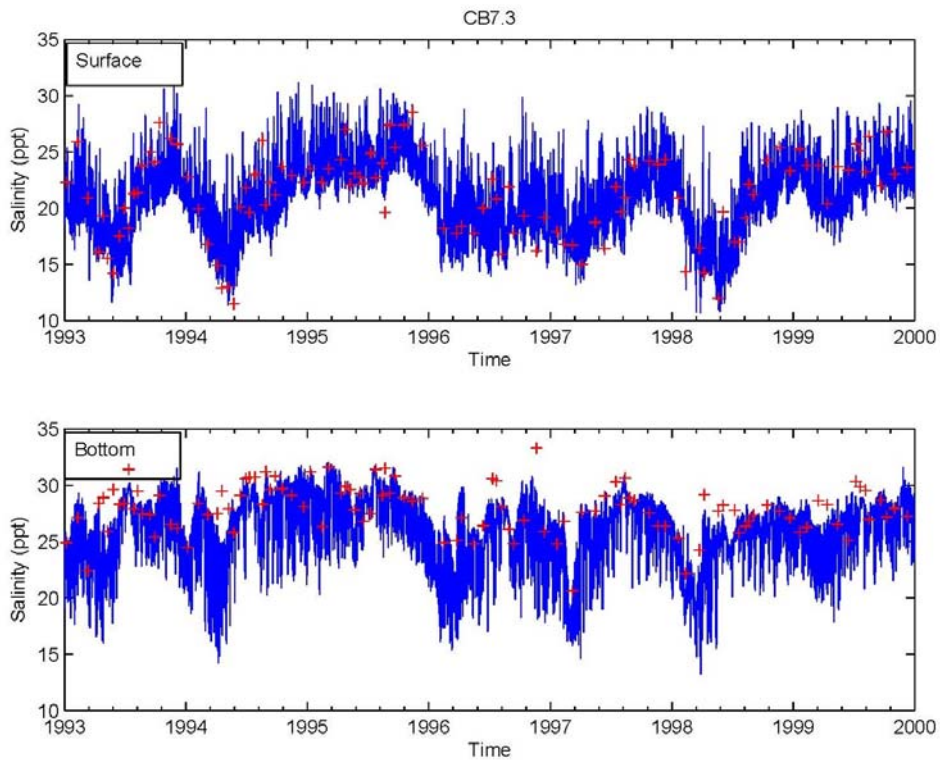
**Figure 12. Observed and computed salinity time series (surface and bottom) at Station CB7.3.**
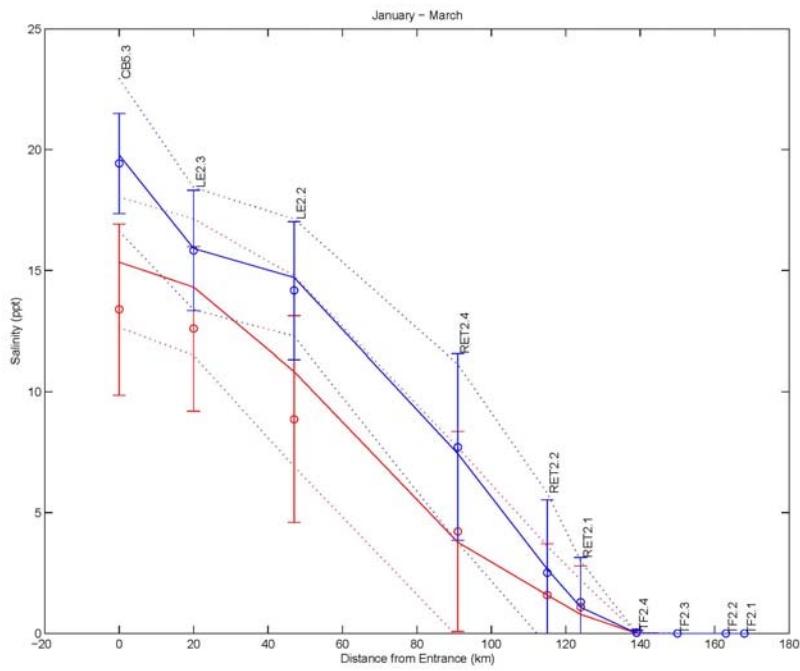
Figure 13. Observed (circles and bars) and computed (solid and dotted lines) surface and bottom salinity (mean and range) along Potomac River axis January – March, 1993 – 1999.
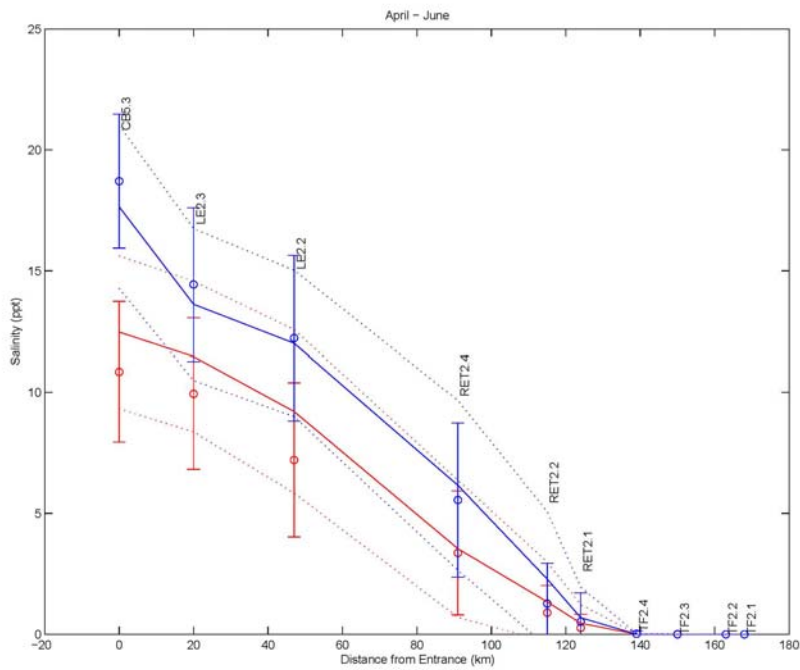
Figure 14. Observed (circles and bars) and computed (solid and dotted lines) surface and bottom salinity (mean and range) along Potomac River axis April - June, 1993 – 1999.
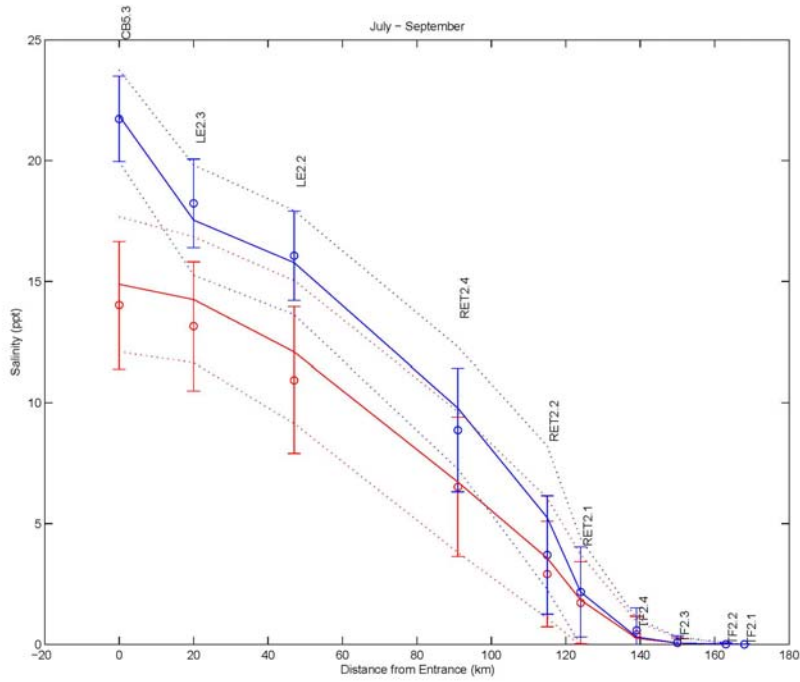
Figure 15. Observed (circles and bars) and computed (solid and dotted lines) surface and bottom salinity (mean and range) along Potomac River axis July - September, 1993 – 1999.
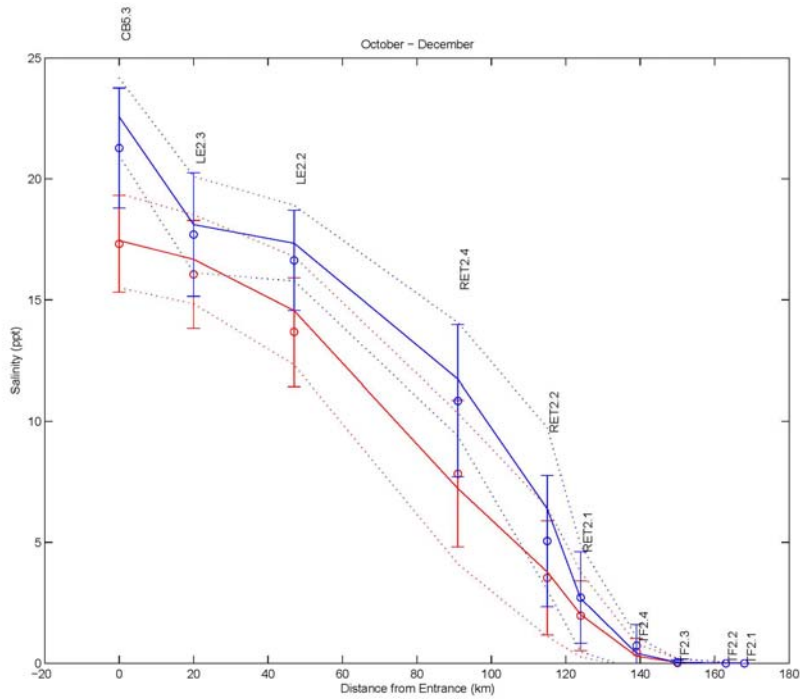
Figure 16. Observed (circles and bars) and computed (solid and dotted lines) surface and bottom salinity (mean and range) along Potomac River axis October - December, 1993 – 1999.
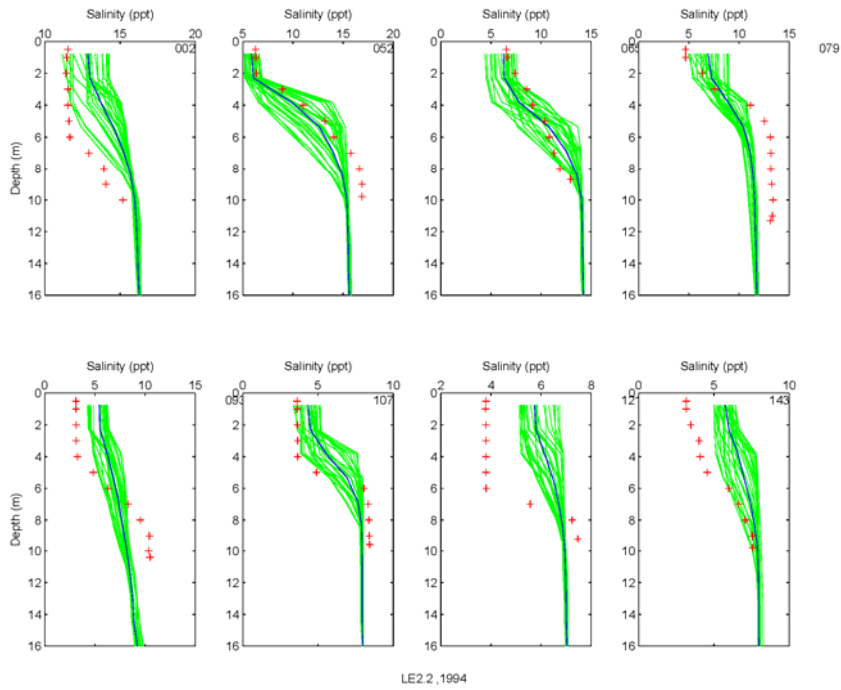
Figure 17. Observed (red crosses) and computed (solid lines) vertical salinity casts at Station LE2.2 for 1994. The green lines are hourly computations while the blue line is daily average on the day of the cast. Julian day is given in the upper right hand corner of each panel.
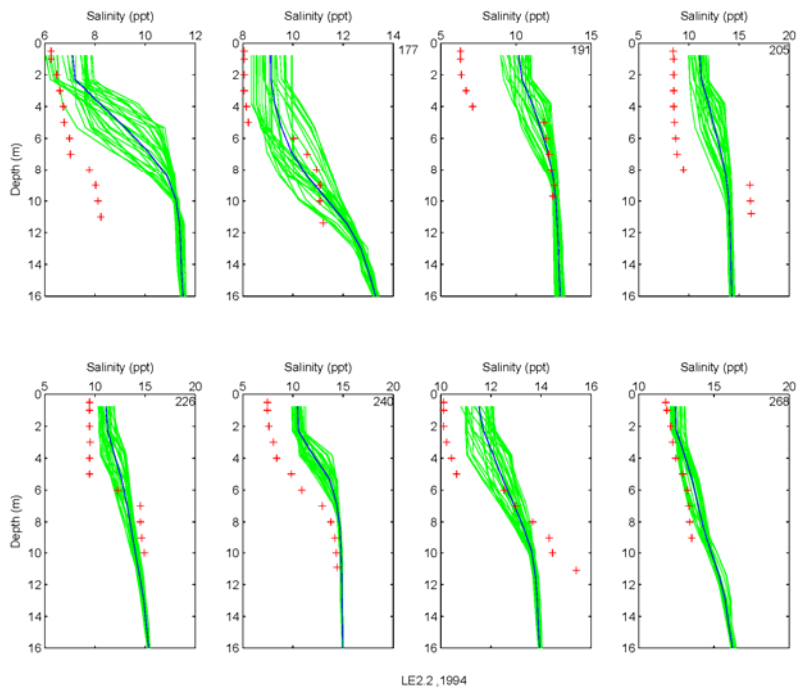

Figure 17 Continued.
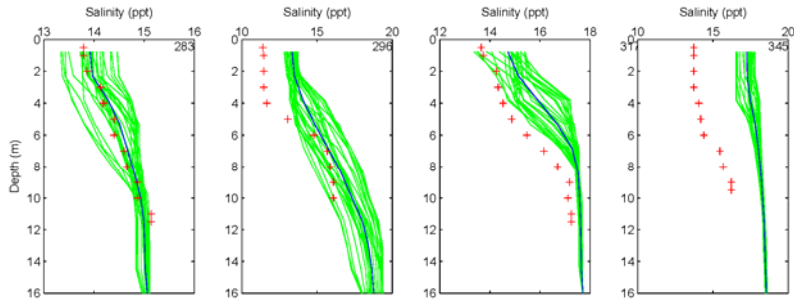
LE2.2 ,1994

Figure 17 Continued.
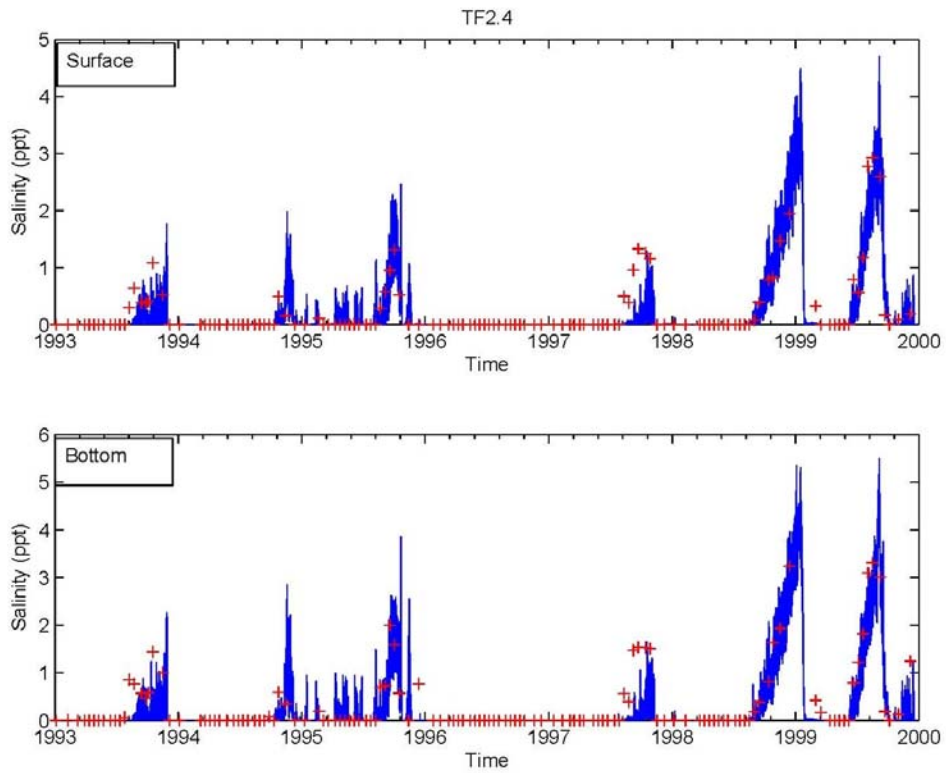
Figure 18. Observed and computed salinity time series (surface and bottom) at Station TF2.4.
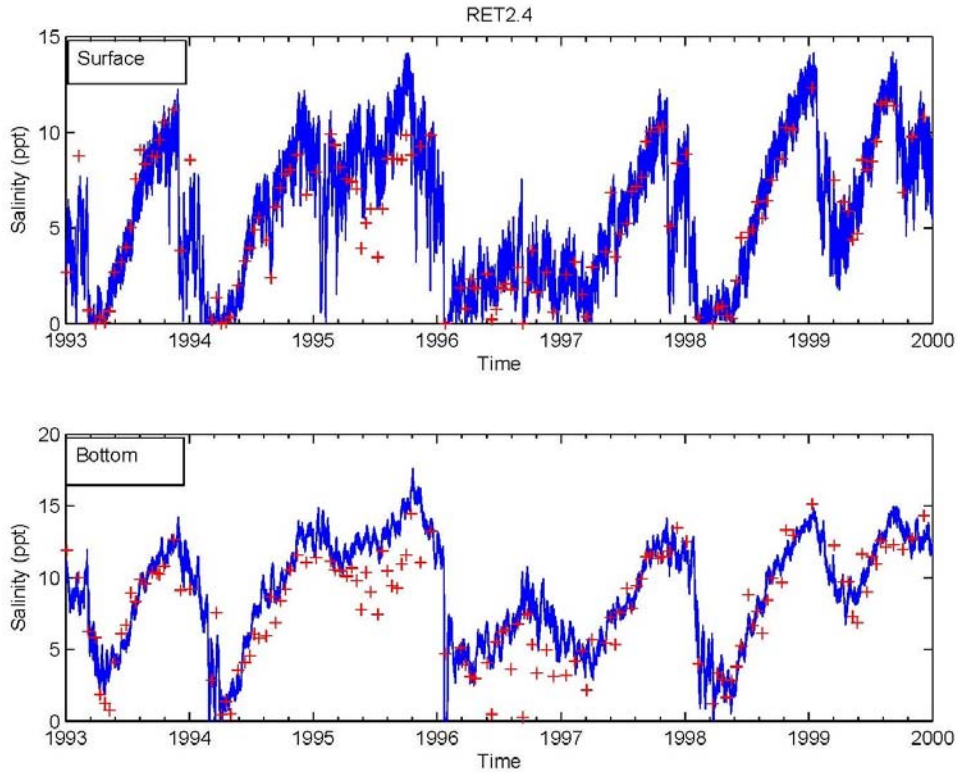
Figure 19. Observed and computed salinity time series (surface and bottom) at Station RET2.4.
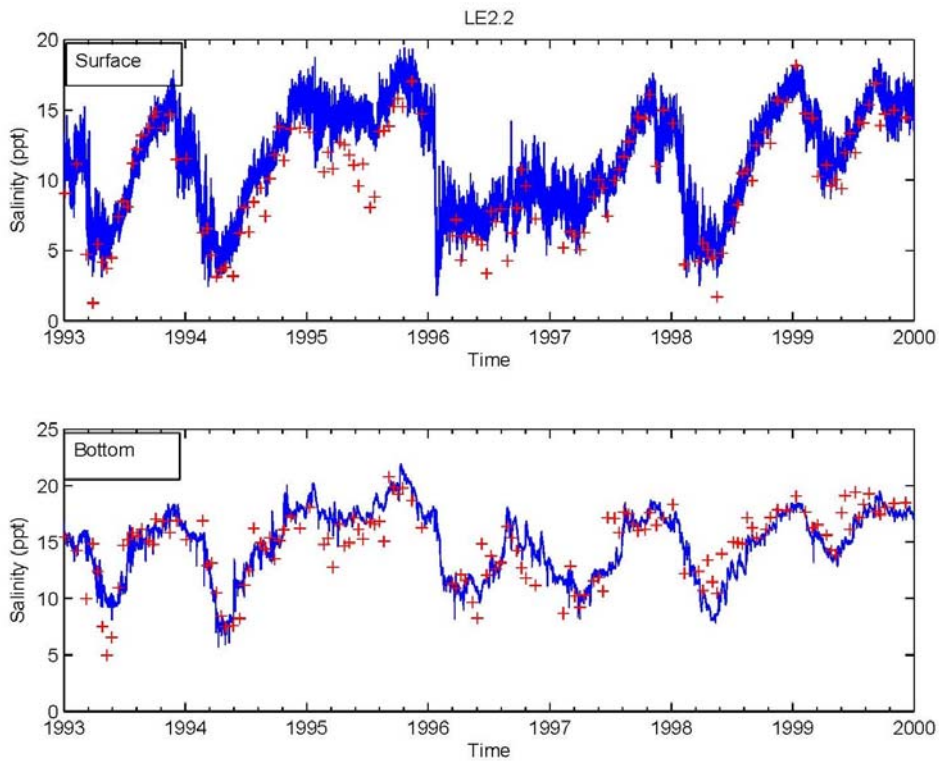

**Figure 20. Observed and computed salinity time series (surface and bottom) at Station LE2.2.**

**Figure 21. Location of Potomac River tide and current stations.**
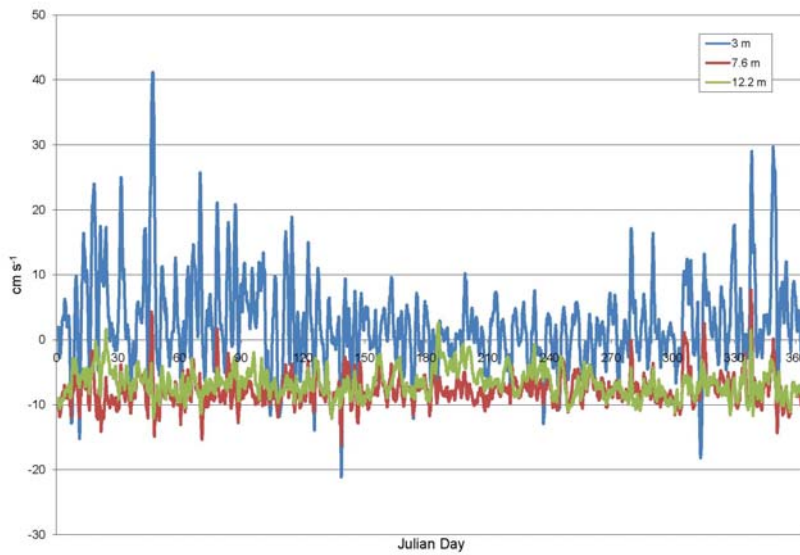
Figure 22. Model residual currents in Potomac River corresponding to Elliott's (1978) measurements.

3 Computation of Waves and Bottom Shear Stress

The Wave Model

Bottom shear stress is the principal forcing factor that produces sediment resuspension. Throughout most of the bay system, bottom shear stress is generated by currents above the bed. Currents are computed by CH3D and the resulting shear stress is computed as well, as one of the boundary conditions in the equations of motion. For some shallow regions of the bay, however, shear stress exerted by surface waves is significant relative to current-generated shear stress (Figure 1). Waves are not computed by CH3D and, consequently, an independent wave model is necessary. Wave-generated stress is combined with current-generated stress and the result is employed as a forcing function in the resuspension algorithms.

The Young and Verhagen (1996) model for fetch- and depth-limited waves is employed. The model computes non-dimensional wave energy, ε, and frequency, ν, as a function of non-dimensional fetch, χ, and depth, δ:

$$\varepsilon = 3.64 \times 10^{-3} \left\{ \tanh A_1 \left[\frac{B_1}{\tanh A_1} \right] \right\}^n \tag{1}$$

$$\nu = 0.133 \left\{ \tanh A_2 \left[\frac{B_2}{\tanh A_2} \right] \right\}^m \tag{2}$$

in which:

$$\varepsilon = wave\,energy, \frac{g^2 E}{U^4}$$

$$\nu = wave\,\,frequency, \frac{f_p U}{g}$$

g = gravitational acceleration
E = total wave energy
U = wind speed measured 10 m above water surface
fp = frequency of spectral peak

Parameters A_1, A_2, B_1, B_2, are given by

$$A_1 = 0.292^{1/n} \delta^{1.3/n} \qquad (3)$$

$$B_1 = \left(4.396 \times 10^{-5}\right)^{1/n} \chi^{1/n} \qquad (4)$$

$$A_2 = 1.505^{1/m} \delta^{3/8m} \qquad (5)$$

$$B_2 = 16.391^{1/m} \chi^{-0.27/m} \qquad (6)$$

in which:

$$\chi = fetch, \frac{g\,x}{U}$$

$$\delta = depth, \frac{g\,D}{U^2}$$

x = fetch (dimensional)
d = water depth (dimensional)
n, m = empirical parameters (1.74, -0.37, respectively)

From these, the significant wave height, h, and period, Tp, used to derive bottom stress and for comparison with observations, are derived

$$h = 4\sqrt{E} \qquad (7)$$

$$T_p = \frac{1}{f_p} \qquad (8)$$

Wave Model Results

Wind velocity over the bay was obtained through interpolation of observations at five locations: Thomas Point Light, Patuxent Naval Air Station, DC National Airport, Richmond International Airport, and Norfolk international Airport (Figure 2). Fetch was determined for each model surface cell for 16 directional bins (each 22.5 degrees). These were used to determine wave properties at hourly intervals for the model application period. Results were compared to wave height and period observed at several mid-bay locations (Figures 3, 4) and at Thimble Shoal, in the lower Bay (Figures 5 – 8). An overall assessment is that the model does well at computing wave height but underestimates wave period. At Thimble Shoal, the discrepancy may be due to the presence of ocean swells as well as locally-generated waves. The reason for the shorter modeled wave period in two of three comparisons at mid-bay is not clear.

Calculation of Bottom Shear Stress

The procedure for combining shear stress from currents and waves and for calculating skin friction is described by Harris et al. (2010). Four tasks are required:

- Characterize sediment grain size throughout the model grid.
- Obtain wave properties (from wave model) and current velocities (from CH3D hydrodynamic model).
- Estimate bed roughness.
- Calculate combined wave-current bed stress and skin-friction shear stress.

Note that the skin friction, which is used in sediment resuspension, is less than the total shear stress exerted on the bed.

Observed and Computed Bottom Shear Stresses

The comparisons of observed and computed bottom shear stresses are based on visual inspection of observed and computed records. The qualitative comparisons are required since, in most cases, the observations are available only in graphical format and, in several cases, represent time periods outside the primary model calibration period.

In the upper bay, observations over several tidal cycles indicate peak bottom shear stress is between 1 and 2 dyne cm^{-2} (Figure 9). Peak model values are of equivalent magnitude although the model shows a larger range since a longer period, with a greater variety of forcing functions is represented. Two independent studies are available from the lower bay. The first indicates peak current-generated bottom shear stresses are between 0.1 and 1 Pa (Figure 10). The model reflects these values well. The second study presents friction velocity, u_*. Observed values range between 0 and 2 cm s^{-1} (Figure 11) and this range is replicated in the model. The final record is of u_* observed in the mid York River (Figures 12, 13). Observed peak values are between 1 and 2 cm s^{-1}. The model reproduces the lower peaks well but falls short of the highest observed values. Overall, the model bottom shear stresses reflect the magnitude of the observations in multiple locations in the bay system and form a suitable basis for the sediment resuspension algorithms.

Acknowledgements

The algorithms for combining current-generated and wave-generated bottom shear stresses were developed by Dr. Courtney Harris and Mr. J. Paul Rinehimer of the Virginia Institute of Marine Science. The Thimble Shoal wave observations were provided by Dr. John Boon of the Virginia Institute of Marine Science. Upper Bay wave observations were provided by Dr. Larry Sanford of the Horn Point Environmental Laboratory, University of Maryland.

References

Fugate, D., and Friedrichs, C. (2002). "Determining concentration and fall velocity of estuarine particle populations using ADV, OBS, and LISST," *Continental Shelf Research* 22(10), 1867-1886.

Harris, C., Rinehimer, J. P., and Kim, S-C. (2010). "Representation of bed stresses within a model of Chesapeake Bay," VIMS Special Report No. XXX, Virginia Institute of Marine Science, Gloucester Point VA. (in press, available from Dr. Courtney Harris ckharris@vims.edu)

Kim, S-C., Friedrichs, C., Maa, J., and Wright, L. D. (2000). "Estimating bottom stress in tidal boundary layer from acoustic Doppler velocimeter data," *Journal of Hydraulic Engineering*, 126(6), 399-406.

Sanford, L., Panageotou, W., and Halka, J. (1991). "Tidal resuspension of sediments in northern Chesapeake Bay," *Marine Geology* 97(1-2), 87-103.

Wright, L. D., Boon, J., Xu, J., and Kim, S-C. (1992). "The bottom boundary layer of the bay stem plains environment of lower Chesapeake Bay," *Estuarine, Coastal and Shelf Science* 35(1), 17-36.

Young, I., and Verhagen, L. (1996). "The growth of fetch limited waves in water of finite depth. Part 1. Total energy and peak frequency," *Coastal Engineering* 29, 47-78.
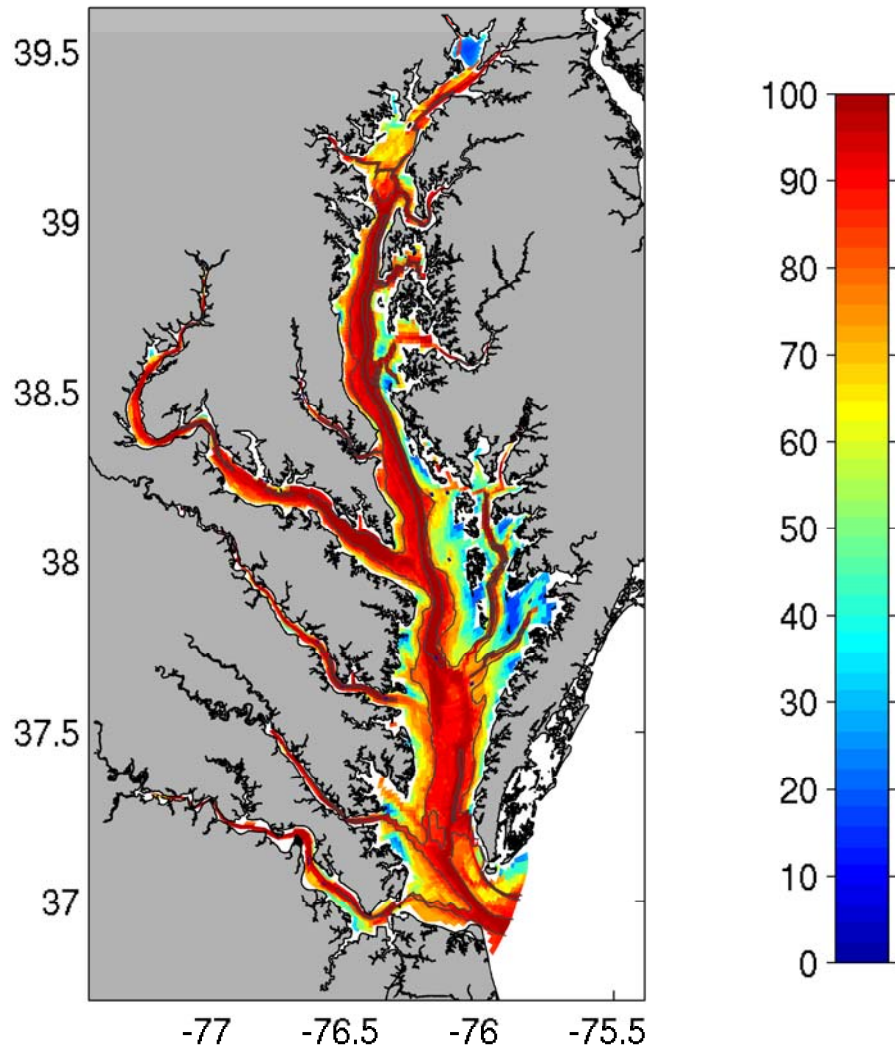
Figure 1. Percent of time that bed shear stress is dominated by currents.
Calculated as the percent of hourly timesteps that u_{*c} / u_{*cw} > 0.9. Wave activity is
**significant in areas colored blue to green. (After Harris et al. 2010)**
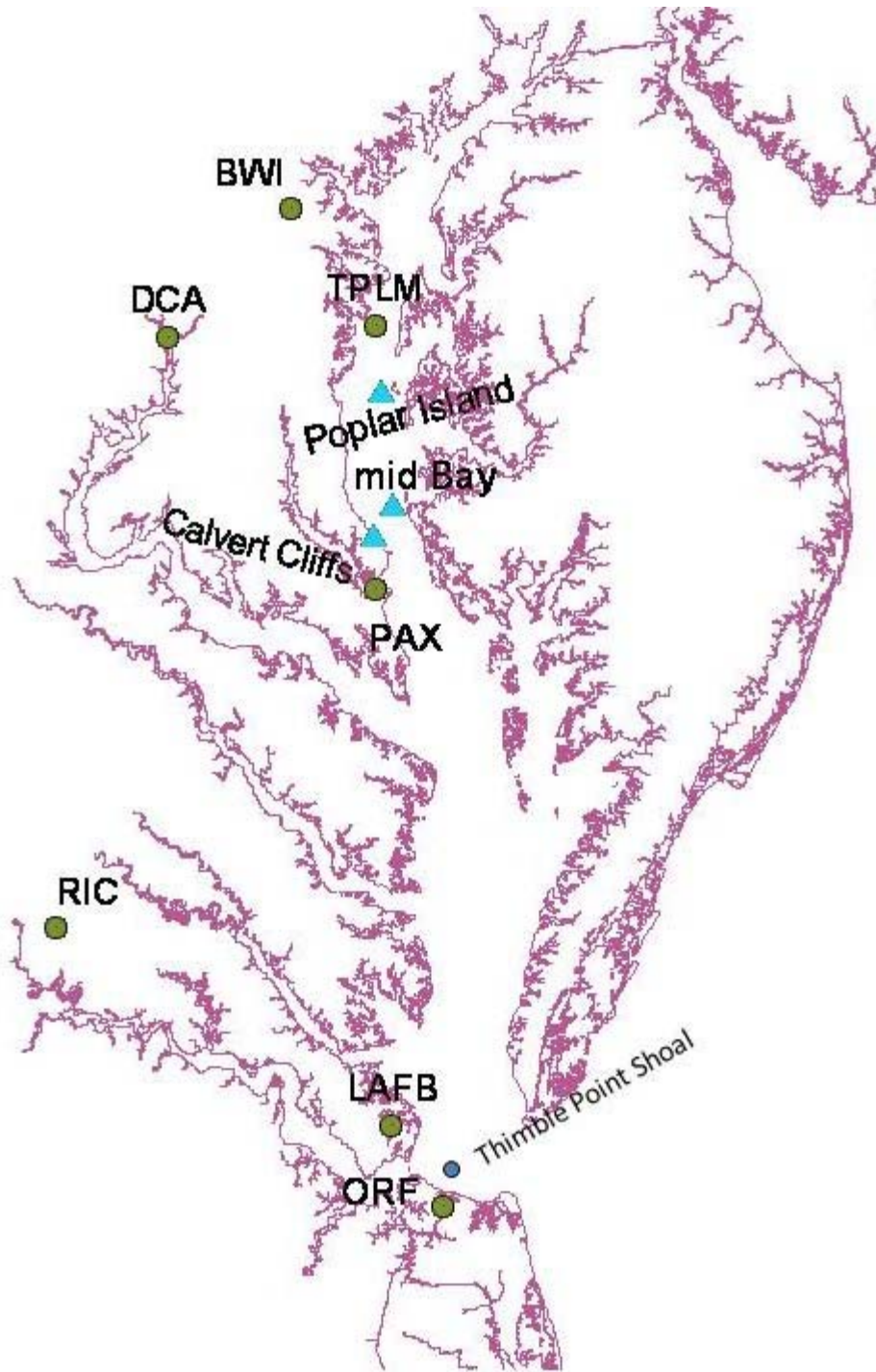
Figure 2. Location map. Stations for wind data include RIC, ORF, PAX, DCA, TPLM. Mid-bay stations for wave data shown as blue triangles. Thimble shoal wave station shown as blue circle.
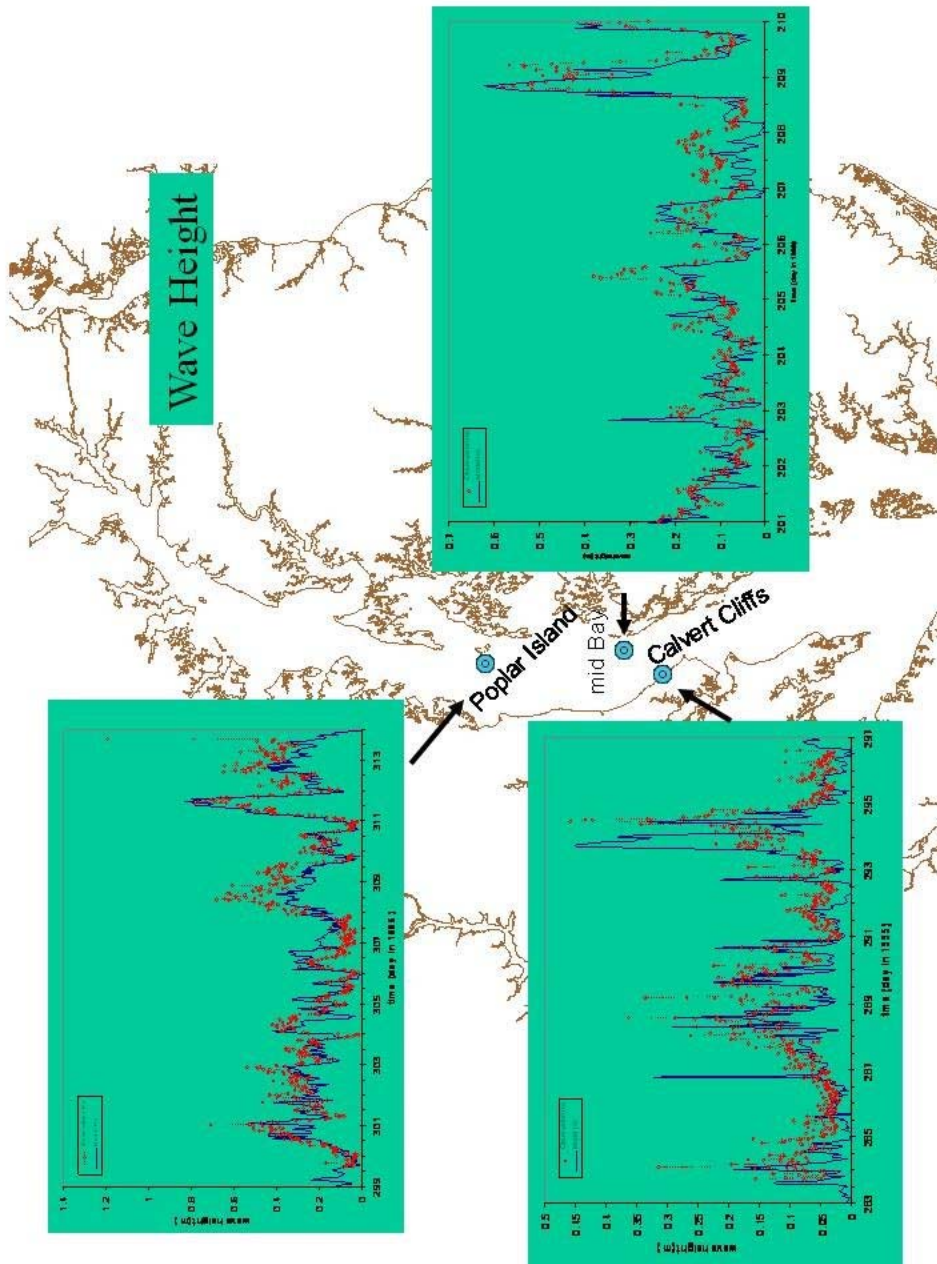
Figure 3. Observed and computed wave height at three mid-bay stations.
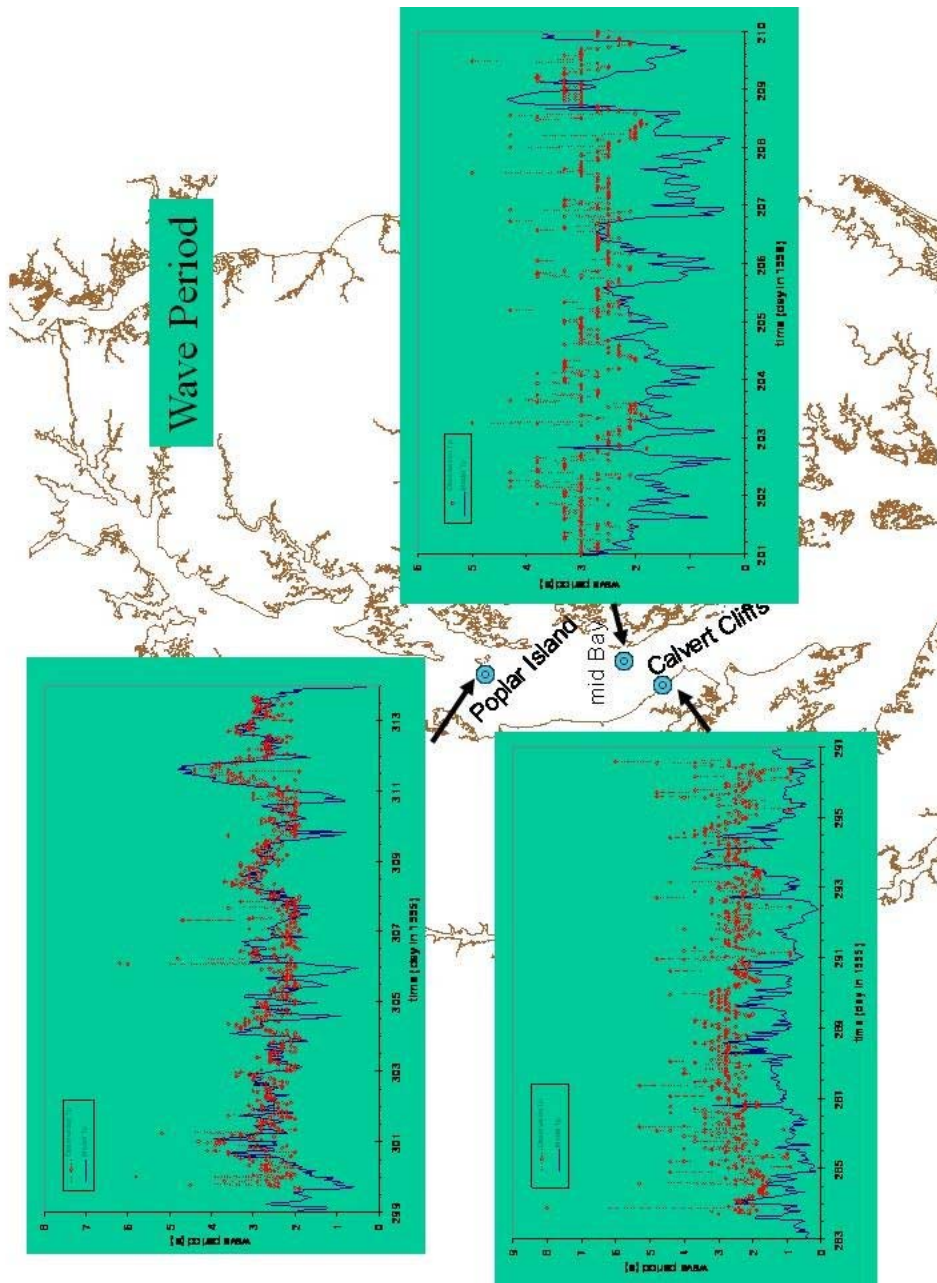
Figure 4. Observed and computed wave period at three mid-bay stations.

Thimble Shoal wave height
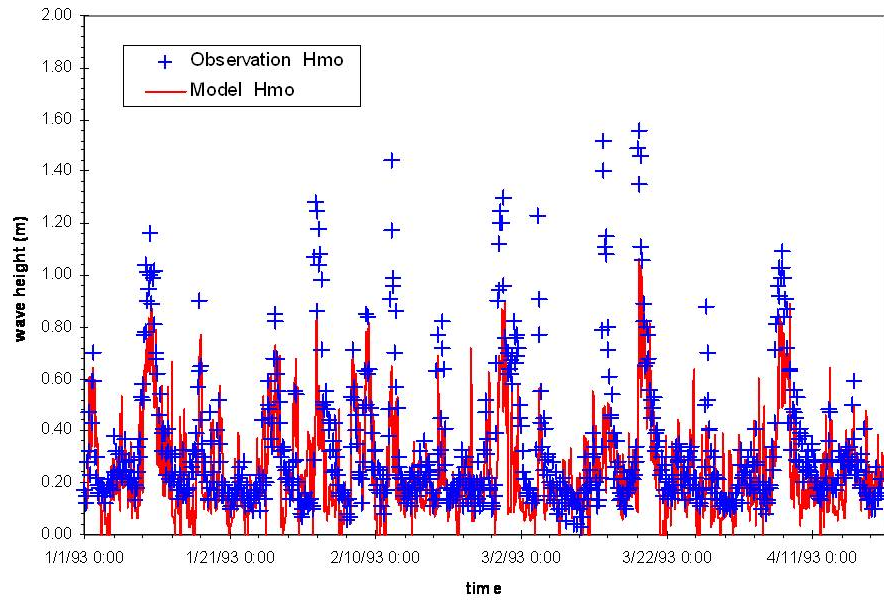
Figure 5. Observed and computed significant wave height at Thimble Shoal January – April 1993.

Thimble Shoal wave height
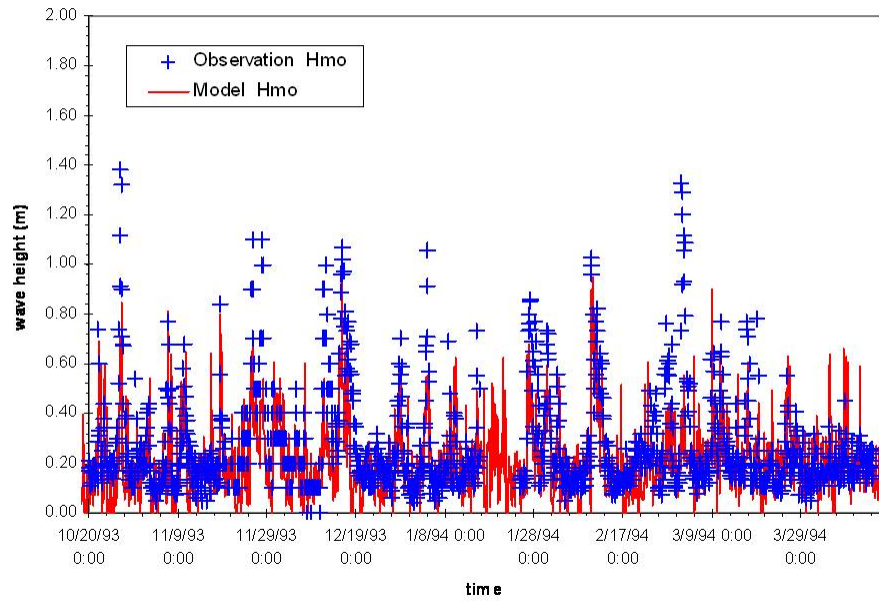
Figure 6. Observed and computed significant wave height at Thimble Shoal October 1993 – March 1994.

Thimble Shoal wave height
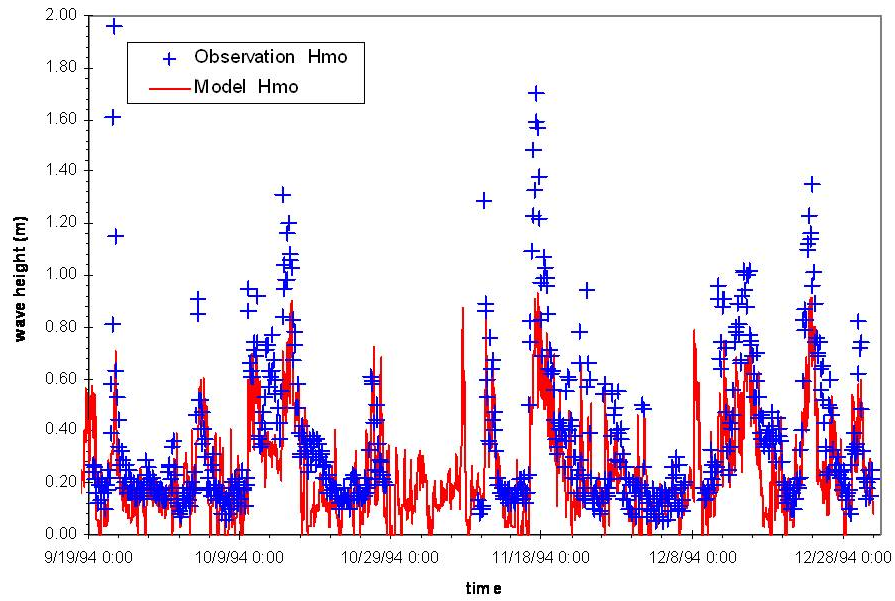
Figure 7. Observed and computed significant wave height at Thimble Shoal September – December 1994.

Thimble Shoal wave period
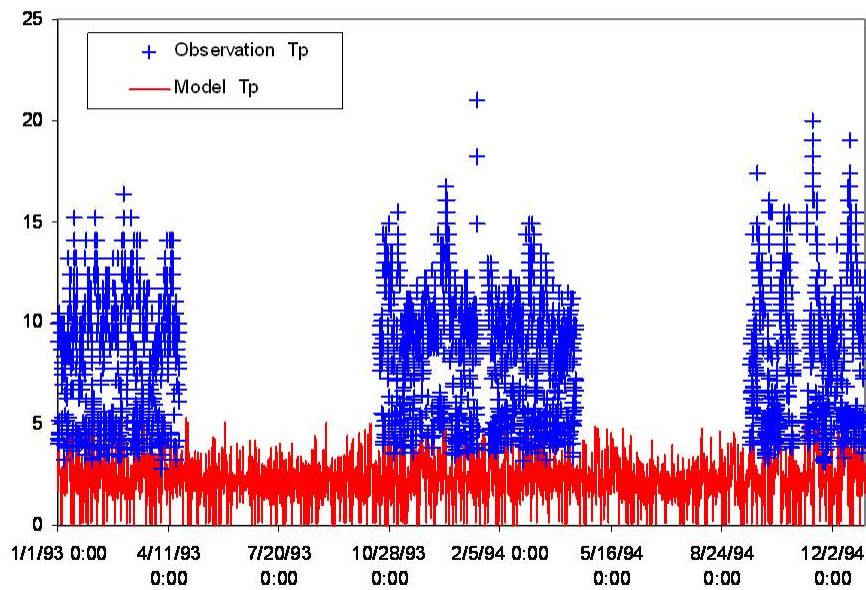
**Figure 8. Observed and computed wave period at Thimble shoal January 1993 – December 1994.**
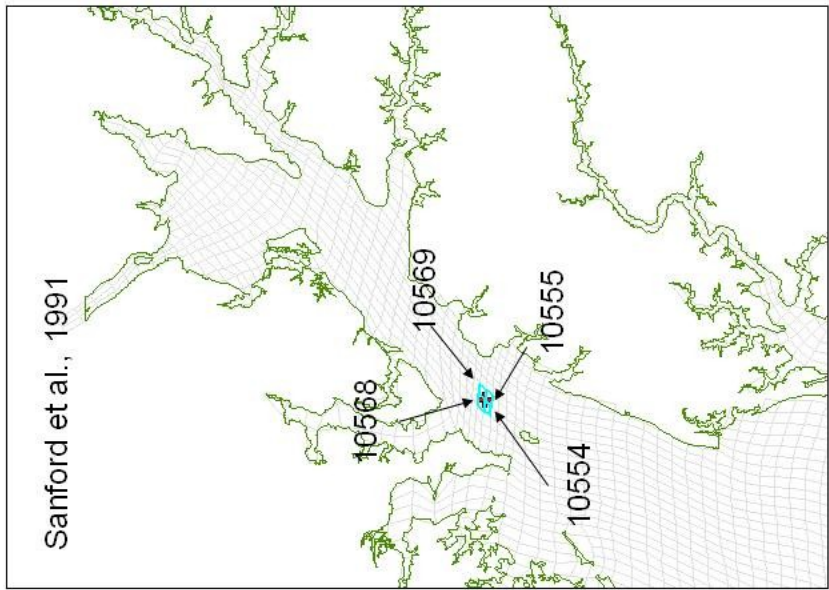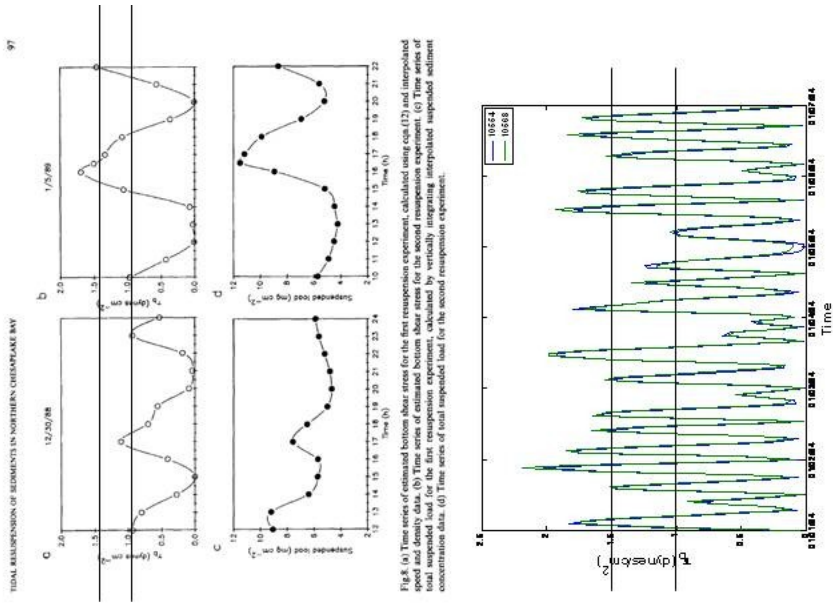
Figure 9. Observed and computed bottom shear stress at an upper bay station. The discrete sample station falls at the intersection of several model cells. Computations are shown for two cells, 10554 and 10569.
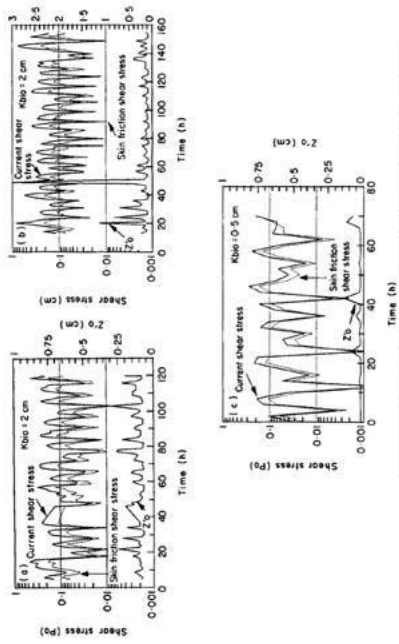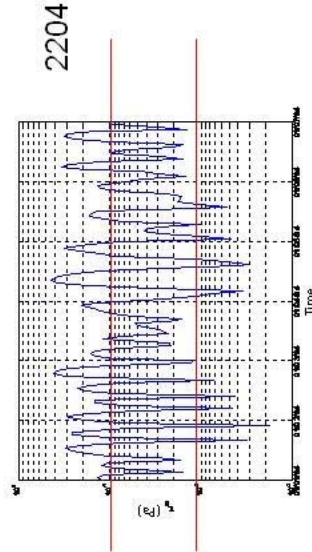
Figure 10. Observed and computed bottom shear stress at a lower bay station. Model results are shown for cell 2204.
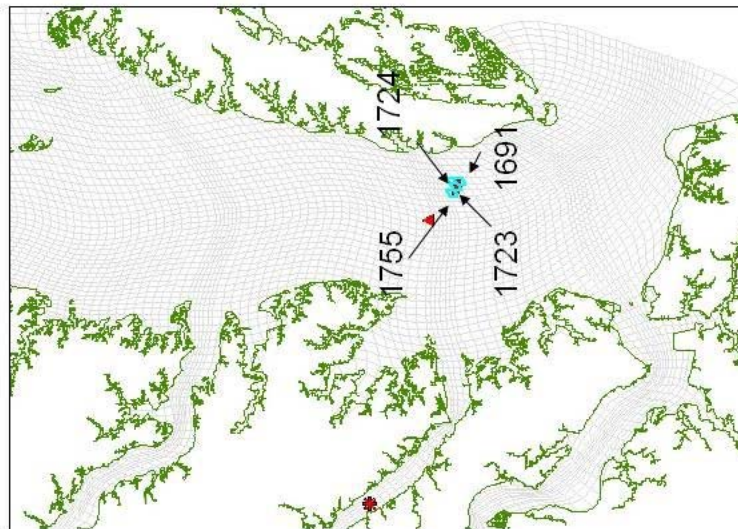
Figure 11. Observed and computed friction velocity at a lower bay station. Computations are shown for model cell 1723.
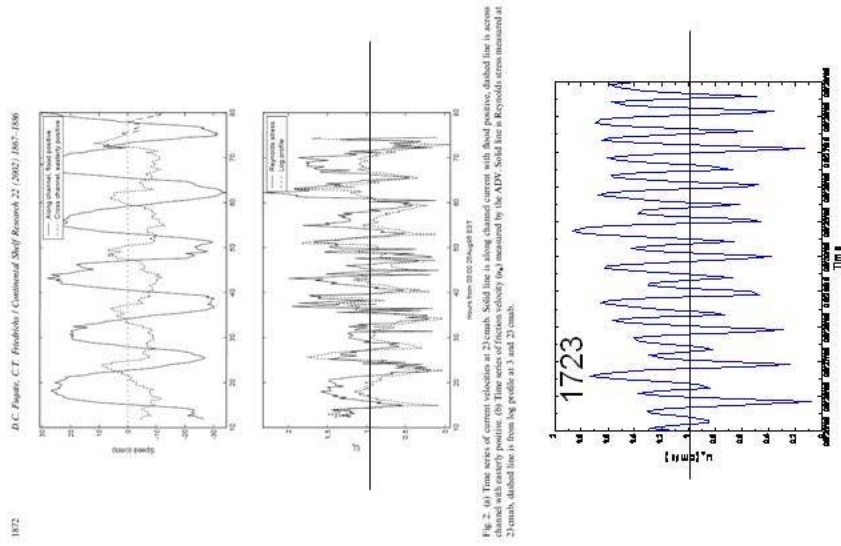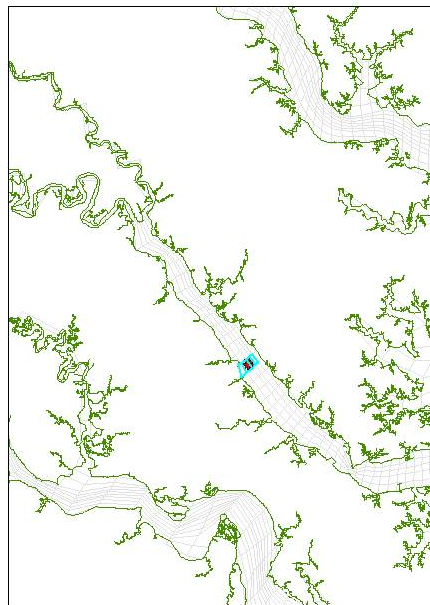
Kim et al., 2000
•Using ADV
•Off Clay Bank
•On secondary channel
•April, 1996
•10 days deployment

Cells from W to E
•1830
•1903
•1973
•2043

Figure 12. Location of measures in the central York River. The sample site intersects with several model cells.

Observed and predicted friction velocity off Clay Bank
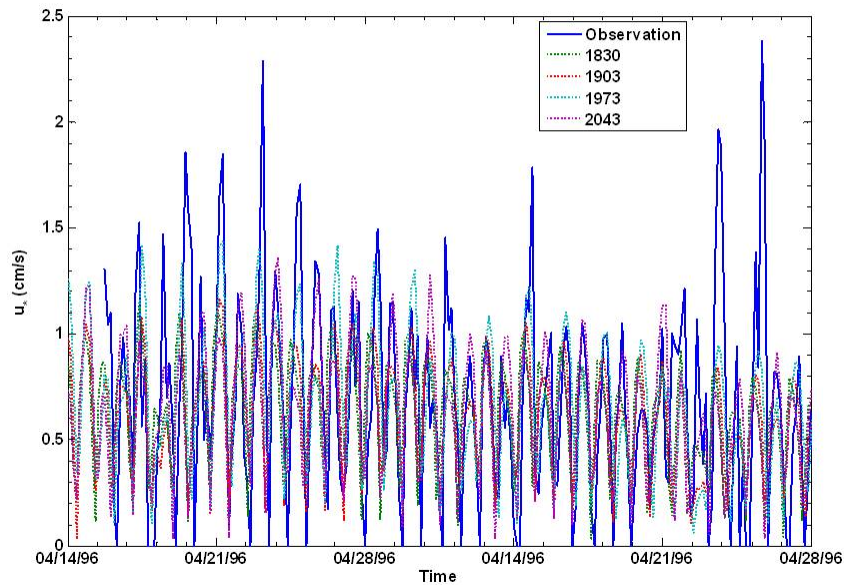
Figure 13. Observed and computed friction velocity in the central York River. Computations are shown for four cells which adjoin the sample site.

4 Bankloads

Introduction

The 2002 study (Cerco and Noel 2004) identified solids loads from bank erosion as a major source of suspended solids to the bay and tributaries. The data base for quantification of loads (USACE 1990) was sparse, however, and the loads were input to the model on a spatially and temporally uniform basis. For the present study, we determined to complete the best possible quantification of bank loads. These loads were to be based on current information and to reflect spatial variability caused by local shoreline characteristics and on the presence of shoreline structures. The resulting estimates were multi-decadal averages based on shoreline recession determined from aerial surveys and hydrographic maps. Temporal variation was determined from computed waves and surface elevation as described herein. Primary references for the determination of bankloads are the report by Hennesee et al. (2006) and a PowerPoint presentation (Halka and Hopkins 2006). Methods for determining bankloads, gleaned from these reports, are summarized below.

Methods

Quantifying solids loads from bank erosion requires two fundamental calculations. First, calculate the volume of sediment lost from erosion. Then, convert sediment volume into sediment mass. The volume is determined:

$$V = L \cdot W \cdot H \tag{1}$$

in which:

V = volume of annual sediment loss from shore erosion ($m^3 \ yr^{-1}$)
L = shoreline length (m)
W = rate of shoreline retreat ($m \ yr^{-1}$)
H = bank height or marsh elevation (m)

Volume is converted to mass via:

$$Mtotal = Bd \cdot V \tag{2}$$

in which:

Mtotal = total mass of annual sediment (sand, silt, and clay) loss from bank erosion (kg yr^{-1})
Bd = dry bulk density of eroding bank (kg m^{-3})

Approximately 250,000 shoreline-normal transects were available for the Maryland shoreline alone to determine the rate of shoreline retreat. Available Maryland shorelines spanned the period from approximately 1850 to1990. For the model calculations the two most recent shorelines in each analyzed reach or section were utilized. For most areas, the two most recent shorelines dated from *circa* 1940 and *circa* 1990, though intervals shorter and longer than 50 years occurred. Shoreline characteristics, notably the presence of protective structures, were reported in surveys conducted by Virginia Institute of Marine Science. Still, complete information for the system-wide characterization of shorelines was missing. When necessary, missing information (recession rate, presence of structures, bulk density) was filled in based on information from adjacent shoreline reaches or on regional average characteristics. Other key assumptions included:

- Erosion of fastland from unprotected shorelines represents 65% of the total load; nearshore erosion represents 35% (Figure 1).
- No sediment is eroded, from fastland or nearshore, along accreting shorelines.
- No sediment is delivered to the bay from fastland protected by structures. However, the nearshore in regions protected by structures erodes at the same rate as nearby unprotected reaches.
- The average dry bulk density of banks is 1.38 g cm^{-3} and of marshes 0.62 g cm^{-3}.
- On average, silts and clays constitute 56% of sediment eroded from banks and 44% of sediment eroded from marshes.
- Organic matter is delivered only from marsh erosion and constitutes 34% of this material.
- Bulk density and composition of nearshore sediments are the same as adjacent fastland.

Summary

Results indicate the bay shoreline above the Potomac River junction produces the largest sediment mass per unit shoreline length (Figure 2). Reaches with high erosion are also found in the Potomac River, the Rappahannock River, and the James River. Although the Virginia shoreline is longer than Maryland and less protected (Table 1), the largest sediment loads originate in the Maryland portion of the bay system. Both the total loading and the loading per unit shoreline length are higher in Maryland than in Virginia.

Mapping Bankloads to the WQSTM

The bankload study resulted in decadal-average mass erosion rates per unit shoreline length throughout the bay system. For some regions, with complete information, the rates were available on the spatial scale of shoreline structures. For other regions, necessary information was lacking (Figures 3, 4)

and uniform erosion rates were employed for kilometers of shoreline length. The CBP GIS team merged three key pieces of information: mass erosion rates, shoreline length, and CBEMP computational grid. Shoreline length was assigned to each cell adjoining the shore (2,928 cells) and the mass loading to each cell was computed. The loading was partitioned into coarse material, fine material, and organic material. This information was supplied to the CBEMP team.

The CBEMP team partitioned the decadal-average loads into daily loads for the model application period (1985-2005). An outline of the procedure is as follows:

- Compute the total bank load to each cell for the application period (21 years * annual average load).
- Compute the daily energy dissipated on the shoreline of each cell by wave action and inundation.
- Sum the daily energy into total energy dissipated on the shoreline of each cell over the application period.
- Assign daily loads according to the fraction of total energy dissipated on each day of the application period.

Waves and Inundation

Erosion of banks is caused by both wave action and flooding. The energy per unit crest width contained in a single wave is (Sorensen 2006):

$$E = \frac{\rho \cdot g \cdot H^2 \cdot L}{8}$$ (3)

in which:

E = energy per unit width in a single wave (kg m^2 s^{-2} m^{-1} or joule m^{-1})
ρ = density of water (kg m^{-3})
g = gravitational acceleration (m s^2)
H = wave height (m)
L = wave length (m)

The total energy exerted in a day is computed by multiplying the energy in a single wave by the number of waves per day (daylength / period).

The energy exerted by inundation was derived as follows. Consider that each wave sits atop a sea surface elevated Δz above mean sea level (Figure 5). The potential energy, relative to mean sea level in one wavelength is the product of mass, gravitational acceleration, and height of the centroid above mean sea level:

$$Ep = \rho \cdot \Delta z \cdot L \cdot g \cdot \frac{\Delta z}{2} = \frac{\rho \cdot g \cdot \Delta z^2 \cdot L}{2}$$ (4)

in which:

Ep = potential energy per unit width in the volume of water between the wave and mean sea level (joules m^{-1})

As with wave energy, this potential energy beneath each wave must be multiplied by the number of waves in a day. Summing the two energies, simplifying, and multiplying yields the total energy exerted per unit crest width in a day:

$$Et = \rho \cdot g \cdot \left[\frac{H^2}{4} + \Delta z^2 \right] \cdot \frac{L}{2} \cdot \frac{D}{T} \tag{5}$$

in which

Et = daily total energy exerted per unit wave crest width (joules m^{-1})
D = daylength (86,400 s)
T = wave period (s)

Occasionally the sea surface exhibits a "set down" due the local or remote wind effects. In the event of set down (negative Δz), the energy exerted by inundation was set to zero.

Results

Energy in individual components, waves and inundation, is shown for four locations (Figure 6) around the bay for the initial model application period, 1994-2000. The inundation energy is dominant (Figures 7 – 10), especially in the riverine portion of the Potomac.   Waves are significant only on the lower eastern shore. The results conform to a conceptual model in which flooding is the dominant erosion process in constrained reaches near major freshwater inflows. Waves are significant on shorelines fronted by large expanses of open water subject to large fetch.

Model computations indicate the bankloads add $\approx$ 5 g m^{-3} suspended solids to adjacent waters, when the loads are averaged over the submerged aquatic vegetation growing season (the period when light attenuation is critical) (Figures 11-13).   The greatest effects take place in narrow tributaries when the ratio of shoreline length to receiving water volume is least.

Interior Marsh Erosion

Erosion from marshes located along the shorelines of the bay and tributaries was included in the estimation of bankloads. Substantial erosion also occurs in interior marshes, however, especially on the eastern shore of the bay between the Choptank and Pocomoke Rivers (Kearney et al. 2002). Mass erosion rate from interior marshes in this area was calculated based on the following principles:

- An annual loss rate of 0.5% of marsh area was assumed.

- For conversion of area eroded to volume, a marsh elevation of 0.5 m was assumed. Erosion depth was 0.5 m.
- The composition of interior marsh material differs from banks and shoreline marshes. Interior marsh material was assigned bulk density of 0.33 g cm^{-3} and the following composition: sand (1%), silt (23%), clay (51%), and organic matter (25%). (Kearney and Ward 1986; Kearney et al. 1988; Kearney et al. 1994)
- Loads were routed to 307 WQSTM surface cells adjacent to the interior marshes.

Marsh erosion is a significant source of fine material to the bay (Table 2), especially in view of the localized nature of the source. Marsh erosion is calculated to increase suspended solids by more than 5 g m^{-3} along the lower eastern shore (Figures 14 – 16).

Wetlands DO Uptake

Tidal wetlands of various types are present throughout the bay system (Figure 17). These wetlands exchange water, dissolved, and particulate substances with the adjacent open waters twice a day. Comprehensive calculation, or even quantification, of the multitude of wetland processes that affect the overlying water is beyond the scope of this study. Experience (Cerco and Noel 2004) has shown, however, that a first-order approximation of wetlands dissolved oxygen uptake is both feasible and required. Based on previous experience, wetlands dissolved oxygen consumption of 1 g m^{-2} d^{-1} at 20 °C was assigned. This rate was adjusted, on a daily basis, according to average temperature in a tidal freshwater system with extensive wetlands (Figures 18, 19):

$$SOD(t) = SODb \cdot e^{0.069 \cdot (T-20)} \qquad (3)$$

in which:

SOD(t) = sediment oxygen consumption on any day, t (g DO m^{-2} d^{-1})
SODb = sediment oxygen consumption at 20 °C (g DO m^{-2} d^{-1})
T = long-term mean temperature on any day, t (°C)

Wetland areas were summed into Phase 5 Watershed Model land-river segments. Individual surface cells in the WQSTM computational grid were assigned wetland areas based on the fraction of the land-river segment drainage area assigned to that cell. Areal DO uptake was converted to a mass basis by multiplying oxygen consumption and wetlands area (g DO m^{-2} d^{-1} * m^{2} * kg / 1000 g = kg DO d^{-1}). This mass was treated as a negative load and input to the model in the same loading file as the bankloads and marsh loads. Wetlands are calculated to remove up to 2 g m^{-3} DO from portions of the system (Figure 20 – 22). The wetlands DO uptake plays a significant role in the DO calibration (Figures 17, 18) although other DO sinks apparently exist and must be correctly represented.

Acknowledgements

Jeff Halka, of the Maryland Department of Natural Resources – Maryland Geological Survey, led the team which computed loads from bank and marsh erosion. Kate Hopkins, of the University of Maryland and EPA Chesapeake Bay Program, performed the GIS operations. Scott Hardaway, of the Virginia Institute of Marine Science, provided invaluable assistance in computing bankloads in the Virginia portion of the bay.

References

Cerco, C., and Noel, M. (2004). "The 2002 Chesapeake Bay eutrophication model," EPA 903-R-04-004, Chesapeake Bay Program Office, US Environmental Protection Agency, Annapolis MD. (available at http://www.chesapeakebay.net/modsc.htm)

Hennessee, L., Offerman, K., and Halka, J. (2006). "Suspended sediment load contributed by shore erosion in Chesapeake Bay, Maryland," Coastal and Estuarine Geology File Report No. 06-03, Maryland Geological Survey, Baltimore MD.

Halka, J., and Hopkins, K. (2006). "Final WQM shoreline report," PowerPoint presentation to Chesapeake Bay Program Modeling and Research Subcommittee, Annapolis MD. (available from Jeff Halka, Maryland Geological Survey, JHalka@dnr.state.md.us)

Hardaway, S., Thomas, G., Glover, J., Smithson, J., Berman, M., and Kenne, A. (1992). "Bank erosion study," SRAMSOE 391, Virginia Institute of Marine Science, Gloucester Pt. VA.

Kearney, M. S., and Ward, L. (1986). "Accretion rates in brackish marshes of a Chesapeake Bay estuarine tributary," *Geo-Marine Letters* 6**,** 41-49.

Kearney, M. S., Grace, R. E., and Stevenson, J. (1988). "Marsh loss in Nanticoke Estuary, Chesapeake Bay," *Geographical Review* 78(2), 205-220.

Kearney, M. S., Stevenson, J., and Ward, L. (1994). "Spatial and temporal changes in marsh vertical accretion rates at Monie Bay: Implications for sea-level rise," *Journal of Coastal Research* 10**,** 1010-1020.

Kearney, M., Rogers, J., Townshend, E., Rizzo, E., Stutzer, D., Stevenson, J., and Sundborg, K. (2002). "Landsat Imagery Shows Decline of Coastal Marshes in Chesapeake and Delaware Bays," *Eos* 83(16), 173, 177-178.

Sorensen, R. (2006). "Two-dimensional wave equations and wave characteristics." *Basic Coastal Engineering*. 3rd ed., Springer, New York, 22-23.

United States Army Corps of Engineers. (1990). "Chesapeake Bay shoreline erosion study," Feasibility Report October 1990, Baltimore District, Corps of Engineers, Baltimore MD.

Table 1
Summary of Shoreline Erosion Loads to Chesapeake Bay
(from Halka and Hopkins 2006)

	Maryland	Virginia
Total Length, m	2,912,000	4,060,000
Unprotected Length, m	1,993,000	3,276,000
Percent Protected	32	19
Loading, metric ton yr^{-1} Fines Coarse Organic	2,425,000 1,331,000 1,018,000 76,000	1,500,000 506,000 994,000 -
Loading, kg m^{-1} d^{-1} Fines Coarse Organic	2.28 1.25 0.96 0.07	1.01 0.34 0.67 -

Table 2
Daily Total Loads from Bank Erosion and Marsh Erosion

|	Coarse, ton d^{-1}	Fine, ton d^{-1}	Organic, ton d^{-1}
Bank Erosion	5,876	5,499	211
Marsh Erosion	24	1,747	590
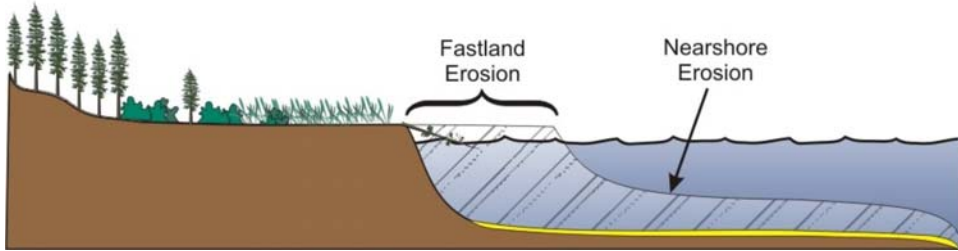
**Figure 1. Fastland versus nearshore erosion (From Hennessee et al. 2006).**
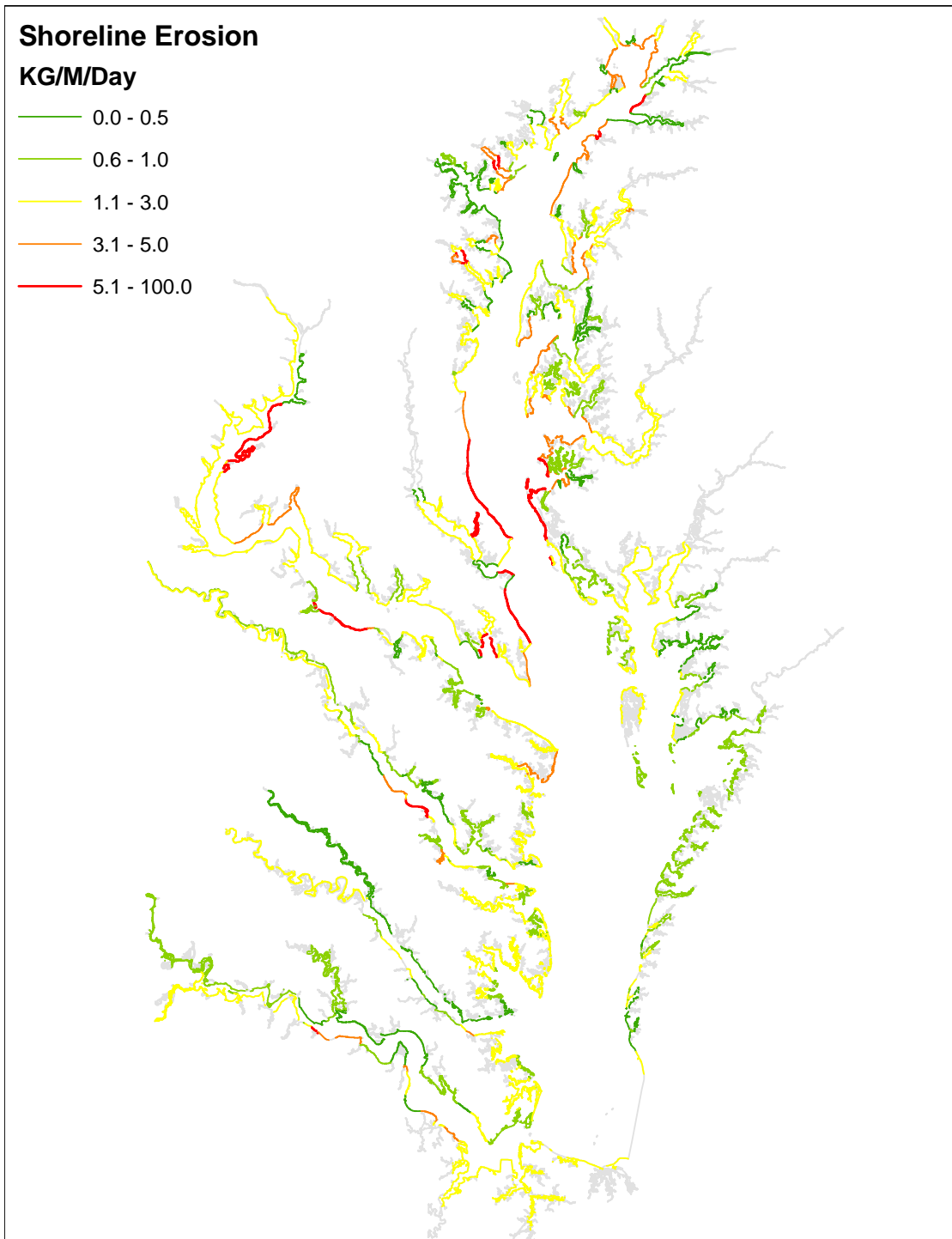
Figure 2. Long-term average shoreline erosion in the Chesapeake Bay system (From Halka and Hopkins 2006).
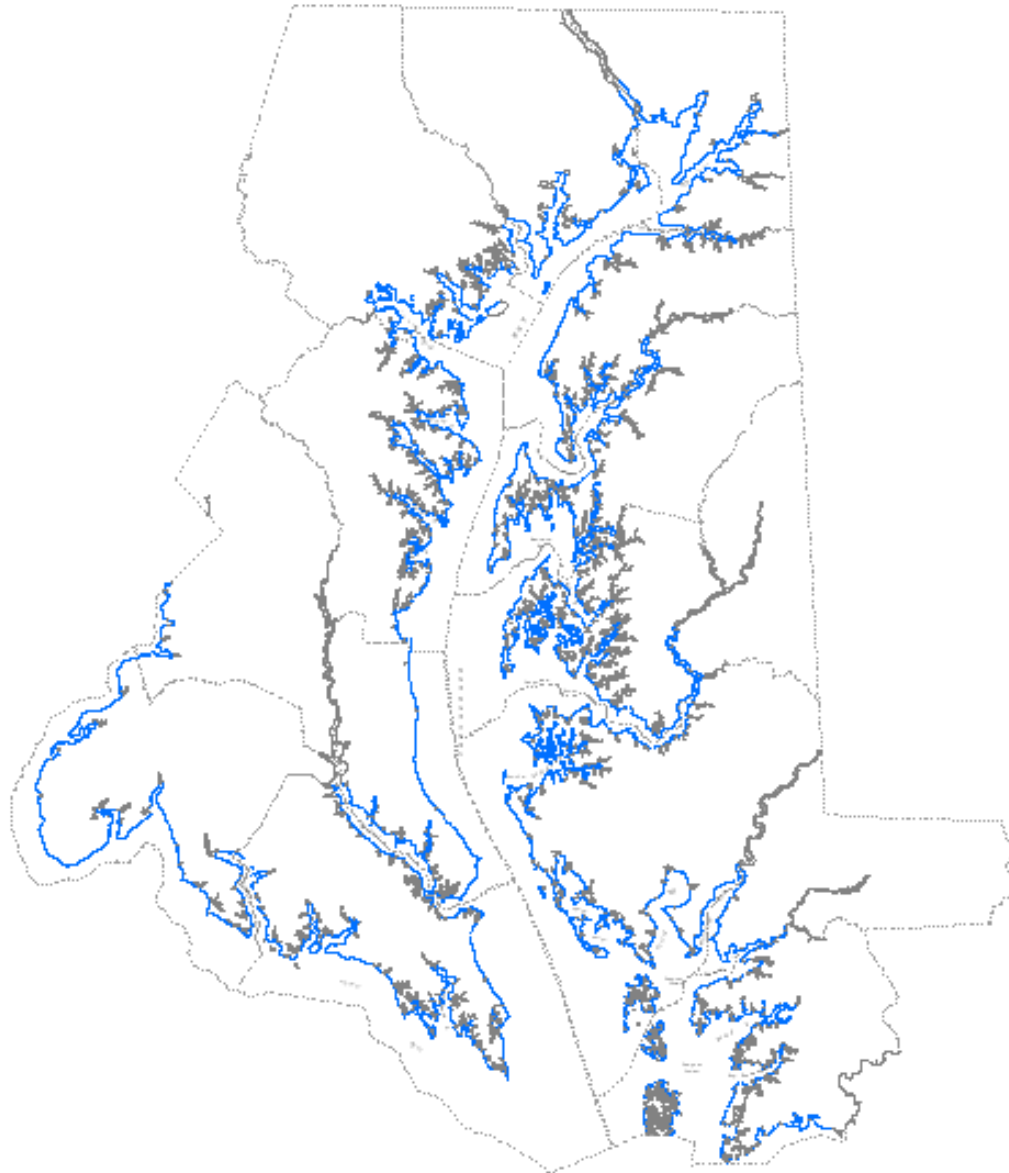
Figure 3. Extent of Maryland shoreline data. No small creeks or upper headwaters. 30% of Maryland shoreline surveyed. (From Halka and Hopkins 2006).
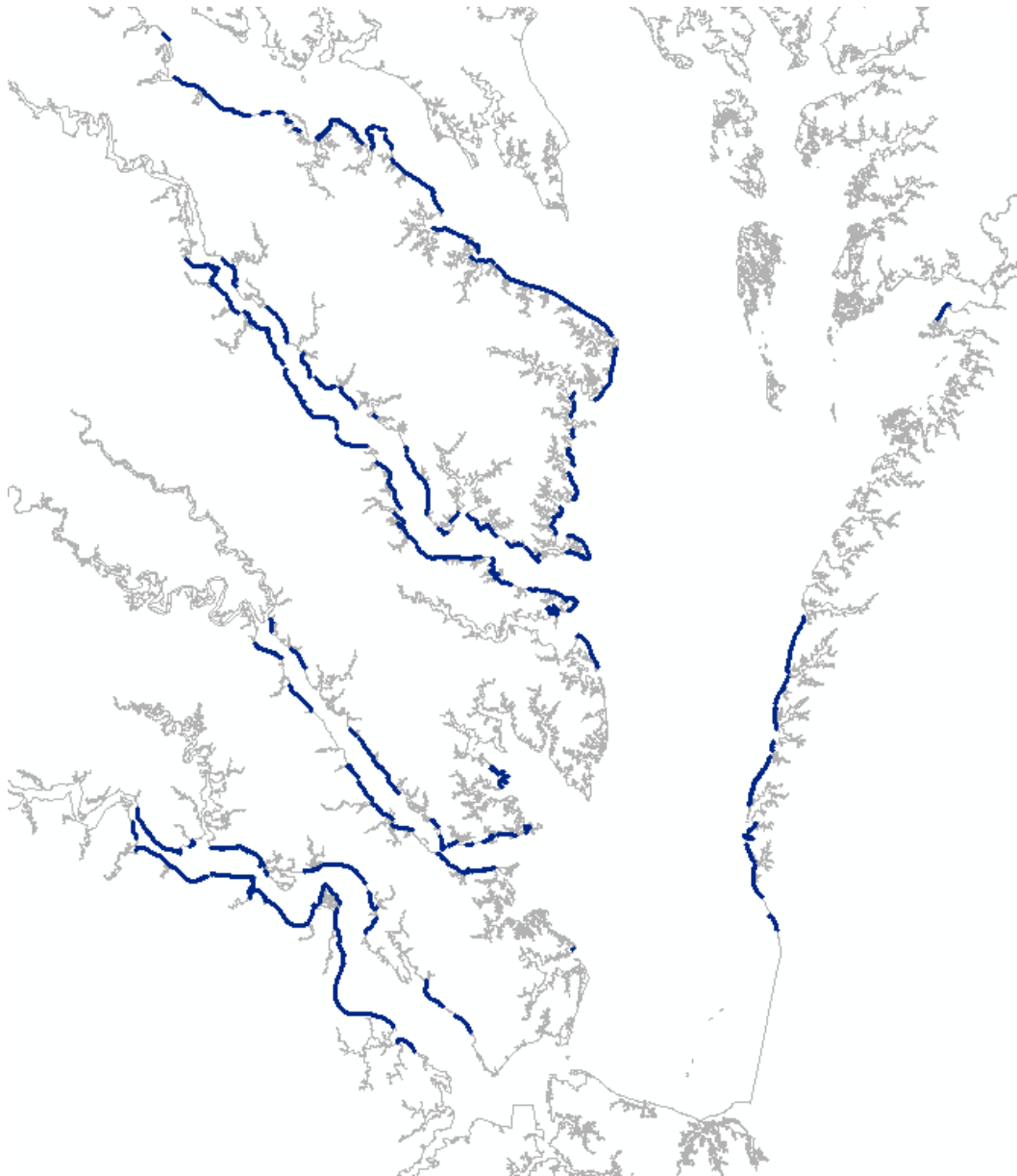
Figure 4. Virginia erosion data available from 1992 Bank Erosion Study (Hardaway et al. 1992). Study incomplete, ends at Westmoreland County on the Potomac. Headwaters of the Potomac, Rappahannock, York and James Rivers missing (Figure from Halka and Hopkins 2006).
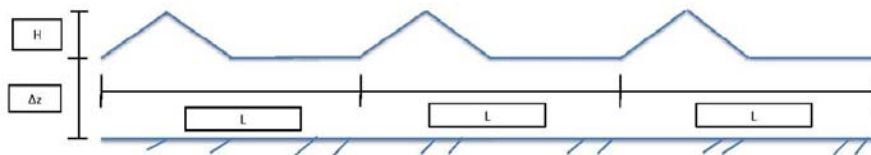
Figure 5. Definition sketch for wave and inundation energy.
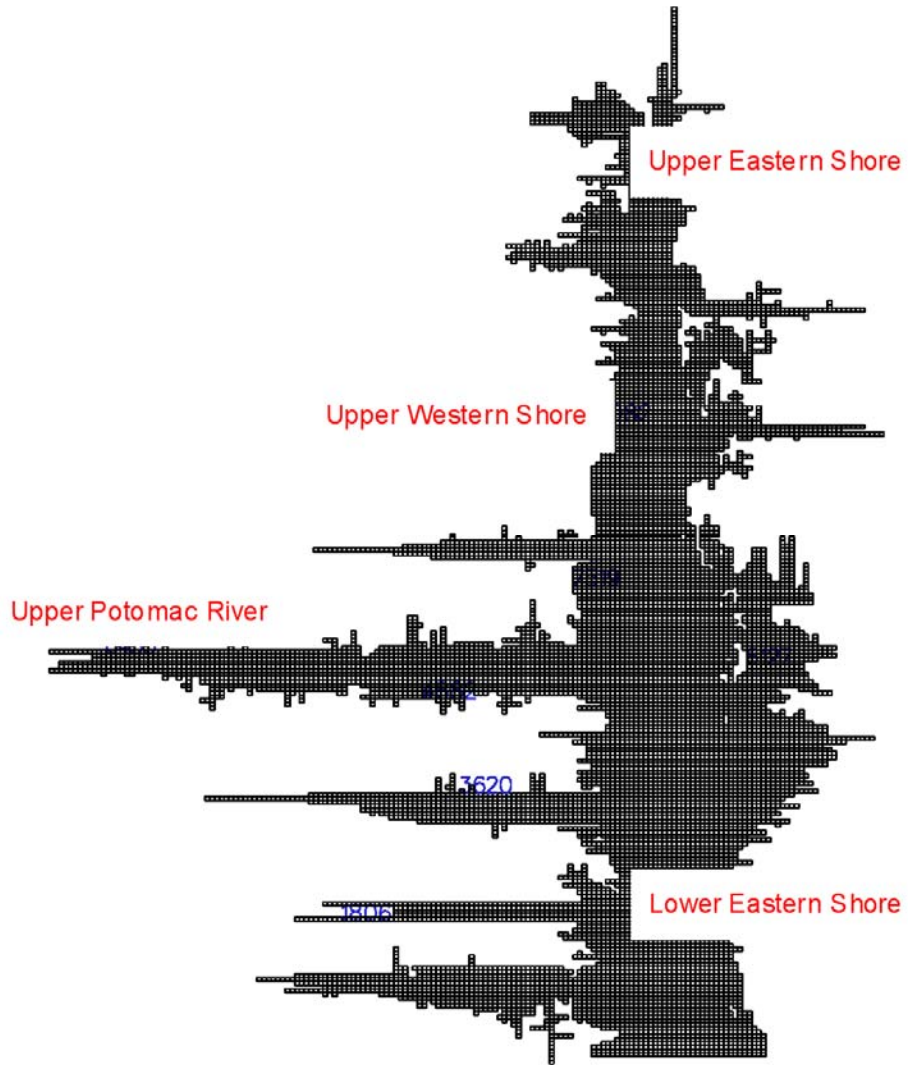
Figure 6. Locations for comparison of wave and inundation energy, superimposed on transformed computational grid.
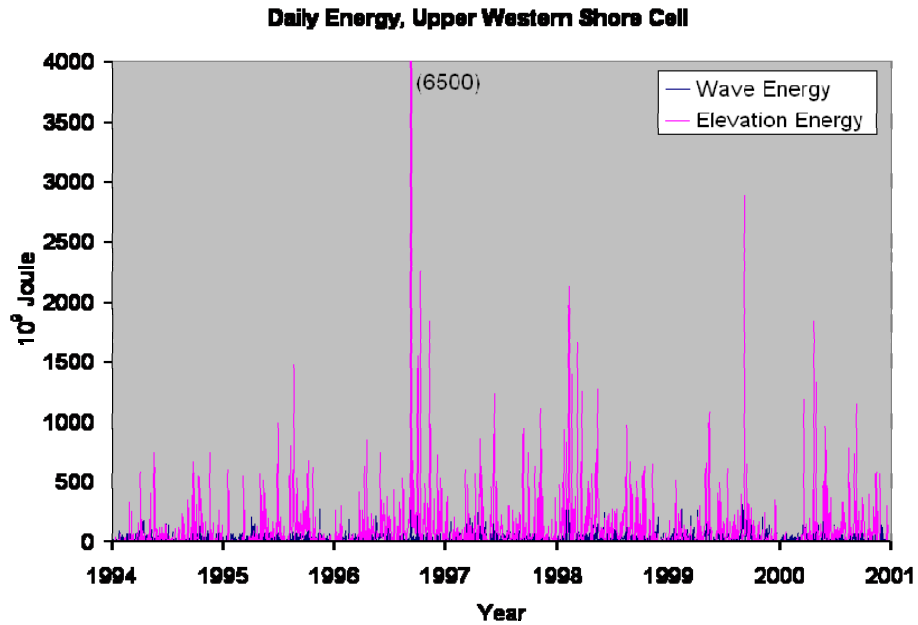
Figure 7. Comparison of computed wave energy and inundation energy at a grid cell on the upper western shore of Chesapeake Bay.
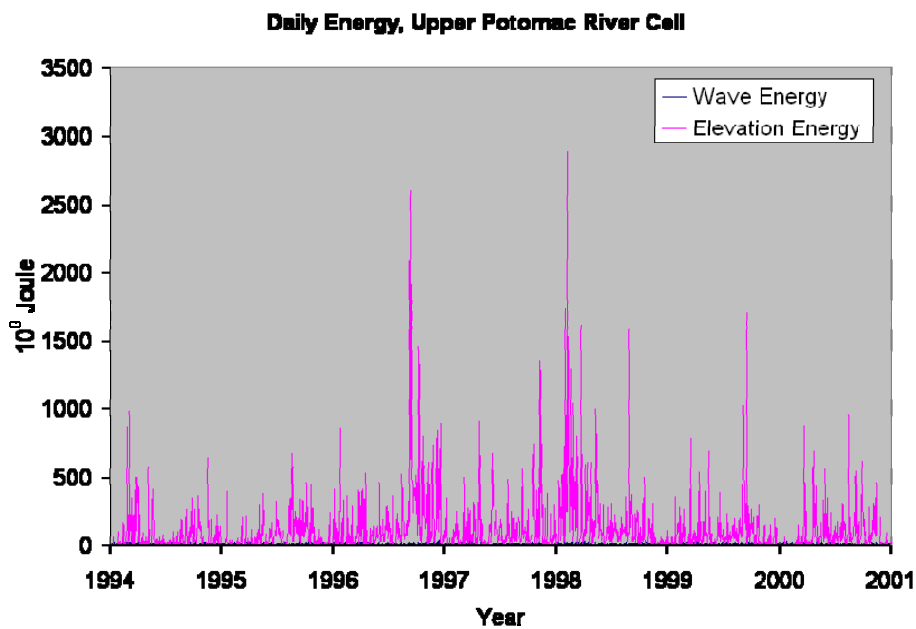
Figure 8. Comparison of computed wave energy and inundation energy at a grid cell in the tidal fresh Potomac River.
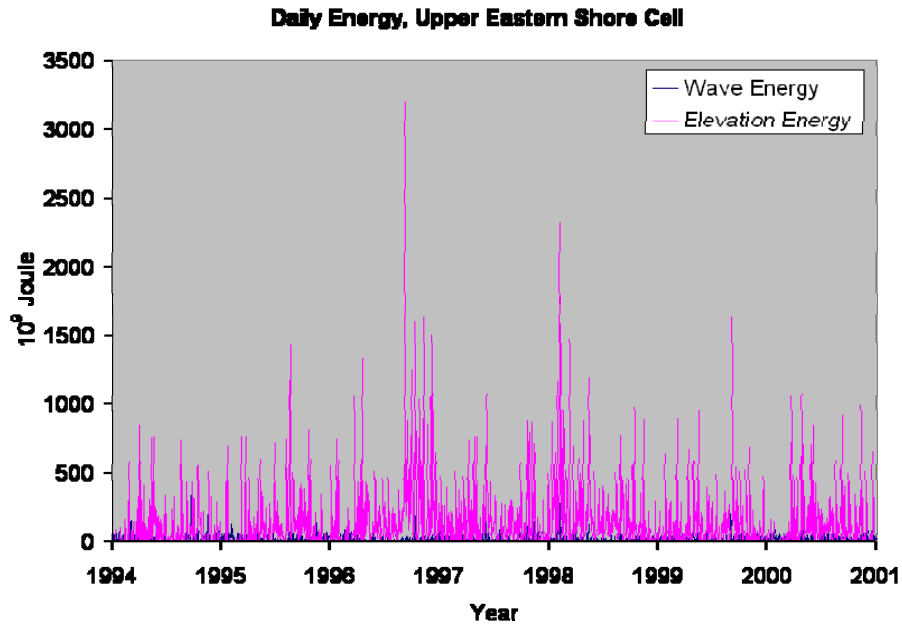
Figure 9. Comparison of computed wave energy and inundation energy at a grid cell on the upper eastern shore of Chesapeake Bay.
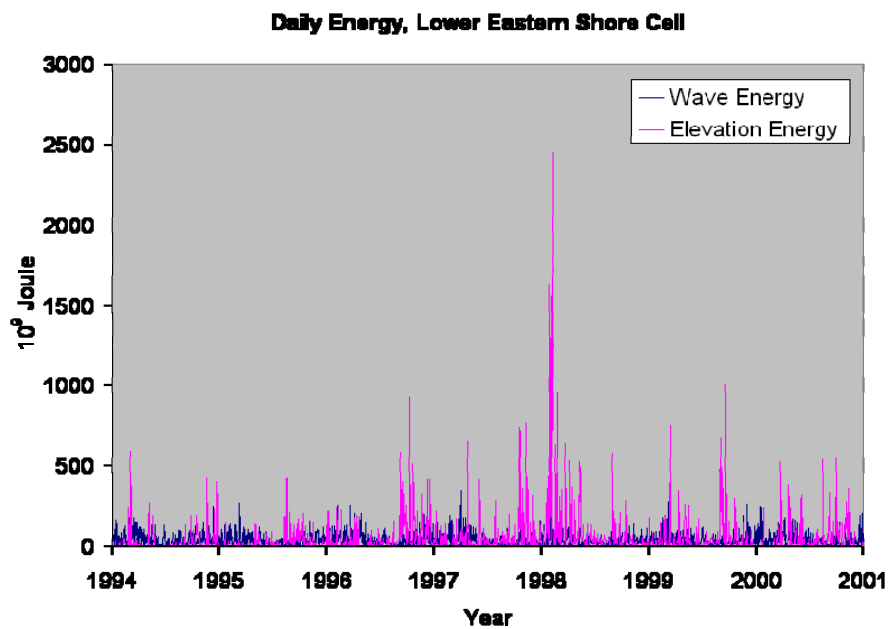
Figure 10. Comparison of computed wave energy and inundation energy at a grid cell on the lower eastern shore of Chesapeake Bay.
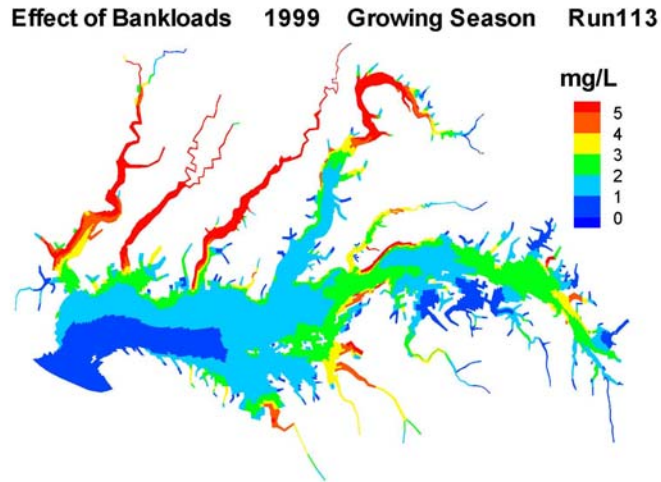
**Figure 11. Incremental effect of bankloads on suspended solids, averaged over an SAV growing season (April – September, 1999). 1999 is considered a year of low flow in the Susquehanna River, the largest tributary to Chesapeake Bay.**
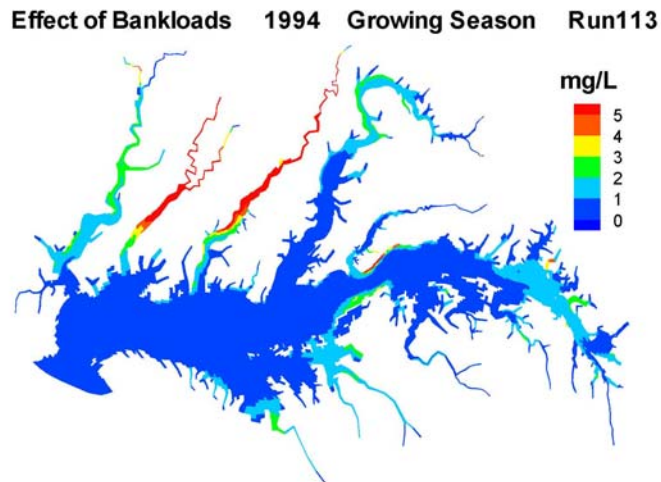
Figure 12. Incremental effect of bankloads on suspended solids, averaged over an SAV growing season (April – September, 1994). 1994 is considered a year of average flow in the Susquehanna River, the largest tributary to Chesapeake Bay.

Effect of Bankloads   1996   Growing Season   Run113

mg/L

5
4
3
2
1
0
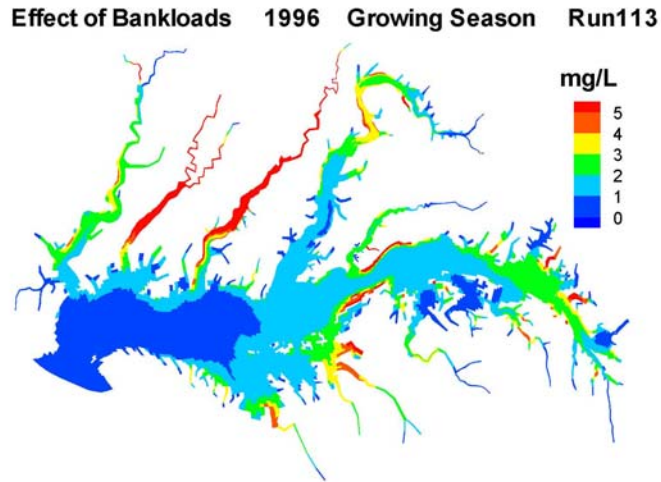
Figure 13. Incremental effect of bankloads on suspended solids, averaged over an SAV growing season (April – September, 1996). 1996 is considered a year of high flow in the Susquehanna River, the largest tributary to Chesapeake Bay.

**Total Suspended Solids
Growing Season 1999
Run178-Run169**

5
4.5
4
3.5
3
2.5
2
1.5
1
0.5
0

Area subject to loads from marsh erosion.
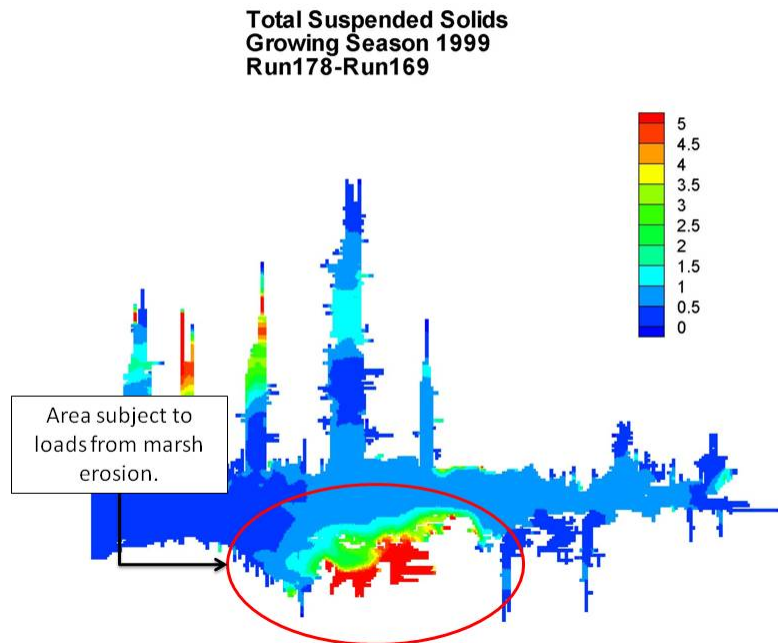
Figure 14. Incremental effect of marsh erosion on suspended solids, averaged over an SAV growing season (April – September, 1999). 1999 is considered a year of low flow in the Susquehanna River, the largest tributary to Chesapeake Bay.

**Total Suspended Solids
Growing Season 1994
Run178-Run169**

Area subject to loads from marsh erosion.
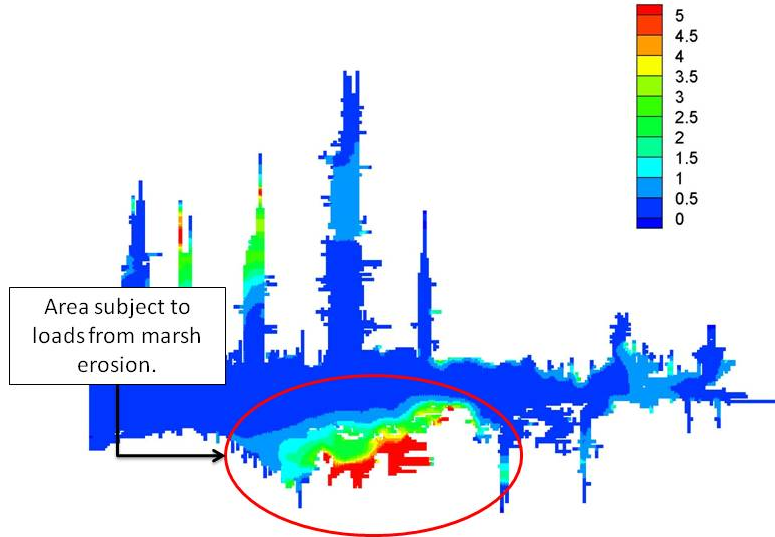
Figure 15. Incremental effect of marsh erosion on suspended solids, averaged over an SAV growing season (April – September, 1994). 1994 is considered a year of average flow in the Susquehanna River, the largest tributary to Chesapeake Bay.

**Total Suspended Solids
Growing Season 1996
Run178-Run169**

Area subject to loads from marsh erosion.
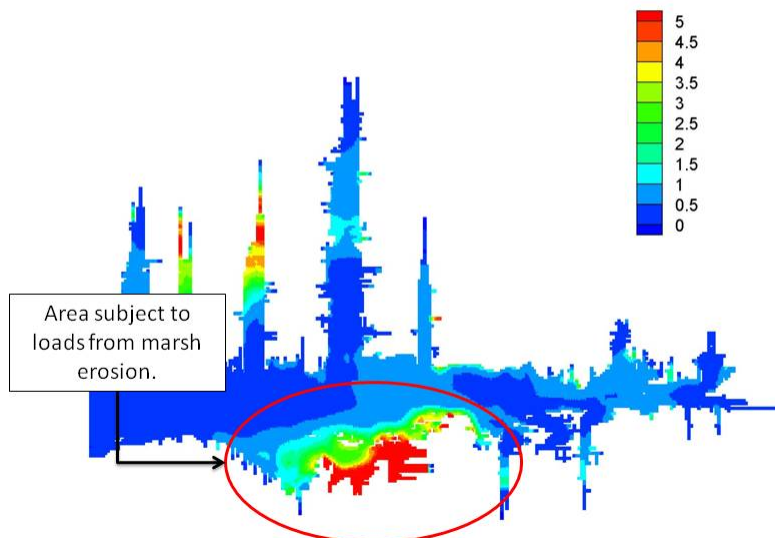
Figure 16. Incremental effect of marsh erosion on suspended solids, averaged over an SAV growing season (April – September, 1996). 1996 is considered a year of high flow in the Susquehanna River, the largest tributary to Chesapeake Bay.
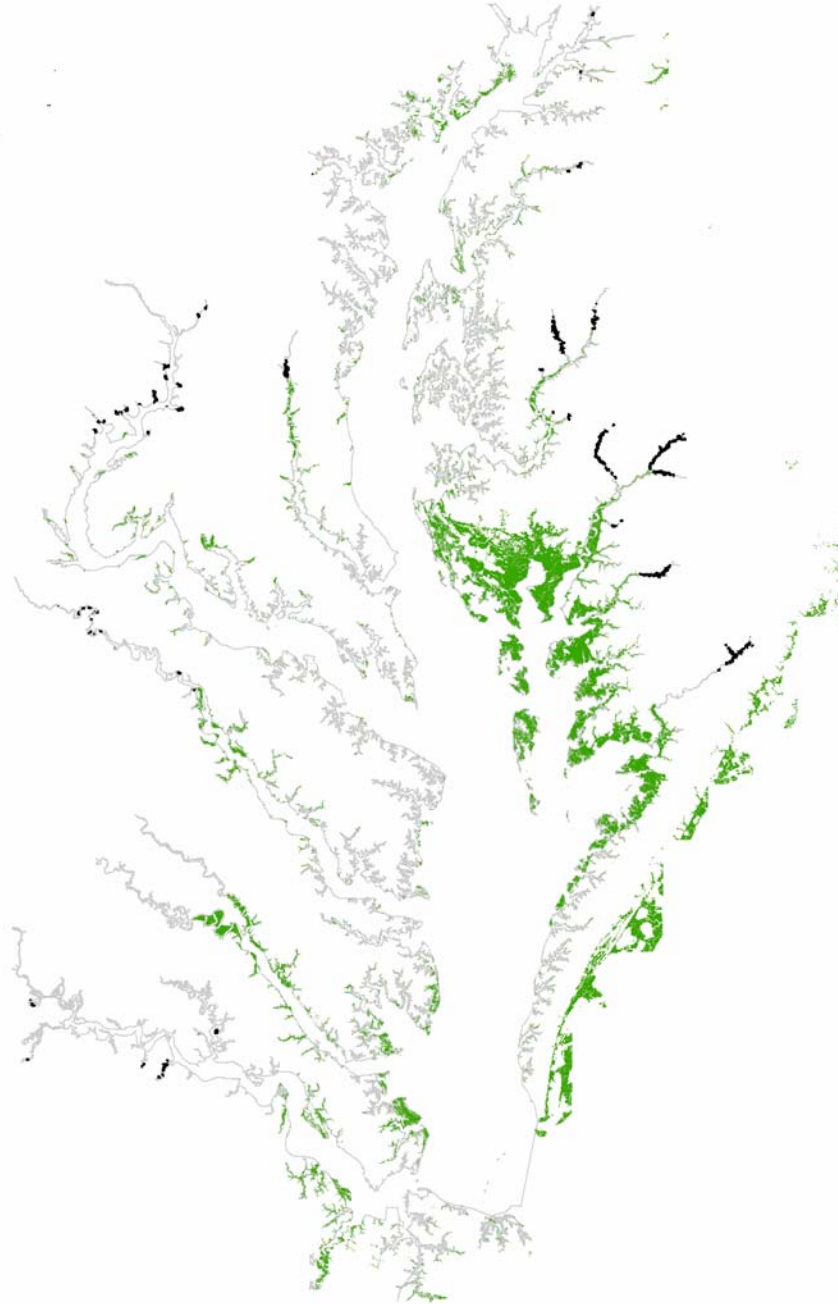
Figure 17. Chesapeake Bay wetlands. Estuarine wetlands are shown in green, riverine wetlands in black.
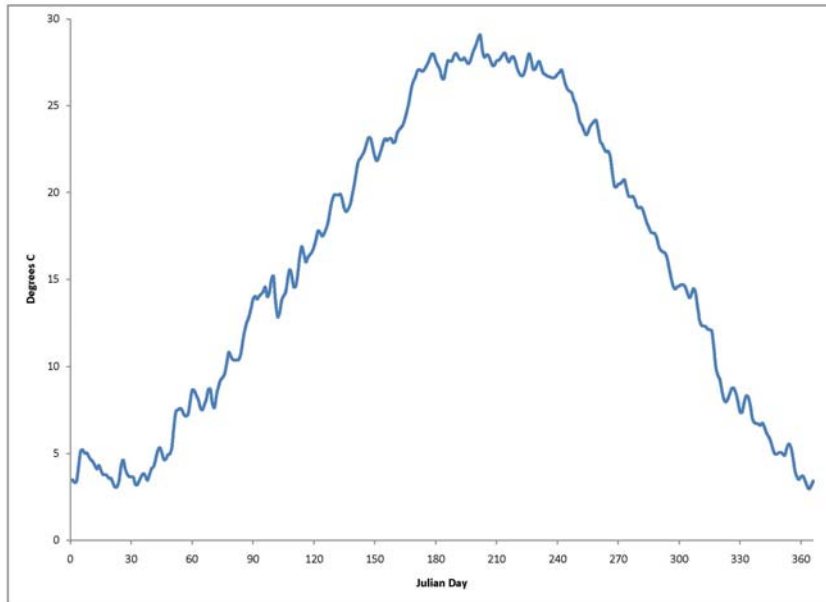
Figure 18. Temperature record used to determine daily sediment oxygen consumption in wetlands.
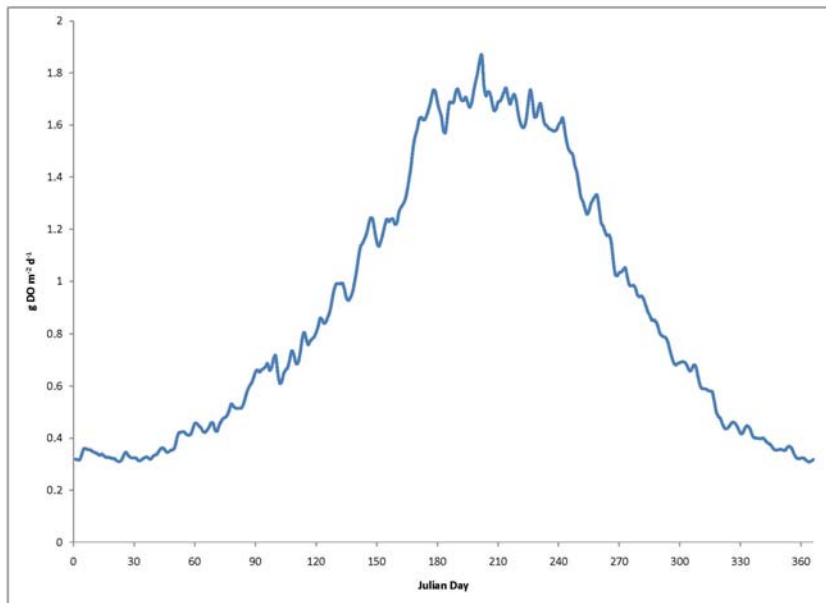
Figure 19. Daily sediment oxygen consumption (g m^{-2} d^{-1}) in wetlands.

Figure 20. Incremental effect of wetlands uptake on dissolved oxygen, averaged over the summer months (June - August, 1999). 1999 is considered a year of low flow in the Susquehanna River, the largest tributary to Chesapeake Bay.

Figure 21. Incremental effect of wetlands uptake on dissolved oxygen, averaged over the summer months (June - August, 1994). 1994 is considered a year of average flow in the Susquehanna River, the largest tributary to Chesapeake Bay.

Dissolved Oxygen
Summer 1996
Run274-Run273
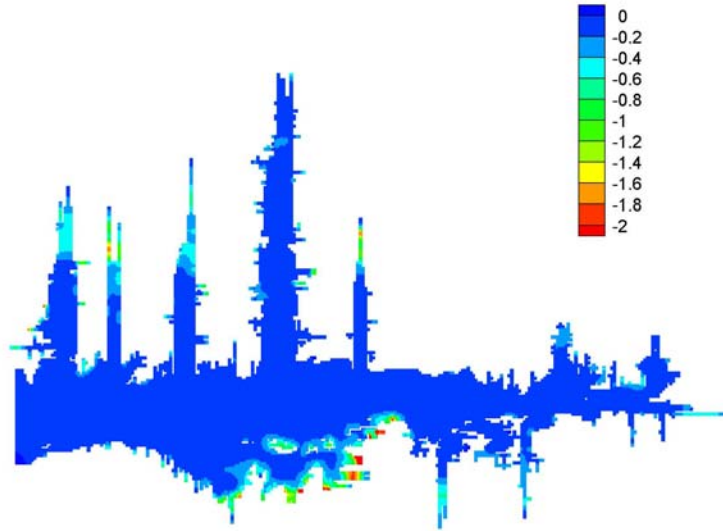
Figure 22. Incremental effect of wetlands uptake on dissolved oxygen, averaged over the summer months (June - August, 1996). 1996 is considered a year of high flow in the Susquehanna River, the largest tributary to Chesapeake Bay.
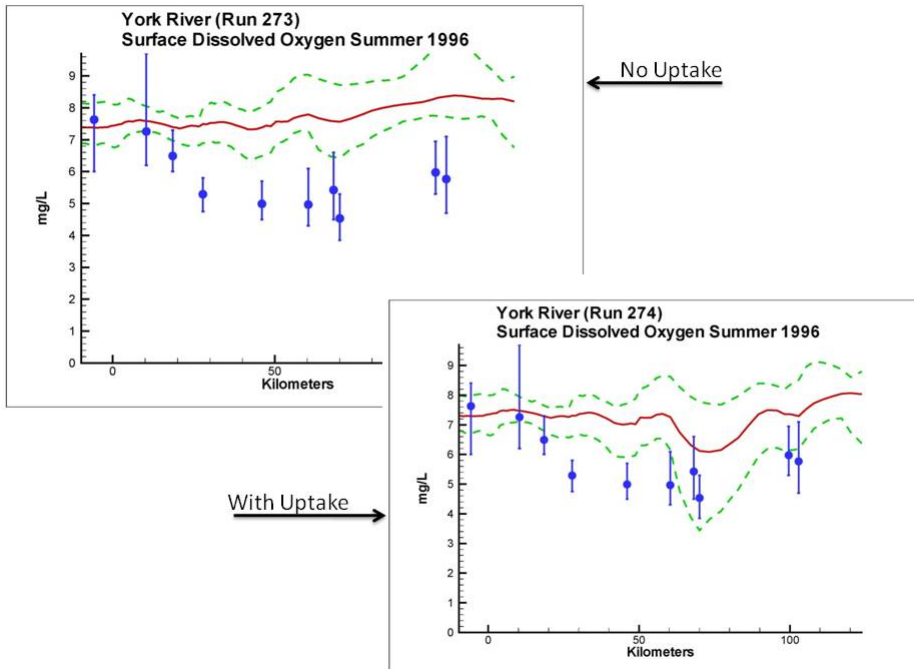
Figure 23. Effect of wetlands DO uptake on longitudinal, summer-average, surface dissolved oxygen in the York River. (Note, this is a sensitivity run, not the final calibration).
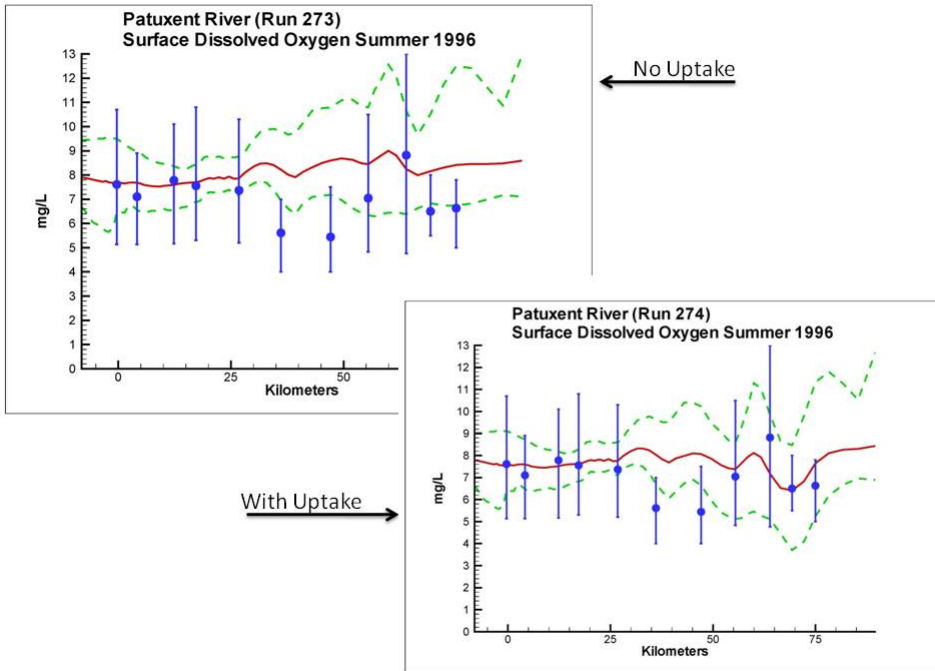
Figure 24. Effect of wetlands DO uptake on longitudinal, summer-average, surface dissolved oxygen in the Patuxent River. (Note, this is a sensitivity run, not the final calibration).

5 The Suspended Solids Model

Suspended solids are included in the CBEMP primarily for their role in light attenuation. Suspended solids are comprised of two fractions, organic (or volatile) and inorganic (or fixed). These fractions may be further subdivided into additional fractions. In the previous model version (Cerco and Noel 2004), organic solids were determined from the multiple particulate organic carbon forms in the eutrophication component. Inorganic solids were represented by a single, independent, state variable.

Exchange of materials between the water column and bed is one of the most important processes determining the concentration and transport of suspended solids. In the previous model version, the exchange was represented by a "net settling velocity." This net settling velocity represented the long term difference between settling and resuspension. However, once a particle settled to the bed it stayed there permanently. This representation potentially over-estimated the benefits of solids load reductions; projected benefits from load reductions might be negated by continuous resuspension of particulate matter already in the bay.

An over-arching theme of the present study is the incorporation of solids resuspension into the model framework. Resuspension is represented for the fixed solids component. At present, the organic solids retain the net settling algorithm. The incorporation of resuspension and emphasis placed on fixed solids necessitate a host of additional model refinements including the division of fixed solids into multiple size classes. The present model is distinguished by the incorporation of the suspended solids model into the eutrophication framework. Conventional sediment transport models commonly couple solids transport solely to hydrodynamics. The suspended solids model is coupled here with the eutrophication framework to allow representation of the myriad processes through which biological activity influences inorganic solids concentration and transport. The effects of seagrasses in damping wave action and solids resuspension is of particular interest.

The Model of the Water Column

Fixed solids are modeled as four size classes: fine clay, clay, silt, and sand. The size classes are distinguished by the magnitude of their settling velocity. Each is represented by the same mass-conservation equation . The equation is the mass conservation equation for a control volume which represents all ICM state variables:

$$\frac{\delta V_j \, C_j}{\delta t} = \sum_{k=1}^{n} Q_k \, C_k + \sum_{k=1}^{n} A_k \, D_k \frac{\delta C}{\delta x_k} + \sum S_j \qquad (1)$$

in which

V_j = volume of jth control volume (m³)
C_j = concentration in jth control volume (g m⁻³)
Q_k = volumetric flow across flow face k of jth control volume (m³ s⁻¹)
C_k = concentration in flow across flow face k (g m⁻³)
A_k = area of flow face k (m²)
D_k = diffusion coefficient at flow face k (m² s⁻¹)
n = number of flow faces attached to jth control volume
S_j = external loads and kinetic sources and sinks in ith control volume
        (g s⁻¹)
t, x = temporal and spatial coordinates

 Solution to the mass-conservation equation is via the finite-difference method using the QUICKEST algorithm (Leonard 1979) in the horizontal plane and a Crank-Nicolson scheme in the vertical dimension. The only internal source/sink for fixed solids in the water column is settling:

$$S_j = Ws_i \cdot \frac{\delta C_i}{\delta z} \qquad (2)$$

in which

C_i = concentration of solids size class i (g m⁻³)
Ws_i = settling velocity of solids size class i (m s⁻¹)

For model cells which interface with the sediment bed, resuspension and settling provide additional source/sink terms which are described below.

Fluxes at the Sediment-Water Interface

        For model cells which interface with the sediment bed, the settling term is modified to incorporate erosion and deposition as well as settling, if any, from above:

$$S_j = Ws_i \cdot \frac{Cup_i}{\Delta z} + \frac{E_i}{\Delta z} - \frac{D_i}{\Delta z} \qquad (3)$$

in which

Cup_i = concentration of solids size class i in the cell overlying the cell which
        interfaces with the bottom (g m⁻³)
Δz = thickness of cell which interfaces with the bottom (m)
E_i = erosion rate of solids size class i (g m⁻² s⁻¹)

D_i = deposition rate of solids size class i (g m^{-2} s^{-1})

Representations of erosion and deposition are limitless. New and revised formulae are continuously published as the field of sediment transport develops. Selection of formulae for any application depends, among other factors, on characteristics of the study site, data availability, and preferences of the investigator. For this study, preference was given to formulations previously applied to Chesapeake Bay and to formulations familiar to the investigators and advisors associated with the study.

Deposition is modeled as a continuous process utilizing the settling velocity through the water column, as outlined by Sanford and Halka (1993):

$$D_i = Ws_i \cdot C_i \tag{4}$$

The representation of erosion from a bed consisting of mixed sediment classes is a complex problem. The characteristics of the mixture differ from the characteristics of the individual fractions and, furthermore, evolve as the mixture ages and compacts. The formulation for clay and silt is adopted from Sanford and Maa (2001):

$$E(z,t) = M(z) \cdot \left[\tau b(t) - \tau c(z) \right] \tag{5}$$

in which

M = erosion rate per unit of excess shear stress (kg m^{-2} s^{-2} P^{-1})
τb = applied shear stress (P)
τc = critical shear stress for erosion (P)
z = depth into sediments (m)
t = time coordinate (s)

The formula allows for erosion rate and critical shear stress to vary with depth into the sediments. Many conventional erosion formulations call for these quantities to increase with depth due to effects of aging and compaction. Sanford and Maa performed a coordinate transformation from z to m, the total eroded mass; the resistance to additional erosion increased with the total amount eroded. The formulation was validated using observations collected with an in-situ annular flume. The formulation based on m was attempted without success here. The major stumbling block was determining the origin for total eroded mass. In a tidal system, erosion commences anew with each tidal acceleration from slackwater to maximum current. The total eroded mass might be re-originated after each slackwater or determined once at some arbitrary commencement time for the simulation. After a great deal of trial-and-error, both m and z were dropped from the relationship of erosion to shear stress (Equation 5). The model relies on two features to limit erosion under the application of continuous excess stress:

- The quantity eroded during any time step is limited to the amount in an "active" sediment layer.
- The bed armors. That is, readily-eroded materials are lost, leaving resistant materials behind.

Equation 5 considers erosion and critical shear stress for a sediment mixture. In the model, M and τc are specified for individual classes of clay and silt.

The erosion of sand is considered differently than clays and silt and follows Harris and Wiberg (2001). The model considers that sand erosion is the product of a near-bed reference concentration, Ca, and settling velocity:

$$E = Ca \cdot Ws \qquad (6)$$

In the Harris and Wiberg formulations, Ca is dimensionless (actually $cm^3 \ cm^{-3}$). For use in the model, E as calculated above is multiplied by ρs, the density of sand, and appropriate units conversions are carried out.

Determination of the reference concentration depends on two quantities. The first is excess shear stress:

$$Ssfm = \frac{\tau sfm - \tau cr}{\tau cr} \qquad (7)$$

in which

Ssfm = excess skin-friction shear stress
τsfm = applied skin-friction shear stress (dyne cm^{-2})
τcr = critical shear stress for erosion of sand (dyne cm^{-2})

The second is the ratio of settling velocity to friction velocity at the bed (Rouse parameter):

$$\frac{Ws}{\kappa \cdot u * sfm} \qquad (8)$$

in which

κ = Von Karman's constant
u*sfm = friction velocity at the bed (cm s^{-1})

For Ssfm > 0 and Ws / κ / u*sfm < 2.5,

$$Ca = \frac{fr \cdot Cb \cdot \gamma 0 \cdot Ssfm}{1 + \gamma 0 \cdot Ssfm} \qquad (9)$$

in which

fr = volumetric fraction of sand in the bed
Cb = bed sediment concentration (= 1 - ϕ, $cm^3 \ cm^{-3}$)
ϕ = porosity
$\gamma 0$ = constant of magnitude 10^{-3} to 10^{-5}

For Ssfm < 0 or Ws / κ / u*sfm > 2.5, Ca = 0. These conditions ensure that erosion will be zero during times of low energy.

The Bed Model

A suspended solids model which includes resuspension must incorporate a sediment bed model. As with erosion formulations, a variety of bed representations exists. The bed model for this study was adapted from the Regional Ocean Modeling System (ROMS). The code[1] was obtained from the ROMS web site (http://www.myroms.org/) and merged with the ICM code. Appropriate modifications were made to incorporate the selected formulations for erosion and deposition and to ensure dimensional consistency.

The ROMS bed model (Warner et al. 2008) consists of a fixed number of bed layers (Figure 1). The thickness and content of each layer is subject to change as material moves between the bed and the water column. An "active" layer is calculated at the sediment-water interface. Erosion during any model time step is restricted to the sediment mass in the active layer plus the amount deposited during the time step.

The ROMS bed model is largely rule-based. Following incorporation into ICM, a number of exploratory model runs were completed to investigate and illustrate the behavior of the coupled models. Several of these runs are illustrated here. The runs were conducted on a thirty-cell, two-dimensional, test grid (Figure 2) configured to roughly represent Chesapeake Bay (300 km x 20 km x 15 m). Continuous circulation was imposed that represents long-term gravitational circulation in the bay. (This circulation was disabled for several tests.) Each bottom cell in the test grid (cells 21 to 30) overlaid a bed cell consisting of multiple layers. The bed model consisted of seven layers, each initially 1 cm thick. The tests were conducted for a base configuration of three sediment classes: clay, silt, and sand (Table 1). Equal portions of clay, silt, and sand (by volume) were assigned to each layer (Figure 3).

Test 1 – Continuous Erosion

An examination of bed behavior under continuous erosion was conducted based on the following conditions:
- Set critical shear stress for all classes to 0.05 P
- Impose constant stress of 0.064 P
- Erosion rate for all classes 0.3 g m^{-2} s^{-1}
- No settling
- Thirty days duration

Under continuous erosion, the surface layer was eroded to a minimum after three days and erosion of the second layer commenced (Figure 4). As erosion of the second layer continued (Figure 5), material was transferred from the bottom layers to replenish the surface; the thickness and mass of the bottom layers

---

[1] The ROMS code was accessed circa July 2006. The present documentation applies to ROMS, as downloaded, and to the existing CBEMP. The ROMS model may have been revised subsequent to the 2006 download.

diminished (Figure 6). Movement of sediment from the bottom to the surface continued (Figure 7) until the bed was completed depleted (Figure 8).   This test illustrated several properties of the bed model:

- The number of layers in the ROMS bed model is fixed. Layers do not appear or disappear.
- No provision exists to reduce erosion as a function of depth in the bed or age of sediments.
- In the limiting case, the bed thickness will go to zero under constant erosion. Material is not entrained from deep sediments beneath the bottom of the bed.
- The model is stable even though the bed is completely eroded.

Test 2 – Continuous Erosion of Clay and Silt

A second test of continuous erosion was conducted in which critical shear stress for sand was increased from 0.05 to 5 P. All other conditions were the same as for Test 1. Under these circumstances, clay and silt eroded from the surface layer but sand was left behind (Figure 9). After a sufficient period, clay and silt were depleted from the surface layer and erosion ceased (Figure 10). The primary illustration from the test was the existence of bed armoring. The thickness of the surface layer diminished as clay and silt disappeared but the total mass of sand in the bed did not change. When the surface layer became all sand, erosion ceased since the critical shear stress for erosion of sand was less than the imposed stress.

Test 3 – Continuous Deposition

For this test, settling was activated in the water column. The magnitude of critical shear stress was specified so that no erosion occurred. All other conditions were as for Test 1. Under these conditions, material deposited in the surface layer was continuously moved downward (Figure 11). The bottom layer accumulated material and increased in thickness indefinitely while the characteristics of the remaining layers approached a continuous condition (Figure 12). This test illustrated several properties of the bed model:

- When a new layer is added at the top, the bottom two layers are combined. Total thickness of the bed increases.
- No long-term burial exists out the bottom of the bed.
- The model is stable while the bed thickness increases indefinitely.

These tests illustrated several favorable properties of the ROMS bed model. In particular, the model was stable under the imposition of extreme conditions including complete erosion of the bed. The stability facilitated the execution of lengthy continuous model runs. Bed armoring was a desirable property. However, the tests also illustrated the presence of artificial dispersion as bed layers split and combined. In practice, we found that the structure of the bed evolved in erratic fashion over the course of lengthy model runs. This development was countered, to some extent, by reinitializing the bed prior to significant model runs.

Parameter Summary

The suspended solids model requires specification of numerous parameters in the water column and bed. Although guidelines and measurements are available, a comprehensive, system-wide set of measurements to parameterize the suspended solids model does not exist. Parameter evaluation is a recursive process in which an initial parameter set is refined based on judgment and quantitative evaluation of model performance. The process is potentially endless, especially if spatial variation of the parameter set is considered. More than 400 calibration runs were performed to evaluate the complete ICM parameter set. Many of these were oriented towards calibration of the suspended solids model. Spatial variation was considered by assigning parameters into broad systems such as "mainstem bay" or "Potomac River." In the end, one universal parameter set was adopted (Table 2) which provides reasonable results systemwide.

Initial Conditions

The suspended solids model requires a set of initial conditions in the bed. The primary requirement is for bed fractions, by volume, for each solids class. These fractions are required for each bed layer (1 through 7) in each model cell ($\approx$ 11,000). Although guidelines exist (Figure 13), comprehensive quantitative data for initializing the model is not available. Attempts were made to convert available information into initial conditions. Experience showed, however, that problem areas inevitably existed. Problems manifested as large discrepancies between initial bed properties and local forcing functions (shear stresses). Portions of the bed were subject to unreasonable, almost instantaneous, erosion or deposition which negated the imposed initial conditions and created unrealistic conditions in the water column. We arrived at a procedure in which initial conditions for a major calibration run or scenario were developed during a "spin-up" run. The procedure was as follows:

- The initial bed for the spin-up consists of seven layers, each one cm thick.
- Set conditions in all cells and layers to the following volume fractions: fine clay (10%), clay (10%), silt (30%), sand (50%).
- Run the model for five years using typical hydrodynamics, boundary conditions, and loadings.
- Save the conditions in the bed at the end of the spin-up run.
- Use this bed as the initial condition for the major calibration run or scenario.

For major calibration runs, the loads and boundary conditions were based on existing conditions. For scenarios, loads and boundary conditions reflected scenario conditions. This procedure provided a bed which was in approximate equilibrium with the local forcings (Figures 14 – 17). The procedure also mitigated the tendency for the ROMS bed to develop erratically over lengthy periods. The equilibrium bed was predominantly sand with sporadic deposits of clay and silt. The contiguous deposits of clay and silt which dominate the observations in the upper bay (Figure 13) were not apparent in the modeled bed.

Net Settling of Particulate Organic Matter

The model retains the concept of net settling of particulate organic matter (carbon, nitrogen, phosphorus, phytoplankton) into the bed sediments. Several lines of evidence indicate that net settling should be less in shallow littoral areas and greater in deep channels. In an analysis of the Patuxent Estuary, Testa and Kemp (2008) found that lateral transport of particulate organic carbon (POC) to the central channel from adjacent shallow waters was required to meet bottom water respiratory demands. A similar analysis of the mesohaline Chesapeake Bay (Kemp et al., 1997) found that the littoral zones were net autotrophic (oxygen production exceeds consumption) while the main channel was net heterotrophic (oxygen consumption exceeds production). The difference between production and consumption suggests the transport of organic matter from the shoals to the channel. Where observations are sufficiently dense, a gradient in sediment organic carbon can be seen from the littoral zone to the channel (Figure 18). We varied net settling according to depth (Table 3). The resulting carbon distribution in the bed (Figure 19) reflects several characteristics of the observations (Figures 18, 20). Computed bed carbon shows a longitudinal gradient from the upper bay to the lower bay. Along the mesohaline section of the main channel, a lateral gradient exists; computed bed carbon is lower in the littoral zones and higher in the deep channel. The model also illustrates high sediment carbon under seagrass beds, for example, along the lower eastern shore. The scheme of net settling utilized improves the model representation of respiration (Figure 21) and is crucial to matching the observed longitudinal distribution of bottom dissolved oxygen in summer (Figure 22).

References

Cerco, C.F. and Cole, T. M. (1994). "Three-dimensional eutrophication model of Chesapeake Bay," Technical Report EL-94-4, U.S. Army Engineer Waterways Experiment Station, Vicksburg MS.

Cerco, C., and Noel, M. (2004). "The 2002 Chesapeake Bay eutrophication model," EPA 903-R-04-004, Chesapeake Bay Program Office, US Environmental Protection Agency, Annapolis MD. (available at http://www.chesapeakebay.net/modsc.htm)

Harris, C., and Wiberg, P. (2001). "A two-dimensional, time-dependent model of suspended sediment transport and bed re-working for continental shelves," *Computers & Geosciences* 27, 675-690.

Kemp, W. M., Smith, E., DiPasquale, M., and Boynton, W. (1997). "Organic carbon balance and net ecosystem metabolism in Chesapeake Bay," *Marine Ecology Progress Series* 150, 229-248.

Leonard, B. (1979). "A stable and accurate convection modelling procedure based on quadratic upstream interpolation," *Computer Methods in Applied Mechanics and Engineering,* 19, 59-98.

Nichols, M., Kim, S., and Brouwer, C. (1991). "Sediment characterization of the Chesapeake Bay and its tributaries," NOAA National Estuarine Inventory, Virginia Institute of Marine Science, Gloucester Pt. VA.

Sanford, L., and Halka, J. (1993). "Assessing the paradigm of mutually exclusive erosion and deposition of mud, with examples from upper Chesapeake Bay," *Marine Geolo*gy 114, 37-57.

Sanford, L., and Maa, J. (2001). "A unified erosion formula for fine sediments," *Marine Geology* 179, 9-23.

Testa, J., and Kemp, W. M. (2008) "Variability of biogeochemical processes and physical transport in a partially stratified estuary: a box modeling analysis," *Marine Ecology Progress Series* 356, 63-79.

Warner, J., Sherwood, C., Signell, R., Harris, C., and Arango, H. (2008). "Development of a three-dimensional, regional, coupled wave, current, and sediment transport model," *Computers & Geosciences* 34, 1284-1306.

Table 1
Base Conditions for Tests of ROMS Bed Model

	Clay	Silt	Sand
D50, µm	3	250	250
ρ, kg m^{-3}	1350	2000	2650
Wstl, µm s^{-1}	0.174	17.4	174
Taucrit, P	0.05	0.5	2
Erate, g m^{-2} s^{-1}	0.3	0.3	0.3

Table 2
Suspended Solids Model Parameters

	Fine Clay	Clay	Silt	Sand
Ws, µm s^{-1}	12	30	100	1000
D50, µm	3	3	30	300
ρ, kg m^{-3}	1350	1350	2000	2650
τc, P	0.03	0.03	0.03	2
M, g m^{-2} s^{-1} P^{-1}	1	1	1	
γ0				0.001

Table 3
Net Settling Velocities for Particulate Organic Matter

	Labile Particles	Refractory Particles	Cyanobacteria	Diatoms	Green Algae
Characteristic Value in Water Column, m d^{-1}	1.0	1.0	0.0	0.5	0.5
Net, Depth < 9.8 m, m d^{-1}	0.01	0.01	0.0	0.005	0.001
Net, 9.8 m < Depth < 23.5 m, m d^{-1}	0.2	0.2	0.0	0.1	0.1
Net, 23.5 m < Depth, m d^{-1}	1.0	1.0	0.0	0.5	0.5

Active layer thickness (Harris and Wiberg, 1997).
$$z_a = k_1(\tau_{sf} - \tau_{ce}) + k_2 D_{50}$$

Erosion. $(\tau_{sf} > \tau_{ce})$
Entrain sediment from lower layers so that surface layer is at least z_a thick. Split bottom layer. Erode from surface layer. For each sediment class
erosion_flux =

$$\text{MIN} \begin{bmatrix} dt*E_s*(1-poro)*frac*(\tau_{sf}/\tau_{ce} -1), \\ \rho_s*(1-poro)*frac*z_a+dep\_flux \end{bmatrix}$$

Deposition.
Create new layer if deposition > user defined thickness. Mix surface layer to be at least z_a thick. Combine bottom layer. For each sediment class
$$\frac{\partial C}{\partial t} = -w_s \frac{\partial C}{\partial z}$$

Figure 1. The ROMS bed model (after Warner et al. 2008).

Figure 2. Thirty-box test grid (elevation).   The grid is patterned after Chesapeake Bay (300 km x 20 km x 15 m). Each cell is 30 km x 20km x 5m.
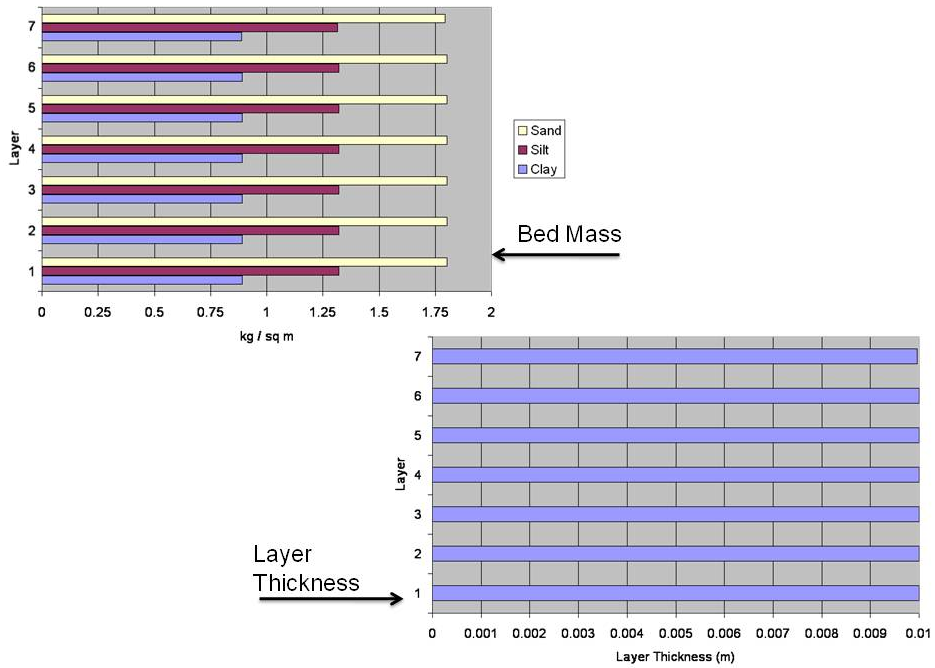
Figure 3. Initial conditions for tests of bed model. These conditions are applied in each sediment cell underlying the 30-box test grid. Layers are numbered in declining order from the sediment-water interface (Layer 7) to the bottom of the bed (Layer 1).
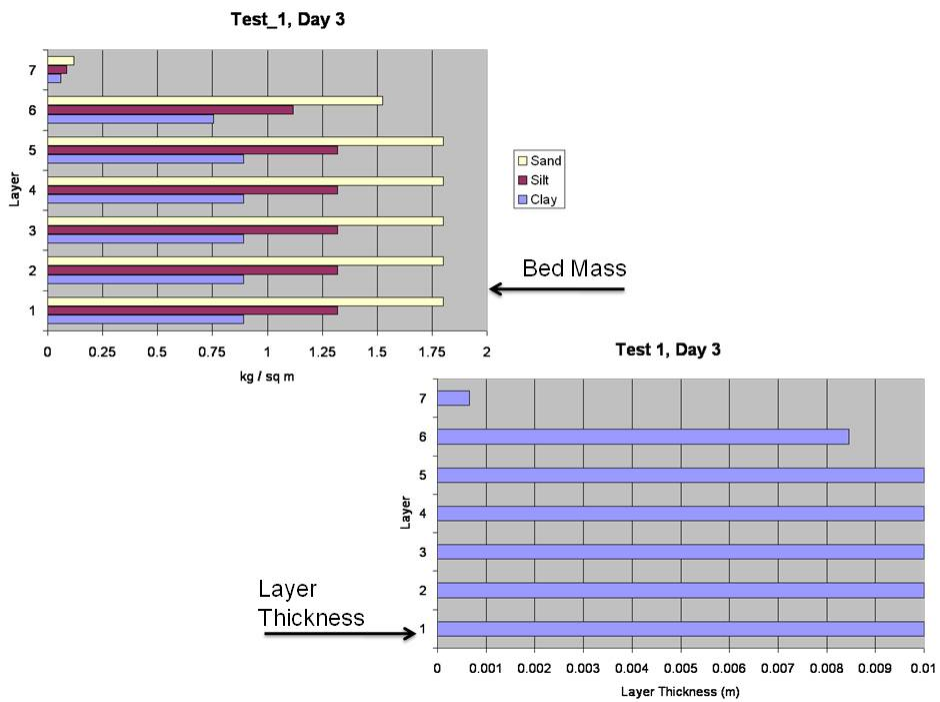

Figure 4. Conditions in the bed after three days of continuous erosion. The surface layer is almost completely eroded.
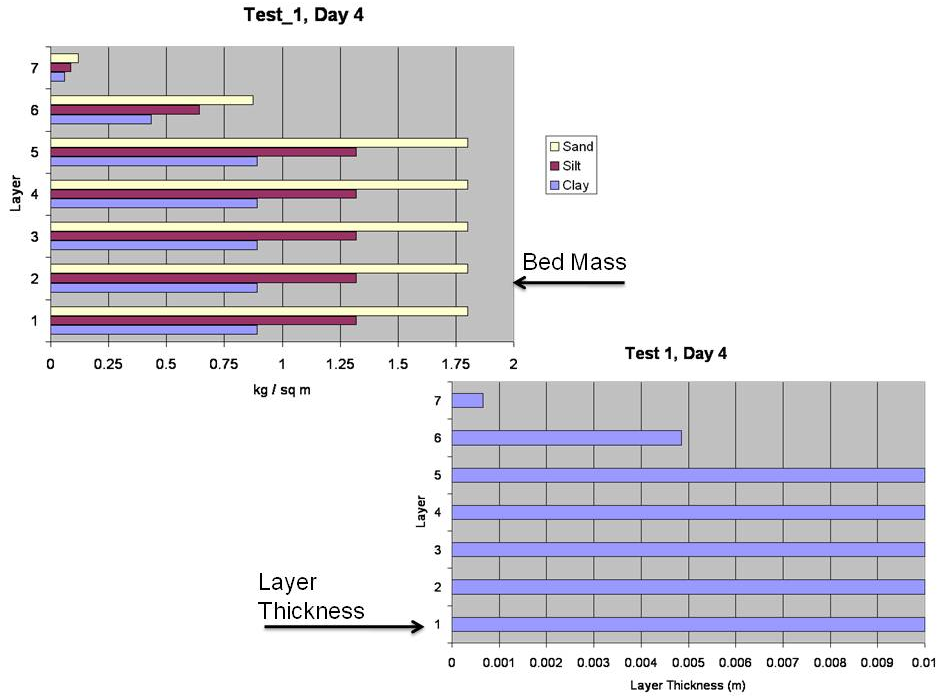
Figure 5. Conditions in the bed after four days of continuous erosion. The surface layer has reached minimum thickness and material is moved upwards from the next layer to replenish erosion from the surface.
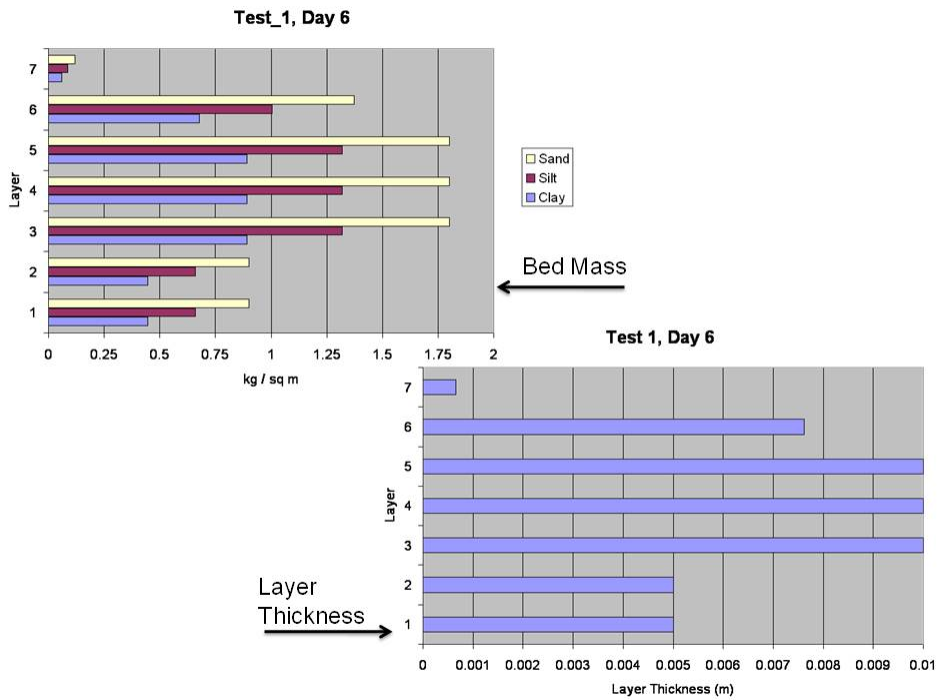

Figure 6. Conditions in the bed after six days of continuous erosion. At this point, the bottom layer is split in two and material is moved from the bottom layer upwards.

Test_1, Day 14

Bed Mass ←

Test 1, Day 14
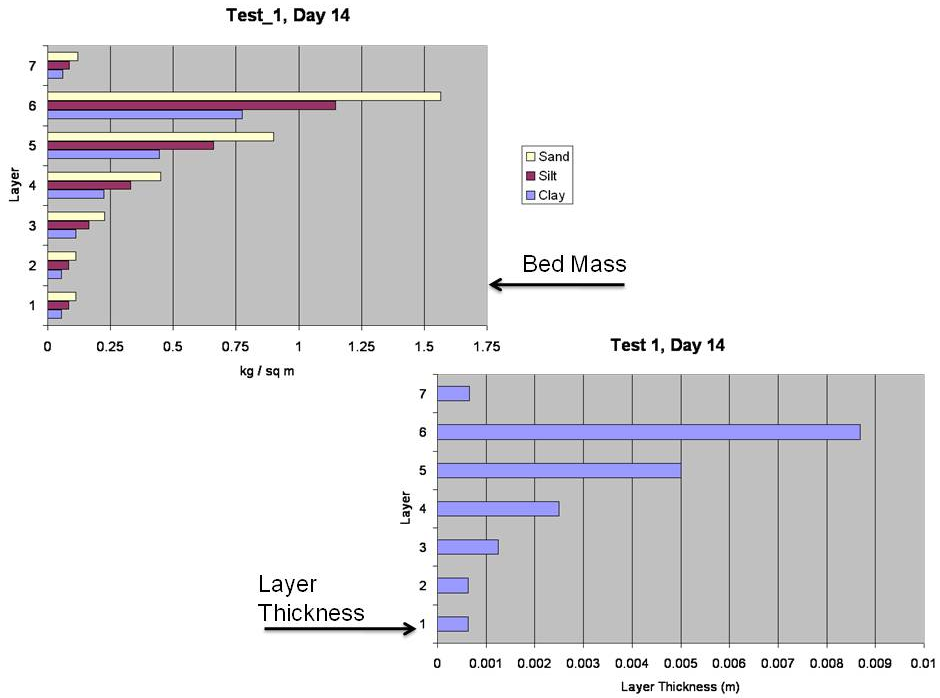
Layer
Thickness →

**Figure 7. Conditions in the bed after seven days of continuous erosion. Material continues to move from subsurface layers towards the surface.**

Test_1, Day 30

Bed Mass ←

Test 1, Day 30

Layer
Thickness →
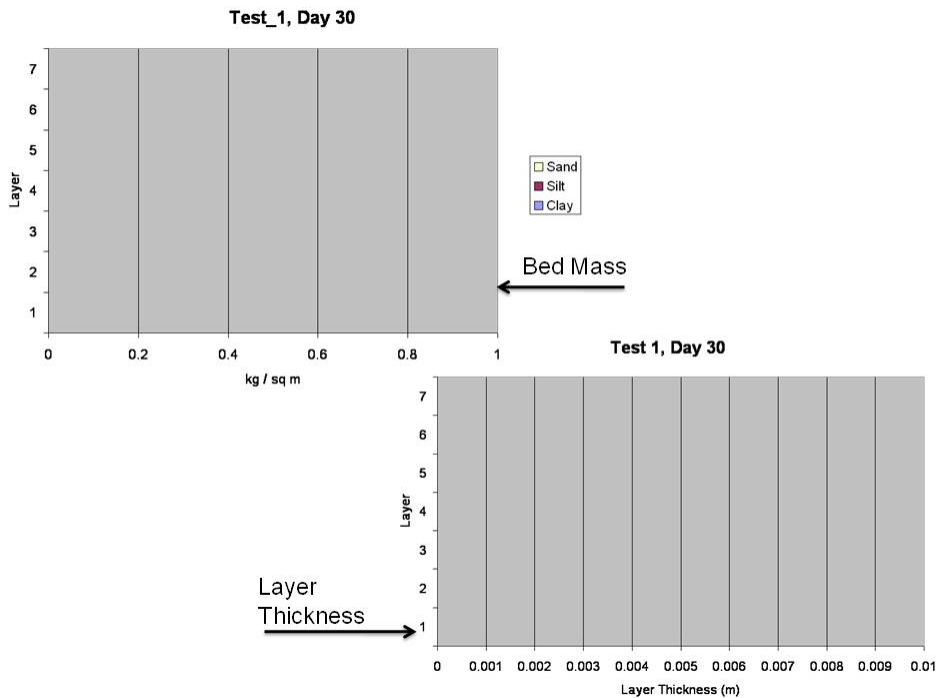
Figure 8. Conditions in the bed after thirty days of continuous erosion. The bed is depleted of solids but the model continues to execute.
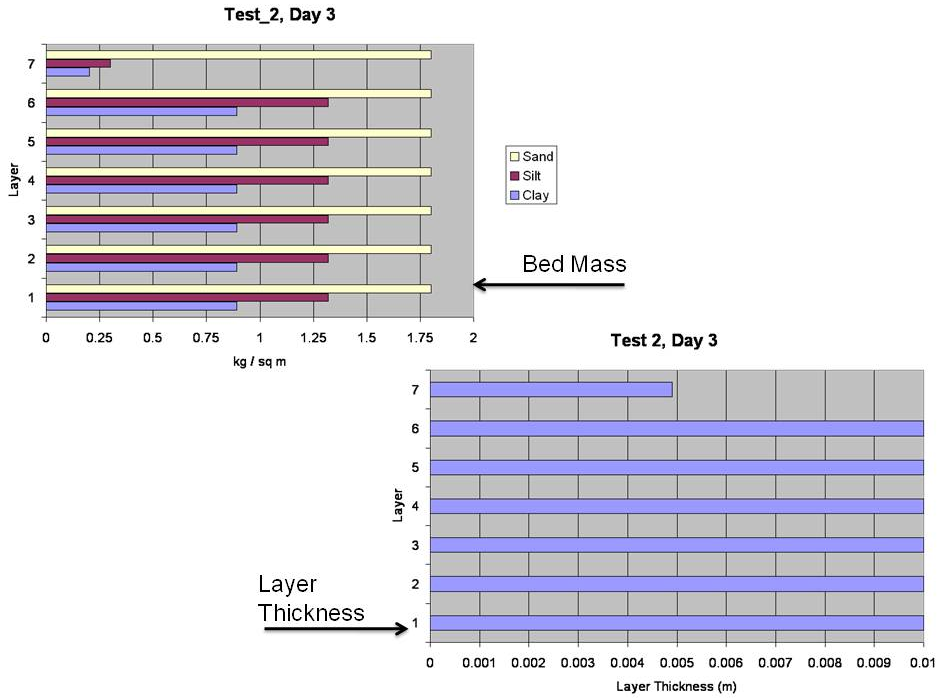
Figure 9. Conditions in the bed after three days of continuous erosion of clay and silt. The amount of sand in the surface layer is unchanged since the critical shear stress for erosion is not exceeded. The thickness of the surface layer is reduced.
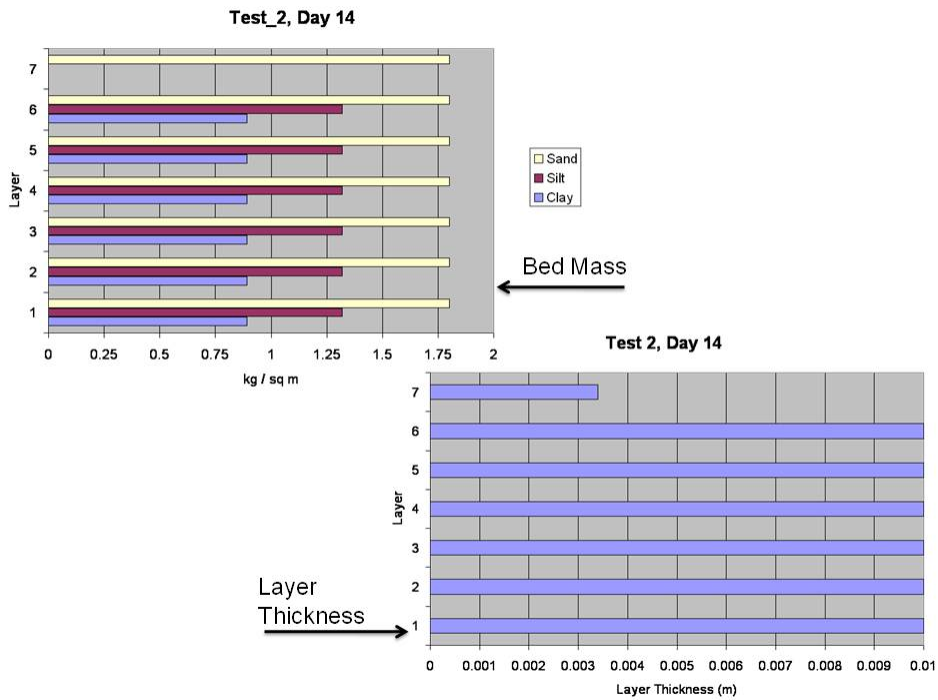
Figure 10. Conditions in the bed after fourteen days of continuous erosion of clay and silt. These materials are completely eroded from the surface layer which now consists exclusively of sand. Erosion ceases. The sub-surface layers are unchanged.
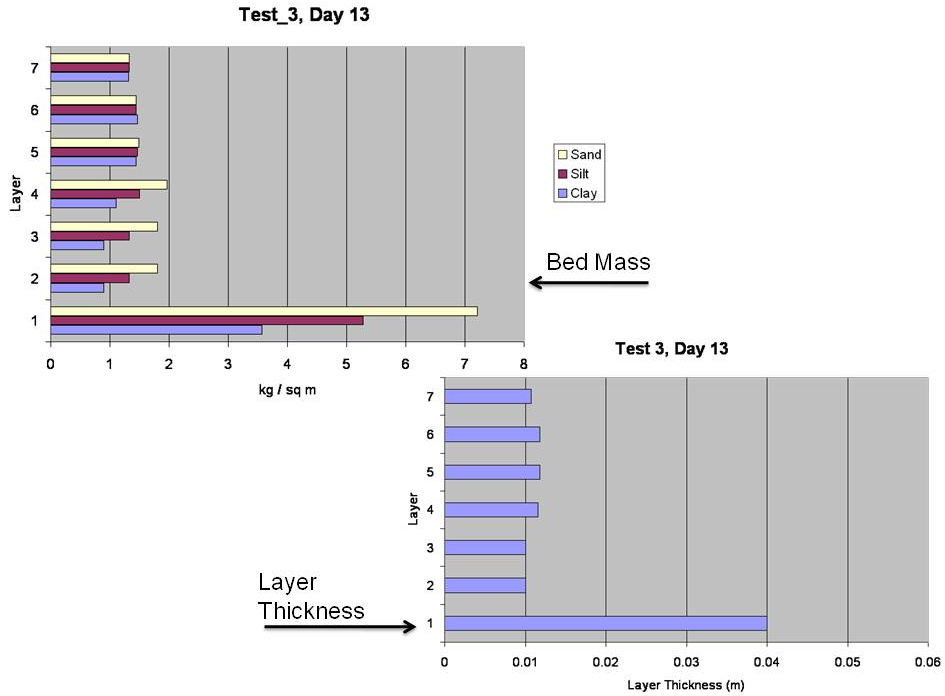
Figure 11. Conditions in the bed after thirteen days of continuous deposition. Material is passed through the bed, down to the bottom layer.
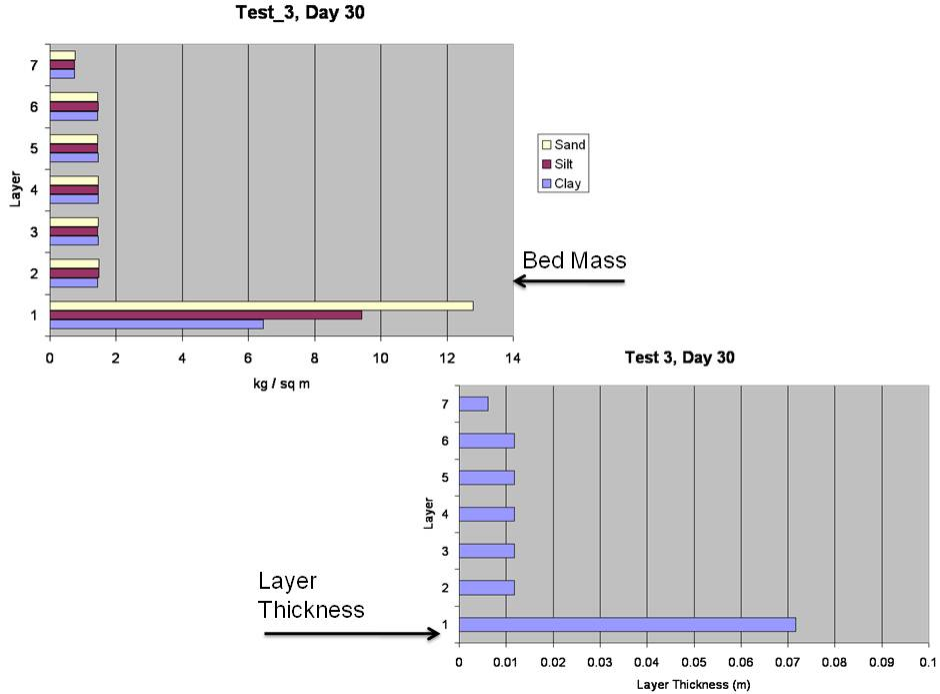
Figure 12. Conditions in the bed after thirty days of continuous deposition. The bottom layer accumulates material, by combining with the overlying layer, while the thickness of the remaining layers remains close to initial conditions.
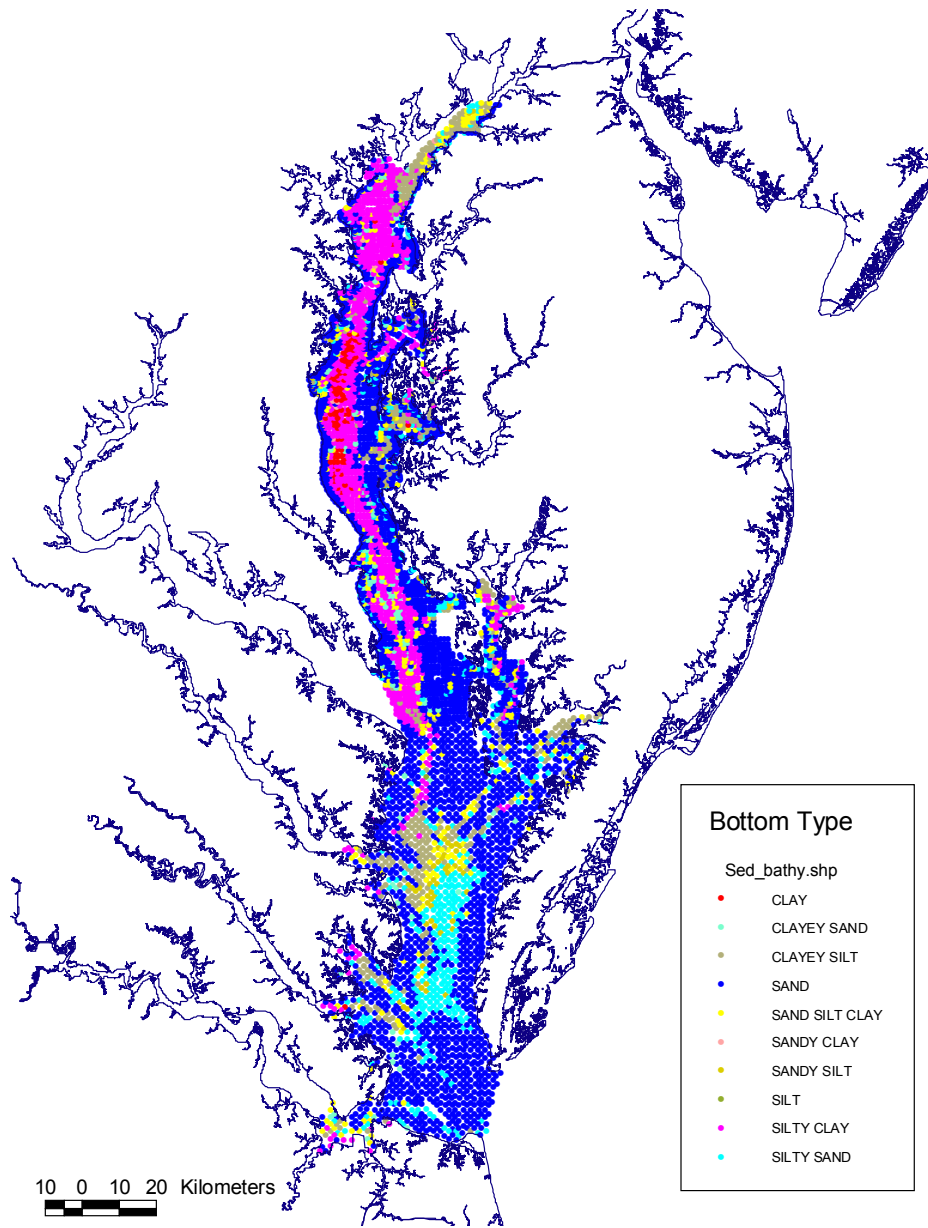
Figure 13. Chesapeake Bay bottom types (Nichols et al. 1991). The bed of the mainstem bay is primarily sand in shallow water. The deeper waters of the upper bay are primarily clay or silty clay. The lower bay is silty sand or sand.

Figure 14. Fine clay fraction, by volume, of equilibrium bed (0 < Fraction < 1). Most of the bed is < 7.5% fine clay although sporadic deposits of 25% to 30% are evident.
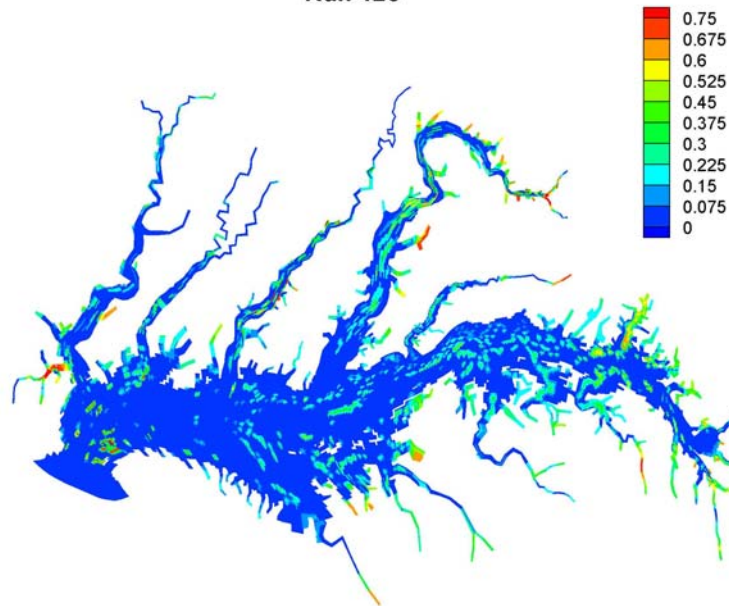
Figure 15. Clay fraction, by volume, of equilibrium bed (0 < Fraction < 1). Most of the bed is < 7.5% clay although sporadic deposits as high as 75% are evident.

Silt Fraction - Initial Conditions in Bed Layer 1
Run 426
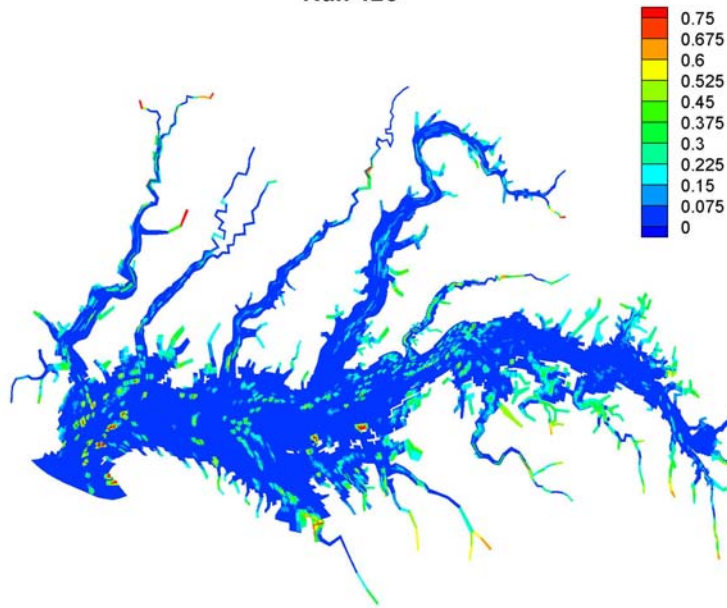
Figure 16. Silt fraction, by volume, of equilibrium bed (0 < Fraction < 1). Most of the bed is < 7.5% silt although sporadic deposits greater than 30% are evident.

Sand Fraction - Initial Conditions in Bed Layer 1
Run 426
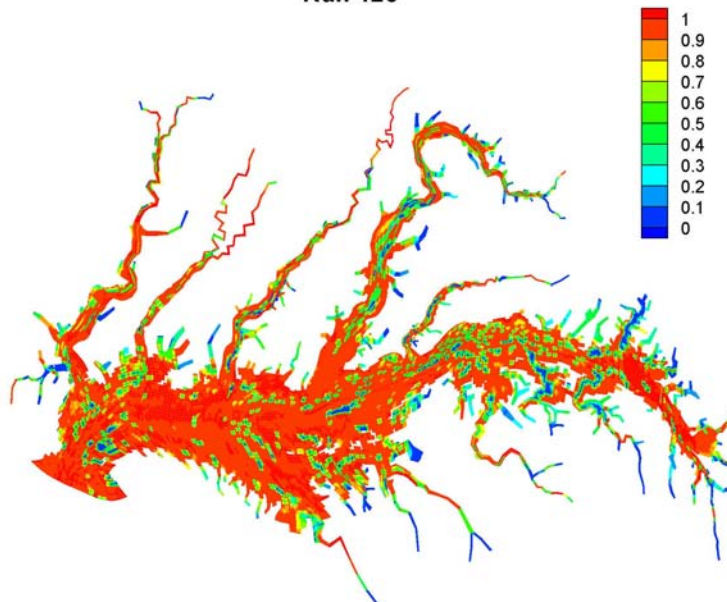
Figure 17. Sand fraction, by volume, of equilibrium bed (0 < Fraction < 1). The bed is predominantly sand except near tributary inputs and for sporadic locations elsewhere.
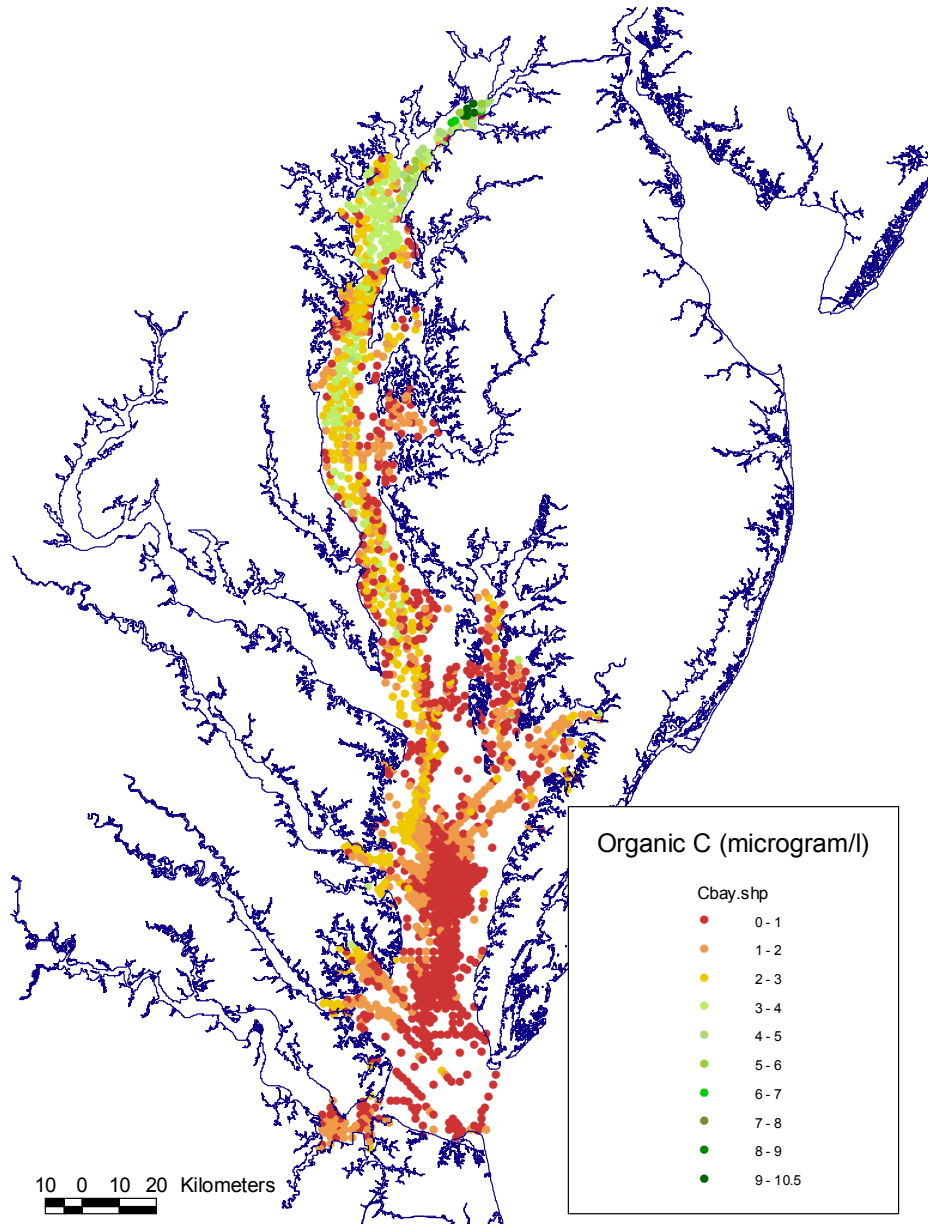
Figure 18. Observed sediment organic carbon (Nichols et al. 1991). A longitudinal gradient exists with highest concentration in the upper bay and lesser concentrations in the lower bay. A lateral gradient exists along the mesohaline section with lower concentrations in the littoral areas and higher concentrations in the channel.
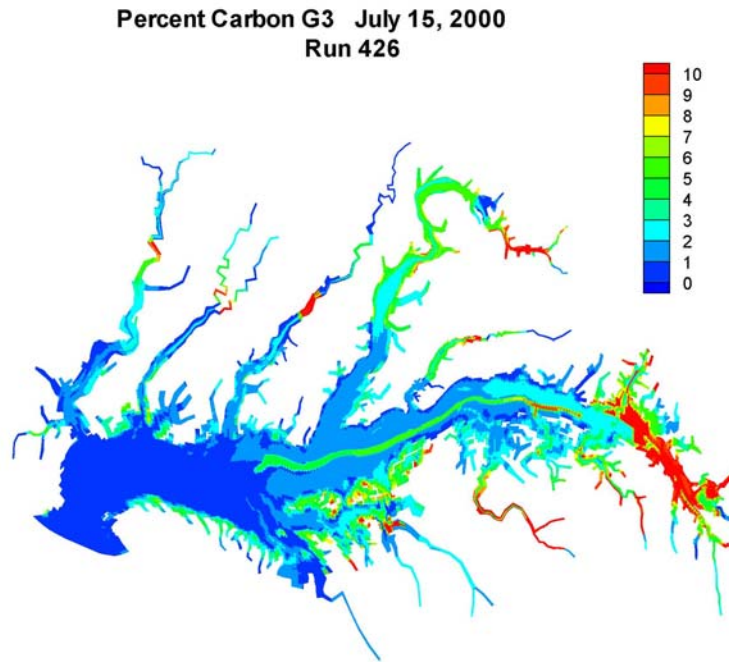
Figure 19. Computed percent sediment organic carbon. The G3 fraction shown comprises more than 90% of the total.
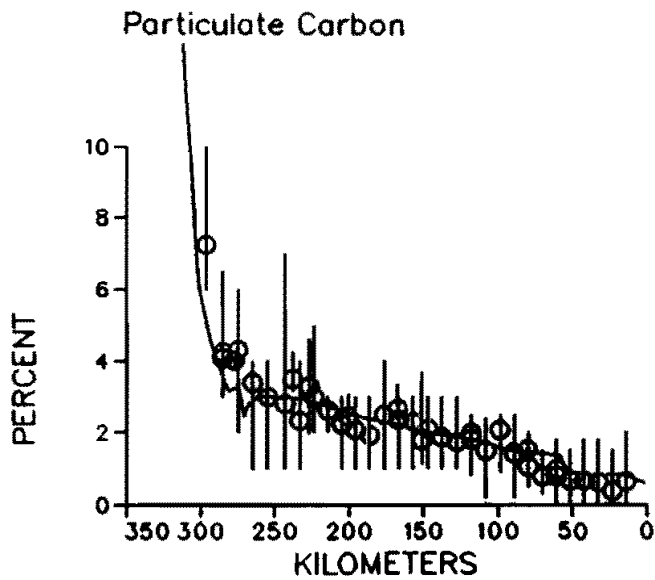
Figure 20. Computed and observed sediment organic carbon from the original eutrophication model (Cerco and Cole 1994). Note that observed sediment carbon is a high as ten percent 300 km from the mouth of the bay. Observed organic carbon declines seaward to less than one percent near the bay mouth.
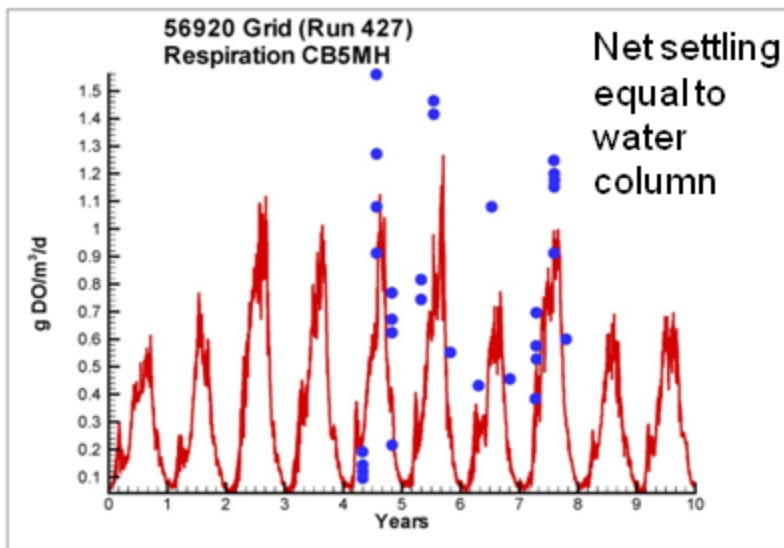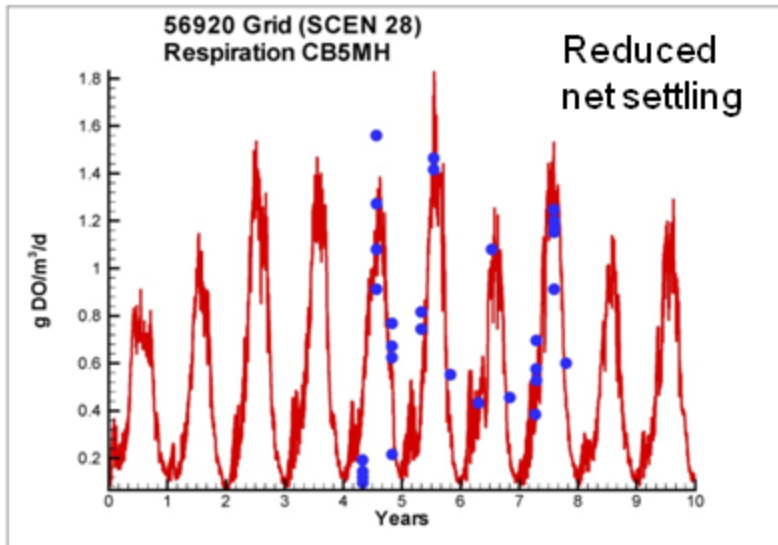
Figure 21. Computed and observed water-column respiration for two conditions. The top panel shows results using the present net settling scheme (Table 3). The bottom panel shows results for a scenario in which particles deposit directly to the sediments. Note the higher, improved respiration computations in the upper panel.
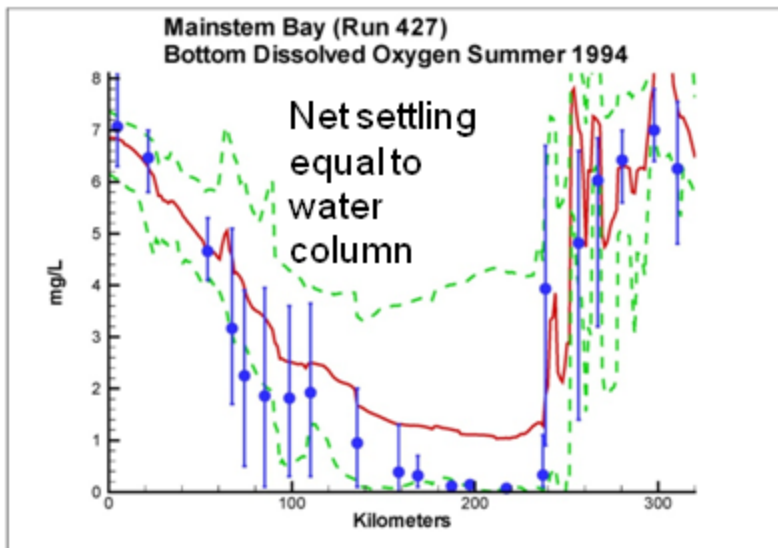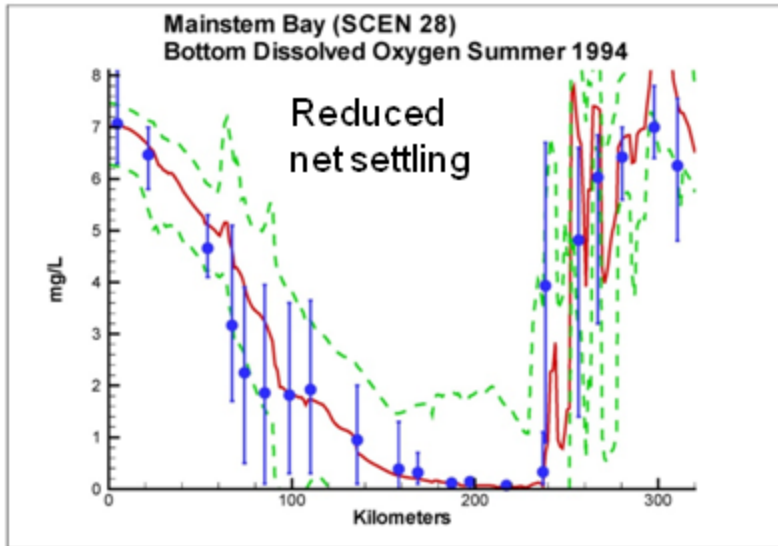
Figure 22. Computed and observed bottom-water dissolved oxygen for two conditions. The top panel shows results using the present net settling scheme (Table 3). The bottom panel shows results for a scenario in which particles deposit directly to the sediments. Note the lower, improved dissolved oxygen computations in the upper panel.

6 Water Quality Model Formulation

Introduction

CE-QUAL-ICM was designed to be a flexible, widely-applicable eutrophication model. Initial application was to Chesapeake Bay (Cerco and Cole 1994). Subsequent additional applications included the Delaware Inland Bays (Cerco et al. 1994), Newark Bay (Cerco and Bunch 1997), San Juan Estuary (Bunch et al. 2000), Virginia Tributary Refinements (Cerco et al. 2002) and the 2002 Chesapeake Bay Model (Cerco and Noel 2004). Each model application employed a different combination of model features and required addition of system-specific capabilities. This chapter describes general features and site-specific developments of the model as presently applied to the water column of Chesapeake Bay.

Conservation of Mass Equation

The foundation of CE-QUAL-ICM is the solution to the three-dimensional mass-conservation equation for a control volume. Control volumes correspond to cells on the model grid. CE-QUAL-ICM solves, for each volume and for each state variable, the equation:

$$\frac{\delta V_j \cdot C_j}{\delta t} = \sum_{k=1}^{n} Q_k \cdot C_k + \sum_{k=1}^{n} A_k \cdot D_k \cdot \frac{\delta C}{\delta x_k} + \Sigma S_j \qquad (1)$$

in which:

V_j = volume of jth control volume (m^3)
C_j = concentration in j^{th} control volume (g m^{-3})
t, x = temporal and spatial coordinates
n = number of flow faces attached to j^{th} control volume
Q_k = volumetric flow across flow face k of jth control volume (m^3 s^{-1})
C_k = concentration in flow across face k (g m^{-3})
A_k = area of flow face k (m^2)
D_k = diffusion coefficient at flow face k (m^2 s^{-1})
S_j = external loads and kinetic sources and sinks in j^{th} control volume (g s^{-1})

Solution of Equation 1 on a digital computer requires discretization of the continuous derivatives and specification of parameter values. The equation is solved using the QUICKEST algorithm (Leonard 1979) in the horizontal plane and an implicit central-difference scheme in the vertical direction. Discrete time steps, determined by computational stability requirements, are ≈15 minutes.

State Variables

At present, the CE-QUAL-ICM model incorporates 24 state variables in the water column including physical variables, multiple algal groups, two zooplankton groups, and multiple forms of carbon, nitrogen, phosphorus and silica (Table 1).

Algae

Algae are grouped into three model classes: cyanobacteria, spring diatoms, and other green algae. The grouping is based upon the distinctive characteristics of each class and upon the significant role the characteristics play in the ecosystem. Cyanobacteria, commonly called blue-green algae, are characterized by their abundance (as picoplankton) in saline water and by their bloom-forming characteristics in fresh water. Cyanobacteria are unique in that some species fix atmospheric nitrogen although nitrogen fixers are not predominant in the Chesapeake Bay system. The cyanobacteria distinguished in the model are the bloom-forming species found in the tidal, freshwater Potomac River. They are characterized as having negligible settling velocity and are subject to low predation pressure. The picoplankton are combined with the other green algae group since insufficient data exists to consider them separately. Spring diatoms are large phytoplankton that produce an annual bloom in the saline portions of the bay and tributaries. Settling of spring diatom blooms to the sediments may be a significant source of carbon for sediment oxygen demand. Diatoms are distinguished by their requirement of silica as a nutrient to form cell walls. Algae that do not fall into the preceding two groups are lumped into the heading of green algae. The green algae represent the mixture that characterizes saline waters during summer and autumn and fresh waters year round. Non-bloom forming diatoms comprise a portion of this mixture.

Zooplankton

Two zooplankton groups are considered: microzooplankton and mesozooplankton. The microzooplankton can be important predators on phytoplankton and they are one of the prey groups for mesozooplankton. Mesozooplankton consume phytoplankton and detritus as well as microzooplankton. The mesozooplankton are an important prey resource for carnivorous finfish such as Bay Anchovy. Zooplankton were included in the model as a first step towards computing the effect of eutrophication management on top-level predators (Cerco et al. 2002). Zooplankton kinetics in the present model are identical to the documentation provided by Cerco and Noel (2004).

Organic Carbon

Three organic carbon state variables are considered: dissolved, labile particulate, and refractory particulate. Labile and refractory distinctions are based upon the time scale of decomposition. Labile organic carbon decomposes on a time scale of days to weeks while refractory organic carbon requires more time. Labile organic carbon decomposes rapidly in the water column or the sediments. Refractory organic carbon decomposes slowly, primarily in the sediments, and may contribute to sediment oxygen demand years after deposition.

Nitrogen

Nitrogen is first divided into available and unavailable fractions. Available refers to employment in algal nutrition. Two available forms are considered: reduced and oxidized nitrogen. Ammonium is the single reduced nitrogen form considered. Nitrate and nitrite comprise the oxidized nitrogen pool. Both reduced and oxidized nitrogen are utilized to fulfill algal nutrient requirements. The primary reason for distinguishing the two is that ammonium is oxidized by nitrifying bacteria into nitrite and, subsequently, nitrate. This oxidation can be a significant sink of oxygen in the water column and sediments. Unavailable nitrogen state variables are dissolved organic nitrogen, labile particulate organic nitrogen, and refractory particulate organic nitrogen.

Phosphorus

As with nitrogen, phosphorus is first divided into available and unavailable fractions. Only a single available form, dissolved phosphate, is considered. The model framework allows for exchange of phosphate between dissolved and particulate (sorbed to solids) forms but this option is not implemented in the present application. Three forms of unavailable phosphorus are considered: dissolved organic phosphorus, labile particulate organic phosphorus, and refractory particulate organic phosphorus.

Silica

Silica is divided into two state variables: dissolved silica and particulate biogenic silica. Dissolved silica is available to diatoms while particulate biogenic silica cannot be utilized. In the model, particulate biogenic silica is produced through diatom mortality. Particulate biogenic silica undergoes dissolution to available silica or else settles to the bottom sediments.

Chemical Oxygen Demand

Reduced substances that are oxidized by abiotic processes are combined in the chemical oxygen demand pool. The primary component of chemical oxygen demand in saltwater is sulfide released from sediments. Oxidation of sulfide to sulfate may remove substantial quantities of dissolved oxygen from the water column. In freshwater, the primary component is methane which is also released from bottom sediments.

Dissolved Oxygen

Dissolved oxygen is required for the existence of higher life forms. Oxygen availability determines the distribution of organisms and the flows of energy and nutrients in an ecosystem. Dissolved oxygen is a central component of the water-quality model.

Salinity

Salinity is a conservative tracer that provides verification of the transport component of the model and facilitates examination of conservation of mass. Salinity also influences the dissolved oxygen saturation concentration and may be used in the determination of kinetics constants that differ in saline and fresh water.

Temperature

Temperature is a primary determinant of the rate of biochemical reactions. Reaction rates increase as a function of temperature although extreme temperatures may result in the mortality of organisms and a decrease in kinetics rates.

Fixed Solids

Fixed solids are the mineral fraction of total suspended solids. In previous model versions, fixed solids contributed to light attenuation and formed a site for sorption of dissolved inorganic phosphorus. The former role of fixed solids is now occupied by the four solids classes incorporated in the suspended solids model. The fixed solids variable is retained but has no present function.

The remainder of this chapter is devoted to detailing the kinetics sources and sinks and to reporting parameter values. For notational simplicity, the transport terms are dropped in the reporting of kinetics formulations.

Algae

Equations governing the three algal groups are largely the same. Differences among groups are expressed through the magnitudes of parameters in the equations. Generic equations are presented below except when group-specific relationships are required.

Algal sources and sinks in the conservation equation include production, metabolism, predation, and settling. These are expressed:

$$\frac{\delta}{\delta t} B = \left(G - BM - Wa \cdot \frac{\delta}{\delta z} \right) B - PR \qquad (2)$$

in which:

B = algal biomass, expressed as carbon (g C m^{-3})
G = growth (d^{-1})
BM = basal metabolism (d^{-1})
Wa = algal settling velocity (m d^{-1})
PR = predation (g C m^{-3} d^{-1})
z = vertical coordinate

Production

Production by phytoplankton is determined by the intensity of light, by the availability of nutrients, and by the ambient temperature.

Light

The influence of light on phytoplankton production is represented by a chlorophyll-specific production equation (Jassby and Platt 1976):

$$P^B = P^Bm\frac{I}{\sqrt{I^2 + Ik^2}} \qquad (3)$$

in which:

P^B = photosynthetic rate (g C g^{-1} Chl d^{-1})
P^Bm = maximum photosynthetic rate (g C g^{-1} Chl d^{-1})
I = irradiance (E m^{-2} d^{-1})

Parameter Ik is defined as the irradiance at which the initial slope of the production vs. irradiance relationship (Figure 1) intersects the value of P^Bm

$$Ik = \frac{P^Bm}{\alpha} \qquad (4)$$

in which:

α = initial slope of production vs. irradiance relationship (g C g^{-1} Chl (E m^{-2})$^{-1}$)

Chlorophyll-specific production rate is readily converted to carbon specific growth rate, for use in Equation 2, through division by the carbon-to-chlorophyll ratio:

$$G = \frac{P^B}{CChl} \qquad (5)$$

in which:

CChl = carbon-to-chlorophyll ratio (g C g^{-1} chlorophyll a)

Nutrients

Carbon, nitrogen, and phosphorus are the primary nutrients required for algal growth. Diatoms require silica, as well. Inorganic carbon is usually available in excess and is not considered in the model. The effects of the remaining nutrients on growth are described by the formulation commonly referred to as "Monod kinetics" (Figure 2; Monod 1949):

$$f(N) = \frac{D}{KHd + D} \tag{6}$$

in which:

f(N) = nutrient limitation on algal production ($0 \leq f(N) \leq 1$)
D = concentration of dissolved nutrient (g m^{-3})
KHd = half-saturation constant for nutrient uptake (g m^{-3})

Temperature

Algal production increases as a function of temperature until an optimum temperature or temperature range is reached. Above the optimum, production declines until a temperature lethal to the organisms is attained. Numerous functional representations of temperature effects are available. Inspection of growth versus temperature data indicates a function similar to a Gaussian probability curve (Figure 3) provides a good fit to observations:

$$f(T) = e^{-KTg1 \cdot (T-Topt)^2} \ when \ T \leq Topt$$
$$= e^{-KTg2 \cdot (Topt-T)^2} \ when \ T > Topt \tag{7}$$

in which:

T = temperature (^{o}C)
Topt = optimal temperature for algal growth (^{o}C)
KTg1 = effect of temperature below Topt on growth (^{o}C^{-2})
KTg2 = effect of temperature above Topt on growth (^{o}C^{-2})

Constructing the Photosynthesis vs. Irradiance Curve

A production versus irradiance relationship is constructed for each model cell at each time step. First, the maximum photosynthetic rate under ambient temperature and nutrient concentrations is determined:

$$P^B m(N,T) = P^B m \cdot f(T) \cdot \frac{D}{KHd + D} \qquad (8)$$

in which:

$P^B m(N,T)$ = maximum photosynthetic rate under ambient temperature and nutrient concentrations (g C g^{-1} Chl d^{-1})

The single most limiting nutrient is employed in determining the nutrient limitation.

Next, parameter Ik is derived from Equation 4. Finally, the production vs. irradiance relationship is constructed using $P^B m(N,T)$ and Ik. The resulting production versus irradiance curve exhibits three regions (Figure 4). For I >> Ik, the value of the term I / (I^2 + Ik^2)$^{1/2}$ approaches unity and temperature and nutrients are the primary factors that influence production. For I << Ik, production is determined solely by α and irradiance I. In the region where the initial slope of the production versus irradiance curve intercepts the line indicating production at optimal illumination, I $\approx$ Ik, production is determined by the combined effects of temperature, nutrients, and light.

Irradiance

Irradiance at the water surface is evaluated at each model time step. Instantaneous irradiance is computed by fitting a sin function to daily total irradiance:

$$Io = \frac{\Pi}{2 \cdot FD} \cdot IT \cdot \sin\left(\frac{\Pi \cdot DSSR}{FD}\right) \qquad (9)$$

in which:

Io = irradiance at water surface (E m^{-2} d^{-1})
IT = daily total irradiance (E m^{-2})
FD = fractional daylength ($0 \leq FD \leq 1$)
DSSR = time since sunrise (d)

Io is evaluated only during the interval:

$$\frac{1 - FD}{2} \leq DSM \leq \frac{1 + FD}{2} \qquad (10)$$

in which:

DSM = time since midnight (d)

Outside the specified interval, Io is set to zero.

Irradiance declines exponentially with depth below the surface. The diffuse attenuation coefficient, Kd, is computed as a function of color and concentrations of organic and mineral solids.

Respiration

Two forms of respiration are considered in the model: photo-respiration and basal metabolism. Photo-respiration represents the energy expended by carbon fixation and is a fixed fraction of production. In the event of no production (e.g. at night), photo-respiration is zero. Basal metabolism is a continuous energy expenditure to maintain basic life processes. In the model, metabolism is considered to be an exponentially increasing function of temperature (Figure 5). Total respiration is represented:

$$R \; = \; Presp \cdot G + BM \cdot e^{KTb \cdot (T - Tr)} \qquad (11)$$

in which:

Presp = photo-respiration ($0 \leq Presp \leq 1$)
BM = metabolic rate at reference temperature Tr (d^{-1})
KTb = effect of temperature on metabolism ($^{o}C^{-1}$)
Tr = reference temperature for metabolism (^{o}C)

Predation

The predation term includes the activity of zooplankton, filter-feeding benthos, and other pelagic filter feeders including planktivorous fish. Formulation and results of the zooplankton computation appear in Cerco and Noel (2004). Details of the benthos computations may be found in Cerco and Noel (2010). Predation by other planktivores is modeled by assuming predators clear a specific volume of water per unit biomass:

$$PR = F \times B \times M \qquad (12)$$

in which:

F = filtration rate ($m^{3} \; g^{-1}$ predator C d^{-1})
M = planktivore biomass (g C m^{-3})

Detailed specification of the spatial and temporal distribution of the predator population is impossible. One approach is to assume predator biomass is proportional to algal biomass, $M = \gamma \, B$, in which case Equation 12 can be rewritten:

$$PR \; = \; \gamma \cdot F \cdot B^{2} \qquad (13)$$

Since neither γ nor F are known precisely, the logical approach is to combine their product into a single unknown determined during the model calibration procedure. Effect of temperature on predation is represented with the same formulation as the effect of temperature on respiration. The final representation of predation, including zooplankton, is:

$$PR = \frac{B}{KHsz + B} \times RMsz \times SZ$$

$$+ \frac{B}{KHlz + B} \times RMlz \times LZ + Phtl \times B^2$$

(14)

in which:

RMsz = microzooplankton maximum ration (g algal C g^{-1} zoo C d^{-1})
SZ = microzooplankton biomass (g C m^{-3})
KHsz = half saturation concentration for carbon uptake by microzooplankton (g C m^{-3})
RMlz = mesozooplankton maximum ration (g algal C g^{-1} zoo C d^{-1})
LZ = mesozooplankton biomass (g C m^{-3})
KHlz = half saturation concentration for carbon uptake by mesozooplankton (g C m^{-3})
Phtl = rate of predation by other planktivores (m^3 g^{-1} C d^{-1})

Predation by filter-feeding benthos is represented as a loss term only in model cells that intersect the bottom.

Accounting for Algal Phosphorus

The amount of phosphorus incorporated in algal biomass is quantified through a stoichiometric ratio. Thus, total phosphorus in the model is expressed:

$$TotP = PO_4 + Apc \times B + DOP + LPOP + RPOP \qquad (15)$$

in which:

TotP = total phosphorus (g P m^{-3})
PO$_4$ = dissolved phosphate (g P m^{-3})
Apc = algal phosphorus-to-carbon ratio (g P g^{-1} C)
DOP = dissolved organic phosphorus (g P m^{-3})
LPP = labile particulate organic phosphorus (g P m^{-3})
RPP = refractory particulate organic phosphorus (g P m^{-3})

Algae take up dissolved phosphate during production and release dissolved phosphate and organic phosphorus through respiration. The fate of phosphorus released by respiration is determined by empirical distribution

coefficients. The fate of algal phosphorus recycled by predation is determined by a second set of distribution parameters.

Accounting for Algal Nitrogen

Model nitrogen state variables include ammonium, nitrate+nitrite, dissolved organic nitrogen, labile particulate organic nitrogen, and refractory particulate organic nitrogen. The amount of nitrogen incorporated in algal biomass is quantified through a stoichiometric ratio. Thus, total nitrogen in the model is expressed:

$$TotN = NH_4 + NO_{23}$$

$$+ Anc \cdot B + DON + LPON + RPON \qquad (16)$$

TotN = total nitrogen (g N m^{-3})
NH$_4$ = ammonium (g N m^{-3})
NO$_{23}$ = nitrate+nitrite (g N m^{-3})
Anc = algal nitrogen-to-carbon ratio (g N g^{-1} C)
DON = dissolved organic nitrogen (g N m^{-3})
LPON = labile particulate organic nitrogen (g N m^{-3})
RPON = refractory particulate organic nitrogen (g N m^{-3})

As with phosphorus, the fate of algal nitrogen released by metabolism and predation is represented by distribution coefficients.

Algal Nitrogen Preference

Algae take up ammonium and nitrate+nitrite during production and release ammonium and organic nitrogen through respiration. Nitrate+nitrite is internally reduced to ammonium before synthesis into biomass occurs (Parsons et al. 1984). Trace concentrations of ammonium inhibit nitrate reduction so that, in the presence of multiple nitrogenous nutrients, ammonium is utilized first. The "preference" of algae for ammonium is expressed by a modification of an empirical function presented by Thomann and Fitzpatrick (1982):

$$PN = NH_4 \cdot \frac{NO_{23}}{(KHNH_4 + NH_4) \cdot (KHNH_4 + NO_{23})}$$

$$\qquad (17)$$

$$+ NH_4 \cdot \frac{KHNH_4}{(NH_4 + NO_{23}) \cdot (KHNH_4 + NO_{23})}$$

in which

PN = algal preference for ammonium uptake ($0 \leq Pn \leq 1$)
KHNH$_4$ = half saturation concentration for algal ammonium uptake (g N m^{-3})

Our modification substitutes a specific half-saturation concentration for ammonium uptake, KHNH₄, for the original use of half-saturation concentration for nitrogen uptake, KHn. We found the modification enforces ammonium use down to lower concentrations that the original formulation.

The preference function has two limiting values (Figure 6). When nitrate+nitrite is absent, the preference for ammonium is unity. When ammonium is absent, the preference is zero. In the presence of ammonium and nitrate+nitrite, the preference depends on the abundance of both forms relative to the half-saturation constant for nitrogen uptake. When both ammonium and nitrate+nitrite are abundant, the preference for ammonium approaches unity. When ammonium is scarce but nitrate+nitrite is abundant, the preference decreases in magnitude and a significant fraction of algal nitrogen requirement comes from nitrate+nitrite.

Effect of Algae on Dissolved Oxygen

Algae produce oxygen during photosynthesis and consume oxygen through respiration. The quantity produced depends on the form of nitrogen utilized for growth. More oxygen is produced, per unit of carbon fixed, when nitrate is the algal nitrogen source than when ammonium is the source. Equations describing algal uptake of carbon and nitrogen and production of dissolved oxygen (Morel 1983) are:

$$106 \ CO_2 + 16 \ NH_4^+ + H_2PO_4^- + 106 \ H_2O \ \text{-->}$$

$$protoplasm + 106 \ O_2 + 15 \ H^+ \qquad\qquad (18)$$

$$106 \ CO_2 + 16 \ NO_3^- + H_2PO_4^- + 122 \ H_2O + 17 \ H^+ \ \text{-->}$$

$$protoplasm + 138 \ O_2 \qquad\qquad (19)$$
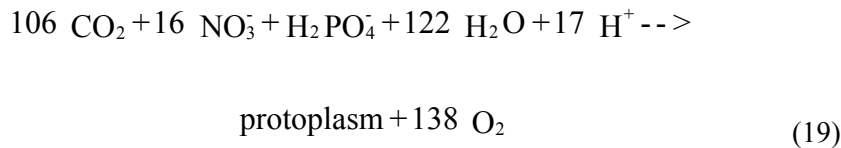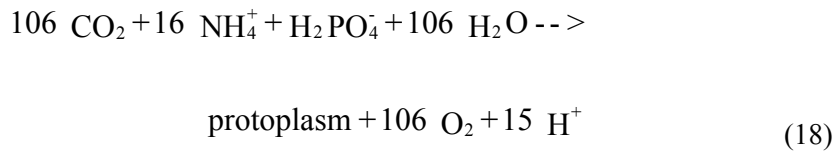
When ammonium is the nitrogen source, one mole oxygen is produced per mole carbon dioxide fixed. When nitrate is the nitrogen source, 1.3 moles oxygen are produced per mole carbon dioxide fixed.

The equation that describes the effect of algae on dissolved oxygen in the model is:

$$\frac{\delta}{\delta t}DO = \left[(1.3 - 0.3 \cdot PN)\cdot P - (1 - FCD)\cdot BM\right]\cdot AOCR \cdot B \quad (20)$$

in which:

FCD = fraction of algal metabolism recycled as dissolved organic carbon ($0 \leq$ FCD ≤ 1)
AOCR = dissolved oxygen-to-carbon ratio in respiration (2.67 g O_2 g^{-1} C)

The magnitude of AOCR is derived from a simple representation of the respiration process:

$$CH_2O + O_2 = CO_2 + H_2O \qquad (21)$$
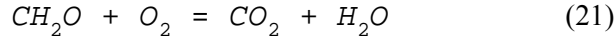
The quantity $(1.3 - 0.3 \cdot PN)$ is the photosynthesis ratio and expresses the molar quantity of oxygen produced per mole carbon fixed. The photosynthesis ratio approaches unity as the algal preference for ammonium approaches unity.

Accounting for Algal Silica

The amount of silica incorporated in algal biomass is quantified through a stoichiometric ratio. Thus, total silica in the model is expressed:

$$TotSi = Dsil + Asc \cdot B + PBS \qquad (22)$$

TotSi = total silica (g Si m^{-3})
Dsil = dissolved silica (g Si m^{-3})
Asc = algal silica-to-carbon ratio (g Si g^{-1} C)
PBS = particulate biogenic silica (g Si m^{-3})

As with the other nutrients, the fate of algal silica released by metabolism and predation is represented by distribution coefficients.

Salinity Toxicity

The cyanobacteria represented in the model are freshwater organisms that cease production when salinity exceeds 1 to 2 ppt (Sellner et al. 1988). The effect of salinity on cyanobacteria was represented by a mortality term in the form of a rectangular hyperbola:

$$STOX1 = STF1 \cdot \frac{S}{KHst1 + S} \qquad (23)$$

in which

STOX1 = mortality induced by salinity on cyanobacteria (d^{-1})
STF1 = maximum salinity mortality on cyanobacteria (d^{-1})
S = salinity (ppt)

KHst1 = salinity at which mortality is half maximum value (ppt)

The spring diatom bloom is limited to saline water. The limiting mechanism is not defined but appears to be related to salinity. The upstream limit of the spring bloom was defined in the model by introducing a mortality term at low salinity:

$$STOX2 = STF2 \times \frac{KHst2}{KHst2 + S} \qquad (24)$$

in which

STOX2 = mortality induced by freshwater on spring diatoms (d^{-1})
STF2 = maximum freshwater mortality on spring diatoms (d^{-1})
S = salinity (ppt)
KHst2 = salinity at which mortality is half maximum value (ppt)

The salinity-related mortality (Figure 7) is added to the basal metabolism.

Organic Carbon

Organic carbon undergoes innumerable transformations in the water column. The model carbon cycle (Figure 8) consists of the following elements:

> Phytoplankton production and excretion
> Zooplankton production and excretion
> Predation on phytoplankton
> Dissolution of particulate carbon
> Heterotrophic respiration
> Settling

Algal production is the primary carbon source although carbon also enters the system through external loading. Predation on algae by zooplankton and other organisms releases particulate and dissolved organic carbon to the water column. A fraction of the particulate organic carbon undergoes first-order dissolution to dissolved organic carbon. Dissolved organic carbon produced by excretion, by predation, and by dissolution is respired at a first-order rate to inorganic carbon. Particulate organic carbon which does not undergo dissolution settles to the bottom sediments.

Organic carbon dissolution and respiration are represented as first-order processes in which the reaction rate is proportional to concentration of the reactant. An exponential function (Figure 5) relates dissolution and respiration to temperature. Former applications of the model (e.g. Cerco and Noel 2004) included carbon loss through water column denitrification. Denitrification remains in the model code but is no longer implemented. The process was difficult to parameterize and was not a major element of the carbon or nitrogen cycles.

Dissolved Organic Carbon

The complete representation of dissolved organic carbon sources and sinks in the model ecosystem is:

$$\frac{\delta}{\delta t} DOC = FCD \cdot R \cdot B + FCDP \cdot PR + Klpoc \cdot LPOC$$

$$+ Krpoc \cdot RPOC - \frac{DO}{KHodoc + DO} \cdot Kdoc \cdot DOC \tag{25}$$

in which:

DOC = dissolved organic carbon (g m^{-3})
LPOC = labile particulate organic carbon (g m^{-3})
RPOC = refractory particulate organic carbon (g m^{-3})
FCD = fraction of algal respiration released as DOC (0 < FCD < 1)
FCDP = fraction of predation on algae released as DOC (0 < FCDP < 1)
Klpoc = dissolution rate of LPOC (d^{-1})
Krpoc = dissolution rate of RPOC (d^{-1})
Kdoc = respiration rate of DOC (d^{-1})

Labile Particulate Organic Carbon

The complete representation of labile particulate organic carbon sources and sinks in the model ecosystem is:

$$\frac{\delta}{\delta t} LPOC = FCL \cdot R \cdot B + FCLP \cdot PR - Klpoc \cdot LPOC$$

$$- Wl \cdot \frac{\delta}{\delta z} LPOC \tag{26}$$

in which:

FCL = fraction of algal respiration released as LPOC (0 < FCL < 1)
FCLP = fraction of predation on algae released as LPOC (0 < FCLP < 1)
Wl = settling velocity of labile particles (m d^{-1})

Refractory Particulate Organic Carbon

The complete representation of refractory particulate organic carbon sources and sinks in the model ecosystem is:

$$\frac{\delta}{\delta t} RPOC = FCR \cdot R \cdot B + FCRP \cdot PR - Krpoc \cdot RPOC$$

$$- Wr \cdot \frac{\delta}{\delta z} RPOC \tag{27}$$

in which:

FCR = fraction of algal respiration released as RPOC (0 < FCR < 1)
FCRP = fraction of predation on algae released as RPOC (0 < FCRP < 1)
Wr = settling velocity of refractory particles (m d^{-1})

Phosphorus

The model phosphorus cycle (Figure 9) includes the following processes:

> Algal uptake and excretion
> Zooplankton excretion
> Predation
> Hydrolysis of particulate organic phosphorus
> Mineralization of dissolved organic phosphorus
> Settling and resuspension

External loads provide the ultimate source of phosphorus to the system. Dissolved phosphate is incorporated by algae during growth and released as phosphate and organic phosphorus through respiration and predation. Dissolved organic phosphorus is mineralized to phosphate. A portion of the particulate organic phosphorus hydrolyzes to dissolved organic phosphorus. The balance settles to the sediments. Within the sediments, particulate phosphorus is mineralized and recycled to the water column as dissolved phosphate.

Hydrolysis and Mineralization

Within the model, hydrolysis is defined as the process by which particulate organic substances are converted to dissolved organic form. Mineralization is defined as the process by which dissolved organic substances are converted to dissolved inorganic form. Conversion of particulate organic phosphorus to phosphate proceeds through the sequence of hydrolysis and mineralization. Direct mineralization of particulate organic phosphorus does not occur.

Mineralization of organic phosphorus is mediated by the release of nucleotidase and phosphatase enzymes by bacteria (Ammerman and Azam 1985; Chrost and Overbeck 1987) and algae (Matavulj and Flint 1987; Chrost and Overbeck 1987; Boni et al. 1989). Since the algae themselves release the enzyme and since bacterial abundance is related to algal biomass, the rate of organic phosphorus mineralization is related, in the model, to algal biomass. A most remarkable property of the enzyme process is that alkaline phosphatase activity is inversely proportional to ambient phosphate concentration (Chrost and Overbeck 1987; Boni et al. 1989). Put in different terms, when phosphate is scarce, algae stimulate production of an enzyme that mineralizes organic phosphorus to phosphate. This phenomenon is simulated by relating mineralization to the algal phosphorus nutrient limitation. Mineralization is highest when algae are strongly phosphorus limited and is least when no limitation occurs.

The expression for mineralization rate is:

$$Kdop \; = \; Kdp \; + \; \frac{KHp}{KHp \; + \; PO_4} \cdot Kdpalg \cdot B \qquad (28)$$

in which:

Kdop = mineralization rate of dissolved organic phosphorus (d^{-1})
Kdp = minimum mineralization rate (d^{-1})
KHp = half-saturation concentration for algal phosphorus uptake (g P m^{-3})
PO_4 = dissolved phosphate (g P m^{-3})
Kdpalg = constant that relates mineralization to algal biomass (m^3 g^{-1} C d^{-1})

Potential effects of algal biomass and nutrient limitation on the mineralization rate are shown in Figure 10.   When nutrient concentration greatly exceeds the half-saturation concentration for algal uptake, the rate roughly equals the minimum.   Algal biomass has little influence.   As nutrient becomes scarce relative to the half-saturation concentration, the rate increases.   The magnitude of the increase depends on algal biomass.   Factor of two to three increases are feasible.   Exponential functions (Figure 5) relate mineralization and hydrolysis rates to temperature.

Dissolved Phosphate

The mass-balance equation for dissolved phosphate is:

$$\frac{\delta}{\delta \, t} \, PO_4 = Kdop \; \cdot \; DOP - APC \; \cdot \; G \; \cdot \; B$$

$$+ \; APC \; \cdot \; \left[FPI \; \cdot \; BM \; \cdot B + FPIP \; \cdot \; PR \right] - Wpo_4 \cdot \frac{\delta}{\delta z} PO_4 \qquad (29)$$

in which:

FPI = fraction of algal metabolism released as dissolved phosphate ($0 \leq$ FPI ≤ 1)
FPIP = fraction of predation released as dissolved phosphate ($0 \leq$ FPIP ≤ 1)
Wpo_4 = settling rate of precipitated phosphate (m d^{-1})

Phosphate settling represents phosphate removal through co-precipitation with iron and manganese during the break-up of seasonal bottom-water anoxia. The settling rate is implemented for a thirty-day period in appropriate portions of the system.

Dissolved Organic Phosphorus

The mass balance equation for dissolved organic phosphorus is:

$$\frac{\delta}{\delta t}DOP = APC \cdot (BM \cdot B \cdot FPD + PR \cdot FPDP) + Klpop \cdot LPOP$$
$$+ Krpop \cdot RPOP - Kdop \cdot DOP \tag{30}$$

in which:

DOP = dissolved organic phosphorus (g P m^{-3})
LPOP = labile particulate organic phosphorus (g P m^{-3})
RPOP = refractory particulate organic phosphorus (g P m^{-3})
FPD = fraction of algal metabolism released as DOP (0 < FPD < 1)
FPDP = fraction of predation on algae released as DOP (0 < FPDP < 1)
Klpop = hydrolysis rate of LPOP (d^{-1})
Krpop = hydrolysis rate of RPOP (d^{-1})
Kdop = mineralization rate of DOP (d^{-1})

Labile Particulate Organic Phosphorus

The mass balance equation for labile particulate organic phosphorus is:

$$\frac{\delta}{\delta t}LPOP = APC \cdot (BM \cdot B \cdot FPL + PR \cdot FPLP) - Klpop \cdot LPOP$$
$$- Wl \cdot \frac{\delta}{\delta z}LPOP \tag{31}$$

in which:

FPL = fraction of algal metabolism released as LPOP (0 < FPL < 1)
FPLP = fraction of predation on algae released as LPOP (0 < FPLP < 1)

Refractory Particulate Organic Phosphorus

The mass balance equation for refractory particulate organic phosphorus is:

$$\frac{\delta}{\delta t}RPOP = APC \cdot (BM \cdot B \cdot FPR + PR \cdot FPRP) - Krpop \cdot RPOP$$
$$- Wr \cdot \frac{\delta}{\delta z}RPOP \tag{32}$$

in which:

FPR = fraction of algal metabolism released as RPOP (0 < FPR < 1)
FPRP = fraction of predation on algae released as RPOP (0 < FPRP < 1)

Nitrogen

The model nitrogen cycle (Figure 11) includes the following processes:

> Algal production and metabolism
> Predation
> Hydrolysis of particulate organic nitrogen
> Mineralization of dissolved organic nitrogen
> Settling
> Nitrification

External loads provide the ultimate source of nitrogen to the system. Available nitrogen is incorporated by algae during growth and released as ammonium and organic nitrogen through respiration and predation. A portion of the particulate organic nitrogen hydrolyzes to dissolved organic nitrogen. The balance settles to the sediments. Dissolved organic nitrogen is mineralized to ammonium. In an oxygenated water column, a fraction of the ammonium is subsequently oxidized to nitrate+nitrite through the nitrification process. Particulate nitrogen that settles to the sediments is mineralized and recycled to the water column, primarily as ammonium. Nitrate+nitrite moves in both directions across the sediment-water interface, depending on relative concentrations in the water column and sediment interstices.

Nitrification

Nitrification is a process mediated by specialized groups of autotrophic bacteria that obtain energy through the oxidation of ammonium to nitrite and oxidation of nitrite to nitrate. A simplified expression for complete nitrification (Tchobanoglous and Schroeder 1987) is:

$$NH_4^+ \ + \ 2\,O_2 \ \text{-->} \ NO_3^- \ + \ H_2O \ + \ 2\,H^+ \qquad (33)$$
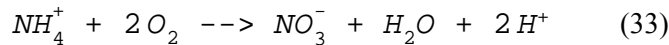
The simplified stoichiometry indicates that two moles of oxygen are required to nitrify one mole of ammonium into nitrate. The simplified equation is not strictly true, however. Cell synthesis by nitrifying bacteria is accomplished by the fixation of carbon dioxide so that less than two moles of oxygen are consumed per mole ammonium utilized (Wezernak and Gannon 1968).

The kinetics of complete nitrification are modeled as a function of available ammonium, dissolved oxygen, and temperature:

$$NT = \frac{DO}{KHont + DO} \ \cdot \ \frac{NH_4}{KHnnt + NH_4} \ \cdot \ f(T) \ \cdot \ NTm \qquad (34)$$

in which:

NT = nitrification rate (g N m^{-3} d^{-1})
KHont = half-saturation constant of dissolved oxygen required for nitrification (g O$_2$ m^{-3})

KHnnt = half-saturation constant of NH_4 required for nitrification (g N m^{-3})
NTm = maximum nitrification rate at optimal temperature (g N m^{-3} d^{-1})

The kinetics formulation (Figure 12) incorporates the products of two Monod-like functions. The first function diminishes nitrification at low dissolved oxygen concentration. The second function expresses the influence of ammonium concentration on nitrification. When ammonium concentration is low, relative to KHnnt, nitrification is proportional to ammonium concentration. For NH4 << KHnnt, the reaction is approximately first-order. (The first-order decay constant $\approx$ NTm/KHnnt.) When ammonium concentration is large, relative to KHnnt, nitrification approaches a maximum rate. This formulation is based on a concept proposed by Tuffey et al. (1974). Nitrifying bacteria adhere to benthic or suspended sediments. When ammonium is scarce, vacant surfaces suitable for nitrifying bacteria exist. As ammonium concentration increases, bacterial biomass increases, vacant surfaces are occupied, and the rate of nitrification increases. The bacterial population attains maximum density when all surfaces suitable for bacteria are occupied. At this point, nitrification proceeds at a maximum rate independent of additional increase in ammonium concentration.

The optimal temperature for nitrification may be less than peak temperatures that occur in coastal waters. To allow for a decrease in nitrification at superoptimal temperature, the effect of temperature on nitrification is modeled in the Gaussian form of Equation 7.

Nitrogen Mass Balance Equations

The mass-balance equations for nitrogen state variables are written by summing all previously-described sources and sinks:

Ammonium

$$\frac{\delta}{\delta t} NH_4 = ANC \cdot [(BM \cdot FNI - PN \cdot P) \cdot B + PR \cdot FNIP]$$
$$+ Kdon \cdot DON - NT \tag{35}$$

in which:

FNI = fraction of algal metabolism released as NH4 ($0 \leq FNI \leq 1$)
PN = algal ammonium preference ($0 \leq PN \leq 1$)
FNIP = fraction of predation released as NH4 ($0 \leq FNIP \leq 1$)

Nitrate+Nitrite

$$\frac{\delta}{\delta t} NO_{23} = - ANC \cdot (1 - PN) \cdot P \cdot B + NT$$
$$\tag{36}$$

Dissolved Organic Nitrogen

$$\frac{\delta}{\delta t} DON = ANC \cdot (BM \cdot B \cdot FND + PR \cdot FNDP) + Klpon \cdot LPON$$
$$+ Krpon \cdot RPON - Kdon \cdot DON \quad (37)$$

in which:

DON = dissolved organic nitrogen (g N m^{-3})
LPON = labile particulate organic nitrogen (g N m^{-3})
RPON = refractory particulate organic nitrogen (g N m^{-3})
FND = fraction of algal metabolism released as DON ($0 < FND < 1$)
FNDP = fraction of predation on algae released as DON ($0 < FNDP < 1$)
Klpon = hydrolysis rate of LPON (d^{-1})
Krpon = hydrolysis rate of RPON (d^{-1})
Kdon = mineralization rate of DON (d^{-1})

Labile Particulate Organic Nitrogen

$$\frac{\delta}{\delta t} LPON = ANC \cdot (BM \cdot B \cdot FNL + PR \cdot FNLP) - Klpon \cdot LPON$$
$$- Wl \cdot \frac{\delta}{\delta z} LPON \quad (38)$$

in which:

FNL = fraction of algal metabolism released as LPON ($0 < FNL < 1$)
FNLP = fraction of predation on algae released as LPON ($0 < FNLP < 1$)

Refractory Particulate Organic Nitrogen

$$\frac{\delta}{\delta t} RPON = ANC \cdot (BM \cdot B \cdot FPR + PR \cdot FPRN) - Krpon \cdot RPON$$
$$- Wr \cdot \frac{\delta}{\delta z} RPON \quad (39)$$

in which:

FNR = fraction of algal metabolism released as RPON ($0 < FNR < 1$)
FNRP = fraction of predation on algae released as RPON ($0 < FNRP < 1$)

Silica

The model incorporates two siliceous state variables, dissolved silica and particulate biogenic silica. The silica cycle (Figure 13) is a simple one in which

diatoms take up disolved silica and recycle dissolved and particulate biogenic silica through the actions of metabolism and predation.   Particulate silica dissolves in the water column or settles to the bottom.   A portion of the settled particulate biogenic dissolves within the sediments and returns to the water column as dissolved silica.   Sources and sinks represented are:

> Diatom production and metabolism
> Predation
> Dissolution of particulate to dissolved silica
> Settling

Dissolved Silica

The kinetics equation for dissolved silica is:

$$\frac{\delta}{\delta t} Dsil = (FSAP \cdot PR - P) \cdot ASC \cdot B + Ksua \cdot PBS \quad (40)$$

in which:

Dsil = dissolved silica (g Si m^{-3})
PBS = particulate biogenic silica concentration (g Si m^{-3})
FSAP = fraction of diatom silica made available by predation
$\quad (0 \leq FSAP \leq 1)$
ASC = algal silica-to-carbon ratio (g Si g^{-1} C)
Ksua = particulate silica dissolution rate (d^{-1})

Particulate Biogenic Silica

The kinetics equation for particulate biogenic silica is:

$$\frac{\delta}{\delta t} PBS = \left(BM + (1 - FSAP) \cdot PR \right) \cdot ASC \cdot B$$

$$\quad (41)$$

$$- Wpbs \frac{\delta}{\delta z} PBS - Ksua \cdot PBS$$

in which:

Wpbs = biogenic silica settling rate (m d^{-1})

An exponential function (Figure 5) describes the effect of temperature on silica dissolution.

Chemical Oxygen Demand

Chemical oxygen demand is the concentration of reduced substances that are oxidized through abiotic reactions. The source of chemical oxygen demand in saline water is sulfide released from sediments. A cycle occurs in which sulfate is reduced to sulfide in the sediments and reoxidized to sulfate in the water column. In freshwater, methane is released to the water column by the sediment model. Both sulfide and methane are quantified in units of oxygen demand and are treated with the same kinetics formulation:

$$\frac{\delta}{\delta t} COD = - \frac{DO}{KHocod + DO} \cdot Kcod \cdot COD \qquad (42)$$

in which:

COD = chemical oxygen demand concentration (g oxygen-equivalents m^{-3})
KHocod = half-saturation concentration of dissolved oxygen required for exertion of chemical oxygen demand (g O_2 m^{-3})
Kcod = oxidation rate of chemical oxygen demand (d^{-1})

An exponential function (Figure 5) describes the effect of temperature on exertion of chemical oxygen demand.

Dissolved Oxygen

Sources and sinks of dissolved oxygen in the water column (Figure 14) include:

> Algal photosynthesis
> Atmospheric reaeration
> Algal respiration
> Heterotrophic respiration
> Nitrification
> Chemical oxygen demand

Reaeration

The rate of reaeration is proportional to the dissolved oxygen deficit in model

$$\frac{\delta}{\delta t} DO = \frac{Kr}{\Delta z} \cdot (DOs - DO) \qquad (43)$$

segments that form the air-water interface:
in which:

DO = dissolved oxygen concentration (g O_2 m^{-3})
Kr = reaeration coefficient (m d^{-1})
DOs = dissolved oxygen saturation concentration (g O_2 m^{-3})
Δz = model layer thickness (m)

In freeflowing streams, the reaeration coefficient depends largely on turbulence generated by bottom shear stress (O'Connor and Dobbins 1958). In lakes and coastal waters, however, wind effects may dominate the reaeration process (O'Connor 1983). For Chesapeake Bay, a relationship for wind-driven gas exchange (Hartman and Hammond 1985) is employed:

$$Kr = Arear \bullet Rv \bullet Wms^{1.5} \qquad (44)$$

in which:

Arear = empirical constant (≈ 0.1)
Rv = ratio of kinematic viscosity of pure water at 20 ^{o}C to kinematic viscosity of water at specified temperature and salinity
Wms = wind speed measured at 10 m above water surface (m s^{-1})

Hartman and Hammond (1985) indicate Arear takes the value 0.157. In the present model, Arear is treated as a variable to allow for effects of wind sheltering, for differences in height of local wind observations, and for other factors. An empirical function (Figure 15) that fits tabulated values of Rv is:

$$Rv = 0.54 + 0.0233 \bullet T - 0.0020 \bullet S \qquad (45)$$

in which:

S = salinity (ppt)
T = temperature (^{o}C)

Saturation dissolved oxygen concentration diminishes as temperature and salinity increase. An empirical formula that describes these effects (Genet et al. 1974) is:

$$DOs = 14.5532 - 0.38217 \cdot T + 0.0054258 \cdot T^2$$
$$- CL \cdot (1.665 \times 10^{-4} - 5.866 \times 10^{-6} \cdot T + 9.796 \times 10^{-8} \cdot T^2) \qquad (46)$$

in which:

CL = chloride concentration (= salinity/1.80655)

Mass Balance Equation for Dissolved Oxygen

$$\frac{\delta}{\delta t} DO = AOCR \cdot \left[(1.3 - 0.3 \cdot PN) \cdot P - (1 - FCD) \cdot BM \right] \cdot B$$

$$- AONT \cdot NT - \frac{DO}{KHodoc + DO} \cdot AOCR \cdot Kdoc \cdot DOC \qquad (47)$$

$$- \frac{DO}{KHocod + DO} \cdot Kcod \cdot COD + \frac{Kr}{H} \cdot (DOs - DO)$$

in which:

AOCR = oxygen-to-carbon mass ratio in production and respiration (= 2.67 g O_2 g^{-1} C)
AONT = oxygen consumed per mass ammonium nitrified (= 4.33 g O_2 g^{-1} N)

Temperature

Computation of temperature employs a conservation of internal energy equation that is analogous to the conservation of mass equation. For practical purposes, the internal energy equation can be written as a conservation of temperature equation. The only source or sink of temperature considered is exchange with the atmosphere. Atmospheric exchange is considered proportional to the temperature difference between the water surface and a theoretical equilibrium temperature (Edinger et al. 1974):

$$\frac{\delta}{\delta t} T = \frac{KT}{\rho \cdot Cp \cdot H} \cdot (Te - T) \qquad (48)$$

in which:

T = water temperature (^{o}C)
Te = equilibrium temperature (^{o}C)
KT = Heat exchange coefficient (watt m^{-2} $^{o}C^{-1}$)
Cp = specific heat of water (4200 watt s kg^{-1} $^{o}C^{-1}$)
ρ = density of water (1000 kg m^{-3})

Salinity

Salinity is modeled by the conservation of mass equation with no internal sources or sinks

Parameter Values

Model parameter evaluation is a recursive process. Parameters are selected from a range of feasible values, tested in the model, and adjusted until satisfactory agreement between predicted and observed variables is obtained. Ideally, the range of feasible values is determined by observation or experiment. For some parameters, however, no observations are available. Then, the feasible range is determined by parameter values employed in similar models or by the judgment of the modeler. A review of parameter values was included in documentation of the first application of this model (Cerco and Cole 1994). Parameters from the initial study were refined in successive applications and refined again for the present model. A complete set of parameter values is provided in Table 2.

Table 1 Water Quality Model State Variables	
Temperature	Salinity
Fixed Solids	Freshwater Cyanobacteria
Spring Diatoms	Other (Green) Algae
Microzooplankton	Mesozooplankton
Dissolved Organic Carbon	Labile Particulate Organic Carbon
Refractory Particulate Organic Carbon	Ammonium
Nitrate+Nitrite	Dissolved Organic Nitrogen
Labile Particulate Organic Nitrogen	Refractory Particulate Organic Nitrogen
Total Phosphate	Dissolved Organic Phosphorus
Labile Particulate Organic Phosphorus	Refractory Particulate Organic Phosphorus
Chemical Oxygen Demand	Dissolved Oxygen
Dissolved Silica	Particulate Biogenic Silica

Table 2
Parameters in Kinetics Equations

Symbol	Definition	Value	Units
ANC	nitrogen-to-carbon ratio of algae	0.167	g N g^{-1} C
AOCR	dissolved oxygen-to-carbon ratio in respiration	2.67	g O$_2$ g^{-1} C
AONT	mass dissolved oxygen consumed per mass ammonium nitrified	4.33	g O$_2$ g^{-1} N
APC	algal phosphorus-to-carbon ratio	0.0125 (cyan), 0.0125 (spring) 0.0220 (green)	g P g^{-1} C
Areaer	empirical constant in reaeration equation	0.156	
ASC	algal silica-to-carbon ratio	0.0 (cyan), 0.3 (spring), 0.1 (green)	g Si g^{-1} C
BM	basal metabolic rate of algae at reference temperature Tr	0.03 (cyan), 0.01 (spring), 0.02 (green)	d^{-1}
CChl	algal carbon-to-chlorophyll ratio	30 (cyan), 75 (spring), 60 (green)	g C g^{-1} Chl
FCD	fraction of dissolved organic carbon produced by algal metabolism	0.0	$0 \leq FCD \leq 1$
FCDP	fraction of dissolved organic carbon produced by predation	0.7	$0 \leq FCDP \leq 1$
FCL	fraction of labile particulate carbon produced by algal metabolism	0.0	$0 \leq FCL \leq 1$
FCLP	fraction of labile particulate carbon produced by predation	0.2	$0 \leq FCLP \leq 1$
FCR	fraction of refractory particulate carbon produced by algal metabolism	0.0	$0 \leq FCR \leq 1$
FCRP	fraction of refractory particulate carbon produced by predation	0.1	$0 \leq FCRP \leq 1$
FNI	fraction of inorganic nitrogen produced by algal metabolism	0.55	$0 \leq FNI \leq 1$
FNIP	fraction of inorganic nitrogen produced by predation	0.7	$0 \leq FNIP \leq 1$
FND	fraction of dissolved organic nitrogen produced by algal metabolism	0.2	$0 \leq FND \leq 1$
FNDP	fraction of dissolved organic nitrogen produced by predation	0.0	$0 \leq FNDP \leq 1$
FNL	fraction of labile particulate nitrogen	0.2	$0 \leq FNL \leq 1$

Table 2
Parameters in Kinetics Equations

Symbol	Definition	Value	Units
	produced by algal metabolism		
FNLP	fraction of labile particulate nitrogen produced by predation	0.2	$0 \leq FNLP \leq 1$
FNR	fraction of refractory particulate nitrogen produced by algal metabolism	0.05	$0 \leq FNR \leq 1$
FNRP	fraction of refractory particulate nitrogen produced by predation	0.1	$0 \leq FNRP \leq 1$
FPD	fraction of dissolved organic phosphorus produced by algal metabolism	0.25	$0 \leq FPD \leq 1$
FPDP	fraction of dissolved organic phosphorus produced by predation	0.0	$0 \leq FPDP \leq 1$
FPI	fraction of dissolved inorganic phosphorus produced by algal metabolism	0.75	$0 \leq FPI \leq 1$
FPIP	fraction of dissolved inorganic phosphorus produced by predation	0.8	$0 \leq FPIP \leq 1$
FPL	fraction of labile particulate phosphorus produced by algal metabolism	0.0	$0 \leq FPL \leq 1$
FPLP	fraction of labile particulate phosphorus produced by predation	0.17	$0 \leq FPLP \leq 1$
FPR	fraction of refractory particulate phosphorus produced by algal metabolism	0.0	$0 \leq FPR \leq 1$
FPRP	fraction of refractory particulate phosphorus produced by predation	0.03	$0 \leq FPRP \leq 1$
FSAP	fraction of dissolved silica produced by predation	0.5	$0 \leq FSAP \leq 1$
Kcod	oxidation rate of chemical oxygen demand	20 (saltwater), 0.025 (fresh)	d^{-1}
Kdoc	dissolved organic carbon respiration rate	0.025 to 0.05	d^{-1}
Kdon	dissolved organic nitrogen mineralization rate	0.025	d^{-1}
Kdp	minimum mineralization rate of dissolved organic phosphorus	0.025	d^{-1}
Kdpalg	constant that relates mineralization rate to algal biomass	0.4	$m^3 \, g^{-1} \, C \, d^{-1}$
KHn	half-saturation concentration for nitrogen uptake by algae	0.01(cyan), 0.025(spring), 0.020 (green)	$g \, N \, m^{-3}$
KHNH4	half-saturation concentration of ammonium in nitrogen preference formula	0.001	$g \, N \, m^{-3}$
KHnnt	half-saturation concentration of NH_4 required for nitrification	1.0	$g \, N \, m^{-3}$

Table 2
Parameters in Kinetics Equations

Symbol	Definition	Value	Units
KHocod	half-saturation concentration of dissolved oxygen required for exertion of COD	0.1	$g\ O_2\ m^{-3}$
KHodoc	half-saturation concentration of dissolved oxygen required for oxic respiration	0.1	$g\ O_2\ m^{-3}$
KHont	half-saturation concentration of dissolved oxygen required for nitrification	1.0	$g\ O_2\ m^{-3}$
KHp	half-saturation concentration for phosphorus uptake by algae	0.0025	$g\ P\ m^{-3}$
KHs	half-saturation concentration for silica uptake by algae	0.0 (cyan), 0.03 (spring), 0.001 (green)	$g\ Si\ m^{-3}$
KHst	salinity at which algal mortality is half maximum value	0.5 (cyan), 2.0 (spring)	ppt
Klpoc	labile particulate organic carbon dissolution rate	0.12	d^{-1}
Klpon	labile particulate organic nitrogen hydrolysis rate	0.12	d^{-1}
Klpop	labile particulate organic phosphorus hydrolysis rate	0.12	d^{-1}
Krpoc	refractory particulate organic carbon dissolution rate	0.005	d^{-1}
Krpon	refractory particulate organic nitrogen hydrolysis rate	0.005	d^{-1}
Krpop	refractory particulate organic phosphorus hydrolysis rate	0.005	d^{-1}
Ksua	biogenic silica dissolution rate	0.1	d^{-1}
KTb	effect of temperature on basal metabolism of algae	0.032	$^{\circ}C^{-1}$
KTcod	effect of temperature on exertion of chemical oxygen demand	0.041	d^{-1}
KTg1	effect of temperature below Tm on growth of algae	0.005 (cyan), 0.0018 (spring), 0.004 (green)	$^{\circ}C^{-2}$
KTg2	effect of temperature above Tm on growth of algae	0.004 (cyan), 0.006 (spring), 0.0 (green)	$^{\circ}C^{-2}$
KThdr	effect of temperature on hydrolysis rates	0.069	$^{\circ}C^{-1}$
KTmnl	effect of temperature on mineralization rates	0.069	$^{\circ}C^{-1}$
KTnt1	effect of temperature below Tmnt on nitrification	0.003	$^{\circ}C^{-2}$

Table 2
Parameters in Kinetics Equations

Symbol	Definition	Value	Units
KTnt2	effect of temperature above Tmnt on nitrification	0.003	$^oC^{-2}$
KTpr	effect of temperature on predation	0.032	$^oC^{-1}$
KTsua	effect of temperature on biogenic silica dissolution	0.092	$^oC^{-1}$
NTm	maximum nitrification rate at optimal temperature	0.125 to 0.25	$g\ N\ m^{-3}\ d^{-1}$
Phtl	predation rate on algae	0.0 (cyan), 0.01 (spring), 0.2 to 0.3 (green)	$m^3\ g^{-1}\ C\ d^{-1}$
Pm^B	maximum photosynthetic rate	200 (cyan), 300 (spring), 450 (green)	$g\ C\ g^{-1}\ Chl\ d^{-1}$
Presp	photo-respiration fraction	0.25	$0 \leq Presp \leq 1$
STF	salinity toxicity factor	0.3 (cyan), 0.1 (spring)	d^{-1}
Topt	optimal temperature for growth of algae	29 (cyan), 16 (spring), 30 (green)	^oC
Tmnt	optimal temperature for nitrification	30	^oC
Tr	reference temperature for metabolism	20	^oC
Trcod	reference temperature for COD oxidation	23	^oC
Trhdr	reference temperature for hydrolysis	20	^oC
Trmnl	reference temperature for mineralization	20	^oC
Trpr	reference temperature for predation	20	^oC
Trsua	reference temperature for biogenic silica dissolution	20	^oC
Wa	algal settling rate	0.0 (cyan), 0.5 (other)	$m\ d^{-1}$
Wl	settling velocity of labile particles	1.0	$m\ d^{-1}$
Wr	settling velocity of refractory particles	1.0	$m\ d^{-1}$
WSpo4	settling velocity for precipitated phosphate	1.0	$m\ d^{-1}$
Wpbs	settling velocity of biogenic silica	0.1	$m\ d^{-1}$
α	initial slope of production vs. irradiance relationship	3.15 (cyan), 8.0 (spring), 10.0 (green)	$g\ C\ g^{-1}\ Chl\ (E\ m^{-2})^{-1}$

References

Ammerman, J., and Azam, F. (1985). "Bacterial 5'-nucleodase in aquatic ecosystems: a novel mechanism of phosphorus regeneration," *Science,* 227, 1338-1340.

Boni, L., Carpene, E., Wynne, D., and Reti, M. (1989). "Alkaline phosphatase activity in *Protogonyaulax Tamarensis*," *Journal of plankton research,* 11, 879-885.

Bunch, B., Cerco, C., Dortch, M., Johnson, B., and Kim, K. (2000). "Hydrodynamic and water quality model study of San Juan Bay and Estuary," ERDC TR-00-1, U.S. Army Engineer Research and Development Center, Vicksburg MS.

Cerco, C., and Cole, T. (1994). "Three-dimensional eutrophication model of Chesapeake Bay," Technical Report EL-94-4, US Army Engineer Waterways Experiment Station, Vicksburg, MS.

Cerco, C., Bunch, B., Cialone, M., and Wang, H. (1994). "Hydrodynamic and eutrophication model study of Indian River and Rehoboth Bay, Delaware," Technical Report EL-94-5, US Army Engineer Waterways Experiment Station, Vicksburg, MS.

Cerco, C., and Bunch, B. (1997). "Passaic River tunnel diversion model study, Report 5, water quality modeling," Technical Report HL-96-2, US Army Engineer Waterways Experiment Station, Vicksburg, MS.

Cerco, C., Johnson, B., and Wang, H. (2002). "Tributary refinements to the Chesapeake Bay model," ERDC TR-02-4, US Army Engineer Research and Development Center, Vicksburg, MS.

Cerco, C., and Noel, M. (2004). "The 2002 Chesapeake Bay eutrophication model," EPA 903-R-04-004, Chesapeake Bay Program Office, US Environmental Protection Agency, Annapolis MD. (available at http://www.chesapeakebay.net/modsc.htm)

Cerco, C., and Noel, M. (2010). "Monitoring, modeling, and management impacts of bivalve filter feeders in the oligohaline and tidal fresh regions of the Chesapeake Bay system," *Ecological Modeling* 221, 1054-1064.

Chrost, R., and Overbeck, J. (1987). "Kinetics of alkaline phosphatase activity and phosphorus availability for phytoplankton and bacterioplankton in Lake Plubsee (north German eutrophic lake)," *Microbial Ecology,* 13, 229-248.

Edinger, J., Brady, D., and Geyer, J. (1974). "Heat exchange and transport in the environment," Report 14, Department of Geography and Environmental Engineering, Johns Hopkins University, Baltimore, MD.

Genet, L., Smith, D., and Sonnen, M. (1974). "Computer program documentation for the Dynamic Estuary Model," US Environmental Protection Agency, Systems Development Branch, Washington, DC.

Hartman, B., and Hammond, D. (1985). "Gas exchange in San Francisco Bay," *Hydrobiologia* 129, 59-68.

HydroQual (2000). "Development of a suspension feeding and deposit feeding benthos model for Chesapeake Bay," Project USCE0410, prepared for US Army Engineer Research and Development Center, Vicksburg MS.

Jassby, A., and Platt, T. (1976). "Mathematical formulation of the relationship between photosynthesis and light for phytoplankton," *Limnology and Oceanography* 21, 540-547.

Leonard, B. (1979). "A stable and accurate convection modelling procedure based on quadratic upstream interpolation," *Computer Methods in Applied Mechanics and Engineering,* 19, 59-98.

Matavulj, M., and Flint, K. (1987). "A model for acid and alkaline phosphatase activity in a small pond," *Microbial Ecology,* 13, 141-158.

Monod, J. (1949). "The growth of bacterial cultures," *Annual Review of Microbiology* 3, 371-394.

Morel, F. (1983). *Principles of Aquatic Chemistry,* John Wiley and Sons, New York, NY, 150.

O'Connor, D., and Dobbins, W. (1958). "Mechanisms of reaeration in natural streams," *Transactions of the American Society of Civil Engineers,* 123, 641-666.

O'Connor, D. (1983). "Wind effects on gas-liquid transfer coefficients," *Journal of the Environmental Engineering Division,* 190, 731-752.

Parsons, T., Takahashi, M., and Hargrave, B. (1984). *Biological oceanographic processes.* 3rd ed., Pergamon Press, Oxford.

Sellner, K., Lacoutre, R., and Parrish, C. (1988). "Effects of increasing salinity on a Cyanobacteria bloom in the Potomac River Estuary," *Journal of Plankton Research,* 10, 49-61.

Stumm, W., and Morgan, J. (1981). *Aquatic chemistry.* 2nd ed., Wiley-Interscience, New York.

Thomann, R., and Fitzpatrick, J. (1982). "Calibration and verification of a mathematical model of the eutrophication of the Potomac Estuary," HydroQual Inc., Mahwah, NJ.

Tchobanoglous, G., and Schroeder, E. (1987). *Water quality,* Addison Wesley, Reading, MA.

Tuffey, T., Hunter, J., and Matulewich, V. (1974). "Zones of nitrification", *Water Resources Bulletin*, 10, 555-564.

Wezernak, C., and Gannon, J. (1968). "Evaluation of nitrification in streams," *Journal of the Sanitary Engineering Division,* 94(SA5), 883-895.
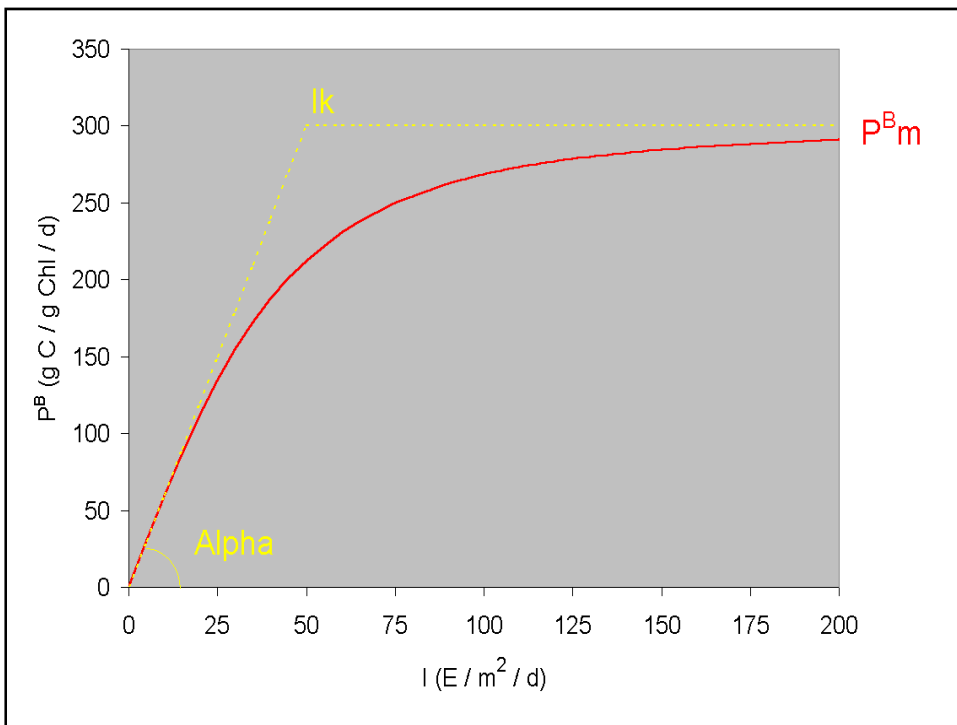
Figure 1.   Production versus irradiance curve.
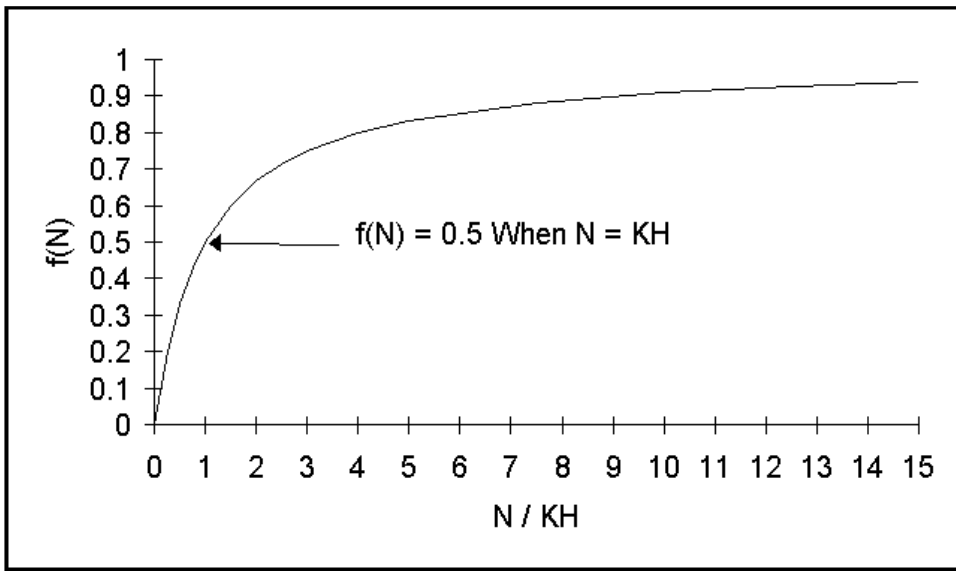
Figure 2.   Monod formulation for nutrient-limited growth
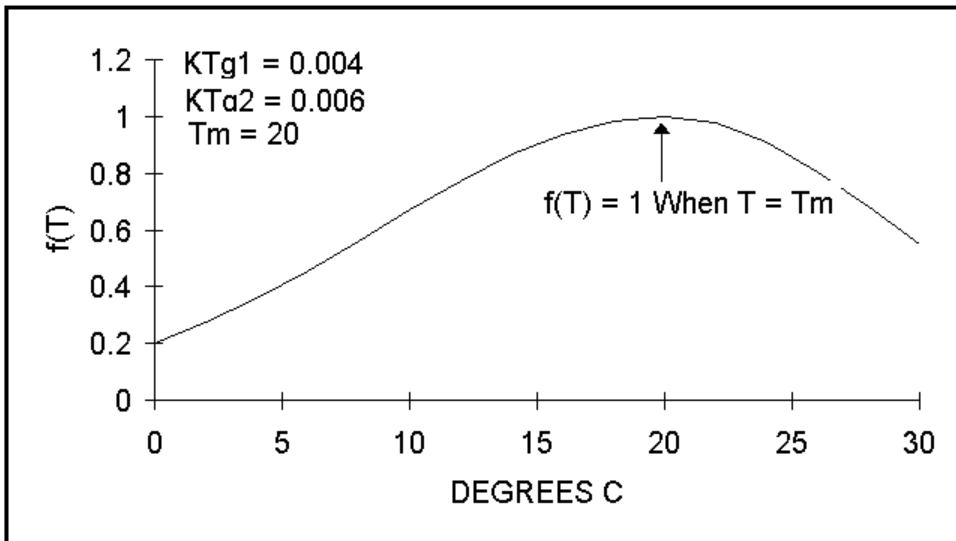
Figure 3.   Relation of algal production to temperature
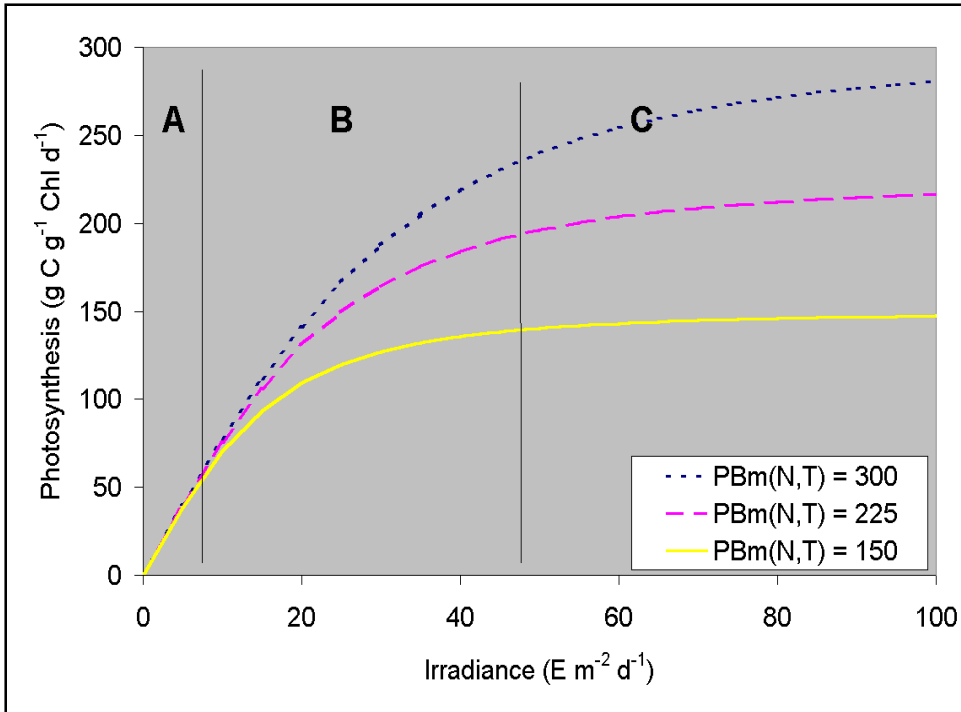
Figure 4. Effects of light and nutrients on production versus irradiance curve, determined for $\alpha = 8$ (g C g^{-1} Chl (E m^{-2})$^{-1}$).
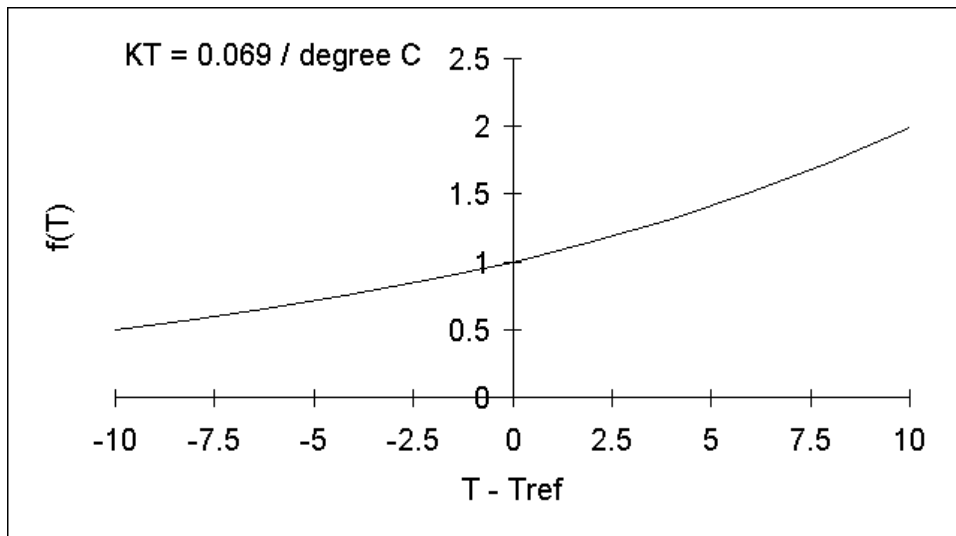
Figure 5. Exponential temperature relationship employed for metabolism and other processes
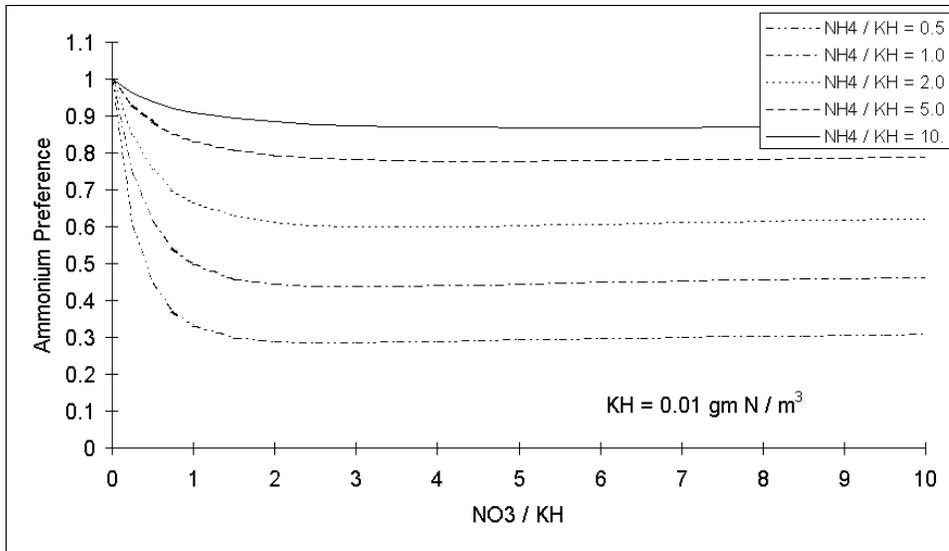
Figure 6. Algal ammonium preference
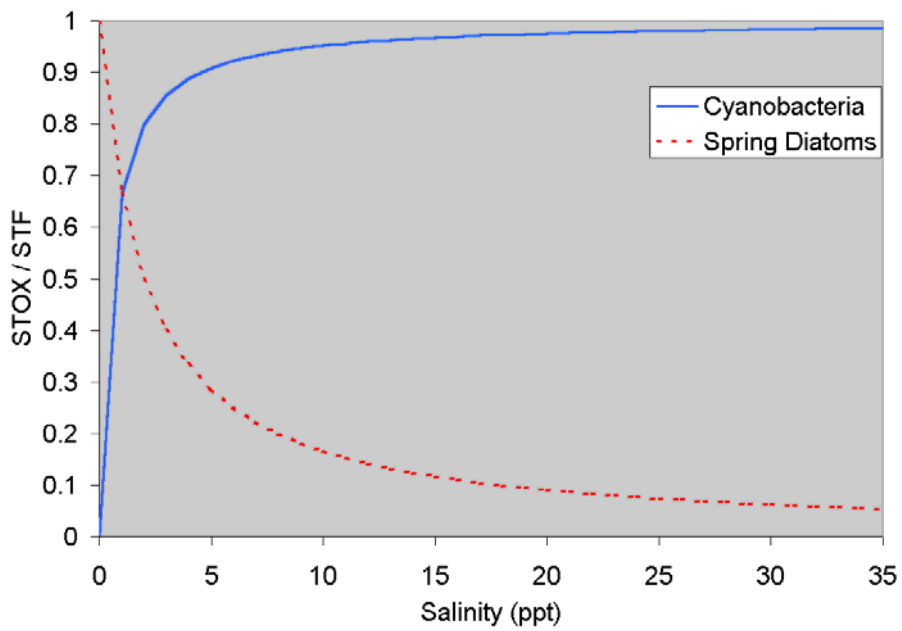
Figure 7. Salinity toxicity relationship
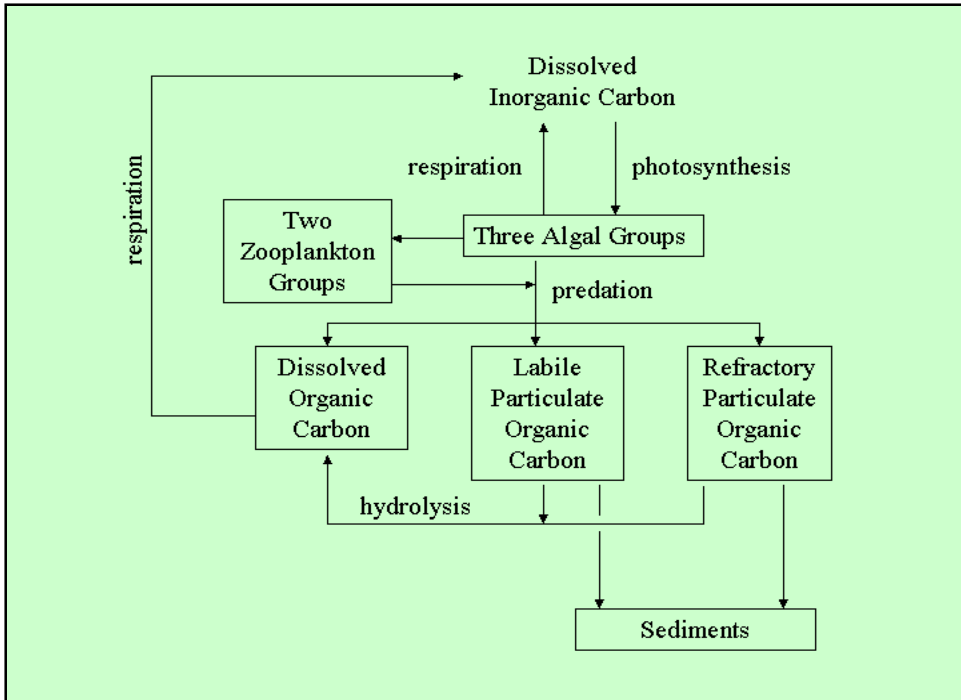
Figure 8.   Model carbon cycle
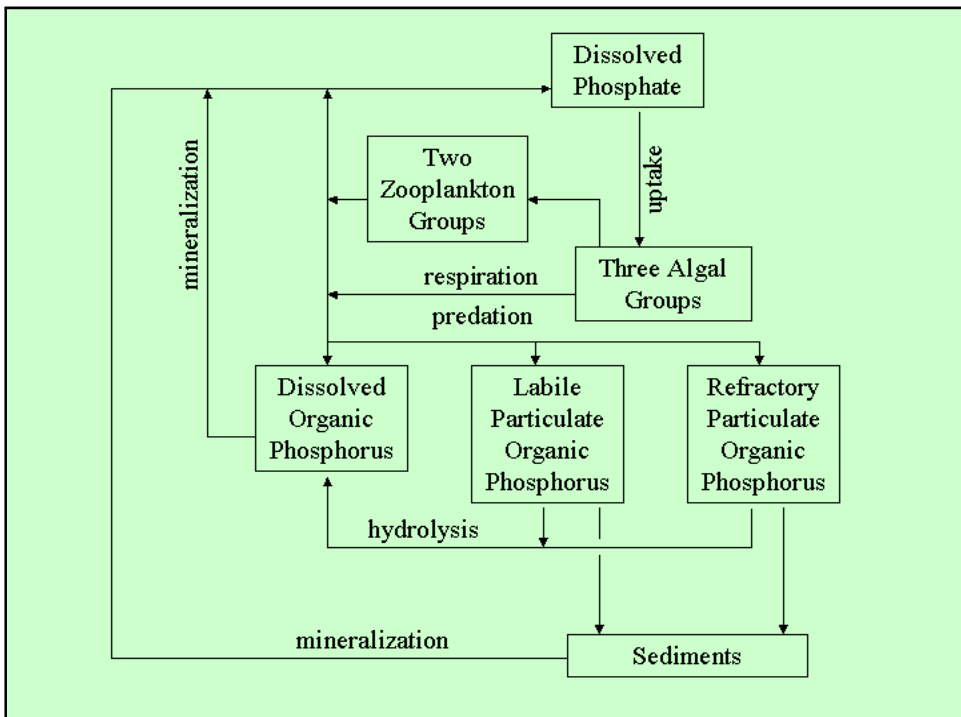
Figure 9.   Model phosphorus cycle
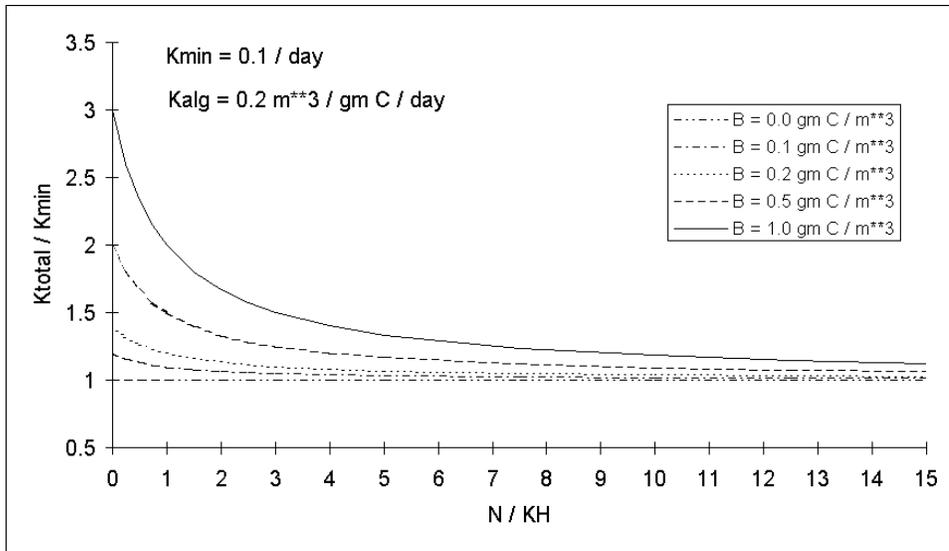
Figure 10.   Effect of algal biomass and nutrient concentration on phosphorus mineralization
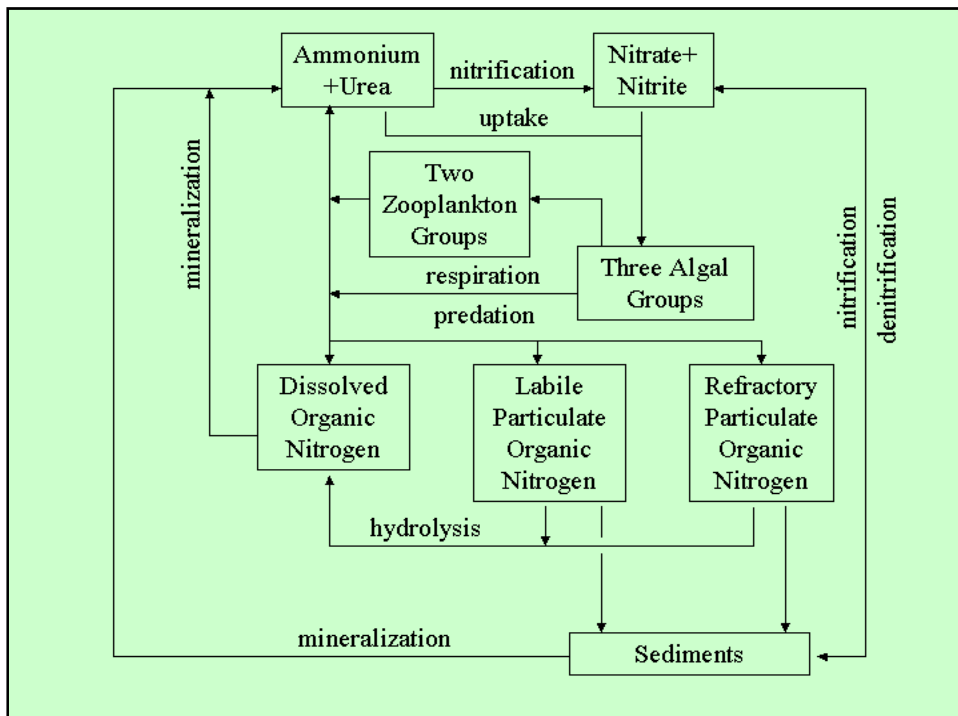
Figure 11.   Model nitrogen cycle
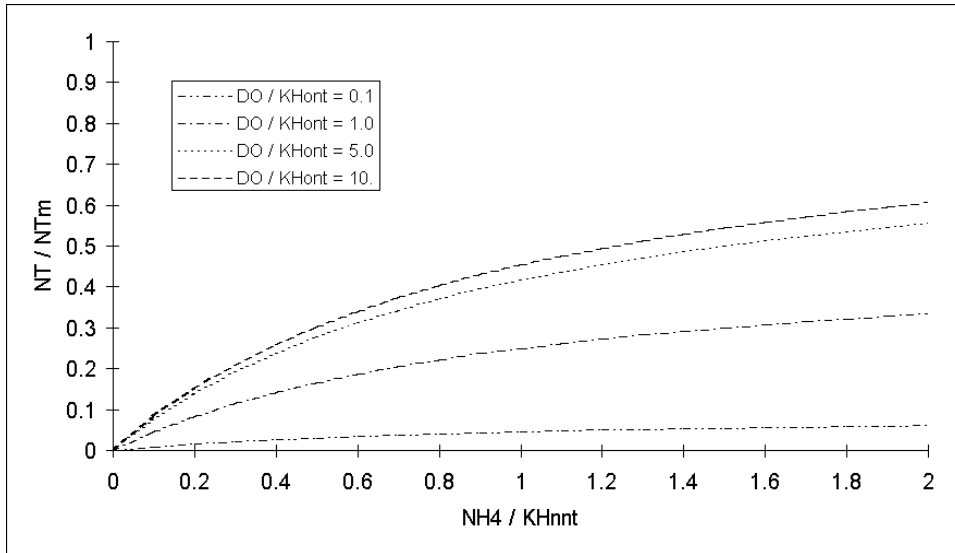
Figure 12. **Effect of dissolved oxygen and ammonium concentration on nitrification rate**
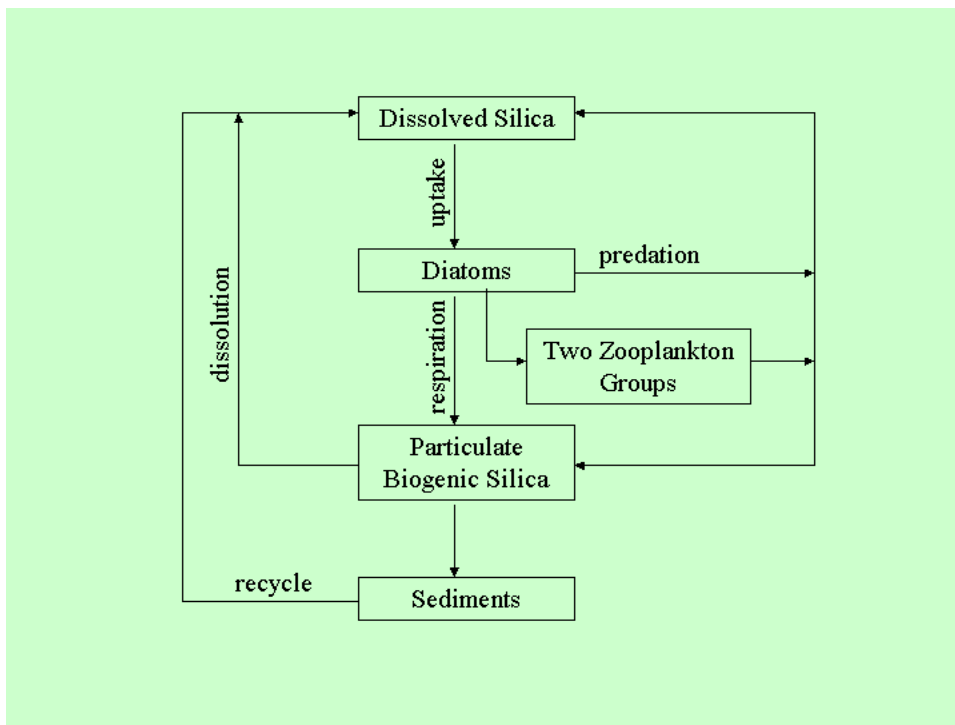
**Figure 13.** **Model silica cycle**
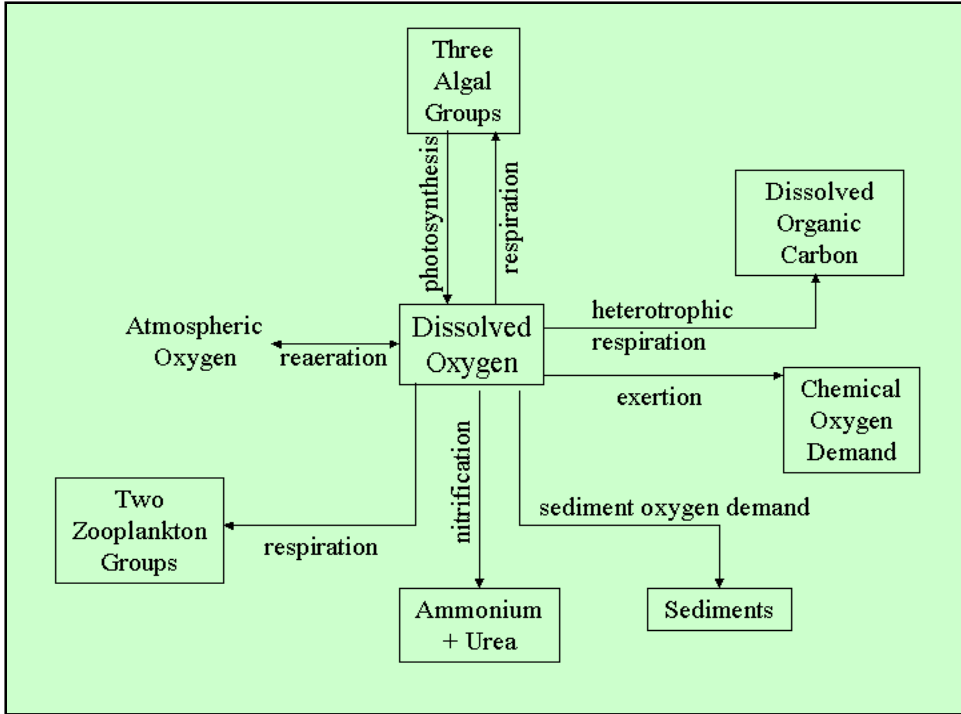
Figure 14. Dissolved oxygen sources and sinks
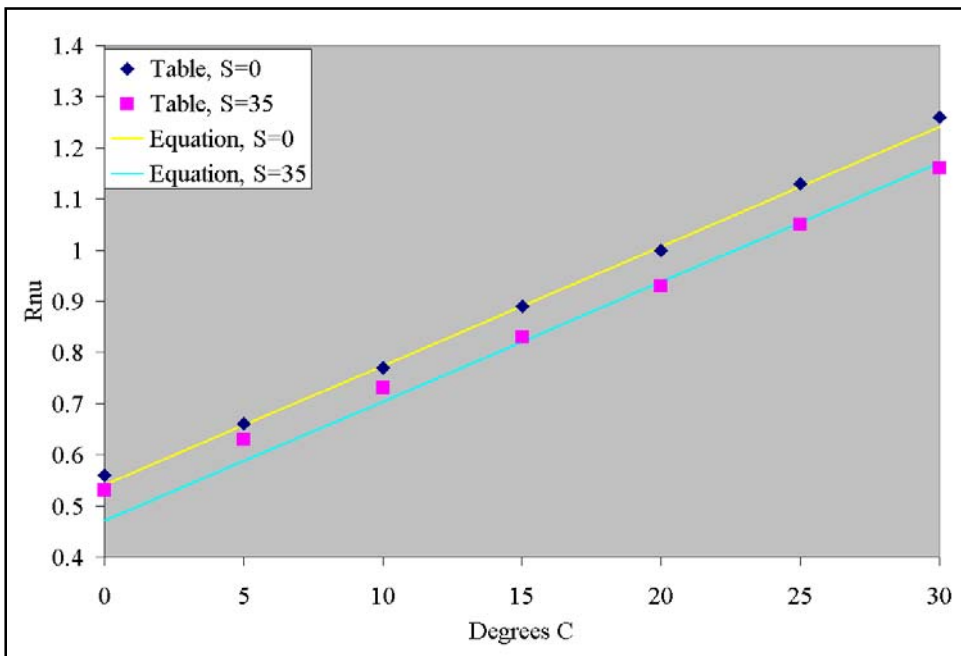
Figure 15. Computed and tabulated values of Rv

7 SAV Model Formulation

Introduction

Submerged aquatic vegetation (SAV) was introduced to CE-QUAL-ICM during the tributary refinements phase of the Chesapeake Bay study (Cerco and Moore 2001, Cerco et al. 2002). Subsequently, the model was modified for application to Florida Bay (Cerco et al. 2000) and the lower St. Johns River, Florida (Cerco and Noel 2006). Two major differences distinguish the present application from the original Chesapeake Bay study:

- Stems and tubers are distinguished in the above- and below-ground SAV biomass, respectively.

- The SAV model operates on an SAV sub-grid independent of the hydrodynamic grid.

Model State Variables

The SAV model (Figure 1) has five state variables, four of which represent plant components:

- **Leaves** – Leaves are the photosynthetic portions of the above-ground plant biomass

- **Stems** – Stems are the structural, non-photosynthetic portions of the above-ground plant biomass

- **Roots** – Roots are the below-ground portions of the plant biomass associated with anchoring the plant and with nutrient uptake

- **Tubers** – Tubers are below-ground organs associated with propagation and with energy storage. In the model, tubers accumulate plant carbon during summer, store this carbon over winter, and transfer the carbon to above-ground biomass in spring.

- **Epiphytes** – Epiphytes are algae that grow attached to leaves. Viable algae are associated with detrital organic matter and with inorganic solids.

The SAV model is formulated to provide a generic representation of SAV. Species are modeled through specification of the model parameter set. Multiple

species can be modeled with multiple parameter sets but the model does not consider competition. No more than one species can be assigned to a model cell.

Mass-Balance Equations for Plant State Variables

All plant production takes place within the leaves. A portion of the gross production is lost through active metabolism (or "photo-respiration"). The remainder is routed to the four plant components. All plant components loose biomass through basal metabolism. Biomass maybe routed from the tubers back to the leaves. The equations describing these processes are:

$$\frac{d\,LF}{dt} = \left[Plf \cdot (1 - Fam) \cdot FPlf - BMlf\right] \cdot LF + TRtblf \cdot TB \qquad (1)$$

in which:

LF = leaf biomass (g C m^{-2})
TB = tuber biomass (g C m^{-2})
Plf = leaf specific production rate (d^{-1})
Fam = Fraction of production devoted to active metabolism ($0 \le Fam \le 1$)
FPlf = fraction of production routed to leaf biomass ($0 \le FPlf \le 1$)
BMlf = leaf basal metabolism (d^{-1})
TRtblf = specific transfer rate from tubers to leaves (d^{-1})

$$\frac{d\,ST}{dt} = Plf \cdot (1 - Fam) \cdot FPst \cdot LF - BMst \cdot ST \qquad (2)$$

in which:

ST = stem biomass (g C m^{-2})
FPst = fraction of production routed to stem biomass ($0 \le FPst \le 1$)
BMst = stem basal metabolism (d^{-1})

$$\frac{d\,RT}{dt} = Plf \cdot (1 - Fam) \cdot FPrt \cdot LF - BMrt \cdot RT \qquad (3)$$

in which:

RT = root biomass (g C m^{-2})
FPrt = fraction of production routed to root biomass ($0 \le FPrt \le 1$)
BMrt = root basal metabolism (d^{-1})

$$\frac{d\,TB}{dt} = Plf \cdot (1 - Fam) \cdot FPtb \cdot LF - (BMtb + TRtblf) \cdot TB \qquad (4)$$

in which:

TB = tuber biomass (g C m^{-2})
FPtb = fraction of production routed to tuber biomass ($0 \le FPtb \le 1$)

BMtb = tuber basal metabolism (d^{-1})

Plant Production and Metabolism

Specific production is computed as the product of a temperature-dependent maximum rate and a limiting factor. The limiting factor is the minimum of independently evaluated light, nitrogen, and phosphorus limitations:

$$Plf = Pm(T) \cdot \min\bigl(f(I), f(N), f(P)\bigr) / Acdw \qquad (5)$$

in which:

Pm(T) = maximum production at temperature T (g C g^{-1} DW d^{-1})
f(I) = light limitation ($0 \le f(I) \le 1$)
f(N) = nitrogen limitation ($0 \le f(N) \le 1$)
f(I) = phosphorus limitation ($0 \le f(P) \le 1$)
Acdw = plant carbon-to-dry-weight ratio (g C g^{-1} DW)

Temperature

The temperature function (Figure 2) allows production to increase as a function of temperature until an optimum temperature or temperature range is reached. Above the optimum, production is constant or declines:

$$f(T) = e^{-KTg1 \cdot (T - Topt)^2} \ when \ T \ \le \ Topt$$

$$\qquad (6)$$

$$= e^{-KTg2 \cdot (Topt - T)^2} \ when \ T \ > \ Topt$$

T = temperature (^{o}C)
Topt = optimal temperature for SAV production (^{o}C)
KTg1 = effect of temperature below Topt on production ($^{o}C^{-2}$)
KTg2 = effect of temperature above Topt on production ($^{o}C^{-2}$)

Light

Light limitation (Figure 3) is selected from one of several functions (Jassby and Platt 1976) that fit observed production versus irradiance curves:

$$f(I) = \frac{Ish}{\sqrt{Ish^2 + Ik^2}} \qquad (7)$$

in which:

Ish = irradiance at leaf surface (E m^{-2} d^{-1})

Parameter Ik is derived from maximum production and an additional parameter, α:

$$Ik = \frac{Pm(T)}{\alpha} \qquad (8)$$

in which:

α = initial slope of production versus irradiance curve (g C g^{-1} DW) (E m^{-2})$^{-1}$

      A long-established conceptual model holds that light reaching SAV shoots is first attenuated by dissolved and particulate matter in the water column and next by epiphytic material (e.g. Kemp et al. 1983). The effects of self-shading must also be considered. Within the model, light available to SAV shoots is computed through a series of sequential attenuations. First, irradiance at the top of the canopy is computed:

$$Iatcnpy = Io \cdot e^{-Kw \cdot Ztc} \qquad (9)$$

in which:

Iatcnpy = irradiance at the canopy top (E m^{-2} day^{-1})
Io = irradiance penetrating the water surface (E m^{-2} day^{-1})
Kw = diffuse light attenuation within the water column (m^{-1})
Ztc = depth from water surface to top of canopy (m)

      Next, mean irradiance within the canopy is calculated. Within the canopy, light is attenuated in the water and by SAV self-shading. Assuming that attenuation by SAV follows an exponential relationship analogous to Eq. 9 (Titus and Adams 1979), the mean irradiance within the canopy is:

$$Iwc = \frac{Iatcnpy}{Kw \cdot Hcan + Ksh \cdot (LF + ST)} \cdot \left[1 - e^{-\left(Kw \cdot Hcan + Ksh \cdot (LF + ST) \right)} \right]$$

$$(10)$$

in which:

Iwc = mean irradiance within the canopy (E m^{-2} day^{-1})
Hcan = canopy height (m)
Ksh = light attenuation by SAV (m^{2} g^{-1} C)

      The mean irradiance within the canopy is available to epiphytes. Light must pass through the epiphytes before reaching the leaves. Material accumulated on the leaves is a combination of viable epiphytes, organic detritus, and inorganic solids. The total amount of light-attenuating material on leaves is quantified as a multiple of the viable material. Light reaching the leaves through the epiphyte layer is computed:

$$Ish = Iwc \cdot e^{-Kep \cdot Adwcep \cdot EP} \qquad (11)$$

in which:

Ish = irradiance at leaf surface (E m^{-2} day^{-1})
EP = viable epiphyte biomass (g C m^{-2} leaf surface)
Kep = light attenuation by epiphytes (m^2 leaf surface g^{-1} DW)
Adwcep = ratio of total to viable epiphytic material (g DW g^{-1} C)

Nutrients

Nutrient limitations for nitrogen and phosphorus are evaluated using a formula (Madden and Kemp 1996) that combines individual Monod-like functions for the roots and shoots:

$$f(N) = \frac{Nw + K^* \cdot Ns}{KHw + Nw + K^* \cdot Ns} \tag{12}$$

in which:

f(N) = nutrient limitation ($0 \leq f(N) \leq 1$)
Nw = nutrient concentration in water column (g m^{-3})
Ns = bulk nutrient concentration in sediments (g m^{-3})
KHw = half-saturation concentration for nutrient uptake by shoots (g m^{-3})
KHs = half-saturation concentration for nutrient uptake by roots (g m^{-3})
K* = KHw / KHs

Basal Metabolism

Basal metabolism of all plant components is considered to be an exponentially increasing function of temperature:

$$BM = BMr \bullet e^{KTb \bullet (T - Tr)} \tag{13}$$

in which:

BMr = metabolic rate at reference temperature Tr (d^{-1})
KTb = effect of temperature on metabolism ($^{\circ}$C^{-1})
Tr = reference temperature for metabolism ($^{\circ}$C)

Epiphytes

Epiphytes are quantified as mass per unit of leaf area:

$$\frac{d\,EP \cdot LF}{dt} = (Pep \cdot DL - BMep - PR \cdot EP - SL) \cdot LF \cdot EP \tag{14}$$

in which:

EP = epiphyte abundance (g epiphyte C m^{-2} leaf area)
Pep = epiphyte specific production rate (d^{-1})
DL = density limitation function ($0 \leq DL \leq 1$)

BMep = epiphyte basal metabolism (d^{-1})
PR = predation on epiphytes (m^2 leaf g^{-1} epiphyte carbon d^{-1})
SL = specific rate of leaf sloughing by SAV (d^{-1})

The formulation provides a change in epiphyte abundance as a function of epiphyte processes and SAV processes. Net production of epiphytes without corresponding production of leaves results in an increase in epiphyte abundance on the leaves. Net production of leaves without corresponding epiphyte production results in diminished epiphyte abundance per unit leaf area. Sloughing results in loss of attached epiphytes and produces no net change in abundance.

Predation and density are considered as two factors that limit epiphyte abundance. Neckles et al. (1993) showed that predation is an important limitation on epiphyte abundance. Absence of data prevents inclusion of predators in the model, however. Instead, a linear proportionality between predators and prey is assumed. Parameter PR incorporates both the proportionality (g predator C g^{-1} epiphyte C) and predation rate (m^2 leaf area grazed g^{-1} predator C d^{-1}). The density limitation incorporates the effects of substrate availability and epiphyte self-shading. An empirical function is defined that diminishes production as leaf substrate fills with epiphytes:

$$DL = \frac{KHep}{KHep + EP} \qquad (15)$$

in which:

KHep = epiphyte abundance at which substrate availability halves the production rate (g epiphyte C m^{-2} leaf area)

Epiphyte production is modeled as a function of light, nutrients, and temperature. Light effects are computed using formulae similar to Equations 8 and 9 while nutrient effects are evaluated with conventional Monod functions.

SAV Interactions with the Water Column

A fundamental assumption of the model is that plants have uniform, constant composition. Nitrogen and phosphorus in plant biomass are quantified as fractions of the carbonaceous biomass. Nutrients are taken up in stoichiometric relation to net production. Proportions removed from the water column and sediments are determined by the relative nutrient limits in each pool. Active and basal metabolism return appropriate quantities of nutrients to the sediments and water column.

Nutrients

Both ammonium and nitrate are available as nitrogenous nutrients in the water column. The fractions of plant nutrition removed from each pool are determined by an empirical preference function:

$$NPRsav = \frac{NH_4}{KHNpr + NO_3} \cdot \left[\frac{NO_3}{KHNpr + NH_4} + \frac{KHNpr}{NH_4 + NO_3} \right] \quad (16)$$

in which:

NPRsav = preference for uptake of ammonium ($0 \leq NPRsav \leq 1$)
KHNpr = ammonium concentration at which half the SAV nitrogen uptake is
      ammonium ($g\ N\ m^{-3}$)
NH_4 = ammonium concentration ($g\ N\ m^{-3}$)
NO_3 = nitrate concentration ($g\ N\ m^{-3}$)

     The preference function is the fraction of nitrogenous nutrition obtained from ammonium and has two limiting values (Figure 4). When nitrate is absent, the preference for ammonium is unity. When ammonium is absent, the preference is zero. In the presence of ammonium and nitrate, the preference depends on the abundance of both forms relative to the half-saturation constant for ammonium uptake. When both ammonium and nitrate are abundant, the preference for ammonium approaches unity. When ammonium is scarce but nitrate is abundant, the preference decreases in magnitude and a significant fraction of the SAV nitrogen requirement comes from nitrate.

     Ammonium and nitrate are also available from the sediments. The sediment ammonium concentration is usually enormous compared to the nitrate concentration so that an ammonium preference of unity is assumed and nitrate is neglected. The nutrient fraction obtained from the sediments, versus the water column, is determined:

$$FNsed = \frac{Nsed}{Nsed + \dfrac{KHNsed}{KHNwat} \cdot Nwat} \quad (17)$$

in which:

FNsed = fraction of nitrogenous nutrient obtained from sediments
      ($0 \leq FNsed \leq 1$)
Nsed = bulk ammonium concentration in sediments ($g\ N\ m^{-3}$)
Nwat = dissolved inorganic nitrogen concentration in water ($g\ N\ m^{-3}$)
KHNsed = half-saturation concentration for nitrogen uptake from sediments
      ($g\ N\ m^{-3}$)
KHNwat = half-saturation concentration for nitrogen uptake from water column
      ($g\ N\ m^{-3}$)

     The fraction is largely determined by the ratio of nutrient concentrations and has the form of a rectangular hyperbola (Figure 5). The "break" in the hyperbola is determined by the ratio of half-saturation concentrations for nutrient uptake. For KHNsed << KHNwat, a significant fraction of nutrition comes from the sediments at a low ratio of nutrient concentration in the sediments relative to the water column. For KHNwat << KHNsed, a significant fraction of nutrition

comes from the water despite potentially large ratios of sediment to water column nutrient concentration.

Active and basal metabolism release nitrogen to the water column. The nitrogen is released as ammonium and in the form of the four modeled organic nitrogen state variables: labile dissolved organic nitrogen, refractory dissolved organic nitrogen, labile particulate organic nitrogen, and refractory particulate organic nitrogen. The fractions released to each pool are specified as model parameters.

Ammonium. SAV source/sink terms in the water column are incorporated into the model three-dimensional mass-conservation equation. The SAV ammonium source/sink term is:

$$
\frac{d\,NH_4}{dt} = Anc \cdot FNI \cdot \big[(BMlf + Plf \cdot Fam) \cdot LF + BMst \cdot ST\big] \\
- Anc \cdot (1 - FNsed) \cdot NPRsav \cdot Plf \cdot LF
\tag{18}
$$

in which:

Anc = SAV nitrogen-to-carbon ratio (g N g^{-1} C)
FNI = ammonium fraction of metabolic nitrogen release ($0 \leq$ FNI ≤ 1)

Nitrate. The SAV nitrate source/sink term is:

$$
\frac{d\,NO_3}{dt} = - Anc \cdot (1 - FNsed) \cdot (1 - NPRsav) \cdot Plf \cdot LF
\tag{19}
$$

Organic Nitrogen. The source/sink terms for all organic nitrogen components have the same form. They differ only in the distribution fractions. The source/sink term for labile dissolved organic nitrogen is provided as an example:

$$
\frac{d\,LDON}{dt} = Anc \cdot FNLD \cdot \big[(BMlf + Plf \cdot Fam) \cdot LF + BMst \cdot ST\big]
\tag{20}
$$

in which:

LDON = labile dissolved organic nitrogen (g N m^{-3})
FNLD = labile dissolved organic fraction of metabolic nitrogen release
        ($0 \leq$ FNLD ≤ 1)

Phosphate. The algorithms and equations governing plant utilization of phosphate are analogous to the equations for nitrogen with one exception. Since phosphate is the only available phosphorus form in the water column, no preference function is necessary.

Dissolved Oxygen and Carbon

Dissolved oxygen production accompanies plant photosynthesis. Active and basal metabolism consume oxygen and release plant organic carbon to the water column. Metabolic fractions assigned to oxygen consumption and to release of organic carbon are specified parameters analogous to the nitrogen fractions. The source/sink term for dissolved oxygen is:

$$\frac{d\,DO}{dt} = Aocr \cdot Plf \cdot LF - Aocr \cdot FDO \cdot \left[\left(BMlf + Plf \cdot Fam\right) \cdot LF + BMst \cdot ST\right]$$

$$(21)$$

in which:

DO = dissolved oxygen concentration (g m^{-3})
Aocr = mass ratio of oxygen to carbon produced in photosynthesis (g DO g^{-1} C)
FDO = fraction of metabolism expressed as oxygen consumption ($0 \leq FDO \leq 1$)

Plant carbon is released into four model state variables: labile dissolved organic carbon, refractory dissolved organic carbon, labile particulate organic carbon, and refractory particulate organic carbon. The source/sink terms for organic carbon components all have the same form. They differ only in the distribution fractions. The source/sink term for labile dissolved organic carbon is provided as an example:

$$\frac{d\,LDOC}{dt} = FCLD \cdot \left[\left(BMlf + Plf \cdot Fam\right) \cdot LF + BMst \cdot ST\right] \quad (22)$$

in which:

LDOC = labile dissolved organic carbon (g C m^{-3})
FCLD = fraction of metabolism released as labile dissolved organic carbon release ($0 \leq FCLD \leq 1$)

SAV Interactions with the Sediments

Nutrients

SAV production removes nutrients, in the form of ammonium and phosphate, from the sediments. Metabolism in the roots and tubers returns nutrients, in organic form, to the sediments. The algorithms and governing equations for nitrogen and phosphorus are analogous. The nitrogen equations are shown below.

Ammonium. The source/sink term for ammonium uptake from the sediments is:

$$\frac{d\,NH_4}{dt} = -\,Anc \cdot FNsed \cdot Plf \cdot LF \quad (25)$$

Organic Nitrogen. The source/sink term for organic nitrogen release to the sediments is:

$$\frac{d\,ORGN}{dt} = Anc \cdot [BMrt \cdot RT + BMtb \cdot TB] \qquad (23)$$

in which:

ORGN = sediment organic nitrogen (g N m^{-3})

The sediment diagenesis model considers three forms of organic matter: labile, refractory, and inert. Organic nitrogen released by SAV is split into modeled fractions within the diagenesis model.

Dissolved Oxygen and Carbon

Basal metabolism by roots and tubers consumes dissolved oxygen and releases organic carbon to the sediments. The source/sink terms for dissolved oxygen and organic carbon are:

$$\frac{d\,DO}{dt} = Aocr \cdot FDO \cdot [BMrt \cdot RT + BMtb \cdot TB] \qquad (24)$$

$$\frac{d\,ORGC}{dt} = Aocr \cdot (1 - FDO) \cdot [BMrt \cdot RT + BMtb \cdot TB] \qquad (25)$$

in which:

ORGC = sediment organic carbon (g C m^{-3})

Dissolved oxygen concentration is not computed in the sediments. Plant respiration is combined with diagenetic oxygen consumption and represented in the model as sediment oxygen demand. Organic carbon released by SAV is split into modeled fractions within the diagenesis model.

Epiphyte Interactions with the Water Column

Epiphyte interactions with the water column follow the pattern detailed for SAV. Epiphyte production removes dissolved inorganic nutrients from the water column. Both ammonium and nitrate are available nitrogenous nutrients: a preference function determines the fraction removed from each pool. Metabolism returns nutrients, in organic and inorganic form, to the water column. Dissolved oxygen is produced by epiphyte photosynthesis. Metabolism results in oxygen consumption and in release of organic carbon to the water column. The splits of metabolic products into model state variables are specified as model parameters.

Epiphyte losses to predation are recycled immediately back to the water column since predator biomass is not represented. The splits of predation losses into model state variables are specified as model parameters. The model identifies leaf sloughing as an epiphyte loss term. Sloughing is quantified as the

metabolic leaf loss routed to particulate organic carbon release. The splits used to route epiphyte predation losses are utilized for epiphyte sloughing losses as well.

Epiphytes are quantified as mass per unit leaf area. Mass balance requires quantification of interactions with the water column on the basis of model cell area or volume. Epiphyte interactions are transformed into appropriate quantities through conversion of leaf area to leaf biomass. Examples of epiphyte interactions with water column phosphate and labile dissolved organic phosphorus are provided below:

$$\frac{d\,PO_4}{dt} = Apc \cdot \left[FPIep \cdot BMep + FPIpep \cdot \left(PR \cdot EP + SL\right) - Pep\right] \cdot EP \cdot Alac \cdot LF$$

(26)

in which

PO4 = phosphate concentration (g P m^{-3})
Apc = epiphyte phosphorus-to-carbon ratio (g P g^{-1} C)
FPIep = phosphate fraction of metabolic phosphorus release ($0 \leq FPIep \leq 1$)
FPIpep = phosphate fraction of epiphyte phosphorus recycled by predation
    ($0 \leq FPIpep \leq 1$)
Alac = leaf area-to-carbon ratio (m^2 g^{-1} leaf C)

$$\frac{d\,LDOP}{dt} = Apc \cdot \left[FPLDep \cdot BMep + FPLDpep \cdot \left(PR \cdot EP + SL\right)\right] \cdot EP \cdot Alac \cdot LF$$

(27)

in which:

LDOP = labile dissolved organic phosphorus concentration (g P m^{-3})
FPLDep = labile dissolved fraction of metabolic phosphorus release
    ($0 \leq FPLDep \leq 1$)
FPLDpep = labile dissolved fraction of epiphyte phosphorus recycled by
    predation ($0 \leq FPLDpep \leq 1$)

Analogous equations apply for epiphyte interactions with other phosphorus components as well as carbon, nitrogen, and dissolved oxygen.

Model Communities

Three major, mutually-exclusive SAV community types were modeled, based on the classification of Moore et al. (2000): ZOSTERA, RUPPIA, and FRESHWATER. Moore et al. (2000) identified a fourth type, POTAMOGETON, but the abundance in this type was negligible compared to the others. Since the distributions of POTAMOGETON and RUPPIA often overlap, the POTAMOGETON community was combined into the RUPPIA community for model purposes.

The spatial distribution of model communities was decided by an SAV Working Group at the time of the original model application (Cerco et al. 2002, Figure 6). This distribution was visually transferred to the present model grid

and then refined based on additional information (Moore 2008). Community assignments were largely based on Chesapeake Bay Program Segments with exceptions, as noted (Table 1).

Parameter Evaluation

Parameters for the SAV model were evaluated at the time of initial model application (Cerco et al. 2002) and subsequently revised as the model was refined and the application expanded. Evaluation involves running the model on a small test grid. Conditions in the model water column are derived from regions of Chesapeake Bay in which each model community is abundant. Parameters are selected from literature values and refined until the model produces satisfactory agreement with typical observed SAV density.

The SAV Component

For ZOSTERA, primary data sources included Wetzel and Penhale (1983), Evans et al. (1986), and Marsh et al. (1986). Parameters (Table 2) were selected to optimize agreement between computed and observed shoot and root biomass (Figures 7, 8). For RUPPIA, primary data sources were Wetzel and Penhale (1983) and Evans et al. (1986). Final parameters (Table 2) were selected to optimize agreement between computed and observed shoot (Figure 9) and root biomass. Insufficient data were found to assemble monthly means and ranges of root biomass. Observations collected by Moore et al. (1994) over a year indicated a range in root biomass of 0.8 to 13 g C m^{-2} with a mean of 6.1 g C m^{-2}. For the FRESHWATER community, primary data sources included Van et al. (1976), Bowes et al (1977; 1979), and Barko and Smart (1981). Final parameters (Table 2) were selected to optimize agreement between computed and observed shoot (Figure 10) and root biomass. As with RUPPIA, insufficient data were found to assemble meaningful monthly means and ranges of root biomass. Available information indicated the roots of freshwater SAV comprise from 4% to 41% of total plant biomass (Haller and Sutton 1975, Barko and Smart 1981).

Epiphytes

Epiphyte accumulation on natural and artificial substrates has been measured at various locations in situ (Carter et al. 1985) and in artificial environments adjacent to the bay (Staver 1984, Twilley et al, 1985). For comparison with the model, reports of in-situ accumulation on natural substrates were desirable. The best data sets identified were collected from *Zostera marina* in the lower eastern shore of the bay (Moore et al. 1994), and in Bogue Sound (Penhale 1977), a lagoon situated 300 km south of the bay. These studies indicated epiphyte accumulation between 0.5 and 2 g DW epiphytes g^{-1} leaf C. Initial parameters for epiphytes were adapted from the phytoplankton component of the CBEMP. Final parameters (Table 3) were selected to obtain epiphyte accumulation within the reported range on modeled Zostera (Figure 11).

Sub-Grid Scale Modeling of Submerged Aquatic Vegetation

Contemporary eutrophication models are based on a computational grid that divides the continuum of the system into discrete cells. The grid is especially suited to hydrodynamic modeling. Direct correspondence can be drawn between cell-based mass and momentum balances and classic finite-difference solutions to the hydrodynamic equations. The hydrodynamic grid is commonly carried over to the water quality component of the eutrophication model since it provides a convenient basis for computing local mass balance and facilitates incorporation of transport into the mass-balance equations. Computational grids have less relevance for modeling of living resources since living resources can violate the assumptions that underlie transformation of the hydrodynamic grid to water quality. Motile resources such as fish do not necessarily move according to computed transport and individuals are not well mixed within cells. For SAV, spatial resolution is a problem. The spatial scale of SAV beds can be smaller than practical computational cells and bathymetry variations that determine bed extent are too small to represent on the most highly-resolved grids. In the Chesapeake, the maximum depth of SAV growth is usually less than 2 m and bathymetry variations of 10 to 20 cm can differentiate between the highest density SAV and virtually none. However, computational cells in regions that support SAV are 2 m deep at mean tide and the depth is uniform within each cell.

The gap between scales is bridged by adapting an SAV sub-grid (Figure 12). Computational grid cells are divided into multiple SAV cells. The SAV cells have incremental depths that reflect the depths of SAV beds. Conditions in the water column and sediments are obtained from the larger grid. Bed extent and depth are based on the SAV sub-grid. The area encompassed by each depth increment is determined from bathymetry and from observed SAV extent. Mass balance is maintained by accounting for the fraction of computational cell area represented by each SAV depth increment. Areal mass fluxes between SAV and water/sediments are multiplied by the area of the local depth increment and then summed over all depth increments.

Irradiance in the Sub-Grid

The purpose of the sub-grid is to represent depth variations on scales significant to SAV. Canopy height at each sub-grid interval is computed based on an empirical relationship between density and height:

$$Hcan(j,k) = Acan + Bcan \cdot B(j,k) \tag{28}$$

in which:

Hcan(j,k) = canopy height in depth interval k of SAV cell j (cm)
B(j,k) = above-ground biomass in depth interval k of SAV cell j (g C m^{-2})
Acan, Bcan = parameters which relate canopy height to above-ground biomass

Distance from the water surface to the canopy is computed:

$$Ztc(j,k) = H(j,k) - Hcan(j,k) \qquad (29)$$

in which:

Ztc(j,k) = distance from water surface to canopy (m)
H(j,k) = depth of interval k in SAV cell j (m)

and irradiance at the canopy is computed:

$$Iatcnpy(j,k) = Io \cdot e^{-Kw(i) \cdot Ztc(j,k)} \qquad (30)$$

in which:

Iatcnpy(j,k) = irradiance at the canopy top in depth interval k of SAV cell j (E m^{-2} day^{-1})
Io = irradiance penetrating the water surface (E m^{-2} day^{-1})
Kw(i) = diffuse light attenuation within the water column cell i (m^{-1})

Advantages and Limitations

The primary advantage of the SAV sub-grid is that it incorporates local variations in geometry that are not represented on the hydrodynamic computational grid. Depth is the most significant variation but not the only one. Bed areas based on irregular shorelines and depth contours can be accommodated provided sufficient information is available. This capability divorces the SAV areas from conventional rectilinear computational cell surface planes. The limitation of this approach is that water column and sediment properties are uniform across all depth increments, as determined by conditions in the corresponding hydrodynamic and water quality model grid cell. In view of the actions of tides, currents, and wind, the enforcement of uniform conditions in the water column is appropriate. Since the sediments in which SAV is rooted are not mobile, however, conditions may vary as a function of SAV density and other factors. Conditions in which SAV is nutrient-limited in near-shore areas but light limited at greater depths cannot be represented. Consequently, this approach is more appropriate for light-limited situations.

A second advantage of the sub-grid is that the area of SAV beds is now quantifiable within the model. Computed SAV will occupy cells and depth increments within cells depending on computed light attenuation. Summation of the computed populated cell areas within each Chesapeake Bay Program Segment (CBPS) allows direct comparison with the SAV areas observed in annual over-flights. Previously the observed SAV area had to be converted to biomass for comparison with the model.

Application to Chesapeake Bay

Four evenly-spaced depth increments were selected to represent the range between zero (at mean tide) and 2 m, the target restoration depth for much of the bay. For computation of available light, the central depth in each increment was

utilized: 0.25m, 0.75m, 1.25m, 1.75m. The location and spatial extent of SAV grid cells was determined in cooperation with the GIS team at the Chesapeake Bay Program Office. The procedure was as follows:

1. Bay Program GIS team provides a list of every hydrodynamic model grid cell that has ever had SAV (2445 out of ≈ 12,000 cells in the surface plane.)
2. Bay program GIS team provides best-ever observed SAV area by Chesapeake Bay Program Segment (CBPS) and depth increment.
3. The water quality model team assigns an SAV grid cell corresponding to every hydrodynamic model cell that has ever had SAV.
4. The water quality model team assigns SAV cell extent and the areas within each depth increment such that the sum of areas within each depth increment and CBPS equals the best-ever SAV area observed in that depth increment and CBPS.

Example

1. Suppose SAV has historically been observed in ten grid cells in a CBPS.
2. Suppose the best-ever observed areas are 1000 hectares (0 to 0.5m), 100 hectares (0.5 to 1m), 50 hectares (1 to 1.5m), 0 hectares (1.5 to 2m).
3. Each of ten SAV cells in the CBPS is assigned the following areas: 100 hectares (0 to 0.5m), 10 hectares (0.5 to 1m), 5 hectares (1 to 1.5 m), 0 hectares (1.5 to 2m).

If all cells on the SAV grid contain SAV in all depth increments, then the modeled SAV extent corresponds to the observed historic extent. This area is typically reflects the SAV management goals.

Model Results

The SAV model was applied over a 21-year period, 1985 – 2005. Loads, boundary conditions, and other forcing functions for the hydrodynamic and water quality models were developed and the application period of these models was extended to correspond to the SAV model. Two forms of validation were conducted. The first compared model performance to SAV habitat criteria based on light attenuation. The second provided comparisons of computed and observed SAV areas by CBPS. Results were examined for a total of 77 individual CBPS. Results are presented here as system-wide total area and for four CBPS, which exhibit significant SAV area and which range across the three SAV communities:

- Susquehanna Flats (CB1TF) – FRESHWATER
- Tidal Fresh Potomac River (POTTF) – FRESHWATER
- Choptank River Mouth (CHOMH1) – RUPPIA
- Virginia Lower Eastern Shore (CB7PH) - ZOSTERA

Habitat Criteria

The original SAV Technical Synthesis (Batiuk et al. 1992) identifies the maximum light attenuation for Tidal Fresh SAV to exist at 1 m depth as 2 m^{-1}. The required light attenuation for Tidal Fresh SAV to exist at 2 m depth is 0.8 m^{-1}. These correspond to optical depth (physical depth x light attenuation) for SAV survival of 1.6 to 2. Similar calculations can be made for oligohaline, mesohaline, and polyhaline regions. In terms of model communities, the survival criteria are:

- Optical Depth 1.6 to 2.0 – FRESHWATER
- Optical Depth 1.5 to 1.6 – RUPPIA
- Optical Depth 1.5 to 1.6 – ZOSTERA

For comparison, the modeled light attenuation and depth in each SAV cell and depth increment were converted to optical depth and averaged over a growing season (April – October), then plotted against computed SAV density (g C m^{-2}). In the FRESHWATER regions, the highest modeled SAV densities obey the habitat criteria (Figures 13, 14). That is, the highest densities are computed at optical density less than 1.6 to 2. Computed SAV survives for at least a growing season at criteria which are not compatible with the habitat requirements, however. It is possible that computed SAV does not survive for multiple seasons for conditions that do not obey criteria although that possibility has not been examined. For the RUPPIA and ZOSTERA communities, the computed SAV corresponds well to habitat criteria. Almost no SAV survives for a growing season when criteria are violated (Figures 15, 16).

Probability of Growth

The initial comparisons of computed and observed SAV area inevitably showed computed areas in excess of observed, even in areas in which habitat criteria were obeyed and computed and observed light attenuation were in good agreement. We suspected the problem originated with factors that influence SAV growth but are not considered in the model e.g. substrate, waves, and propagation (Koch 2001). Consequently the concept of "probability of growth" was introduced (Figure 17). The major purpose of introducing probability was to relate SAV production in any year to the presence of SAV in the preceding year. The existence of SAV above a threshold density would ensure growth of SAV in the succeeding year, provided habitat criteria were met. Otherwise, SAV might or might not grow, even if habitat criteria were met, depending on unquantifiable conditions.

The concept of probability was eventually extended to comprise a tuning tool. Three applications of the probability concept were identified (Table 4). In the tidal fresh and oligohaline regions, probability accounted for SAV propagation and for modification of the environment by SAV. Assigned probability was a variable which was higher in later years, corresponding to the increasing trend in SAV area over the model simulation period (Figure 18). Observed SAV area in the mesohaline regions was erratic and not well simulated (Figure 19). Probability provided a means to reproduce mean observed areas. In the polyhaline regions, computed SAV varied smoothly although it was usually greater than observed (Figure 20). Constant probabilities were assigned to

represent the effects of waves, currents, and substrate which affect SAV but are not represented in the model.

Results

The Bay Program GIS team provided 1985 observed SAV distributed into model grid cells. These were used to initialize a 21-year model run. System-wide, the model provided reasonable representation of SAV area for the second half of the simulation (Figure 21). Computed SAV was higher than observed for the first ten years. The model demonstrated the tendency to leap from initial conditions to an area much greater than observed within a single growing season. Overall, computed areas predominantly exceed observed (Figure 22). Long-term trends within the FRESHWATER community, typified by the Susquehanna Flats (Figure 23), are well-represented due to the probability feature. In the tidal fresh Potomac, which exhibits no long-term trend, the model represents the central tendency of the observations (Figure 24). Observed areas within the RUPPIA community, typified by the mouth of the Choptank River (Figure 25) are erratic. Factor-of-two differences in area in successive years are common. The model does not replicate this erratic behavior at all and provides little agreement with areas observed in individual years. The observed ZOSTERA, typified along the Virginia lower eastern shore, exhibits year-to-year variation and multi-year trends although monotonic trends which extend through the course of the simulation do not prevail. In the same region, the model indicates a simulation-long upward trend in SAV area (Figure 25). The model reproduces the magnitude of the observed area but not the year-to-year trends.

Feedback Between SAV and Suspended Solids

The ability of SAV to damp suspended solids has been observed in multiple environments (e.g. Ward et al. 1984, Carter et al. 1988, James et al. 2004). Damping arises from suppression of waves, anchoring of bottom sediments, and filtering of the water column. Relationships to quantify the effects of SAV on solids have been proposed. The utility of proposed relationships in the model is limited, however, due to inconsistancies between state variables, forcing functions, spatial and temporal scales. For the model an approach was taken in which the presence of SAV damps bottom shear stress:

$$\frac{\tau sav}{\tau} = \exp^{-k \cdot DEN} \tag{31}$$

in which:

τsav = shear stress as affected by SAV ($m^2 \, s^{-2}$)
τ = shear stress on unvegetated bottom ($m^2 \, s^{-2}$)
DEN = SAV density averaged over SAV cell area ($g \, C \, m^{-2}$)
k = empirical constant which relates shear stress to density ($m^2 \, g^{-1} \, C$)

Model experiments indicate $k = 0.015 \, m^2 \, g^{-1} \, C$ reduces suspended solids 1 to 2 $g \, m^{-3}$ in SAV beds. The value $k = 0.1 \, m^2 \, g^{-1} \, C$ reduces suspended solids 5 to 10 $g \, m^{-3}$. Caution is necessary in evaluating the constant, however, since

solids attenuation in SAV beds can influence the overall suspended solids calibration of the model. The value k = 0.015 was adopted for the model calibration and considered reflective of current SAV densities.

Summary and Conclusions

The present SAV model provides mixed results. In some segments, the model provides good comparisons to observed areas (e.g. Figure 23) while in other segments, little correspondence exists between computed and observed areas (Figure 25). The best agreement often exists where the model is subject to tuning through the probability feature. The present status of the model reflects years of application and development, tens of calibration runs for this application, and input from numerous review sessions. Still, the predictive ability of the model to compute long-term trends in SAV area is minimal. The likelihood of improving beyond the present status is slim. Although we can't say with certainty what is missing, the absence of plant structure and of plant reproduction are suggested as critical omissions. The present model emphasizes SAV production as a function of light. If conditions are appropriate, production will take place. This feature is responsible for the leap in SAV area at the initiation of the simulation. SAV area is initialized at $\approx$ 150 km^2 on January 1, 1985 and more than doubles by summer, when the model is compared to results from aerial surveys (Figure 21). A more realistic representation of propagation, requiring dissemination and growth from seeds or runners would slow the expansion of SAV area. A different model approach is also required to accommodate the extreme year-to-year variations in SAV extent demonstrated by the RUPPIA community (Figure 25). The SAV model is retained within the larger model system, largely for its feedback effects on solids and for other environmental interactions. However, employment of the model in a predictive mode to aid in determination of Total Maximum Daily Loads, relies on computations of light attenuation rather than SAV area.

References

Barko, J., and Smart, M. (1981). "Comparative influences of light and temperature on the growth and metabolism of selected freshwater macrophytes," *Ecological Monographs*, 51(2), 219-235

Batiuk, R., Orth, R., Moore, K., Dennison, W., Stevenson, J., Staver, L., Carter, V., Rybicki, N., Hickman, R., Kollar, S., Bieber, S., and Heasly, P. (1992). "Chesapeake Bay submerged aquatic vegetation habitat requirements and restoration targets: A technical synthesis," CBP/TRS 83/92, United States Environmental Protection Agency Chesapeake Bay Program, Annapolis MD.

Bowes, G., Van, T., Garard, L., and Haller, W. (1977). "Adaptation to low light levels by hydrilla," *Journal of Aquatic Plant Management*, 15, 32-35

Carter, V., Paschal, J., and Bartow, N. (1985). "Distribution and abundance of submersed aquatic vegetation in the tidal Potomac River and estuary, Maryland and Virginia, May 1978 to November 1981," United States

Geological Survey Water-Supply Paper 2234-A, US Geological Survey, Alexandria VA.

Carter, V., Barko, J., Godshalk, G, and Rybicki, N. (1988). "Effects of submersed macrophytes on water quality in the tidal Potomac River, Maryland," *Journal of Freshwater Ecology*, 4(4),493-501

Cerco, C., Bunch, B., Teeter, A., and Dortch, M. (2000). "Water quality model of Florida Bay," ERDC TR-00-10, US Army Engineer Research and Development Center, Vicksburg MS.

Cerco, C., and Moore, K. (2001). "System-wide submerged aquatic vegetation model for Chesapeake Bay," *Estuaries*, 24(4), 522-534.

Cerco, C., Johnson, B., and Wang, H. (2002). "Tributary refinements to the Chesapeake Bay model," ERDC TR-02-4, US Army Engineer Research and Development Center, Vicksburg MS.

Cerco, C., and Noel, M. (2006). "Modeling submerged aquatic vegetation in the lower St. Johns River, Florida," report to the St. Johns River Water Management District (available from the first author Carl.F.Cerco@usace.army.mil)

Evans, A., Webb., K.,and Penhale, P. (1986). "Photosynthetic acclimation in two coexisting seagrass systems, *Zostera marina L.* and *Ruppia maritima L.*," *Aquatic Botany*, 24, 185-197

Haller, W., and Sutton, D. (1975). "Community structure and competition between hydrilla and vallisneria," *Hyacinth Control Journal*, 13, 48-50.

James, W., Barko, J., and Butler, M. (2004). "Shear stress and sediment resuspension in relation to submersed macrophyte biomass," *Hydrobiologia* 515, 181-191.

Jassby, A., and Platt, T. (1976). "Mathematical formulation of the relationship between photosynthesis and light for phytoplankton," *Limnology and Oceanography*, 21, 540-547.

Kemp, W., R. Twilley, J. Stevenson, W. Boynton, and J. Means. (1983). "The decline of submerged vascular plants in the upper Chesapeake Bay: Summary of results concerning possible causes," *Marine Technology Science Journal*, 17(2), 78-89.

Koch, E. (2001). "Beyond light: Physical, geological, and geochemical parameters as possible submersed aquatic vegetation habitat parameters," *Estuaries* 24(1), 1-17.

Madden C. and W. Kemp. (1996). "Ecosystem model of an estuarine submersed plant community: Calibration and simulation of eutrophication responses," *Estuaries*, 19(2B),457-474.

Marsh, J., Dennison, W., and Alberte, R. (1986). "Effects of temperature on photosynthesis and respiration in eelgrass (Zostera marina L.)," *Journal of Experimental Marine Biology and Ecology*, 101, 257-267

Moore, K., Goodman, J., Stevenson, J., Murray, L., and Sundberg, K. (1994). "Chesapeake Bay nutrients, light and SAV: Relations between variable water quality and SAV in field and mesocosm studies," Year 1 Draft Final Report, United States Environmental Protection Agency Chesapeake Bay Program, Annapolis MD.

Moore, K. (2008). "Percent SAV area in a segment by species group," (spreadsheet available from the first author Carl.F.Cerco@usace.army.mil)

Neckles, H., Wetzel, R., and Orth, R. (1993). "Relative effects of nutrient enrichment and grazing on epiphyte-macrophyte (*zostera marina L.*) dynamics," *Oecologia*, 93, 285-295.

Penhale, P. (1977). "Macrophyte - epiphyte biomass and productivity in an eelgrass (*zostera marina L.*) community," *Journal of Experimental Marine Biology and Ecology*, 26, 211-224.

Staver, K. (1984). "Responses of epiphytic algae to nitrogen and phosphorus enrichment and effects on productivity of the host plant, *potamogeton perfoliatus L.*, in estuarine waters," M.S. thesis, University of Maryland, College Park.

Titus, J., and Adams, M. (1979). "Coexistence and comparative light relations of the submersed macrophytes *Myriophyllum spicatum L.* and *Vallisneria americana Michx*," *Oecologia (Berl.)*, 40, 273-286.

Twilley, R., W. Kemp, K. Staver, J. Stevenson, and W. Boynton. (1985). "Nutrient enrichment of estuarine submersed vascular plant communities. 1. Algal growth and effects on production of plants and associated communities," *Marine Ecology Progress Series*, 23, 179-191.

Van, T., Haller, W., and Bowes, G. (1976). "Comparison of the photosynthetic characteristics of three submersed aquatic plants," *Plant Physiology*, 58, 761-768

Ward, L., Kemp, W., and Boynton, W. (1984). "The influence of waves and seagrass communities on suspended particulate matter in an estuarine embayment,"*Marine Geology*, 59, 85-103.

Wetzel, R., and Penhale, P. (1983). "Production ecology of seagrass communities in the lower Chesapeake Bay," *Marine Technology Society Journal*, 17(2), 22-32.

Table 1	
SAV Community Assignments	
Segment	**Community**
All tidal fresh (TF) and oligohaline (OH) segments, except as noted.	FRESHWATER
All mesohaline (MH) segments, except as noted.	RUPPIA
All polyhaline (PH) segments.	ZOSTERA
Mid-Chesapeake Bay adjacent to Potomac River mouth (CB5MH).	Half RUPPIA, Half ZOSTERA
Piankatank River (PIAMH).	ZOSTERA
Rappahannock River mouth (RPPMH).	Mostly ZOSTERA
Tangier Sound (TANMH).	Half RUPPIA, Half ZOSTERA
Oligohaline Potomac River (POTOH).	Half FRESHWATER, half RUPPIA.

Table 2
Parameters in SAV Model

Parameter	Definition	Freshwater	Ruppia	Zostera	Units
Acdw	carbon to dry weight ratio	0.38	0.38	0.38	g C g^{-1} DW
Fam	fraction of production devoted to active metabolism	0.2	0.1	0.1	$0 \leq Fam \leq 1.0$
FPlf	fraction of production routed to leaf biomass	0.64 to 0.80	0.63 to 0.9	0.63	$0 \leq FPlf \leq 1.0$
FPst	fraction of production routed to stems	0.064 to 0.08	0.07 to 0.1	0.07	$0 \leq FPst \leq 1.0$
FPrt	fraction of production transferred to roots	0.096 to 0.12	0 to 0.27	0.27	$0 \leq FPrt \leq 1.0$
FPtb	fraction of production transferred to tubers	0 to 0.2	0 to 0.03	0.03	$0 \leq FPtb \leq 1.0$
TRtblf	transfer from tubers to leaves	0 to 0.05	0	0	d^{-1}
SMlf	leaf sloughing	0 to 0.05	0 to 0.016	0 to 0.01	d^{-1}
Ksh	light attenuation by leaves and stems	0.045	0.045	0.045	m^2 g^{-1} C
Khnw	half-saturation concentration for nitrogen uptake by leaves	0.01	0.01	0.01	g N m^{-3}
Khns	half-saturation concentration for nitrogen uptake by roots	0.10	0.10	0.10	g N m^{-3}
Khpw	half-saturation concentration for phosphorus uptake by leaves	0.001	0.001	0.002	g P m^{-3}
Khps	half-saturation concentration for phosphorus uptake by roots	0.01	0.01	0.01	g P m^{-3}
Pmax	maximum production at optimum temperature	0.1	0.09	0.06	g C g^{-1} DW d^{-1}
BMlf	leaf basal metabolism at reference temperature	0.02	0.015	0.013	d^{-1}
BMst	stem basal metabolism at reference temperature	0.02	0.015	0.013	d^{-1}
BMrt	root basal metabolism at reference temperature	0.02	0.015	0.013	d^{-1}
BMtb	tuber basal metabolism at reference temperature	0.0	0.015	0.013	d^{-1}
Topt	optimal temperature for production	32	30	22.5	^{o}C
Trbm	reference temperature for basal metabolism	20	20	0.0	^{o}C
KTg1	effect of temperature below optimum on production	0.003	0.0016	0.0025	^{o}C^{-2}
KTg2	effect of temperature below optimum on production	0.005	0.01	0.01	^{o}C^{-2}
KTbm	effect of temperature on basal metabolism	0.069	0.069	0.069	^{o}C^{-1}
α	initial slope of PvsI curve	0.006	0.0035	0.003	(g C g^{-1} DW) (E m^{-2})$^{-1}$

Table 3
Parameters in Epiphyte Model

Parameter	Definition	Value	Units
Acchl	carbon to chlorophyll ratio of viable epiphytes	75	g C g^{-1} Chl
Adwcep	ratio of epiphyte dry weight to viable epiphyte carbon	18	g DW g^{-1} C
Kep	light attenuation coefficient	0.04	m^2 leaf surface g^{-1} epiphyte DW
Khep	density at which growth is halved	0.25	g epiphyte C m^{-2} leaf area
Khn	half-saturation concentration for nitrogen uptake	0.025	g N m^{-3}
Khp	half-saturation concentration for phosphorus uptake	0.001	g P m^{-3}
Pep	maximum production at optimum temperature	350	g C g^{-1} Chl d^{-1}
PR	predation rate	0.3	m^2 leaf g^{-1} epiphyte C d^{-1}
BMep	basal metabolism at reference temperature	0.05	d^{-1}
α	initial slope of PvsI curve	8	(g C g^{-1} Chl) (E m^{-2})$^{-1}$

Table 4
Examples of SAV Probability

Community	Region	Probability
FRESHWATER	Susquehanna Flats	0.2 1985 – 1994 0.5 1995 – 1999 1.0 2000 - 2005
FRESHWATER	Tidal Fresh Potomac River	0.7
RUPPIA	Choptank River Mouth	0.5
ZOSTERA	Virginia Lower Eastern Shore	0.3
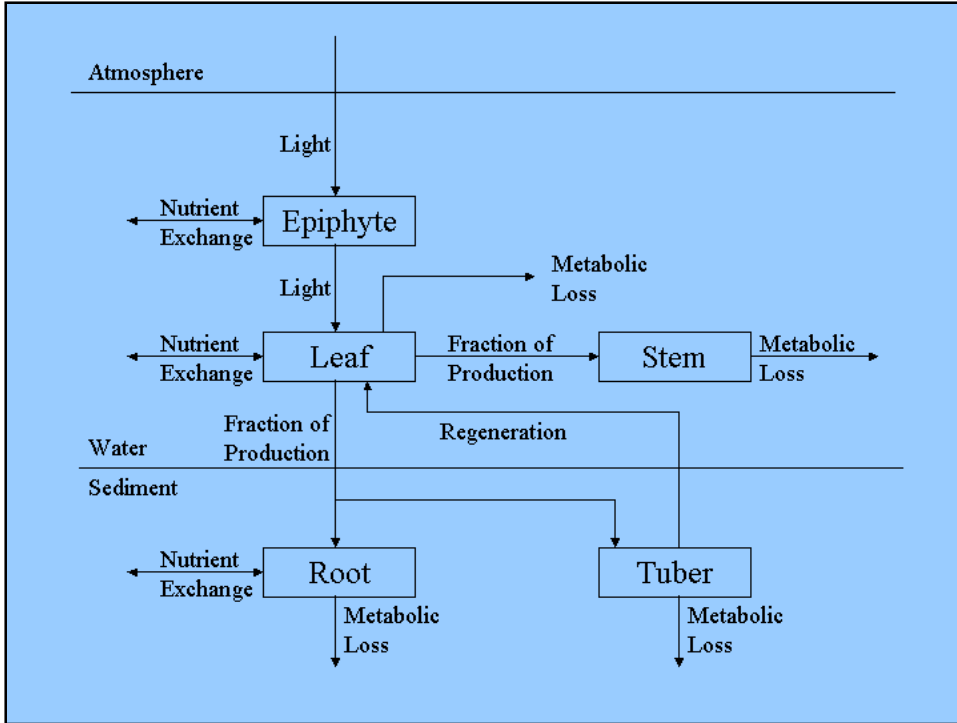
Figure 1. SAV model schematic.

KTg1 = 0.003
KTg2 = 0.005
Topt = 25

f(t) = 1 when T = Topt
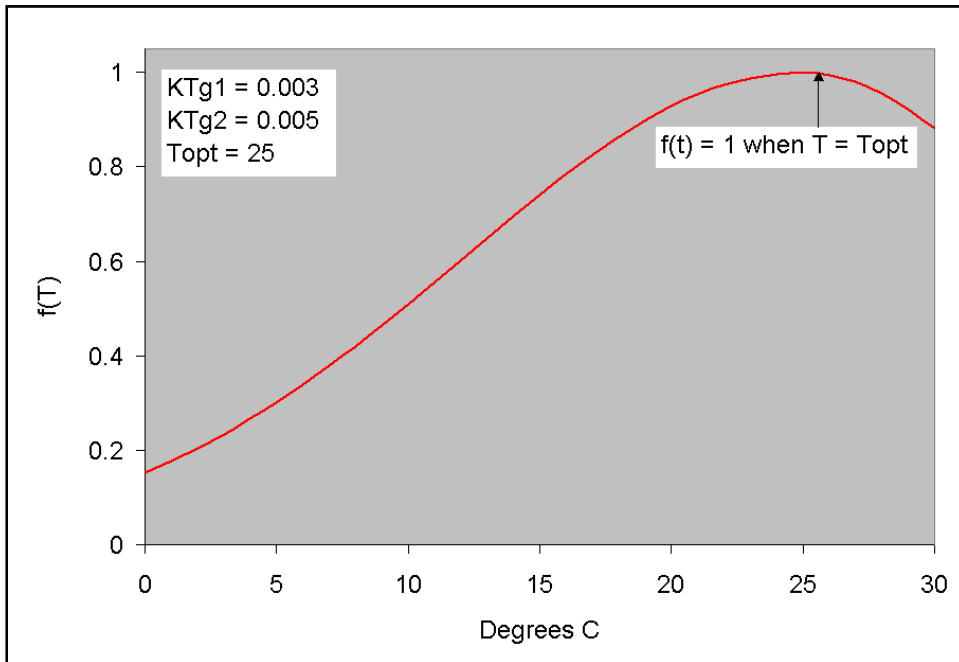
Figure 2. Effect of temperature on plant production.
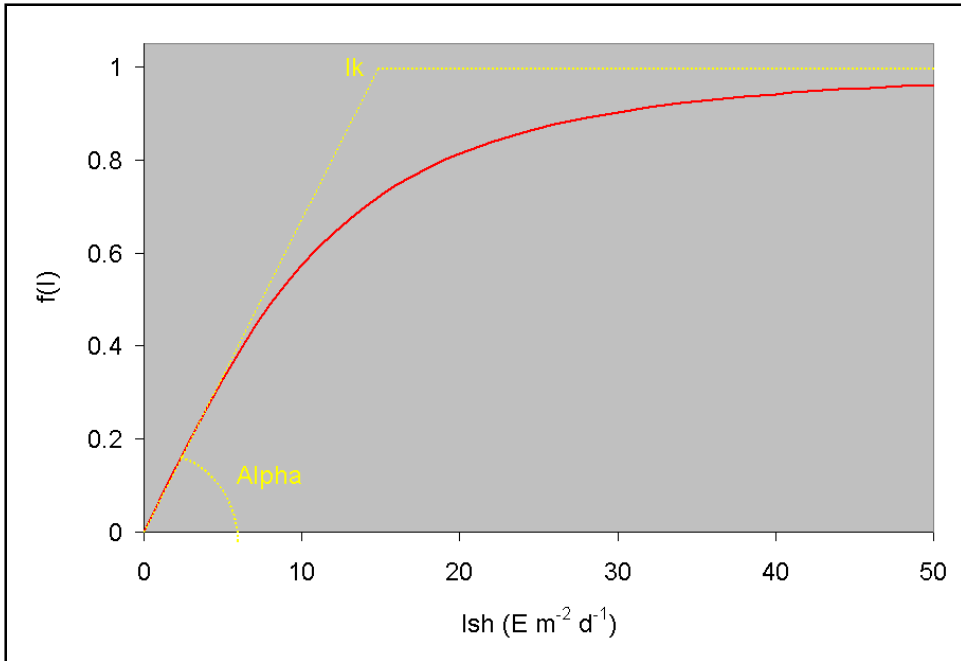
Figure 3. SAV production versus irradiance curve.
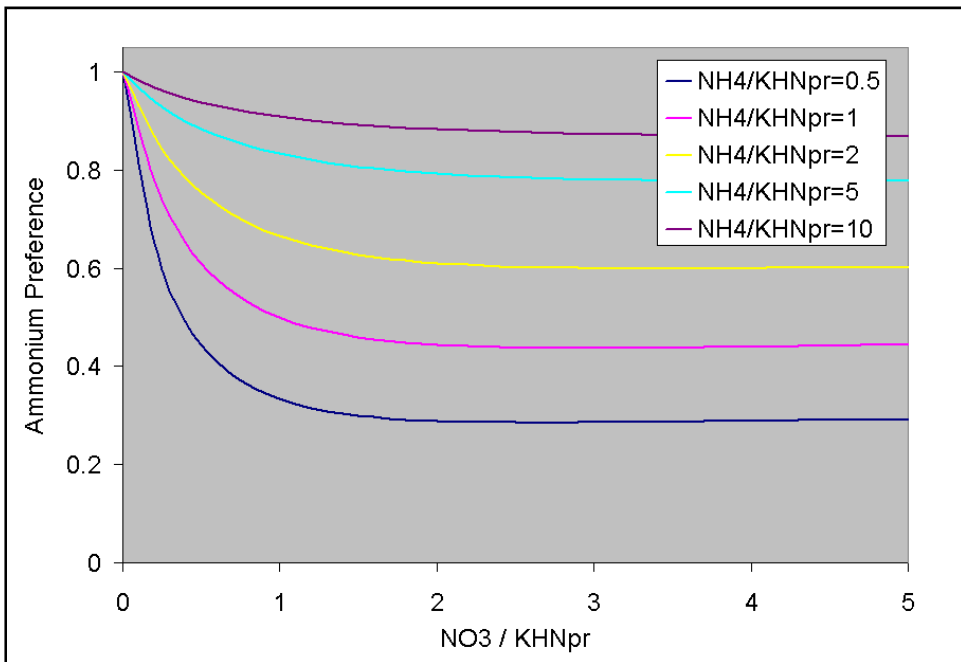
Figure 4. The ammonium preference function.
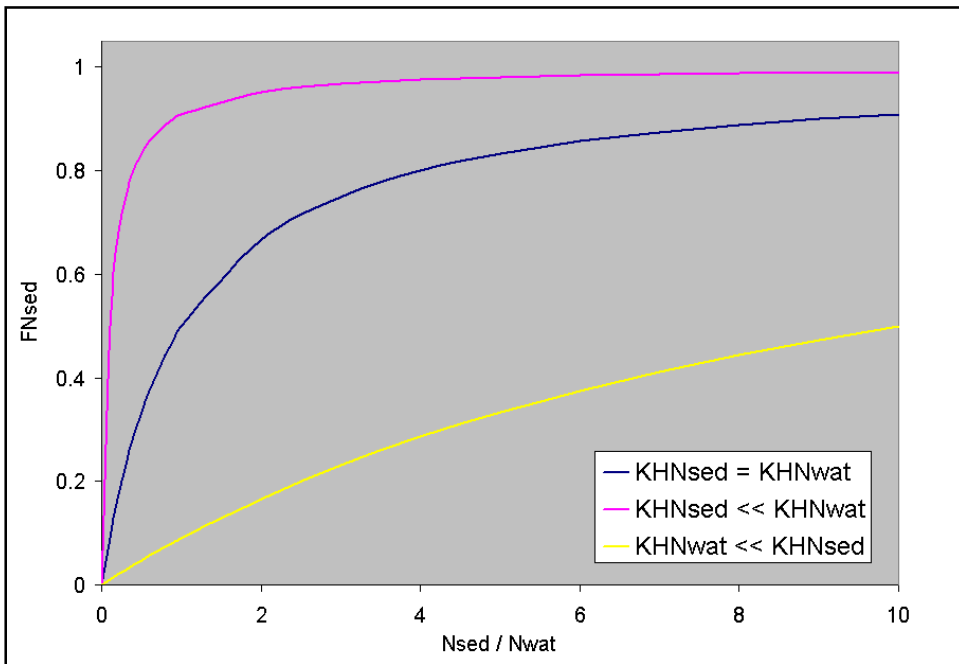
Figure 5. Fraction of nutrients obtained from sediments.
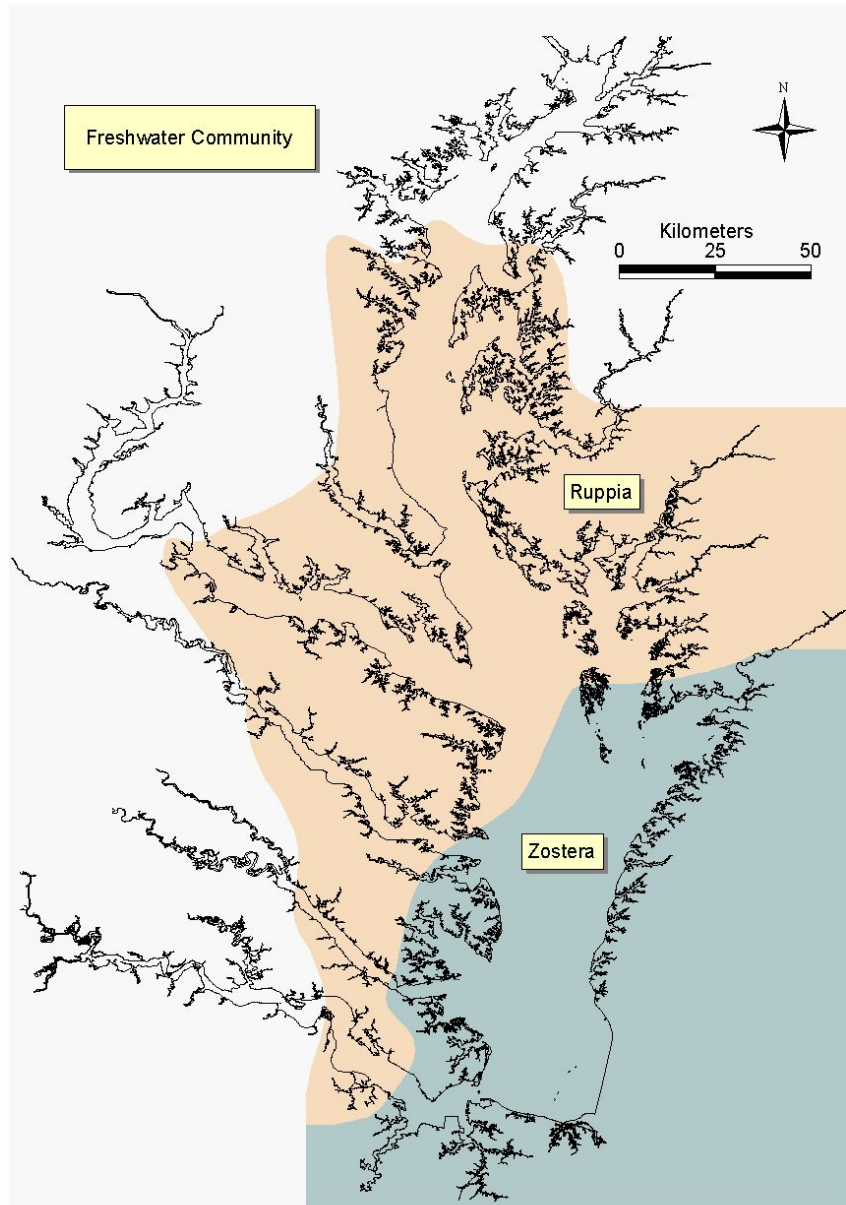
Figure 6. SAV community distribution from original model application (Cerco at al. 2002).
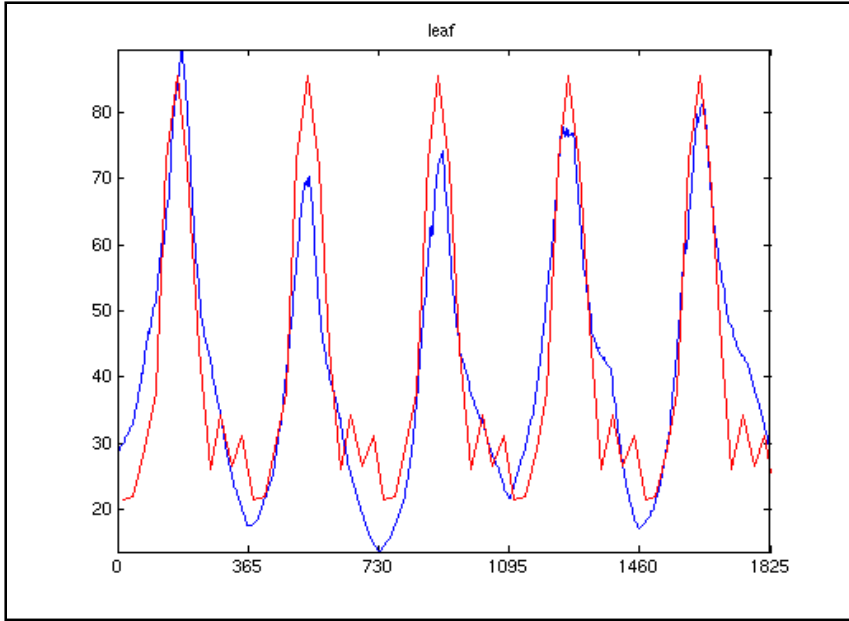
Figure 7. Results from a "standalone" model application used to determine the ZOSTERA parameter set. The red line is observed above-ground biomass (g C m^{-2}), determined on a monthly basis from an assembled data set. The blue line is the model result based on the York River mouth from 1988 to 1994 (1825 days).
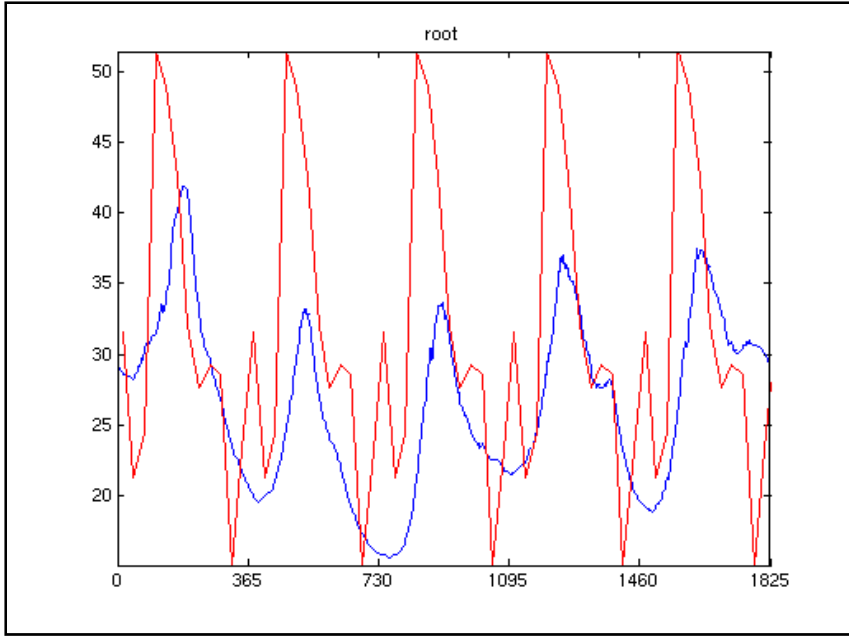
Figure 8. Results from a "standalone" model application used to determine the ZOSTERA parameter set. The red line is observed below-ground biomass (g C m^{-2}), determined on a monthly basis from an assembled data set. The blue line is the model result based on the York River mouth from 1988 to 1994 (1825 days).
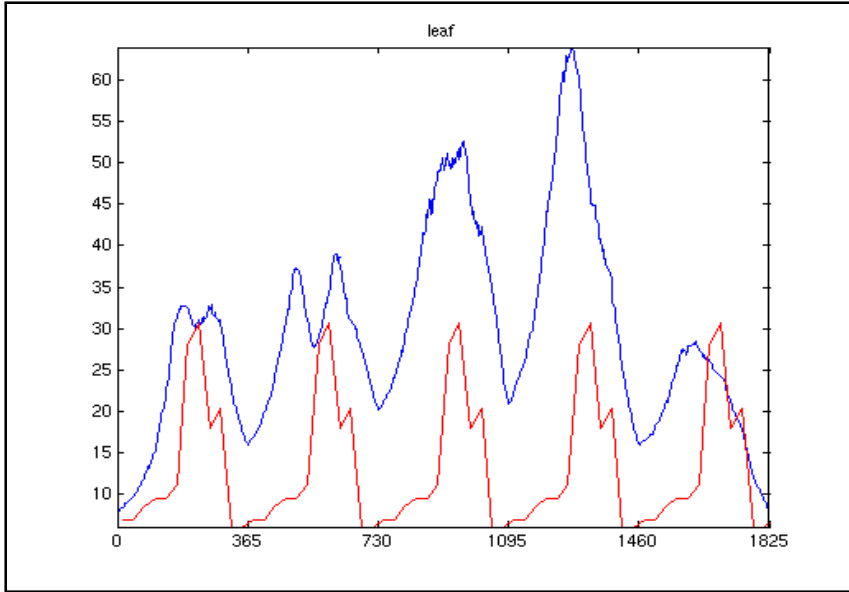
Figure 9. Results from a "standalone" model application used to determine the RUPPIA parameter set. The red line is observed above-ground biomass (g C m^{-2}), determined on a monthly basis from an assembled data set. The blue line is the model result based on the Choptank River mouth from 1988 to 1994 (1825 days).
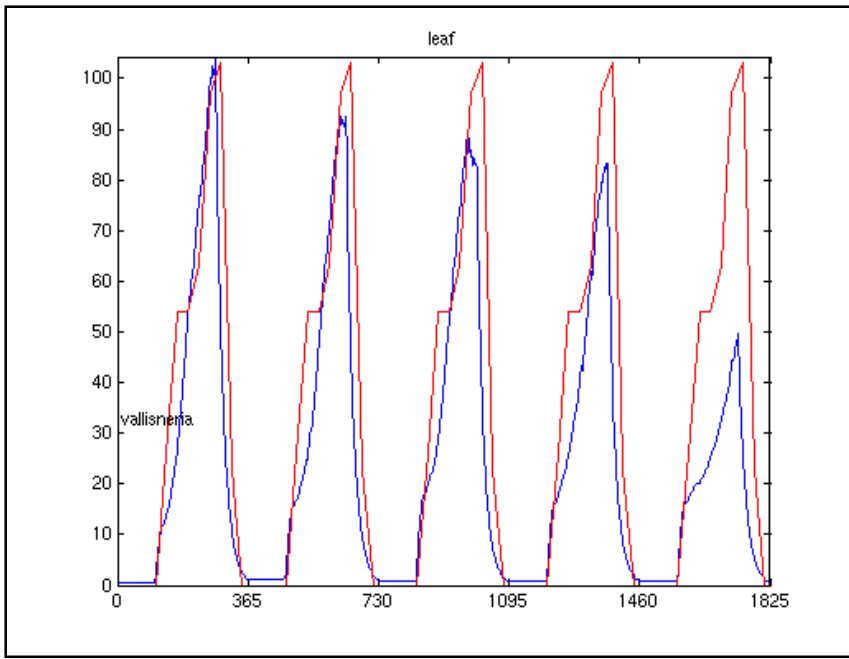
Figure 10. Results from a "standalone" model application used to determine the FRESHWATER parameter set. The red line is observed above-ground biomass (g C m^{-2}), determined on a monthly basis from an assembled data set. The blue line is the model result based on the Susquehanna Flats from 1988 to 1994 (1825 days).
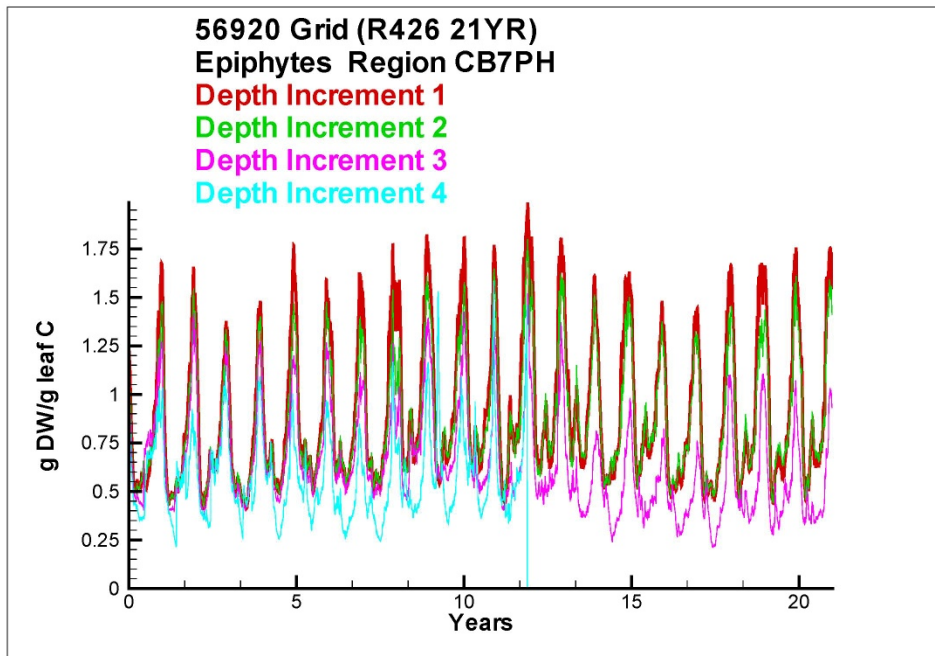
Figure 11. Computed epiphyte density on ZOSTERA along the lower eastern shore of Chesapeake Bay (CB7PH). Epiphytes are shown at four depth increments centered on 0.375. 0.75, 1.25, and 1.75 m. The simulation is from 1985 to 2005. Approximately 12 years into the simulation, SAV between 1.5 and 2 m disappears and epiphyte density goes to zero.
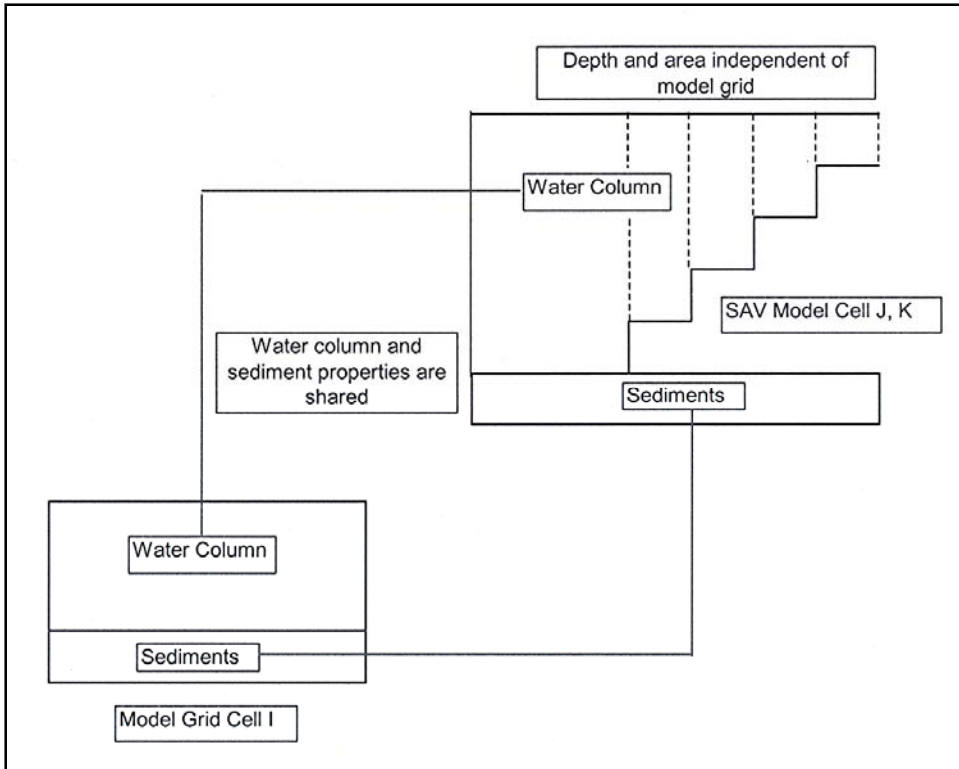
Figure 12. Schematic of SAV Sub-Grid. The SAV grid is independent of the computational grid shared by the hydrodynamic and water quality models. SAV cell J is divided into K depth increments and shares certain properties with computational cell I.
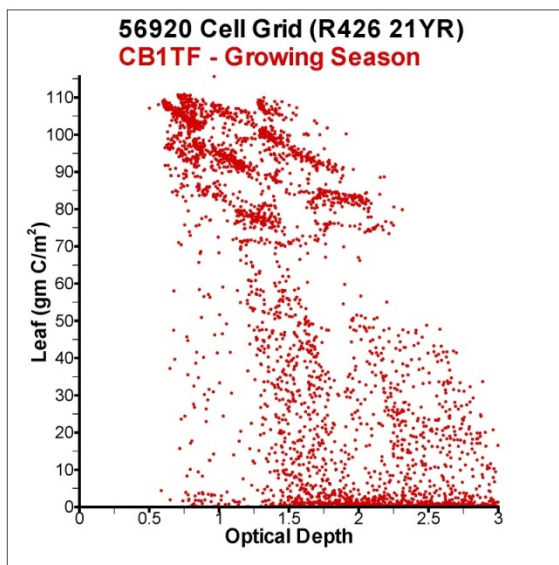
Figure 13. Comparison to Habitat Criteria for FRESHWATER community in Susquehanna Flats. Criteria indicate SAV should not survive when optical depth exceeds 1.6 to 2.
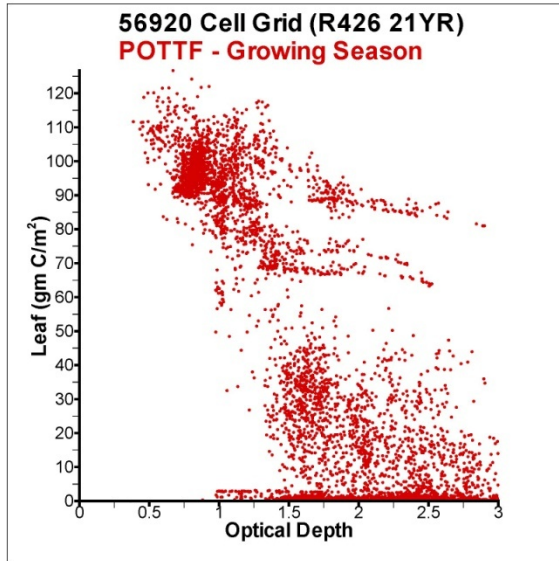
Figure 14. Comparison to Habitat Criteria for FRESHWATER community in the tidal fresh Potomac River. Criteria indicate SAV should not survive when optical depth exceeds 1.6 to 2.
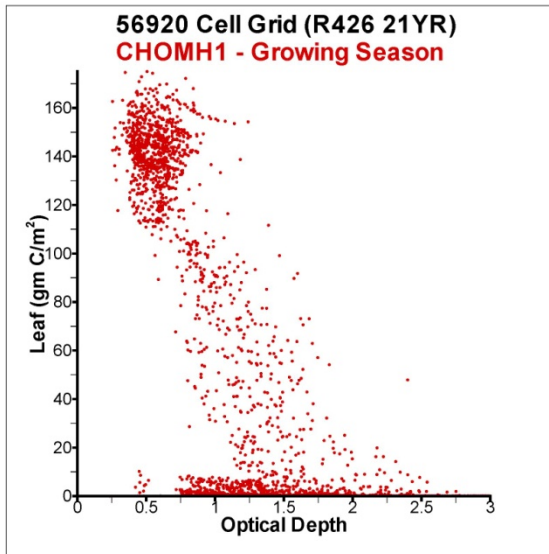
Figure 15. Comparison to Habitat Criteria for RUPPIA community at the mouth of the Choptank River. Criteria indicate SAV should not survive when optical depth exceeds 1.5 to 1.6.
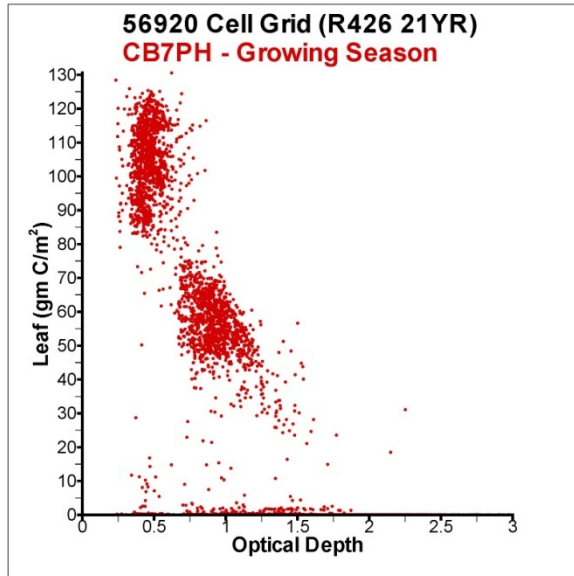
Figure 16. Comparison to Habitat Criteria for ZOSTERA community in the Virginia lower eastern shore. Criteria indicate SAV should not survive when optical depth exceeds 1.5 to 1.6.
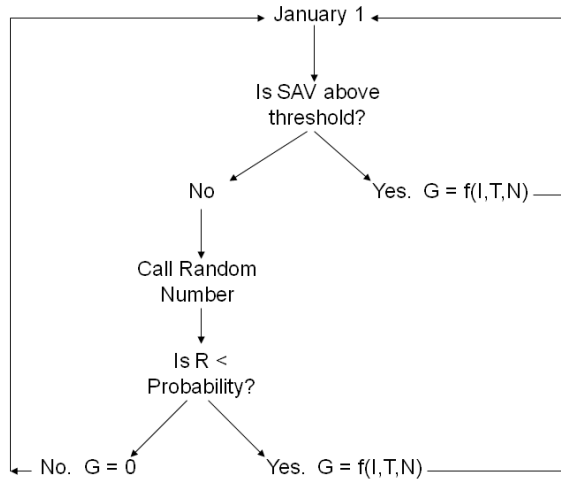
Figure 17. SAV Probability. The probability algorithm is accessed on January 1 of each model year for each SAV cell and depth increment. If SAV density exceeds a threshold, the model proceeds. If density is below the threshold, a random number generator is called and the probability of success is calculated. If the probability of success is achieved, the model proceeds. Otherwise, no growth occurs for that year. The original intention of this algorithm is to limit SAV propagation despite achievement of modeled criteria for growth.
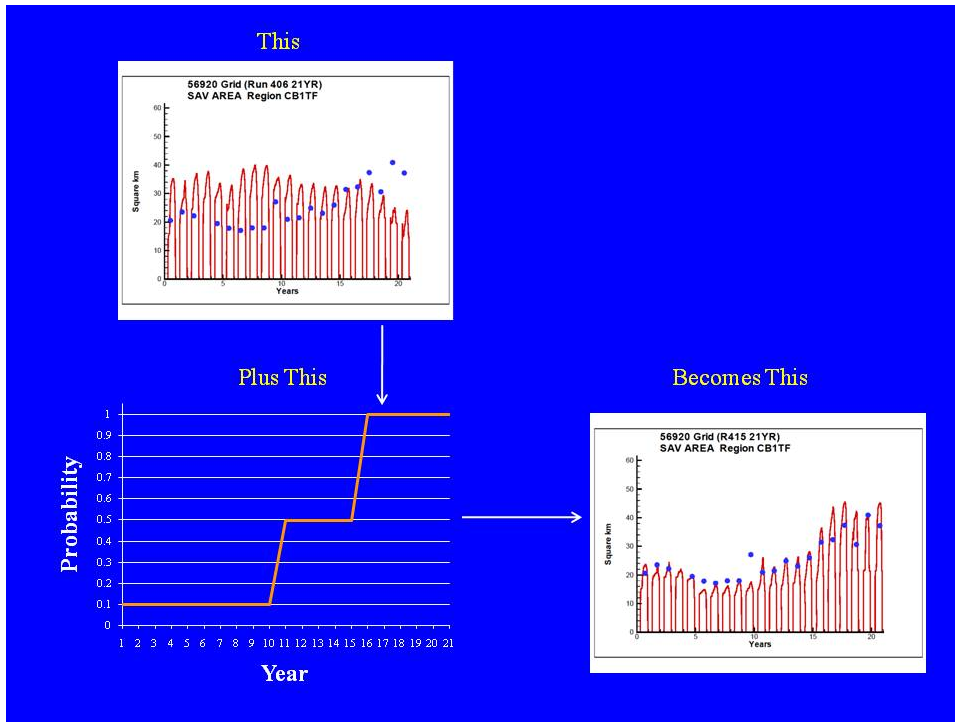
Figure 18. Utility of SAV Probability in the FRESHWATER community. Increasing probability of success allows the model to reproduce the observed trend in SAV area.
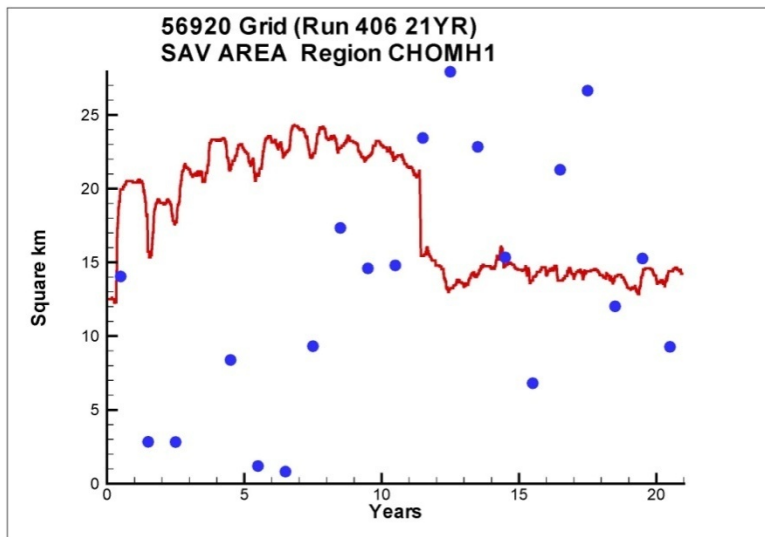
Figure 19. Utility of SAV Probability in the RUPPIA Community. The model cannot reproduce the erratic observed year-to-year variability in SAV area. Probability will be used as a tuning tool to reproduce the mean observed area.
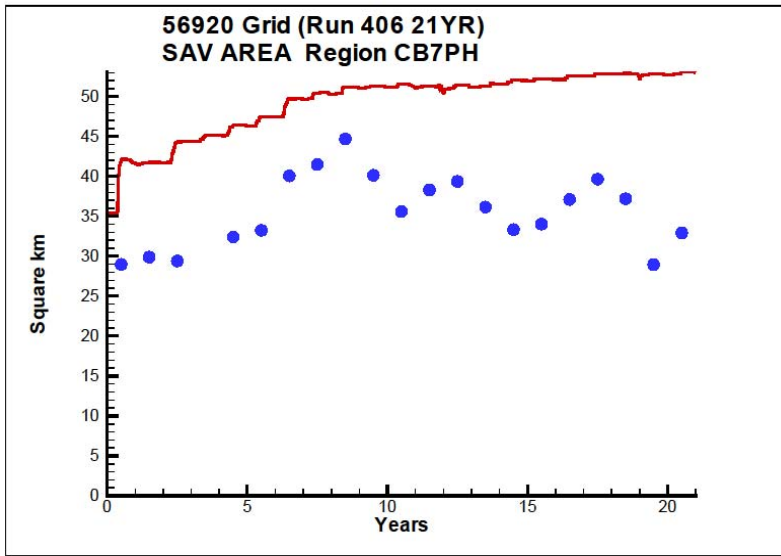
Figure 20. Utility of SAV Probability in the ZOSTERA Community. The model over-estimates SAV area. Probability will be used as a tuning tool to reduce area due to effects of waves, currents, and substrate which are otherwise not accounted for.
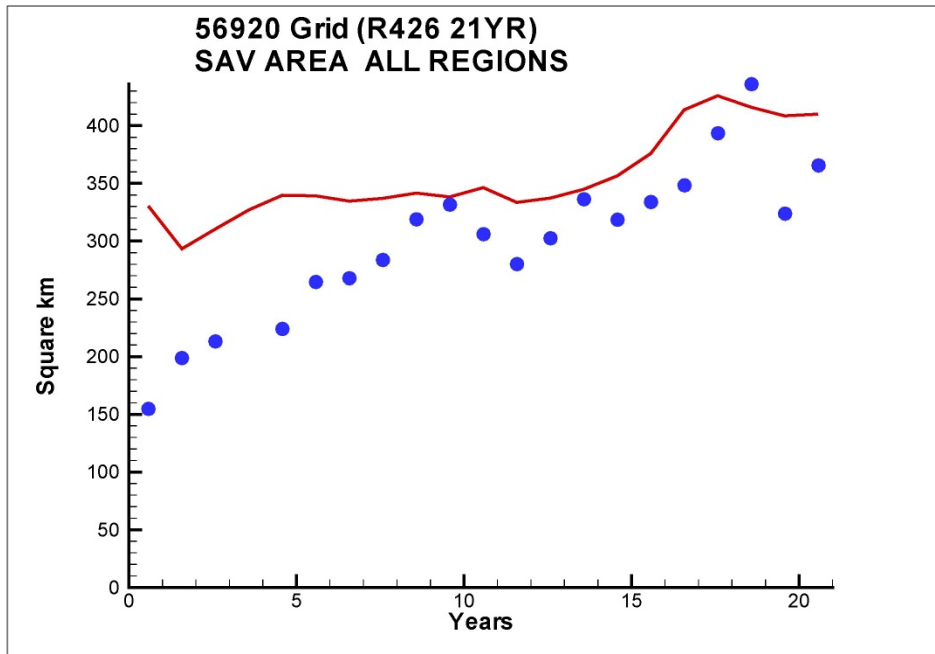
Figure 21. Time series of computed and observed system-wide SAV total area 1985 – 2005. Observations are from annual overflights conducted at various times during the growing season. Model results are plotted at the time of the overflight.
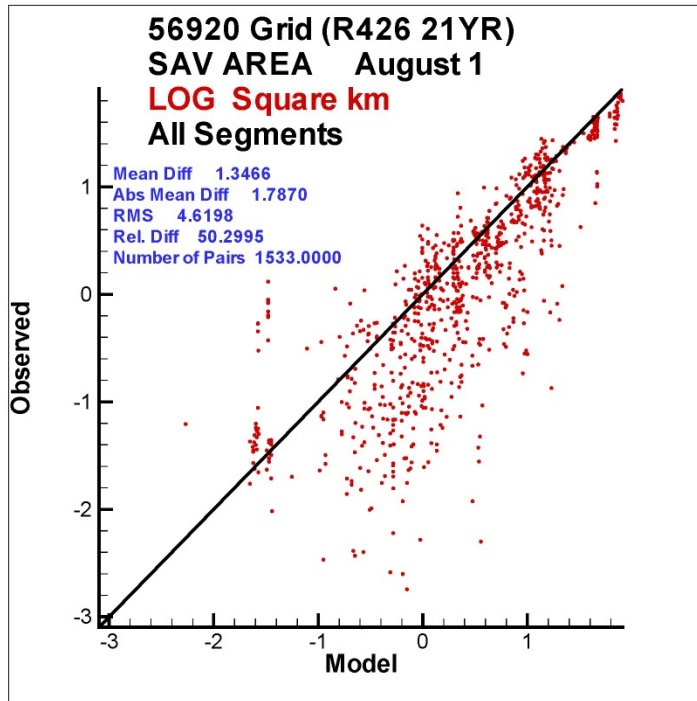
Figure 22. Scatter plot of computed and observed SAV area 1985 – 2005. Each data point represents SAV area in a CBPS in one year.
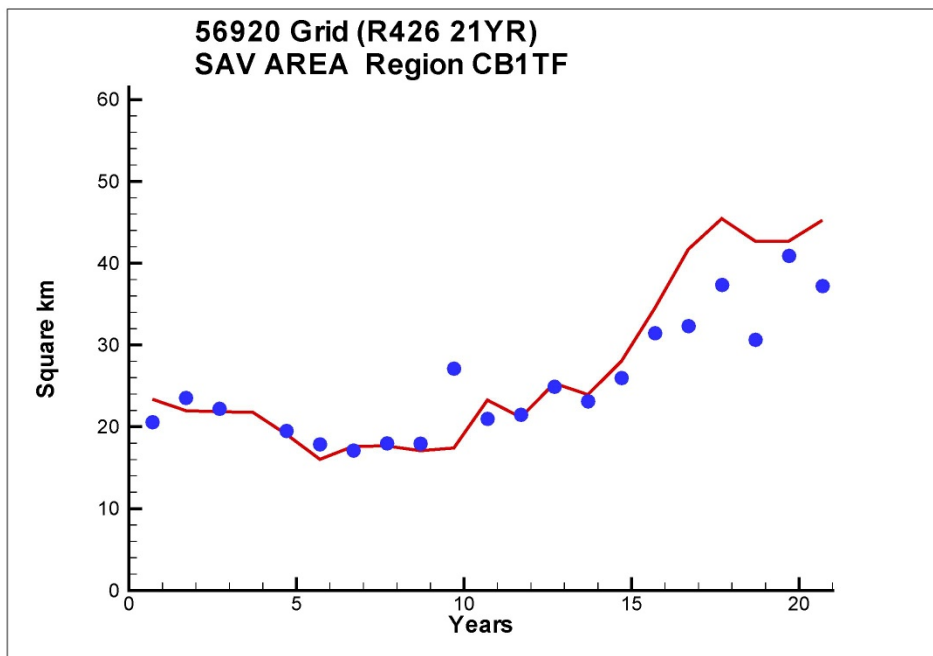
Figure 23. Time series of computed and observed SAV area for FRESHWATER community in Susquehanna Flats 1985 – 2005.
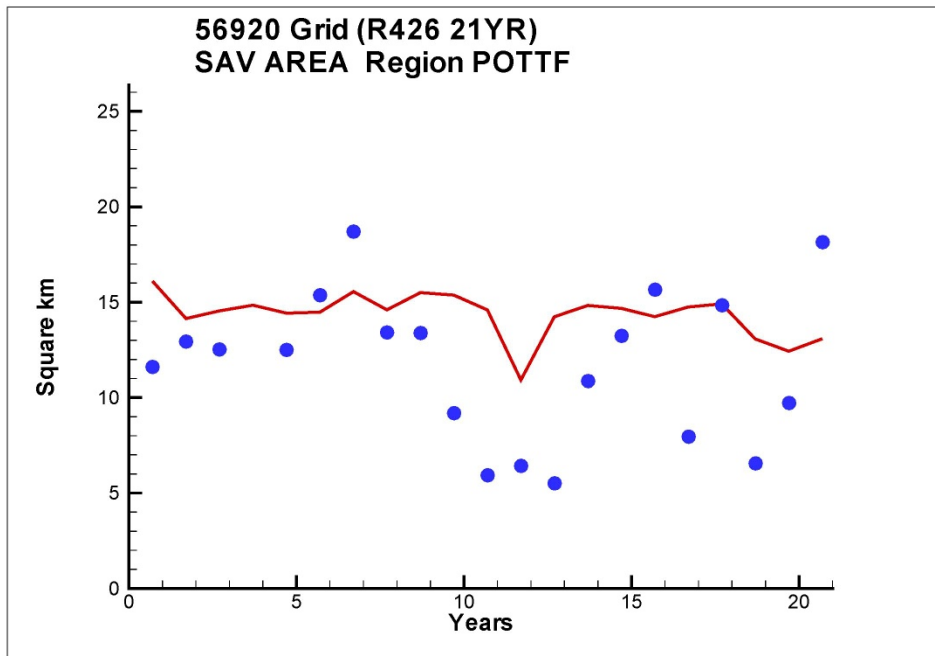
Figure 24. Time series of computed and observed SAV area for FRESHWATER community in the tidal fresh Potomac River 1985 – 2005.
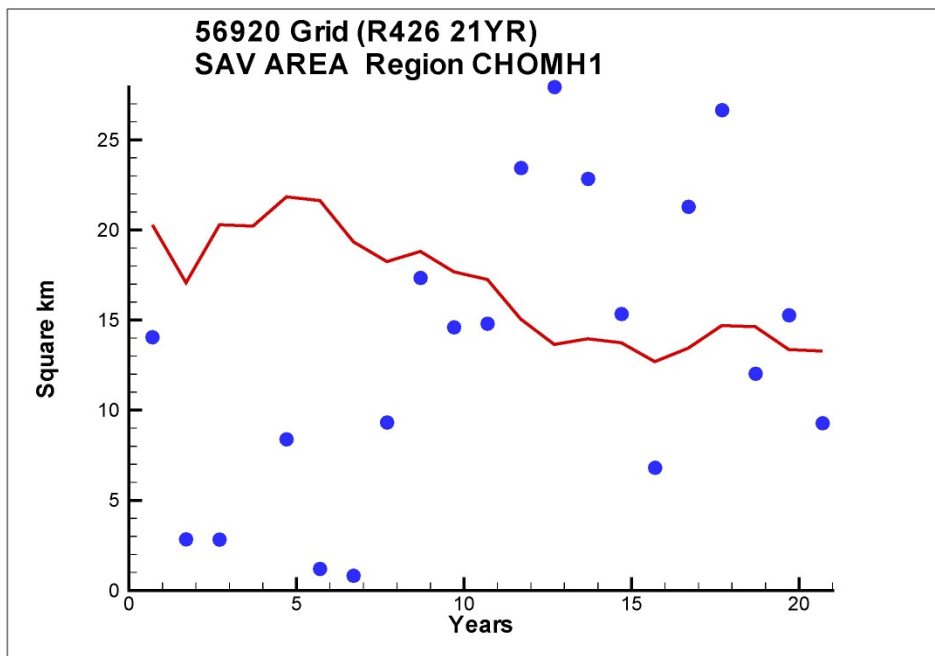
Figure 25. Time series of computed and observed SAV area for RUPPIA community in the Choptank River mouth 1985 – 2005.
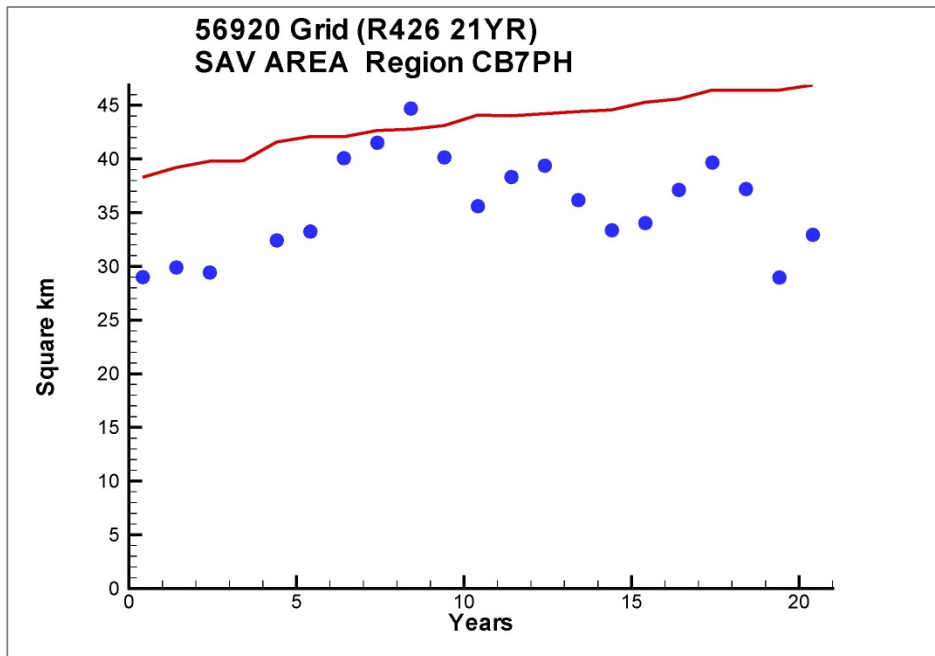
Figure 26. **Time series of computed and observed SAV area for ZOSTERA community on the Virginia lower eastern shore 1985 – 2005.**

8 Light Attenuation

Introduction

Computed light attenuation plays a crucial role in the subsequent computation of phytoplankton and submerged aquatic vegetation. In addition, maintenance of sufficient water clarity is one objective of the Total Maximum Daily Load requirements. Previous versions of the Chesapeake Bay model (Cerco et al. 2002, Cerco and Noel 2004) used a "partial attenuation model" for light attenuation. Light attenuation was computed as a function of suspended solids in the water column:

$$Ke = a1 + a2 \cdot ISS + a3 \cdot VSS \qquad (1)$$

in which:

Ke = coefficient of diffuse light attenuation (m^{-1})
a1 = background attenuation (m^{-1})
a2 = attenuation by inorganic suspended solids ($m^2\ g^{-1}$)
a3 = attenuation by organic suspended solids ($m^2\ g^{-1}$)
ISS = inorganic (fixed) suspended solids concentration ($g\ m^{-3}$)
VSS = organic (volatile) suspended solids concentration ($g\ m^{-3}$)

Partial attenuation relationships are robust and widely-employed although they lack the rigor of more advanced models. A second drawback is in the evaluation of the parameters a1 – a3. For the previous models, these were evaluated by linear regression and then adjusted, where necessary, to improve the fit to observed attenuation. For the present study, the decision was made to apply a rigorous optical model parameterized, to the greatest extent possible, with direct observations of appropriate quantities.

Field and Studies and Model Development

The Smithsonian Environmental Research Center completed a study entitled "Coupling Suspended Sediment Dynamics and Light Penetration in the Upper Chesapeake Bay" under contract to the US Army Corps of Engineers. The objective of this work was to develop a FORTRAN callable subroutine to calculate light penetration in Chesapeake Bay based on state-of-the-art understanding of radiative transfer theory and size-dependent variability in inherent optical properties (i.e. absorption and scattering coefficients) of organic and inorganic particulate matter. In connection with this work (Gallegos et al.

2006), field surveys of optical properties and suspended solids were conducted in the Potomac River and upper Chesapeake Bay. The light penetration model was parameterized with this data as well as with existing data from other portions of the bay.

Optical Model Basics[1]

Three water quality constituents contribute to light attenuation in estuaries: colored dissolved organic matter absorbs light selectively at blue wavelengths; phytoplankton chlorophyll a both scatters and absorbs light, having absorption peaks at blue and red wavelengths; and suspended solids scatter and absorb light, with absorption predominately in the blue wavelength region. The problem of modeling light attenuation in estuaries, therefore, consists of specifying the contribution of water itself plus the three optically active water quality constituents to the absorption and scattering of light, then relating absorption and scattering to light attenuation using relationships derived from radiative transfer theory.

The absorption and scattering coefficients are inherent optical properties, which have the advantageous property that their values are proportional to the concentration of the causative factor. That is, we can model the absorption due to, e.g. chlorophyll, as:

$$a_\varphi(\lambda) = a_\varphi(\lambda)[CHLA] \qquad (2)$$

in which:

λ = wavelength of light
$a_\varnothing(\lambda)$ = absorption due to phytoplankton
$a_\varphi^*(\lambda)$ = specific absorption spectrum of phytoplankton chlorophyll
CHLA = chlorophyll a concentration

Similar expressions can be written for absorption by other constituents, as well as for scattering.

In a series of papers, Kirk (1981, 1984, 1994) established a relationship between the diffuse attenuation coefficient, Ke, an apparent optical property, and the inherent optical properties total absorption coefficient, a_t, and particulate scattering coefficient, b_p:

$$Ke(\lambda) = \frac{1}{\mu_0} \sqrt{a_t^2(\lambda) + G(\mu_0) \cdot a_t(\lambda) \cdot b_p(\lambda)}$$

$$(3)$$

in which:

μ_0 = the cosine of the solar angle of incidence after refraction at the air-water interface

---

[1] This section is adopted from Gallegos et al (2006). Details are available in the source document.

$G(\mu_0)$ is a function of μ_0 that scales the effect of scattering on attenuation

A number of the assumptions used by Kirk limit the applicability of Equation 3 for use in shallow, turbid waters. Alternative expressions for calculating Ke from a_t and b_p have been proposed. Albert and Mobley (2003) used a simplified expression to relate Ke to absorption and backscattering:

$$Ke = \kappa_0 \cdot \frac{a_t + b_p}{\mu_0}$$

(4)

in which:

κ_0 = empirical constant (= 1.0546)

In this study, κ_0 is considered to be a variable which depends on backscatter probability (B), μ_0, the ratio of b_p to a_t, and optical depth (($a_t + b_p$) · Z)

Incorporation into the CBEMP

More than 20 equations must be solved to fully implement the solution to Equation 4 (Gallegos et al. 2006). The computational burden to solve the full suite of equations at each model time step for every cell was extensive. A procedure was implemented based on a look-up table. An array of simulated Ke was generated based on six independent variates:

- colored dissolved organic matter
- phytoplankton absorption
- particulate scattering
- non-algal particulate absorption
- solar zenith angle
- backscatter fraction

Nearly 2,000,000 values of Ke were generated based on nested loops of the six independent variates.

Parameter sets that related absorption and scattering to particle concentration were generated on a seasonal basis for 78 Chesapeake Bay Program Segments (CBPS). These parameter sets were based on measurements in the Potomac and Patuxent Rivers and on a few other locations, mostly in the upper Chesapeake Bay. Parameters for CBPS with no observations were adopted from similar segments with observations.

The look-up table was expressed as a FORTRAN subroutine which was incorporated into the larger model. Ke was calculated at every model iteration and location as follows:

- The model provides the following information to the subroutine:
  - CBPS of the model cell
  - Day of year

- o   Computed chlorophyll concentration
- o   Computed total suspended solids concentration
- The subroutine determines the six independent variates based on information provided by the model.
- The subroutine returns the value of Ke from the look-up table.

Parameter Adjustments

Accurate computation of light attenuation requires accurate computation of suspended solids and chlorophyll. We found, however, regions where computations of light attenuation were unsatisfactory even when solids and chlorophyll were well-represented. The ready explanation for unsatisfactory computation of Ke was the extrapolation of parameter values to segments lacking observations of optical properties. We found in some cases, however, notably the Potomac, where computations of Ke were unsatisfactory despite site-specific measures of optical properties. In this case, the problem might originate in the measures of Ke. In portions of the Potomac and Patuxent Rivers, attenuation measures for validation of the water quality model were calculated based on observed disk visibility. Light attenuation derived in this manner is only approximate and may not agree with attenuation calculated from rigorous principles and measurements. Nevertheless, the preponderance of measures of attenuation in the Potomac, Patuxent, and a few other regions are derived from disk visibility and the water quality model must reproduce these measures.

At times, significant discontinuities in computed Ke were apparent at the transitions between CBPS (Figure 1). The spatial discontinuities were attributed to two sources. The first was a discrete step in parameter values between adjacent CBPS. The second was the use of the look-up table. Small differences in solids or chlorophyll concentration might produce a step change in the bin of scattering or absorption and a resulting step change in computed Ke.

The needs to match available attenuation data and to provide smooth transitions in computed attenuation were met by adjusting the original parameter set supplied with the optical model. The number of model parameters is large and a trial-and-error approach to parameter evaluation would result in an endless process and, potentially, unrealistic parameter combinations. We limited the adjustment process to adopting complete parameter sets from nearby or similar segments (Table 1). For the most part, the adjustment process amounted to revising the original parameter assignment in segments lacking sufficient observations of optical properties.

Summary of Results

Time series plots and statistics of computed and observed light attenuation are presented for individual stations in an appendix to this report. Summary plots and statistics are presented here. No standard set of model performance statistics exists. We employ summary statistics that were developed as part of our initial Chesapeake Bay model study (Cerco and Cole 1994). Use of a consistent set of statistics facilitates comparisons with earlier model versions

and with applications to other systems. Statistics computed were mean difference, absolute mean difference, and relative difference:

$$MD = \frac{\sum(P - O)}{N}$$

(4)

$$AMD = \frac{\sum|P - O|}{N}$$

(5)

$$RD = \frac{\sum|P - O|}{\sum O}$$

(6)

in which:

MD = mean difference
AMD = absolute mean difference
RD = relative difference
O = observation
P = prediction
N = number of observations

The mean difference describes whether the model over-estimates or under-estimates the observations, on average. The mean difference can attain its ideal value, zero, while discrepancies exist between individual observations and computations.   The absolute mean difference is a measure of the characteristic difference between individual observations and computations. An absolute mean difference of zero indicates the model perfectly reproduces each observation. Relative difference is the absolute mean difference normalized by the mean of the observations.

Quantitative statistics were determined using the same model-data pairs as in the time series plots. The selected stations and number of pairs depends on the system or station grouping (Table 2). For comparison, summary statistics were retrieved from the 2002 model (Cerco and Noel 2004). Caution is required in comparing the statistics since the model periods differ (1985-1994 for 2002 model vs. 1991-2000 for 2010 model) as well as the number of stations and observations. Still the comparisons provide insights into the different means of computing light attenuation.

The MD statistic shows little trend (Figure 2). For the most systems, MD is $\approx$ 0.2 m^{-1} in magnitude and shows no bias for high or low computations. The Patuxent River provides an exception; MD is greater than 0.8 in magnitude and distinguishes this system from the others. The same magnitude and lack of bias characterized the results from the 2002 model. In the previous version, the Patuxent River demonstrated MD similar to the other western tributaries.

The AMD statistic for the mainstem bay is roughly half the tributaries, $\approx$ 0.5 vs. $\approx$ 1 respectively (Figure 3). The Western minor stations stand out as having AMD roughly double the other systems. The previous model showed

similar comparison between the bay and tributaries although AMD was consistently lower in 2002 versus 2010.

RD is 40% to 50% for all systems except the Western Minor Stations where RD exceeds 80% (Figure 4). The 2010 model results for RD are not clearly distinguished from the 2002 model results although the 2010 results are, perhaps, greater than in 2002.

Our graphical summaries are in the form of cumulative distribution plots. Creation of the plots first requires pairing in space and time of observations and computations. These were from the same stations used in the time series plots and statistical summaries. Observations were paired with daily average computations in the cell corresponding to sample location and depth. Next, the observations and computations were individually sorted from smallest to largest. The sorted arrays were divided into quantiles and plotted as cumulative distributions. A point on the line in x-y space indicates the percentage of observations or computations (y-axis) less than the indicated concentration (x-axis). The 50th percentile indicates the median value. Perfect correspondence is indicated when the cumulative distribution of modeled values exactly overlays the cumulative distribution of observed values. The cumulative distribution plots present information about the magnitude of computations and observations. However, the sorting process removes direct comparison between individual computations and observations.

The cumulative distribution for the mainstem bay indicates computed attenuation is greater than observed throughout the range of observed values (Figure 5). For most other groupings, the median observed value exceeds the median computed value (Figures 6 through 12). The curves often exhibit a crossover in the higher percentiles. That is, the model tends to reflect the highest observed values of light attenuation but not the central tendency of the observations. As with other statistics, the Patuxent is a standout; observations exceed computations throughout the range (Figure 10). In terms of matching the observed distribution of light attenuation, the Rappahannock (Figure 8) is the premier system. The cumulative distribution for light attenuation for all groupings closely follows the cumulative distribution for suspended solids.

Shallow-Water Monitoring

The summary statistics presented above are from regularly-monitored stations in the Chesapeake Bay monitoring program. These stations are typically located in the channel and characterize the deeper portions of the water column. A separate Shallow-Water Monitoring Program (SWMP) monitors shallow water areas which are representative of SAV habitat and for which light attenuation is critical. Use of the SWMP observations for model validation presents several problems. The primary SWMP measure of water clarity is turbidity which cannot be directly related to the diffuse coefficient of light attenuation measured in the mainstem monitoring stations and computed in the model. Owing to their shallow-water locations, the SWMP stations often fall off the computational grid. The SWMP was initiated in 2000 and few of the measures were collected within the model calibration period of 1991 to 2000. There is, however, a data base of

true light attenuation measures collected when the monitoring stations are serviced. The data collected during 2000 – 2005 falls within the 21-year model extension run to validate the SAV model. This data was screened to eliminate locations off the model grid leaving ≈ 1,000 observations concentrated along the Maryland eastern shore (Figure 13). The individual observations show little correspondence to the model (Figure 14). This is not surprising; it is unrealistic to expect the model to match instantaneous individual observations collected in extreme reaches of the computational domain. The observational data set is more suited to the cumulative distribution analysis. The cumulative distribution (Figure 15) is remarkably similar to the distribution from many of the regular monitoring stations. The observations exceed the model through much of the distribution. There is a cross-over in the upper range so that the model matches the highest observations. At the median, the observations exceed the model by ≈ 0.75 m^{-1} (the MD statistic is -0.35 m^{-1}, the AMD is 1.46 m^{-1}).

Partial Attenuation

Partial attenuation models such as Equation 1 lend themselves readily to analysis of the contributions of individual dissolved and particulate substances to total light attenuation. Concentrations of individual substances can be supplied to the equation in succession while concentrations of alternate substances are set to zero. Derivation of partial attenuation of individual substances in an advanced optical model is not as facile. Although concentrations of individual substances can be successively run through the equations, non-linearities in the relationships cause the sum of attenuation from individual substances to exceed the attenuation calculated when all substances are considered together. Biber et al. (2007) forged down this path despite the limitations with the justification that the partial attenuations obtained from the non-linear model provide accurate indication of the relative importance of the individual substances. We employ here a modification of their method.

Model results were assembled for 82 CBPS. Computed chlorophyll, particulate organic carbon, fine clay, clay, silt, and sand were averaged across all cells in each segment, across SAV growing seasons (April – October), and across the years 1993 – 1995. These years were selected because they are emphasized in the TMDL calculations. The average concentrations of the modeled substances were supplied individually to the same algorithms used to compute attenuation in the water quality model. Pure water and colored dissolved organic matter (CDOM) were considered as well. Attenuation from the individual components was normalized by the sum of the attenuations to provide partial attenuation values which sum to unity. The individual partial attenuations were finally summed into water plus CDOM, organic matter (algae plus detritus), and fixed solids. These are presented along with the average water quality model component concentrations and Ke in Table 3. These partial attenuations are approximations but provide useful insights into the factors that influence computed attenuation.

Acknowledgements

Field investigations, laboratory analyses, and optical model development were all conducted under the direction of Dr. Charles Gallegos of the Smithsonian Environmental Research Center, Edgewater MD.

References

Albert, A., and Mobley, C. D. (2003). "An analytical model for subsurface irradiance and remote sensing reflectance in deep and shallow case-2 waters," *Optics Express* 11, 2873-2890.

Biber, P., Gallegos, C., and Kenworthy, W. (2007). "Calibration of a bio-optical model in the North River, North Carolina (Albemarle-Pamlico Sound: A tool to evaluate water quality impacts on seagrasses," *Estuaries and Coasts* 31, 177-191.

Cerco, C.F. and Cole, T. M. (1994). "Three-dimensional eutrophication model of Chesapeake Bay," Technical Report EL-94-4, U.S. Army Engineer Waterways Experiment Station, Vicksburg MS.

Cerco, C., Johnson, B., and Wang, H. (2002). "Tributary refinements to the Chesapeake Bay model," ERDC TR-02-4, US Army Engineer Research and Development Center, Vicksburg MS.

Cerco, C., and Noel, M. (2004). "The 2002 Chesapeake Bay eutrophication model," EPA 903-R-04-004, Chesapeake Bay Program Office, US Environmental Protection Agency, Annapolis MD. (available at http://www.chesapeakebay.net/modsc.htm)

Gallegos, C., Lewis, E., and Kim, H-C. (2006). "Coupling suspended sediment dynamics and light penetration in Chesapeake Bay," Smithsonian Environmental Research Center, Edgewater MD (available at http://www.chesapeakebay.net/content/publications/cbp_13364.pdf)

Kirk, J. (1981). "Monte Carlo study of the nature of the underwater light field in, and the relationships between optical properties of, turbid, yellow waters," *Australian Journal of Marine and Freshwater Research* 32, 517-532.

Kirk, J. (1984). "Dependence of relationship between apparent and inherent optical properties of water on solar altitude," *Limnology and Oceanography* 29, 350-356.

Kirk, J. (1994). "The relationship between the inherent and the apparent optical properties of surface waters and its dependence on the shape of the volume scattering function." *Ocean Optics*, R. Spinrad, K. Carder, and M. Perry eds., Oxford University Press, New York, 40-58.

Table 1 Parameter Replacements in Optical Model		
Substitute	**into**	
BIGMH	MANMH	Use the Big Annemessex River to characterize the Mannokin, Wicocomico, and Lower Nantikoke Rivers.
	WICMH	
	NANMH	
CB4	EASMH	Use the middle Chesapeake Bay to characterize the adjacent Eastern Bay.
CB3	CHSMH	Use the upper Chesapeake Bay to characterize the adjacent lower Chester River.
CB7	CB6	Use the lower eastern shore region of the mainstem bay to characterize two adjacent bay segments.
	CB5	
CB2	CB1	Use a region from the upper mainstem to characterize the Susquehanna Flats
YRKMH	MPNTF	Use the middle York River to characterize the Mattaponi and Pamunkey Rivers.
	PMKTF	
	MPNOH	
	PMKOH	
RPPMH	RPPOH	Use the lower Rappahannock River to characterize the upper Rappahannock River.
	RPPTF	
CB5	PAXMH	Use a portion of the lower Chesapeake Bay to characterize the adjacent portion of the Patuxent River.
POTMH	POTOH	Use the lower Potomac River to characterize the system including the Piscataway River, Mattawoman Creek, and the Anacostia River.
	POTTF	
	PISTF	
	MATTF	
	ANATF	
LCHMH	FSBMH	Use the Little Choptank River to characterize Fishing Bay.

Table 2
Summary Statistics for Light Attenuation[2]

Grouping	Stations	Number Obs.	MD, 1 / m	AMD, 1 / m	RD, %
Chesapeake Bay	CB1.1, CB2.2, CB3.3C, CB4.2, CB5.2, CB6.1, CB7.3, CB7.4, CB7.4N, CB8.1E, EE3.1, EE3.2	1072	0.300	0.552	50.1
James River	TF5.5, RET5.2, LE5.3	233	0.195	1.475	48.7
York River	TF4.2, RET4.3, LE4.2, WE4.2	332	-0.275	0.944	42.3
Rappahannock River	TF3.3, RET3.2, LE3.2	232	0.119	1.228	50.7
Potomac River	TF2.1, RET2.4, LE2.2	307	-0.011	0.934	44.1
Patuxent River	TF1.7, RET1.1, LE1.3	366	-0.847	1.363	55.3
Eastern Shore Tributaries	EE1.1, EE2.1, ET1.1, ET3.2, ET4.2, ET5.2, ET6.2, ET9.1	732	0	0.957	50.6
Western Shore Tributaries	WT1.1, WT2.1, WT5.1, WT8.1	302	-0.086	2.254	85.2

---

[2] Attenuation at the following stations was calculated from disk visibility: EE3.1, EE3.2, EE1.1, EE2.1, ET1.1, ET2.3, ET4.2, ET6.2, ET9.1, WT1.1, WT2.1, WT8.1, RET2.4, TF2.1, LE1.3, RET1.1.   Attenuation at the remaining stations was measured in-situ.

Table 3
Computed Concentrations, Light Attenuation, and Partial Attenuation Coefficients

CBPS	CDOM, 1/m	Chlorophyll, ug/L	TSS, mg/L	Ke, 1/m	Partial attenuation, water + CDOM	Partial attenuation, organic matter	Partial attenuation, fixed solids
ANATF	0.666	51.867	19.479	1.811	0.153	0.455	0.392
APPTF	1.3	19.083	21.692	2.579	0.162	0.303	0.536
BACOH	2.559	6.222	23.053	3.072	0.168	0.151	0.681
BIGMH	0.844	4.129	25.999	2.111	0.175	0.172	0.654
BOHOH	0.633	7.343	12.67	2.121	0.159	0.268	0.573
BSHOH	0.891	6.684	25.288	2.53	0.146	0.168	0.687
CB1TF	0.599	4.741	23.842	2.621	0.136	0.224	0.64
CB2OH	0.599	6.851	31.879	3.349	0.123	0.166	0.711
CB3MH	0.481	10.395	21.34	2.459	0.132	0.217	0.651
CB4MH	0.332	12.805	12.453	1.499	0.182	0.329	0.491
CB5MH	0.274	12.895	8.715	0.991	0.201	0.348	0.451
CB6PH	0.274	10.5	8.43	0.969	0.207	0.329	0.464
CB7PH	0.274	9.107	7.802	0.924	0.194	0.309	0.495
CB8PH	0.24	9.403	10.313	0.809	0.205	0.294	0.502
CHKOH	1.081	4.938	28.848	3.766	0.123	0.109	0.769
CHOMH1	0.576	10.993	8.868	1.094	0.235	0.304	0.46
CHOMH2	0.72	16.739	6.52	1.273	0.215	0.397	0.386
CHOOH	1.815	19.268	9.155	1.837	0.211	0.39	0.398
CHOTF	1.09	15.763	5.942	1.048	0.268	0.418	0.316
CHSMH	0.481	12.92	6.948	1.12	0.224	0.32	0.457
CHSOH	1.942	23.683	7.237	1.196	0.302	0.393	0.304
CHSTF	1.393	25.622	11.6	2.254	0.196	0.578	0.228
CRRMH	0.486	12.154	4.732	1.303	0.208	0.384	0.407
C&DOH	0.575	15.162	4.689	0.957	0.254	0.38	0.364
DCPTF	0.666	30.098	28.913	2.285	0.132	0.282	0.585
EASMH	0.332	10.983	5.038	0.846	0.237	0.357	0.406
EBEMH	0.984	19.928	8.84	1.746	0.186	0.518	0.296
ELIPH	0.829	16.706	8.96	1.65	0.176	0.391	0.434
ELKOH	0.566	6.938	13.645	1.816	0.174	0.234	0.591
FSBMH	4.592	14.032	136.105	8.475	0.077	0.293	0.629
GU1OH	0.659	4.949	28.109	2.69	0.139	0.164	0.696
GUNOH	0.659	4.437	22.28	2.245	0.148	0.175	0.679
HNGMH	0.574	5.678	15.54	1.741	0.176	0.207	0.618
JMSMH	0.812	9.687	28.198	3.214	0.121	0.163	0.715
JMSOH	0.728	9.097	36.1	4.122	0.105	0.144	0.751
JMSPH	0.386	11.369	15.429	1.673	0.16	0.264	0.576
JMSTF	1.101	18.113	27.694	3.026	0.144	0.284	0.571
LAFMH	0.796	17.487	8.161	1.326	0.221	0.394	0.384
LCHMH	0.422	7.313	10.049	1.157	0.202	0.266	0.532
MAGMH	0.772	9.211	11.703	2.572	0.142	0.228	0.63
MANMH	0.844	10.134	29.292	2.295	0.167	0.263	0.569

MATTF	0.666	26.234	17.446	1.74	0.163	0.254	0.582
MIDOH	0.505	5.088	21.347	2.801	0.119	0.155	0.725
MOBPH	0.544	7.242	11.821	1.134	0.214	0.224	0.562
MPCOH	5.51	11.327	29.734	3.52	0.197	0.233	0.571
MPNOH	0.857	5.05	9.459	1.452	0.217	0.263	0.52
MPNTF	0.857	2.177	4.275	0.916	0.295	0.265	0.44
NANMH	0.844	19.114	52.379	3.673	0.115	0.34	0.547
NANOH	5.2	14.059	57.552	6.339	0.128	0.358	0.513
NANTF	2.392	21.063	34.411	5.049	0.119	0.421	0.459
NORTF	0.727	7.284	30.943	4.679	0.097	0.158	0.746
OCEAN	0.24	5.741	12.85	0.933	0.205	0.271	0.524
PATMH	0.64	16.967	12.7	2.807	0.13	0.291	0.578
PAXMH	0.323	12.665	7.602	1.057	0.214	0.324	0.461
PAXOH	0.752	16.774	13.363	2.268	0.162	0.339	0.499
PAXTF	0.961	20.343	16.356	2.481	0.165	0.444	0.392
PIAMH	0.486	11.429	7.81	1.11	0.224	0.32	0.457
PISTF	0.666	49.475	13.465	1.425	0.175	0.396	0.429
PMKOH	0.857	6.985	19.954	2.439	0.15	0.145	0.704
PMKTF	0.857	3.794	18.259	2.27	0.162	0.189	0.649
POCMH	0.943	6.36	18.821	1.723	0.198	0.203	0.599
POCOH	5.51	11.327	29.734	3.52	0.197	0.233	0.571
POCTF	8.606	12.181	22.441	2.379	0.288	0.307	0.405
POTMH	0.666	16.978	10.638	1.284	0.223	0.37	0.408
POTOH	0.666	14.925	32.582	2.762	0.131	0.169	0.701
POTTF	0.666	41.009	24.229	2.155	0.15	0.303	0.545
POVMH	0.666	19.259	10.207	1.256	0.223	0.37	0.408
RHDMH	0.734	16.248	20.621	2.583	0.132	0.284	0.585
RPPMH	0.596	13.388	18.323	1.865	0.16	0.266	0.573
RPPOH	0.596	11.713	51.322	4.078	0.098	0.163	0.738
RPPTF	0.596	13.147	40.266	3.067	0.104	0.207	0.689
SASOH	0.895	13.139	12.389	2.74	0.149	0.358	0.493
SBEMH	2.198	24.905	11.181	1.902	0.241	0.484	0.275
SEVMH	0.507	22.057	16.452	2.403	0.14	0.406	0.454
SOUMH	0.573	17.99	28.071	4.156	0.089	0.242	0.669
TA1MH	0.574	11.445	13.703	1.351	0.192	0.304	0.503
TANMH	0.574	11.263	13.128	1.312	0.202	0.269	0.53
WBEMH	1.004	15.128	10.435	1.515	0.208	0.338	0.455
WICMH	0.844	20.728	47.637	3.419	0.118	0.415	0.466
WSTMH	0.603	16.585	23.774	1.296	0.196	0.284	0.519
YRKMH	0.857	11.452	20.334	2.483	0.148	0.242	0.611
YRKPH	0.697	9.819	11.82	1.476	0.193	0.263	0.543
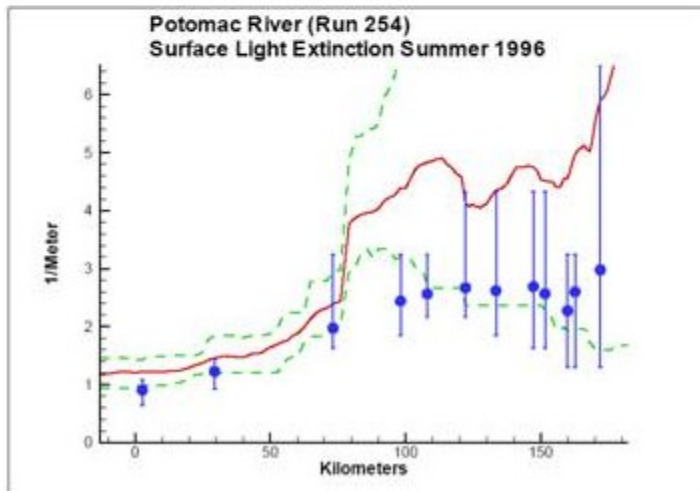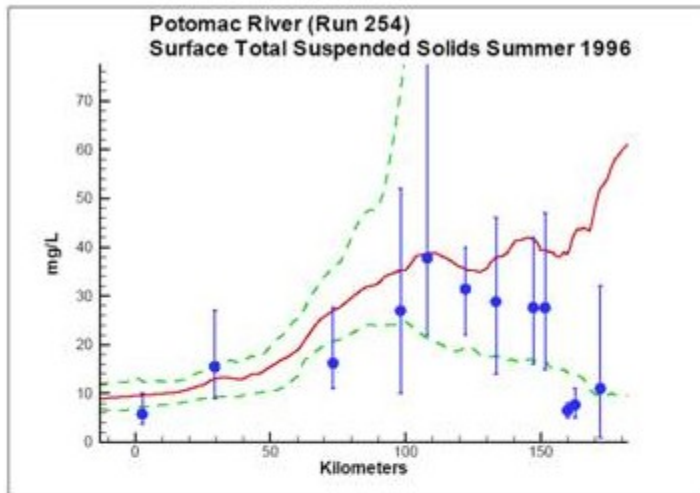
Figure 1. Example of a discontinuity due to parameter change and/or step change in look-up table. The computed value of Ke changes around km 75 even though the computed solids profile is continuous.
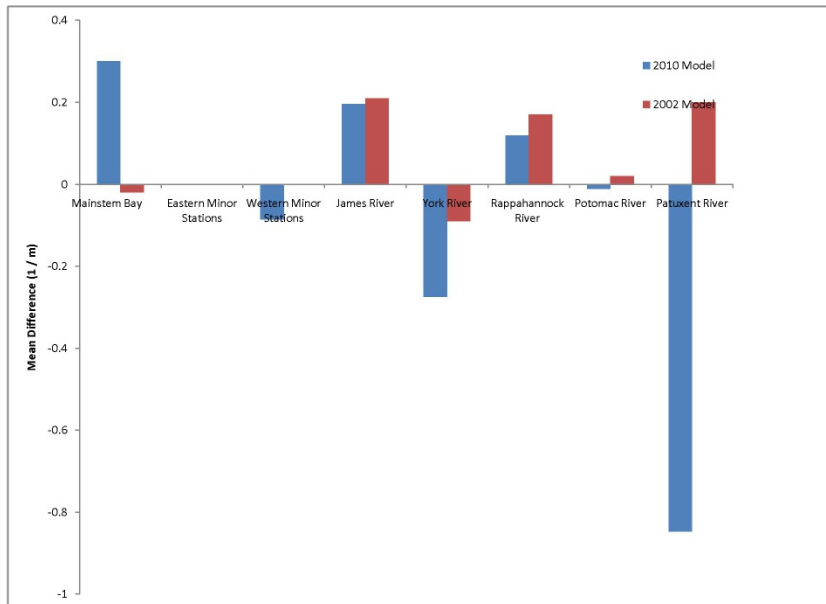
Figure 2. Mean Difference statistic for two model versions, 2002 and 2010. 2002 statistics were not computed for the eastern shore and western shore minor tributaries.
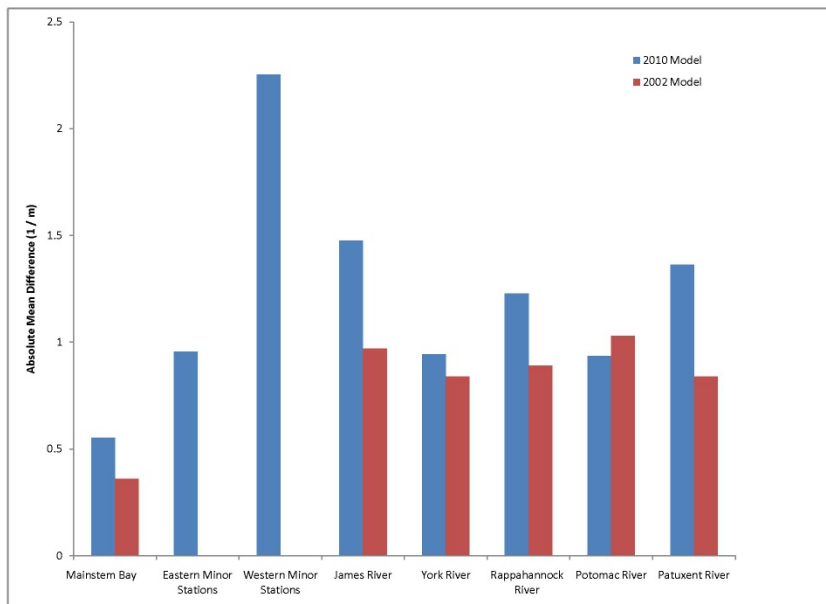
Figure 3. Absolute Mean Difference statistic for two model versions, 2002 and 2010.
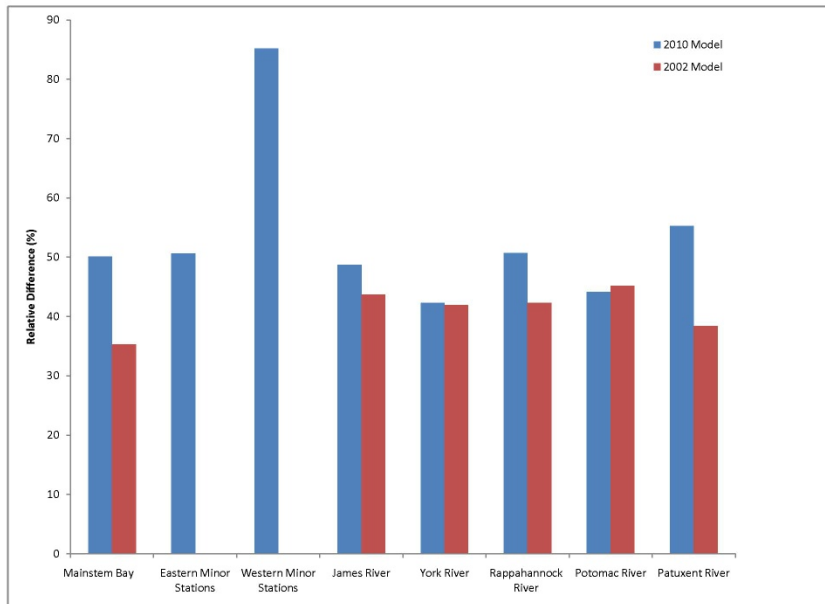
Figure 4. Relative Difference statistic for two model versions, 2002 and 2010.
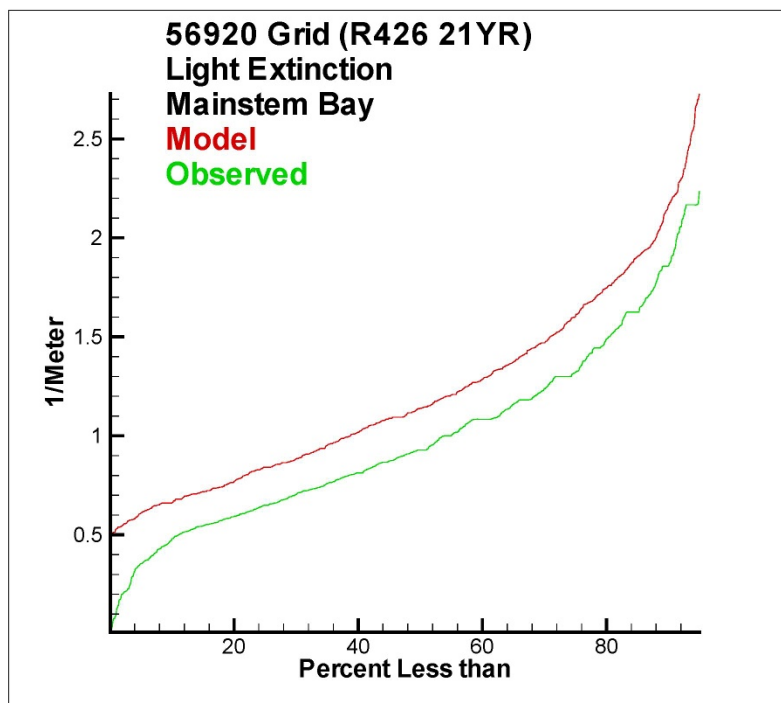
Figure 5. Cumulative distribution plot of observed and computed light attenuation for Chesapeake Bay stations.
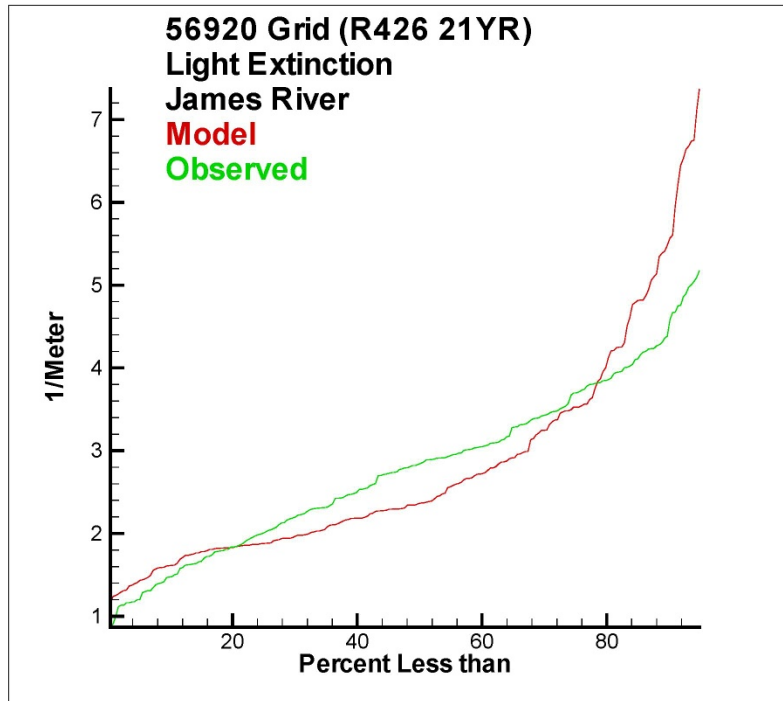
Figure 6. Cumulative distribution plot of observed and computed light attenuation for James River stations.
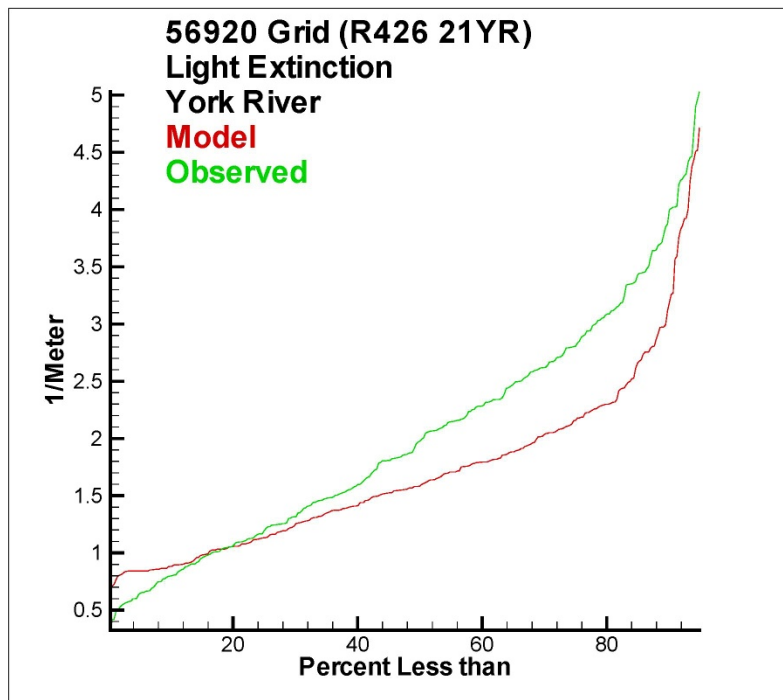
Figure 7. Cumulative distribution plot of observed and computed light attenuation for York River stations.
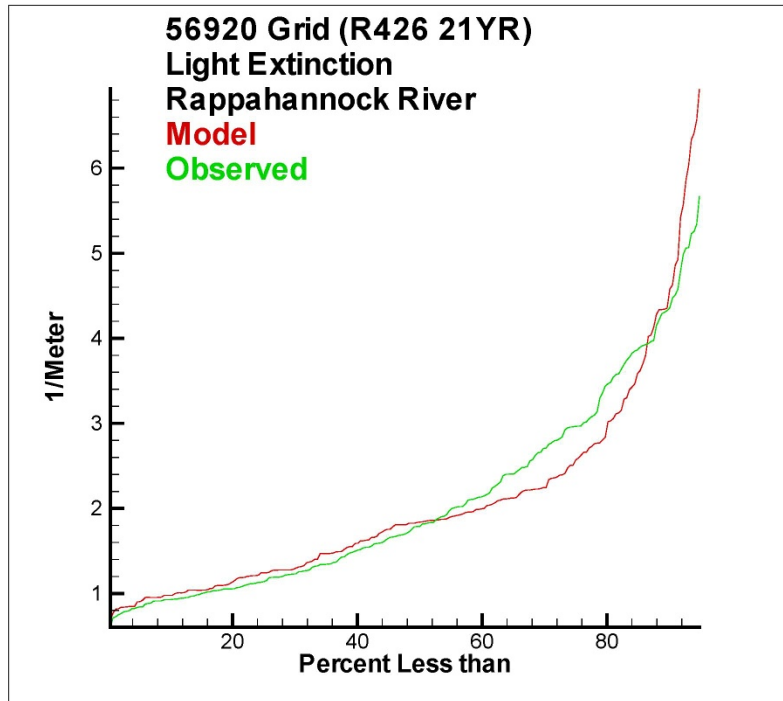
Figure 8. Cumulative distribution plot of observed and computed light attenuation for Rappahannock River stations.
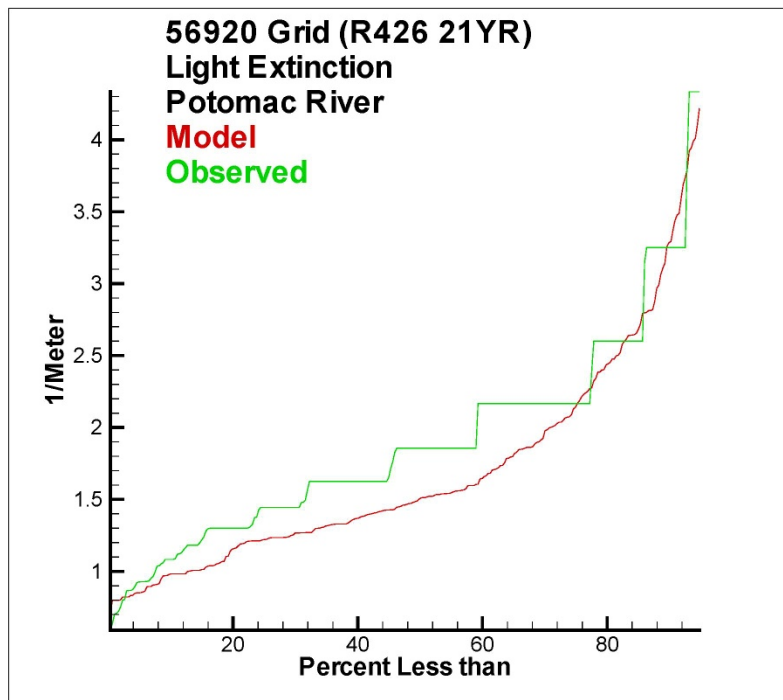
Figure 9. Cumulative distribution plot of observed and computed light attenuation for Potomac River stations.
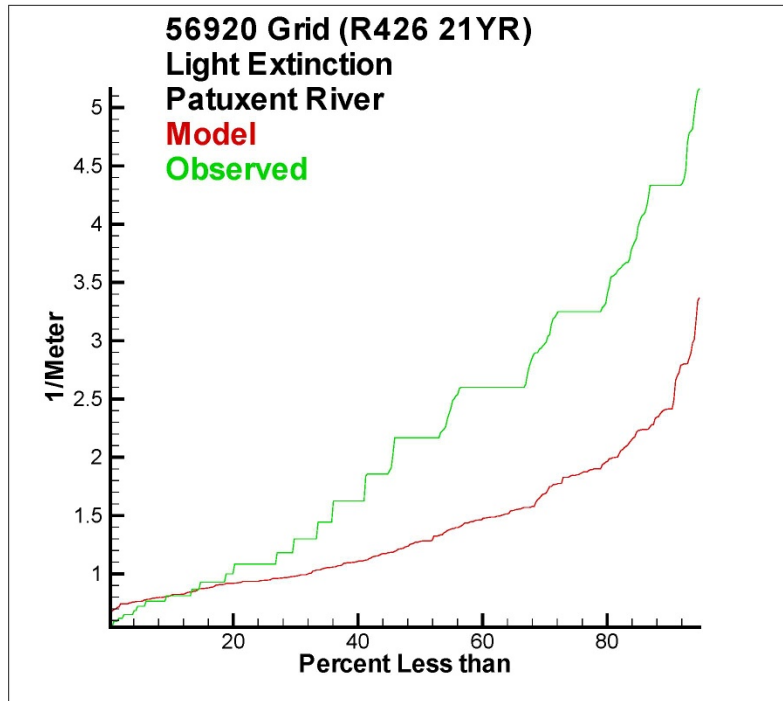
Figure 10. Cumulative distribution plot of observed and computed light attenuation for Patuxent River stations.
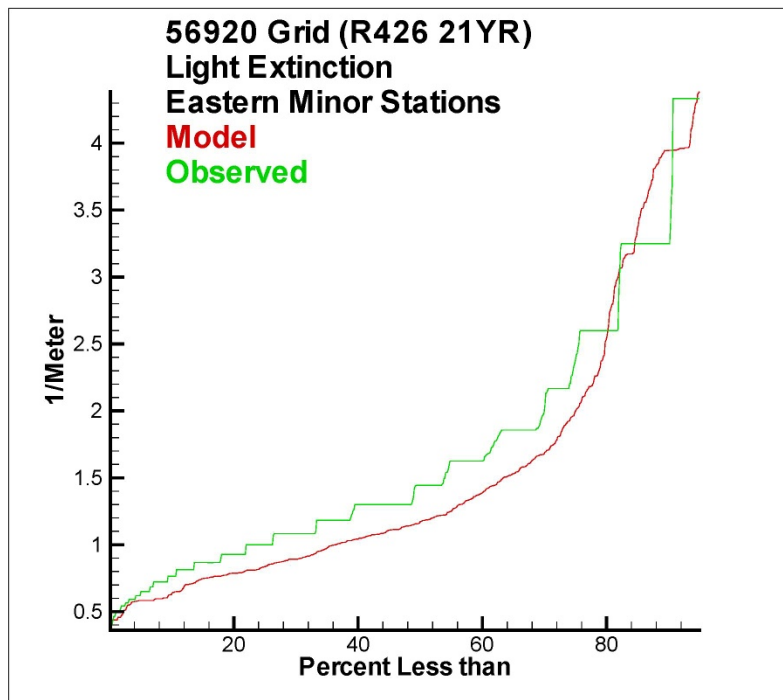
Figure 11. Cumulative distribution plot of observed and computed light attenuation for Eastern Shore minor tributary stations.
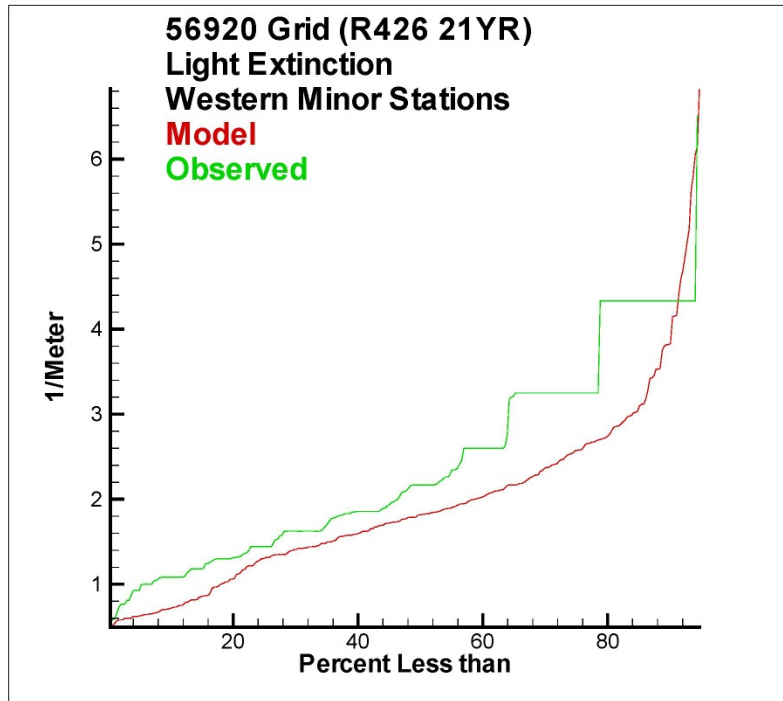
Figure 12. Cumulative distribution plot of observed and computed light attenuation for Western Shore minor tributary stations.
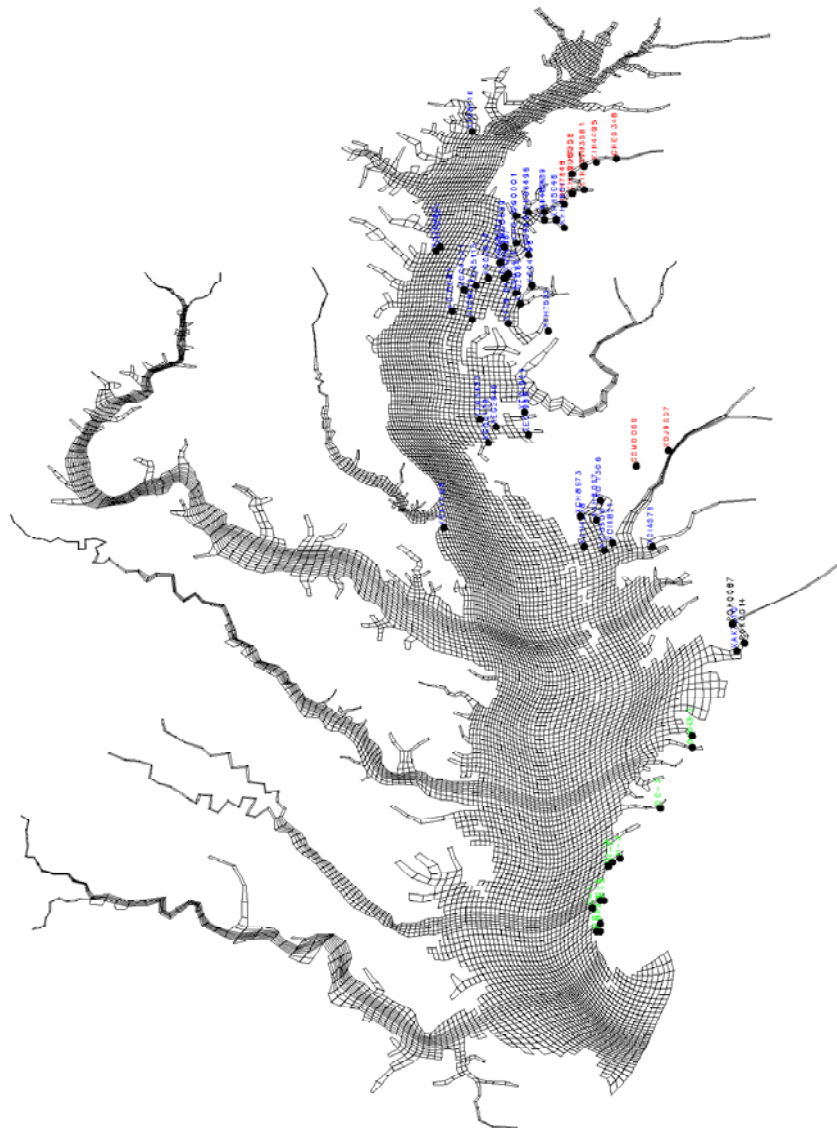
Figure 13. Shallow-water monitoring stations superimposed on model computational grid.
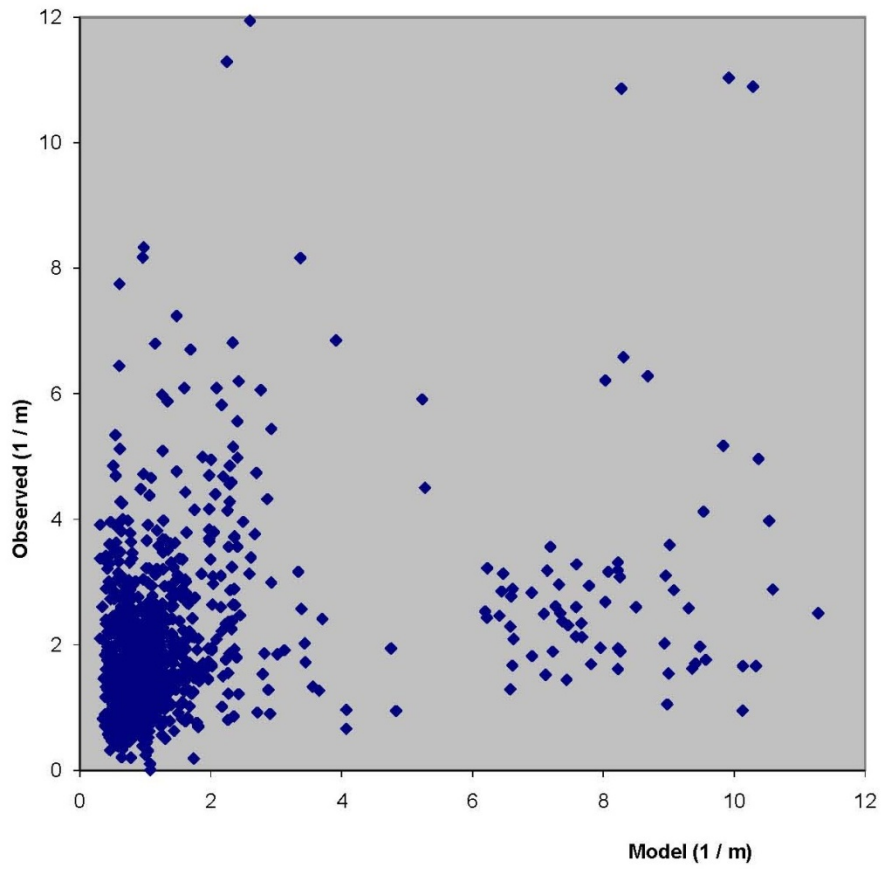
Figure 14. Scatter plot of observed and computed light attenuation from SWMP.
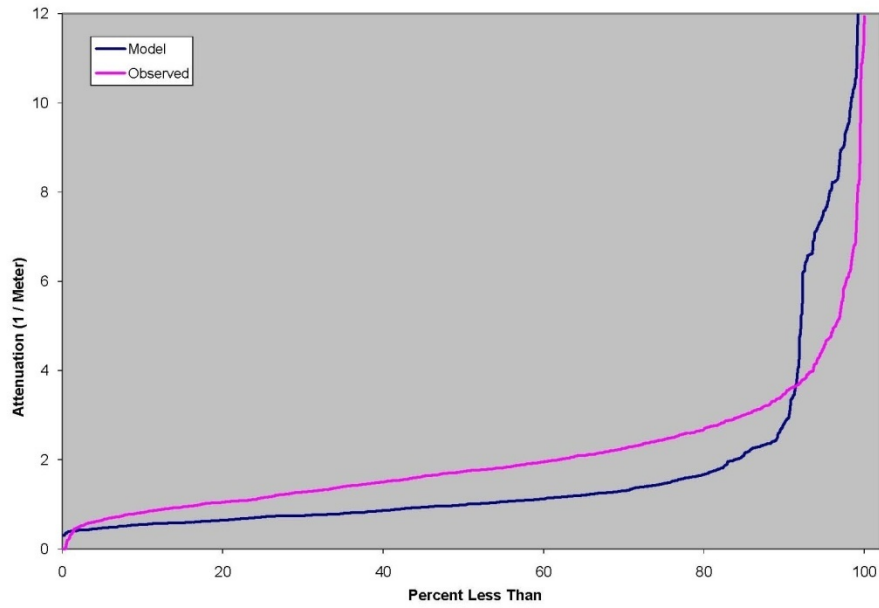
Figure 15. Cumulative distribution plot of observed and computed light attenuation from Shallow Water Monitoring Program.

9 Statistical Summary of Calibration

Introduction

The calibration of the model involved the comparison of hundreds of thousands of observations with model results in various formats. Comparisons involved conventional water quality data, process-oriented data, and living-resources observations. The graphical comparisons produced thousands of plots which cannot be assimilated in their entirety. Evaluation of model performance requires statistical and/or graphical summaries of results. We present summaries here for major water quality constituents in the mainstem bay and tributaries. Additional graphical comparisons are available in an appendix to this report.

Methods

No standard set of model performance statistics exists. We employ summary statistics that were developed as part of our initial Chesapeake Bay model study (Cerco and Cole 1994). Use of a consistent set of statistics facilitates comparisons with earlier model versions and with applications to other systems. Statistics computed were mean difference, absolute mean difference, and relative difference:

$$MD = \frac{\sum(P - O)}{N}$$

(1)

$$AMD = \frac{\sum|P - O|}{N}$$

(2)

$$RD = \frac{\sum|P - O|}{\sum O}$$

(3)

in which:

MD = mean difference
AMD = absolute mean difference
RD = relative difference
O = observation
P = prediction
N = number of observations

The mean difference describes whether the model over-estimates (MD > 0) or under-estimates (MD < 0) the observations, on average. The mean difference can attain its ideal value, zero, while discrepancies exist between individual observations and computations. The absolute mean difference is a measure of the characteristic difference between individual observations and computations. An absolute mean difference of zero indicates the model perfectly reproduces each observation. Relative difference is the absolute mean difference normalized by the mean of the observations.

Current Model Statistics

Quantitative statistics were determined using the same model-data pairs as in the time series plots. The stations and number of pairs depend on the system or station grouping (Table 1). In most cases, for stations classed as TF, ET, and WT, surface samples only were considered. Surface and bottom samples were considered for most RET and EE stations. Surface, mid-depth, and bottom samples were considered for most CB and LE stations. Statistics (Table 2) were calculated from samples collected during all seasons except for dissolved oxygen. Dissolved oxygen observations were restricted to summer only (June – August) to isolate the model performance during the critical time of year. Indication of model performance in deep water subject to hypoxia was isolated by elaborating dissolved oxygen statistics into three levels:

- Level I, Depth < 6.7m
- Level II, 6.7m < Depth < 12.8m
- Level III, 12.8m < Depth

The statistics alone provide little insight; comparisons within the current calibration and with previous calibrations provide grounds for interpreting the model behavior and the effects of various developments. The RD statistics lends itself well to these comparisons. Salinity and dissolved oxygen are the substances with the lowest RD (Figure 1). One interpretation of this performance is that these substances are largely influenced by physics and vary within limited ranges. Of course, neither can fall below zero. Within the bay system, salinity cannot exceed the oceanic value. Oxygen excursions above saturation concentration are rare. At the other extreme, chlorophyll and total suspended solids (TSS) exhibit the greatest RD. Computation of chlorophyll depends almost completely on biology and the range of potential values is unlimited. Rigorous computation of TSS is perhaps most difficult of all since the physics involved are not completely determined and biology has both known and unknown influences as well. Nitrogen, phosphorus, and light attenuation fall mid-way between the extremes of physically and biologically-determined substances.

The AMD for salinity is roughly equivalent in all systems (Table 2). Since salinity computation involves pure physics, this statistic suggests representation of physical processes in all systems is roughly equivalent. When the AMD is normalized to obtain RD, however, systems with lower mean salinity, such as the western shore tributaries, demonstrate higher RD.

The western shore tributaries (Bush, Gunpowder, Patapsco, and South Rivers) are distinguished by a shortfall in chlorophyll predictions (MD < -10 μg m^{-3}). Inspection of model outputs indicates these tributaries run out of inorganic nutrients before the observed chlorophyll concentrations of 50 to 100 μg m^{-3} can be attained by the model. The western shore tributaries also exhibit the greatest total nitrogen deficit (MD ≈ -0.12 g m^{-3}) of any grouping and a total phosphorus deficit. The origin of these nutrient shortfalls is not immediately apparent. The Potomac demonstrates high chlorophyll RD due to the difficulty in predicting algal blooms in the tidal fresh portion.

The mainstem bay exhibits the best absolute accuracy in total phosphorus predictions, as indicated by the AMD statistic. This statistic is higher and roughly equivalent in the remaining groupings. The RD statistic is influenced by the average observed values used to normalize the AMD; the eastern shore tributaries and the Rappahannock River demonstrate considerably higher total phosphorus RD than the other groupings. Distinctions are difficult to identify in the total nitrogen statistics although the mainstem bay is among the most accurate, as quantified by AMD, and the eastern and western shore tributaries are among the least accurate.

The statistics for TSS and light attenuation (Ke) exhibit a range of variation. Ke computations in the western shore tributaries are the least accurate, as determined by AMD. This statistic results from two influences. Computed solids and light attenuation in these systems are extremely "flashy." The computations (Figures 2, 3) resemble a comb function and are difficult to compare with instantaneous observations. We believe the shape of the computations is influenced by the loads from the adjacent watershed. A second influence, at several stations, is the reporting interval of disk visibility, which is inverted to calculate light attenuation. The continuous model values are difficult to relate to the banded observations. One trend in the statistics for TSS and Ke is that the systems with the greatest RD in TSS (western shore tributaries, Rappahannock River, mainstem bay) tend to have the greatest RD in Ke. The systems with the lowest RD for TSS (Potomac River, York River) have the lowest RD for Ke. This relationship emphasizes the close relationship between solids and light attenuation.

In most cases, the model computes surface dissolved oxygen (DO) concentrations which exceed observations (MD > 0) by as much as 2 g m^{-3}. We have noted that surface DO in the York and Patuxent Rivers is as low as 4 g m^{-3}. The origin of these low concentrations is unexplained and they are not modeled. The model computes sub-surface DO which is lower than observed in the eastern and western shore tributaries (MD < 0). Along the western shore, Level III DO is restricted to the Patapsco River. Along the eastern shore, the computed shortfalls are in the eastern bay. The James River, which is free from bottom-water hypoxia exhibits the most accurate sub-surface DO computations, as indicated by the DO AMD. Computations in the mainstem bay, which are based on multiple stations, are also among the most accurate. Due to the location of stations and to the selection process for statistical analysis, the statistics of bottom-water hypoxia in several tributaries are dependent on single stations. The statistics for these systems (e.g. the Potomac) reflect lower accuracy and higher RD that for the systems with statistics based on multiple stations.

Comparison with Previous Versions

For comparison, summary statistics were retrieved from three previous model versions: the original Chesapeake Bay Model (Cerco and Cole 1994), the Virginia Tributary Refinements (Cerco et al. 2002), and the 2002 model (Cerco and Noel 2004). Caution is required in comparing the statistics (Tables 3, 4) since the model periods differ as well as the number of stations and observations. Still the comparisons, especially the RD statistic, provide insights into the successive model developments.

The RD for salinity in the mainstem bay (Table 4) has been stationary since the first model version while the salinity RD for the western tributaries is now the best ever. One interpretation of these trends is that the grid refinements subsequent to the original segmentation have done little to improve the physical representation of the mainstem channel regions while improved resolution has improved the channel regions of the major tributaries.

The chlorophyll, total nitrogen, and total phosphorus RD's have varied over 20 years but show no trend or significant difference among model versions. In one sense, this is not surprising since the model algorithms that describe these substances have changed little since the original application. The absence of a trend also suggests that the representation of these substances is not significantly impacted by model resolution. We speculate that improvement awaits the development and application of a truly different conceptual model. (We do not advocate application of the same concepts expressed in a different code).

The interpretation of the DO statistics requires some caution. The statistics through the 2002 model version were based on summer, bottom, DO, regardless of the depth of the bottom. The 2010 model statistics are based on summer DO in Level III (depth > 12.8 m). In the current configuration, the Level III DO statistic for the Potomac River is based on one station, LE2.2. Previously, the bottom DO statistic for the Potomac was derived from multiple stations. The apparent deterioration of bottom DO computations in the Potomac results, at least in part, from this change in statistical basis. The Rappahannock is subject to this same failing. In the mainstem, multiple stations are included in both the bottom DO and Level III DO statistics so the RD here is likely reliable and the system shows little change since 2002. The James does not exhibit hypoxia. As noted previously, the sub-surface DO computations for 2010 are superior to other systems in the 2010 model. So the apparent improvement in the James DO computation in this model version, compared to earlier versions, is genuine. No trend is apparent in the York or Patuxent.

No improvement is noted in light attenuation in this model version. In fact, in all cases for which statistics are available, RD has increased over the original 4,000-cell model. In several cases, RD is greater than in 2002. This result seems disappointing in view of the effort devoted to the suspended solids model and to the advanced optical model. In this case, we have traded realism for accuracy, a trade-off that has been previously noted (Cerco and Noel 2005). Light attenuation in the original model was derived from observations and, in

some cases, from regression relationships to runoff. Little or no predictive capability was available. Subsequent versions of the model added predictive capability, especially with regards to solids (Cerco and Noel 2002, 2004). Following the solids computation, the partial attenuation model in these earlier versions was tuned to improve calculation of light attenuation. In the present model stage, both the TSS and optical models are the most rigorous available although the computations are not as accurate as previously. Improvement awaits model developments but also improvements in observations. Optical model parameters are unavailable in all portions of the system and Ke is still derived from disk visibility in some regions.

Graphical Performance Summaries

Our graphical summaries are in the form of cumulative distribution plots (Figures 4 – 59). Creation of the plots first requires pairing in space and time of observations and computations. These were from the same stations used in the statistical summaries. (The dissolved oxygen graphical summaries include surface and sub-surface samples throughout the year.) Observations were paired with daily average computations in the cell corresponding to sample location and depth. Next, the observations and computations were individually sorted from smallest to largest. The sorted arrays were divided into quantiles and plotted as cumulative distributions. A point on the line in x-y space indicates the percentage of observations or computations (y-axis) less than the indicated concentration (x-axis). The 50th percentile indicates the median value. Perfect correspondence in the range of computed and observed variables is indicated when the cumulative distribution of modeled values exactly overlays the cumulative distribution of observed values.

References

Cerco, C.F. and Cole, T. M. (1994). "Three-dimensional eutrophication model of Chesapeake Bay," Technical Report EL-94-4, U.S. Army Engineer Waterways Experiment Station, Vicksburg MS.

Cerco, C., Johnson, B., and Wang, H. (2002). "Tributary refinements to the Chesapeake Bay model," ERDC TR-02-4, US Army Engineer Research and Development Center, Vicksburg, MS.

Cerco, C., and Noel, M. (2004). "The 2002 Chesapeake Bay eutrophication model," EPA 903-R-04-004, Chesapeake Bay Program Office, US Environmental Protection Agency, Annapolis MD. (available at http://www.chesapeakebay.net/modsc.htm)

Cerco, C., and Noel, M. (2005). "Incremental improvements in Chesapeake Bay Environmental Model Package," *Journal of Environmental Engineering* 131(5), 745-754.

Table 1
Stations and Observations in Statistical Summary

Grouping	Stations	Salinity Obs.	Chlorophyll Obs.	Total Nitrogen Obs.	Total Phosphorus Obs.	Dissolved Oxygen Obs.	Total Susp. Solids Obs.
Chesapeake Bay	CB1.1, CB2.2, CB3.3C, CB4.2, CB5.2, CB6.1, CB7.3, CB7.4, CB7.4N, CB8.1E, EE3.1, EE3.2	5811	5695	5657	5738	1703	5757
James River	TF5.5, RET5.2, LE5.3	823	831	465	812	214	802
York River	TF4.2, RET4.3, LE4.2, WE4.2	1153	1134	754	1114	294	1138
Rappahannock River	TF3.3, RET3.2, LE3.2	844	822	472	820	201	831
Potomac River	TF2.1, RET2.4, LE2.2	1097	1068	1036	1083	299	1094
Patuxent River	TF1.7, RET1.1, LE1.3	1190	1166	1188	1188	312	1183
Eastern Shore Tributaries	EE1.1, EE2.1, ET1.1, ET3.2, ET4.2, ET5.2, ET6.2, ET9.1	1886	1832	1762	1848	498	1866
Western Shore Tributaries	WT1.1, WT2.1, WT5.1, WT8.1	904	870	838	888	246	898

Table 2
Statistical Summary

Salinity	Bay	Eastern Shore Tribs	Western Shore Tribs	James	York	Rappahannock	Potomac	Patuxent
MD, ppt	-0.01	0.18	-0.78	-1.14	-0.64	-0.26	0.72	0.45
AMD, ppt	1.83	1.11	1.30	1.55	1.39	1.33	1.22	1.15
RD, %	10.2	10.6	19.2	17.2	9.5	12.0	13.6	11.3
Chlorophyll	Bay	Eastern Shore Tribs	Western Shore Tribs	James	York	Rappahannock	Potomac	Patuxent
MD, $\mu g\ m^{-3}$	-0.34	-0.63	-10.16	-0.78	-2.22	1.98	3.95	2.44
AMD, $\mu g\ m^{-3}$	3.86	7.63	14.40	7.24	5.25	6.84	11.53	9.45
RD, %	53.6	67.0	66.0	61.7	55.7	70.7	98.4	76.7
Total Nitrogen	Bay	Eastern Shore Tribs	Western Shore Tribs	James	York	Rappahannock	Potomac	Patuxent
MD, $g\ m^{-3}$	-0.09	-0.09	-0.12	0.09	-0.07	0.07	-0.09	-0.04
AMD, $g\ m^{-3}$	0.18	0.37	0.36	0.23	0.18	0.17	0.35	0.19
RD, %	25.9	40.0	28.0	31.7	29.6	26.5	26.9	23.0
Total Phosphorus	Bay	Eastern Shore Tribs	Western Shore Tribs	James	York	Rappahannock	Potomac	Patuxent
MD, $g\ m^{-3}$	0.005	0.010	-0.014	-0.011	-0.021	0.024	0.003	-0.006
AMD, $g\ m^{-3}$	0.017	0.037	0.036	0.046	0.031	0.045	0.034	0.036
RD, %	41.4	71.0	48.7	45.1	40.8	72.4	46.5	48.0
Total Susp. Solids	Bay	Eastern Shore Tribs	Western Shore Tribs	James	York	Rappahannock	Potomac	Patuxent
MD, $g\ m^{-3}$	3.80	-5.16	-2.77	-9.36	-11.74	3.02	-0.92	-2.86
AMD, $g\ m^{-3}$	13.66	12.03	13.99	27.49	18.46	16.31	14.84	11.43
RD, %	75.3	65.0	84.5	67.2	61.5	75.3	64.0	65.2
Light Attenuation	Bay	Eastern Shore Tribs	Western Shore Tribs	James	York	Rappahannock	Potomac	Patuxent
MD, m-1	0.3	0	-0.09	0.2	-0.28	0.12	-0.01	-0.85
AMD, m-1	0.55	0.96	2.25	1.48	0.94	1.23	0.93	1.36
RD, %	50.1	50.6	85.2	48.7	42.3	50.7	44.1	55.3
DO Level I	Bay	Eastern Shore Tribs	Western Shore Tribs	James	York	Rappahannock	Potomac	Patuxent
MD, $g\ m^{-3}$	-0.14	0.78	0.41	1.67	1.62	0.95	1.36	2.15
AMD, $g\ m^{-3}$	0.85	1.32	1.48	1.96	1.84	1.19	1.86	2.39
RD, %	11.2	18.4	17.9	27.6	31.0	18.0	25.8	42.0
DO Level II	Bay	Eastern Shore Tribs	Western Shore Tribs	James	York	Rappahannock	Potomac	Patuxent
MD, $g\ m^{-3}$	0.30	-1.46	-1.87	0.59	0.89	0.91	0.97	-0.83
AMD, $g\ m^{-3}$	0.94	2.74	1.96	0.93	1.11	1.85	1.85	2.28
RD, %	19.4	41.1	26.2	14.7	22.9	38.7	102.3	50.9
DO Level III	Bay	Eastern Shore	Western Shore	James	York	Rappahannock	Potomac	Patuxent

		Tribs	Tribs					
MD, g m^{-3}	-0.45	-0.66	-3.37	0.76	-1.13	1.30	1.38	0.89
AMD, g m^{-3}	1.19	1.10	3.42	0.84	1.53	1.59	1.58	1.28
RD, %	28.7	32.4	64.1	14.1	34.9	102.9	384.9	30.2

Table 3
Mean Difference in Four Model Phases

Salinity, ppt	Mainstem	James	York	Rappahannock	Potomac	Patuxent
Original	0.06	0.95	-0.08	-2.43		
VA Tributaries	0.62	-0.55	0.94	1.64		
2002 Model	-1.69	-0.32	-1.68	-1.14	-0.45	-0.16
2010 Model	-0.01	-1.14	-0.64	-0.26	0.72	0.45

Chlorophyll, ug m^{-3}	Mainstem	James	York	Rappahannock	Potomac	Patuxent
Original	1.59	-0.24	1.19	-0.54		
VA Tributaries	1.19	4.84	1.66	-2.25		
2002 Model	0.32	2.47	1.46	0.14	1.85	1.53
2010 Model	-0.34	-0.78	-2.22	1.98	3.95	2.44

Light Attenuation, m^{-1}	Mainstem	James	York	Rappahannock	Potomac	Patuxent
Original	0.146	0.329	-0.021	0.169		
VA Tributaries	0.206	0.425	-0.222	0.599		
2002 Model	-0.065	-0.009	-0.125	-0.135	0.02	0.2
2010 Model	0.299	0.195	-0.275	0.119	-0.011	-0.847

Total Nitrogen, g m^{-3}	Mainstem	James	York	Rappahannock	Potomac	Patuxent
Original	0.003	-0.108	-0.057	-0.197		
VA Tributaries	-0.011	0.174	-0.092	-0.128		
2002 Model	-0.025	0.205	-0.004	-0.098	-0.32	0.13
2010 Model	-0.092	0.088	-0.069	0.066	-0.095	-0.037

Total Phosphorus, g m^{-3}	Mainstem	James	York	Rappahannock	Potomac	Patuxent
Original	-0.012	0.0077	-0.0146	-0.0265		
VA Tributaries	-0.0091	0.0456	-0.0149	-0.0043		
2002 Model	-0.0115	0.0534	0.0025	0.0008	-0.032	-0.041
2010 Model		-0.0111	-0.0207	0.0239	0.0027	-0.0062

Summer, Bottom DO, g m^{-3}	Mainstem	James	York	Rappahannock	Potomac	Patuxent
Original	0.89	1.88	0.48	2.96		
VA Tributaries	-0.58	-0.26	0.08	-0.81		
2002 Model	0.03	0.53	-0.4	-0.72	1.31	0.92
2010 Model	-0.45	0.76	-1.13	1.3	1.38	0.89

Table 4
Relative Difference (%) in Four Model Phases

Salinity	Mainstem	James	York	Rappahannock	Potomac	Patuxent
Original	9.1	19.1	17.4	24		
VA Tributaries	9.5	19.4	11.6	18.3		
2002 Model	13.1	25.4	15.6	16.5	22.5	17.5
2010 Model	10.2	17.2	9.5	12.0	13.6	11.3
Chlorophyll	**Mainstem**	**James**	**York**	**Rappahannock**	**Potomac**	**Patuxent**
Original	61.6	74.1	64	83.4		
VA Tributaries	57.6	78.6	66.2	64.8		
2002 Model	59.2	66.4	49.1	70.8	80.2	65.4
2010 Model	53.6	61.7	55.7	70.7	98.4	76.7
Light Attenuation	**Mainstem**	**James**	**York**	**Rappahannock**	**Potomac**	**Patuxent**
Original	36.5	32.6	39.9	32.8		
VA Tributaries	45.2	59.8	46.6	57.6		
2002 Model	38.5	39.7	44	41	45.2	38.4
2010 Model	50.1	48.7	42.3	50.7	44.1	55.3
Total Nitrogen	**Mainstem**	**James**	**York**	**Rappahannock**	**Potomac**	**Patuxent**
Original	22.1	31.9	20.8	32.5		
VA Tributaries	21.3	46	20.4	31.9		
2002 Model	21.9	48.5	28.1	28.6	31.9	41.5
2010 Model	25.9	31.7	29.6	26.5	26.9	23.0
Total Phosphorus	**Mainstem**	**James**	**York**	**Rappahannock**	**Potomac**	**Patuxent**
Original	42.5	49.3	41	53.4		
VA Tributaries	38.5	67.9	43.9	41.2		
2002 Model	41.5	78.3	47	41.3	58.9	47.6
2010 Model	41.4	45.1	40.8	72.4	46.5	48.0
Summer, bottom DO	**Mainstem**	**James**	**York**	**Rappahannock**	**Potomac**	**Patuxent**
Original	44.9	31.7	41.4	63.9		
VA Tributaries	31.6	38.1	25.9	46.6		
2002 Model	27.9	40.5	22.7	32.2	40.5	39.3
2010 Model	28.7	14.1	34.9	102.9	384.9	30.2
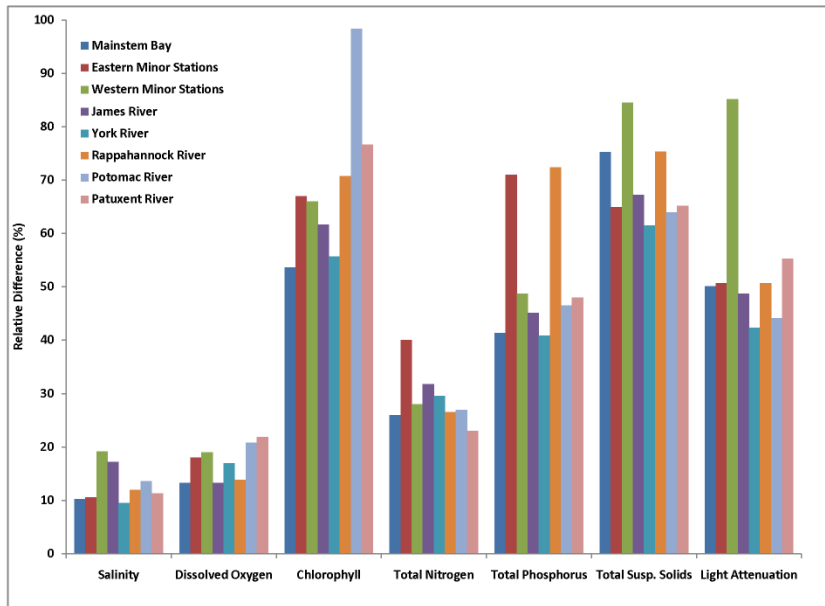
Figure 1. The relative difference statistic for key model constituents. Note that dissolved oxygen is summarized at all levels and seasons.
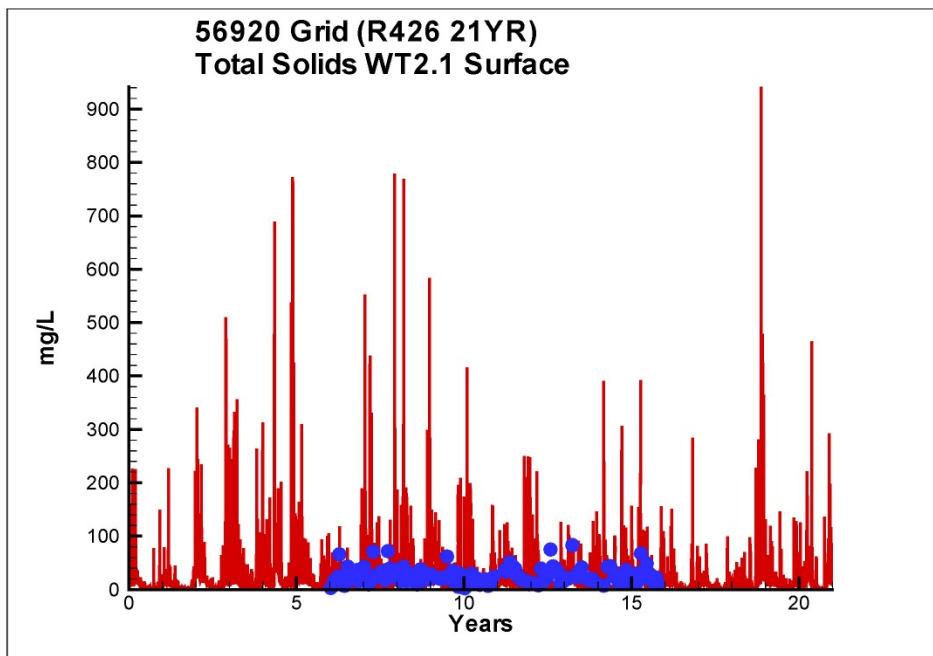
Figure 2. Computed and observed total suspended solids in the Gunpowder River. Note the "comb-like" nature of the computations.
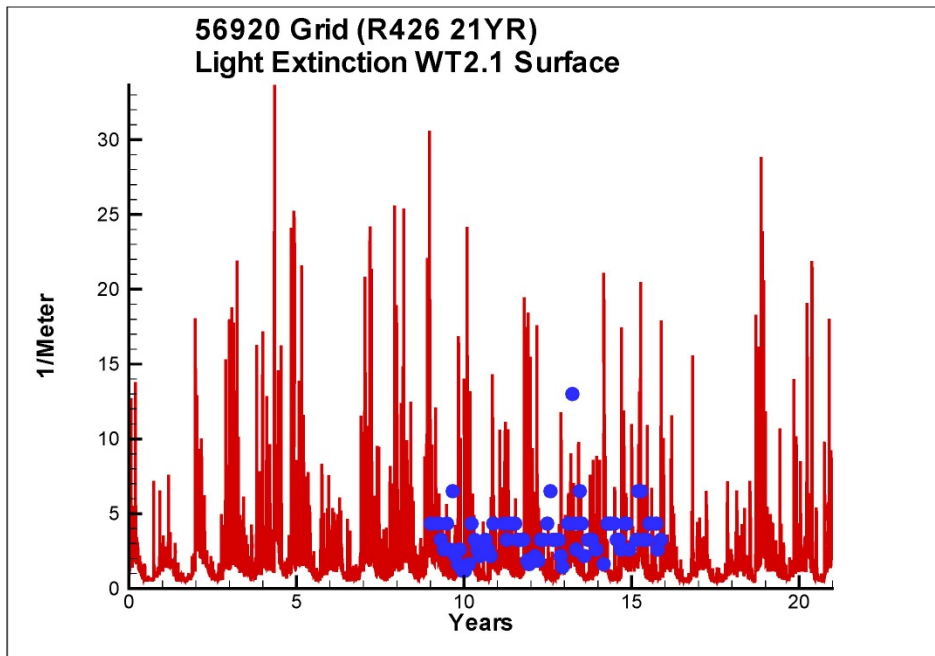
Figure 3. Computed and observed light attenuation in the Gunpowder River. Comparisons are affected by the "flashy" nature of the model and by the reporting interval of disk visibility (which is subsequently converted to light attenuation).
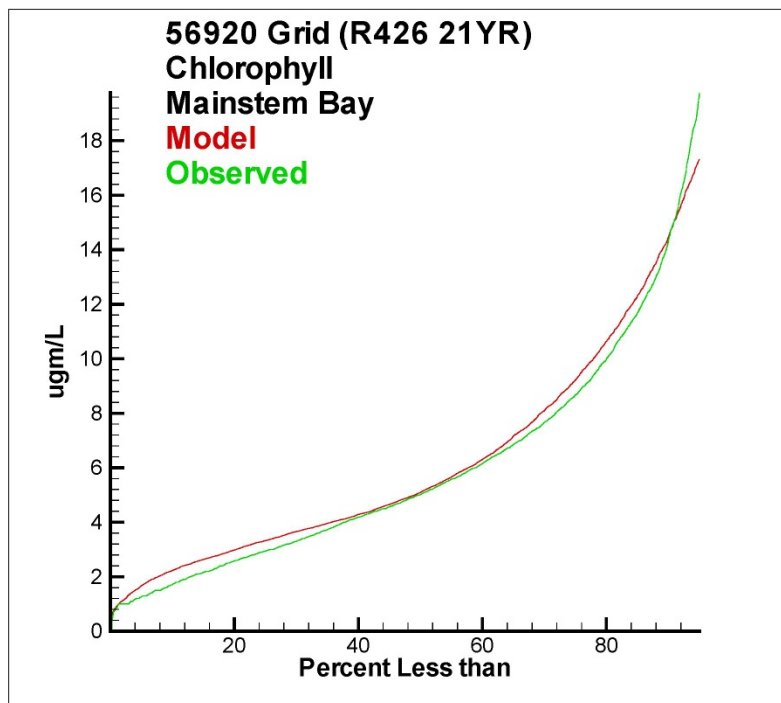
Figure 4. Cumulative distribution plot for observed and computed chlorophyll in the mainstem bay.
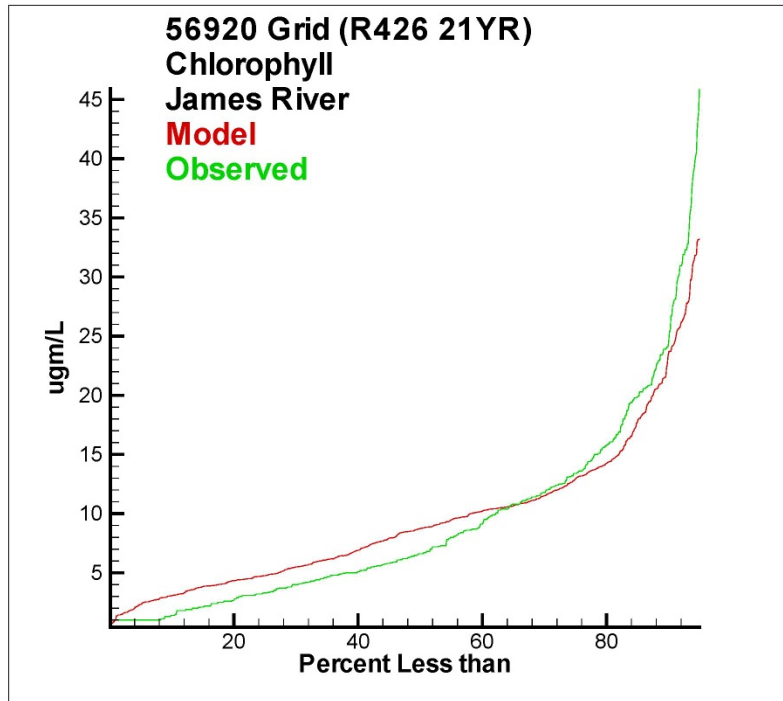
**Figure 5. Cumulative distribution plot for observed and computed chlorophyll in the James River.**
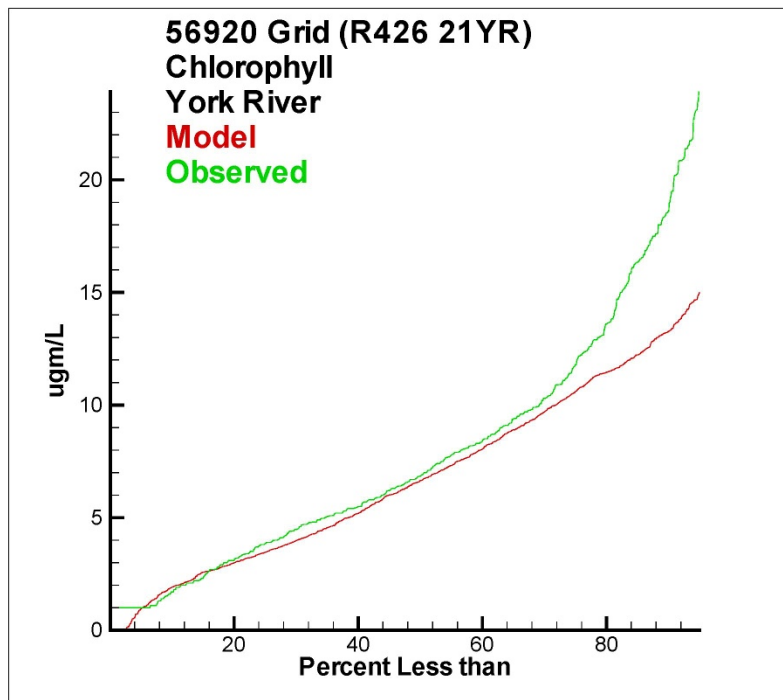
Figure 6. Cumulative distribution plot for observed and computed chlorophyll in the York River.
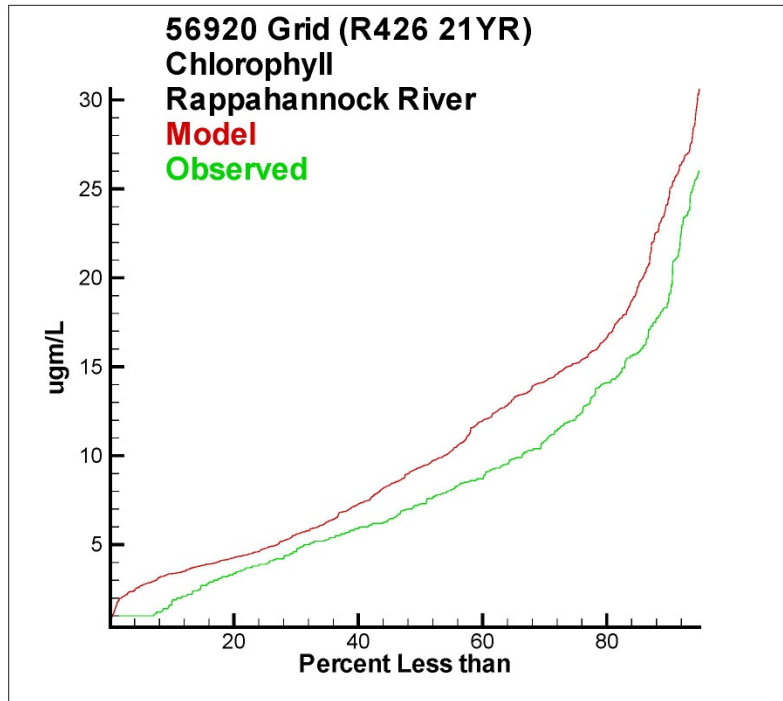
Figure 7. Cumulative distribution plot for observed and computed chlorophyll in the Rappahannock River.
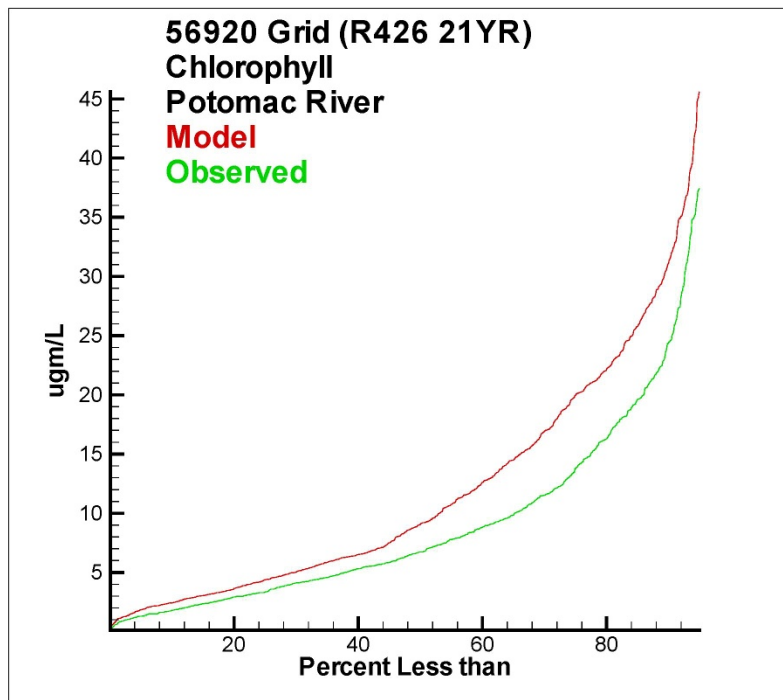
Figure 8. Cumulative distribution plot for observed and computed chlorophyll in the Potomac River.
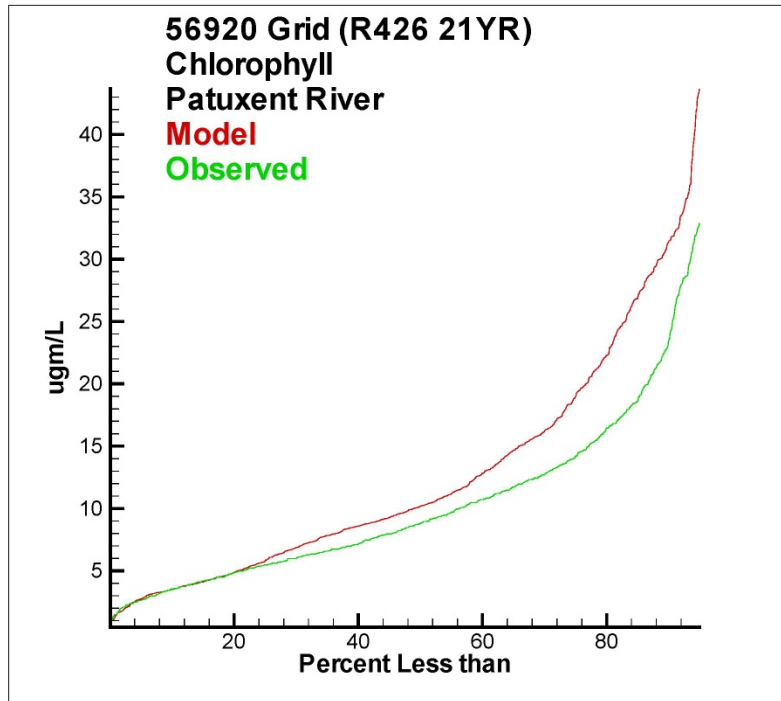
Figure 9. Cumulative distribution plot for observed and computed chlorophyll in the Patuxent River.
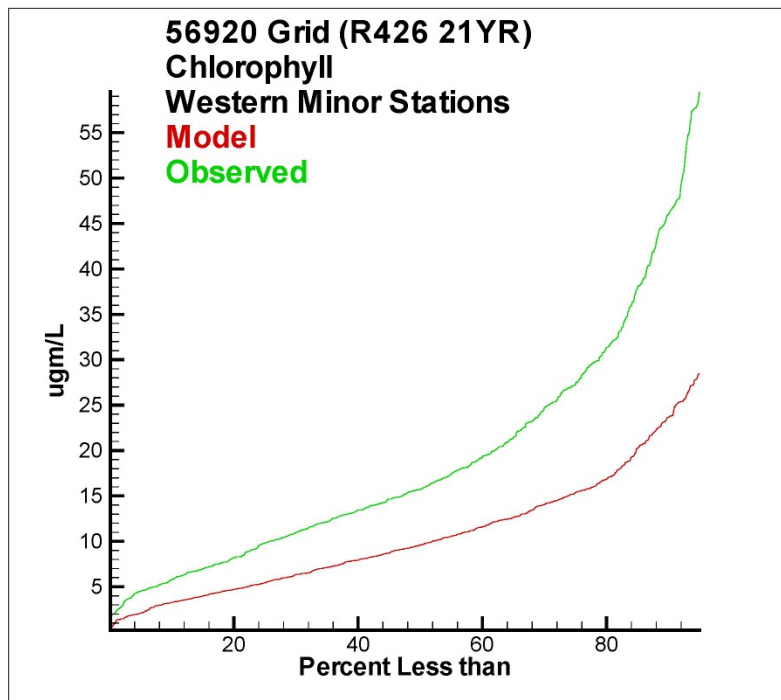
Figure 10. Cumulative distribution plot for observed and computed chlorophyll in the western shore tributaries.
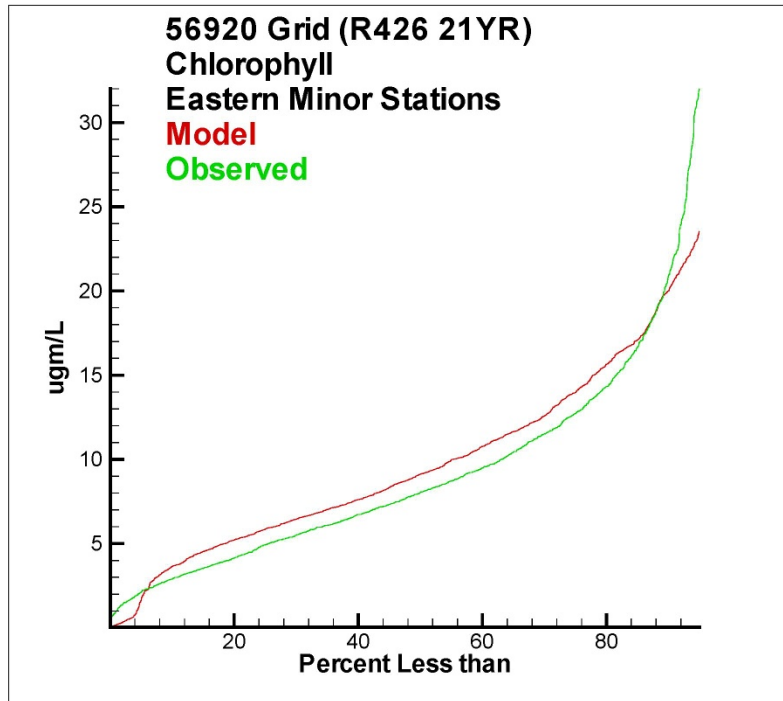
Figure 11. Cumulative distribution plot for observed and computed chlorophyll in the eastern shore tributaries.
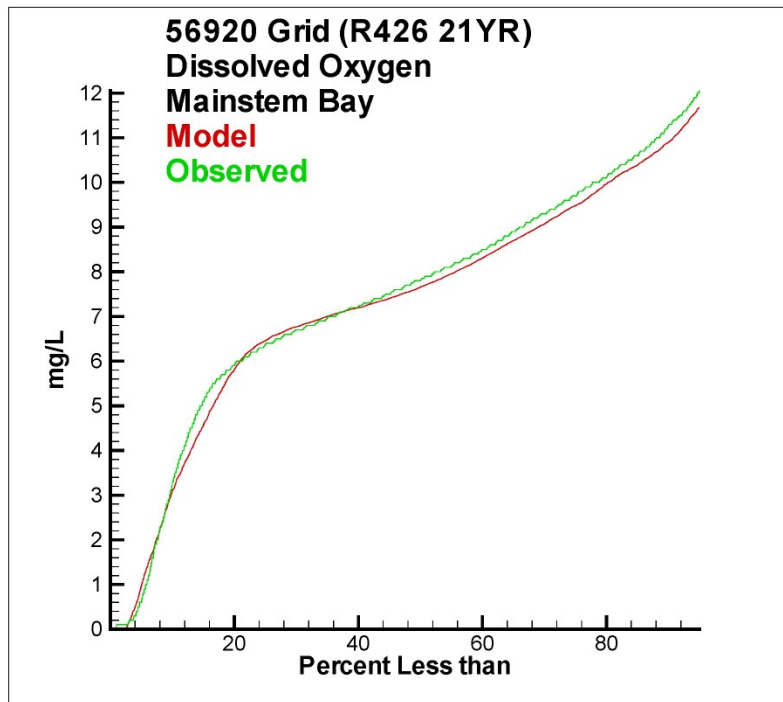
**Figure 12. Cumulative distribution plot for observed and computed dissolved oxygen in the mainstem bay.**
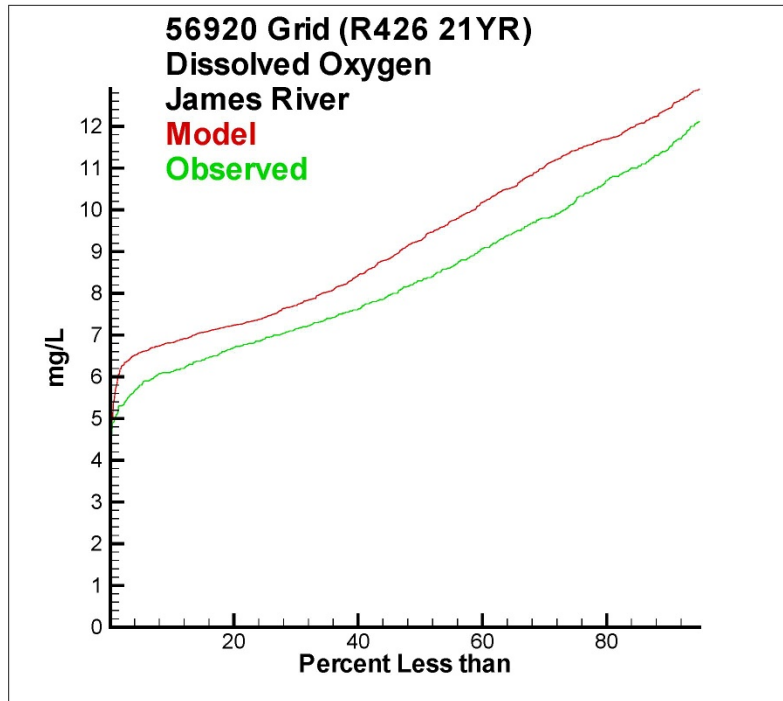
Figure 13. Cumulative distribution plot for observed and computed dissolved oxygen in the James River.
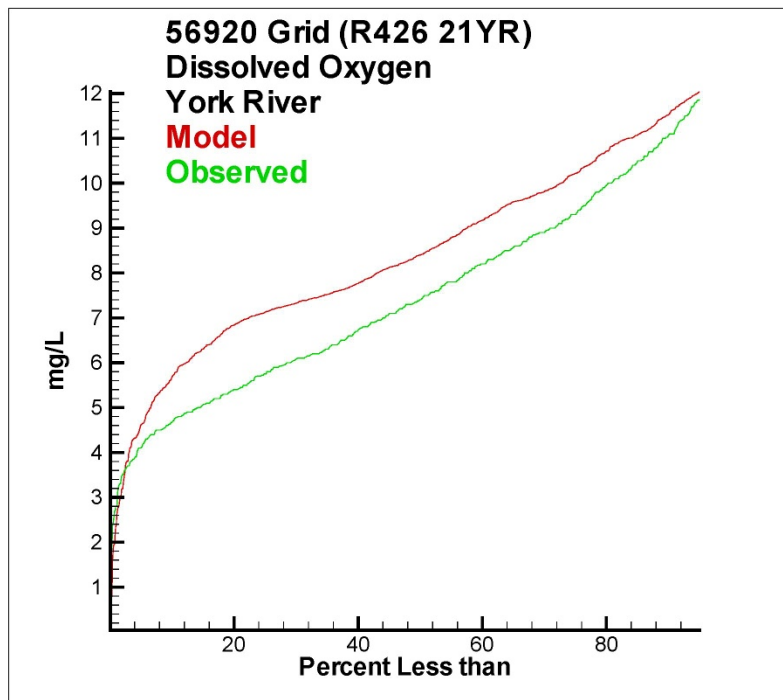
Figure 14. Cumulative distribution plot for observed and computed dissolved oxygen in the York River.
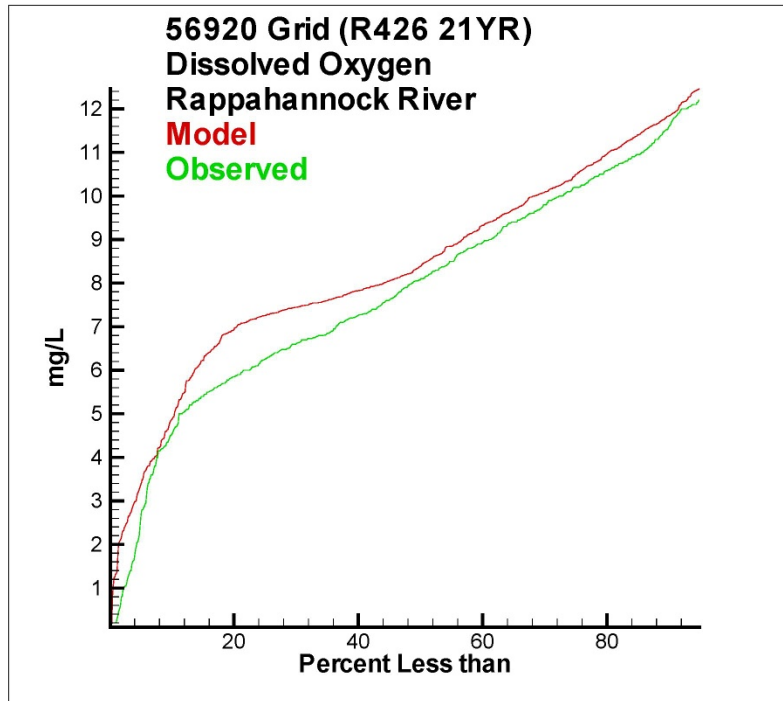
Figure 15. Cumulative distribution plot for observed and computed dissolved oxygen in the Rappahannock River.
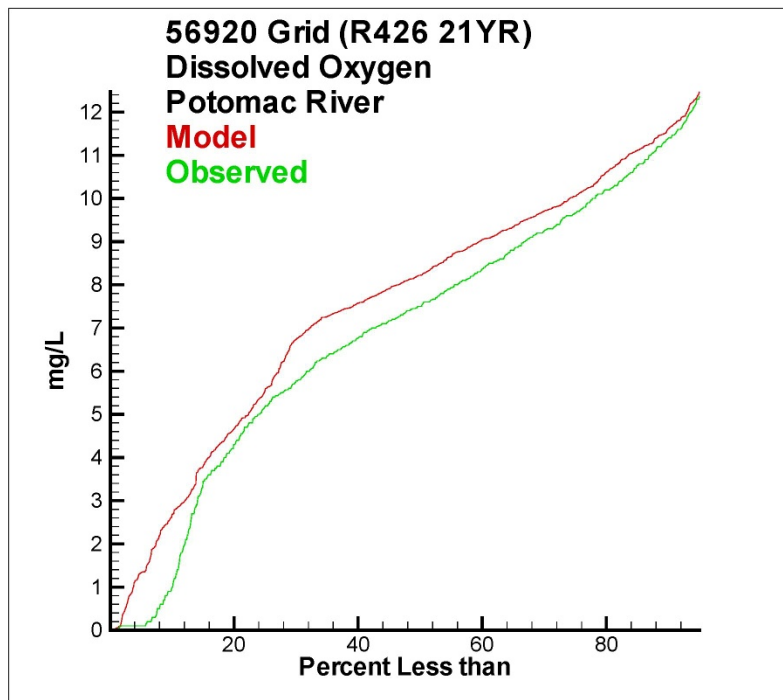

Figure 16. Cumulative distribution plot for observed and computed dissolved oxygen in the Potomac River.
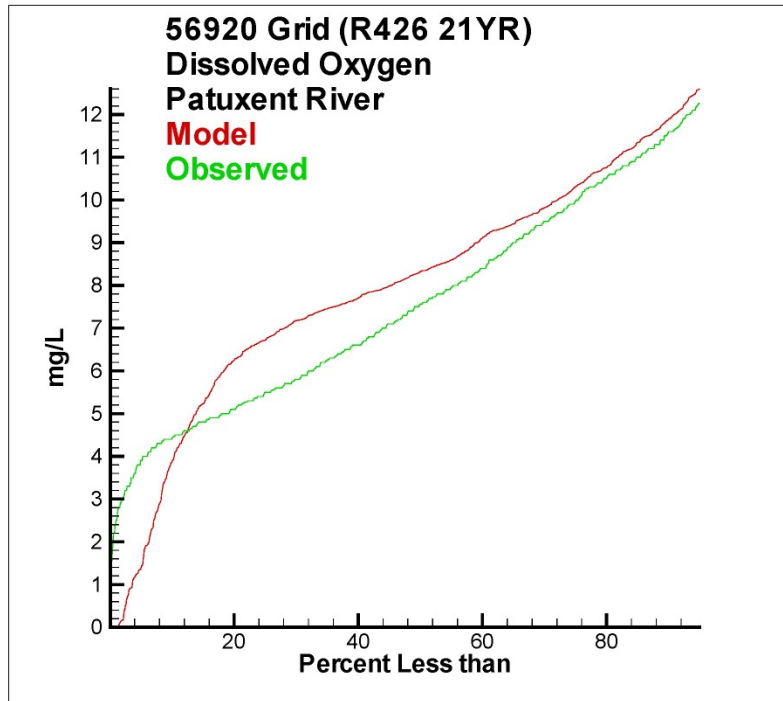
Figure 17. Cumulative distribution plot for observed and computed dissolved oxygen in the Patuxent River.
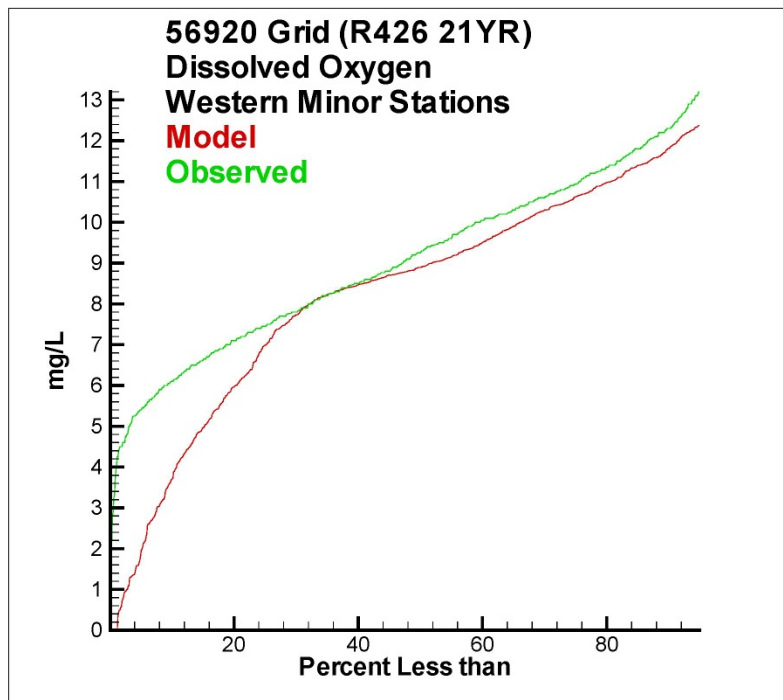

Figure 18. Cumulative distribution plot for observed and computed dissolved oxygen in the western shore tributaries.
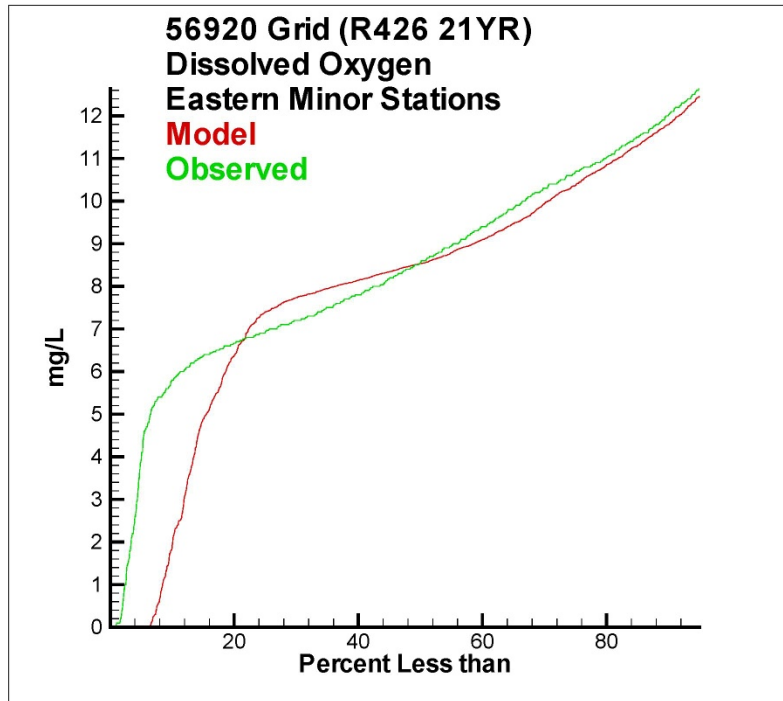
Figure 19. Cumulative distribution plot for observed and computed dissolved oxygen in the eastern shore tributaries.
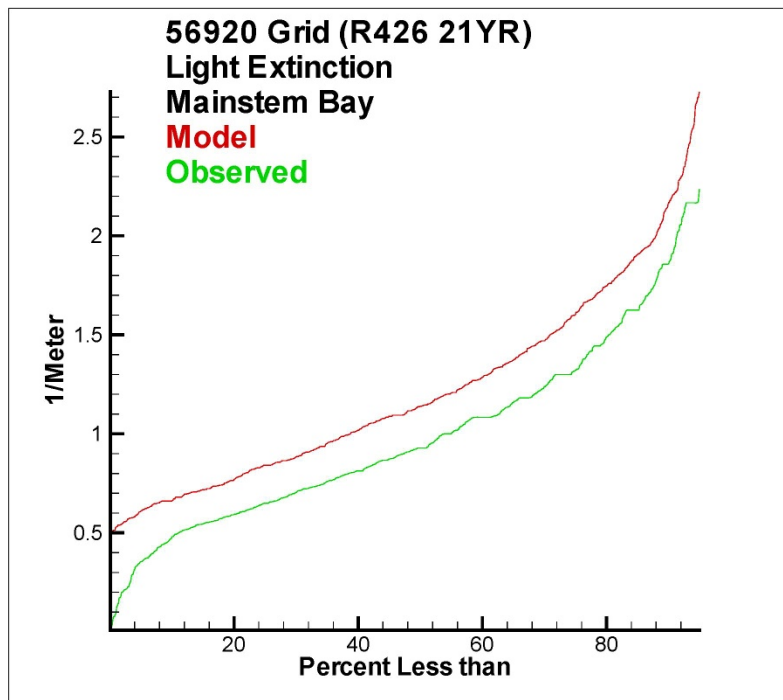
Figure 20. Cumulative distribution plot for observed and computed light attenuation in the mainstem bay.
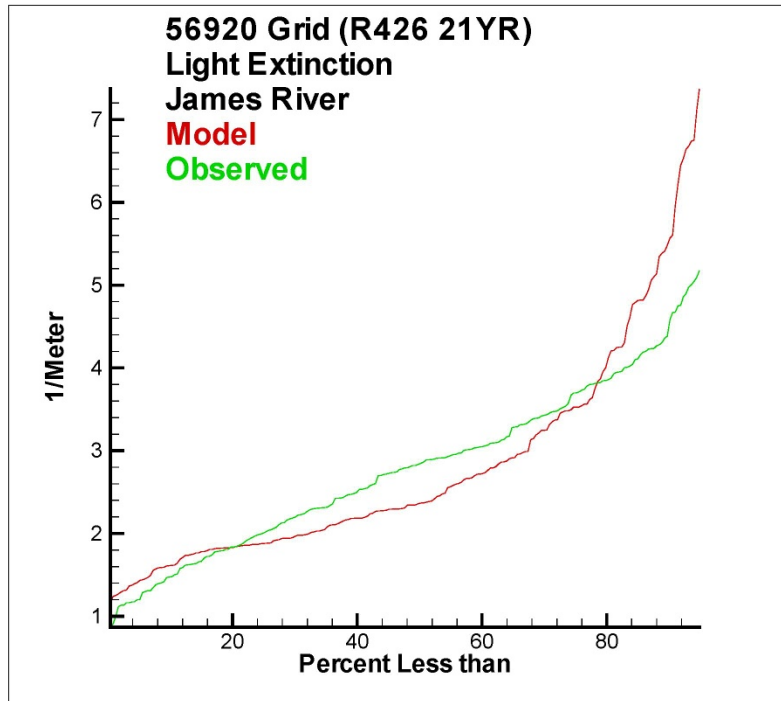
Figure 21. Cumulative distribution plot for observed and computed light attenuation in the James River.
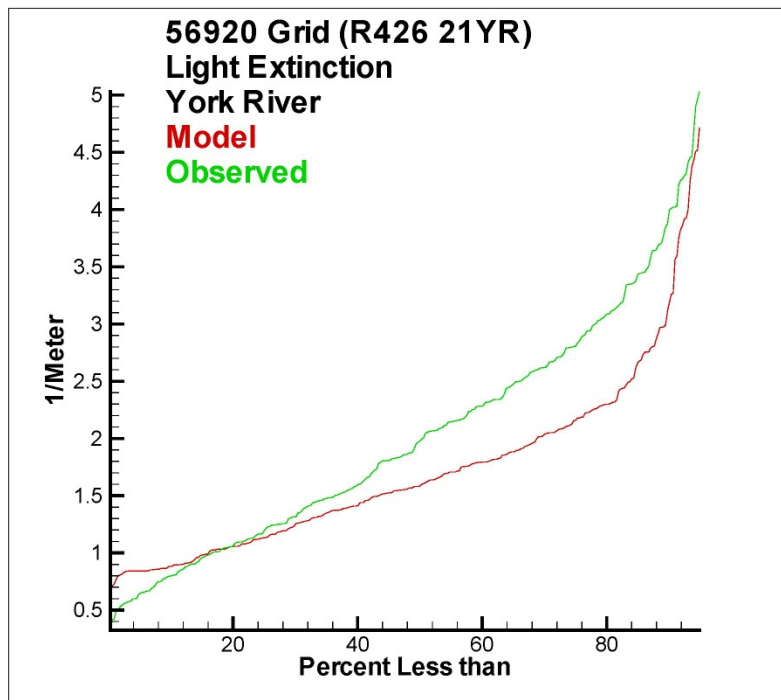
Figure 22. Cumulative distribution plot for observed and computed light attenuation in the York River.
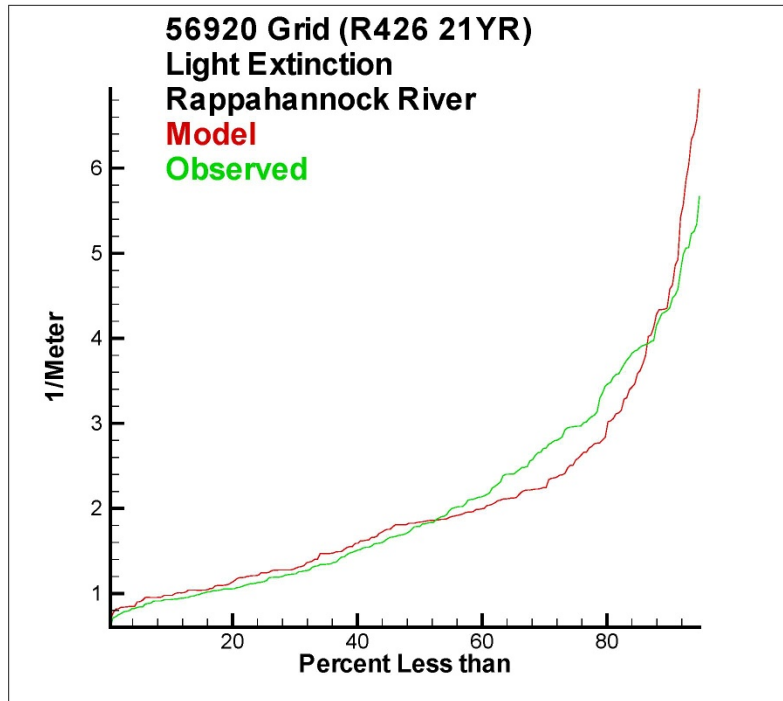
Figure 23. Cumulative distribution plot for observed and computed light attenuation in the Rappahannock River.
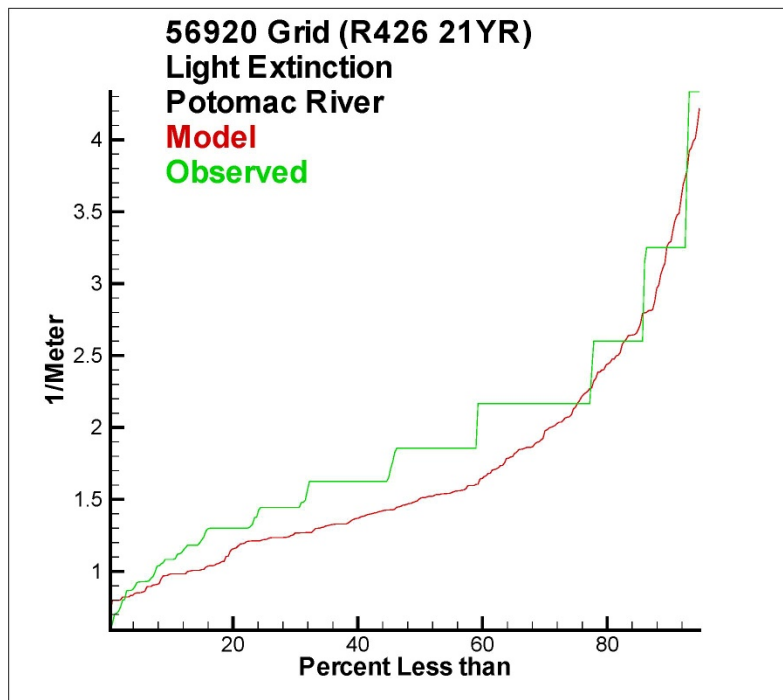
Figure 24. Cumulative distribution plot for observed and computed light attenuation in the Potomac River.
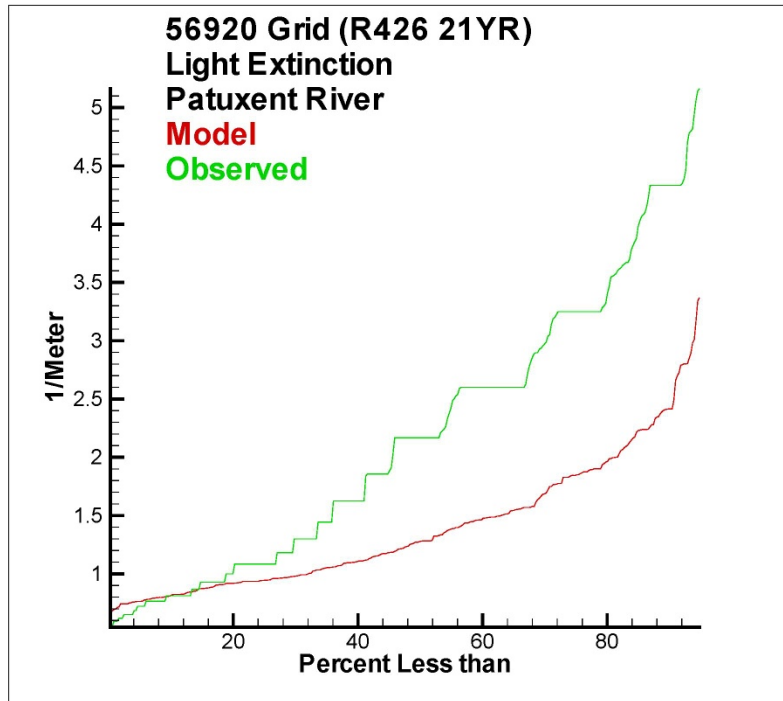
Figure 25. Cumulative distribution plot for observed and computed light attenuation in the Patuxent River.
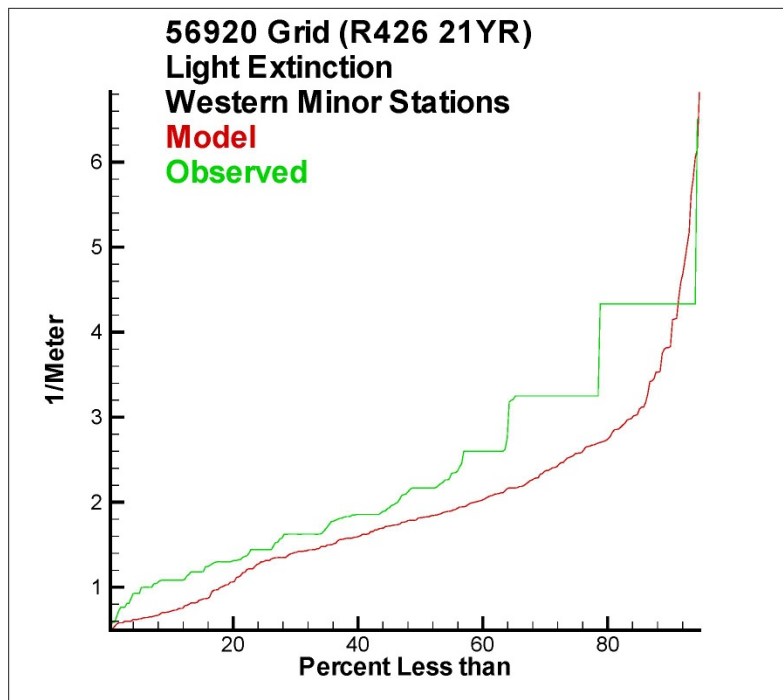
Figure 26. Cumulative distribution plot for observed and computed light attenuation in the western shore tributaries.
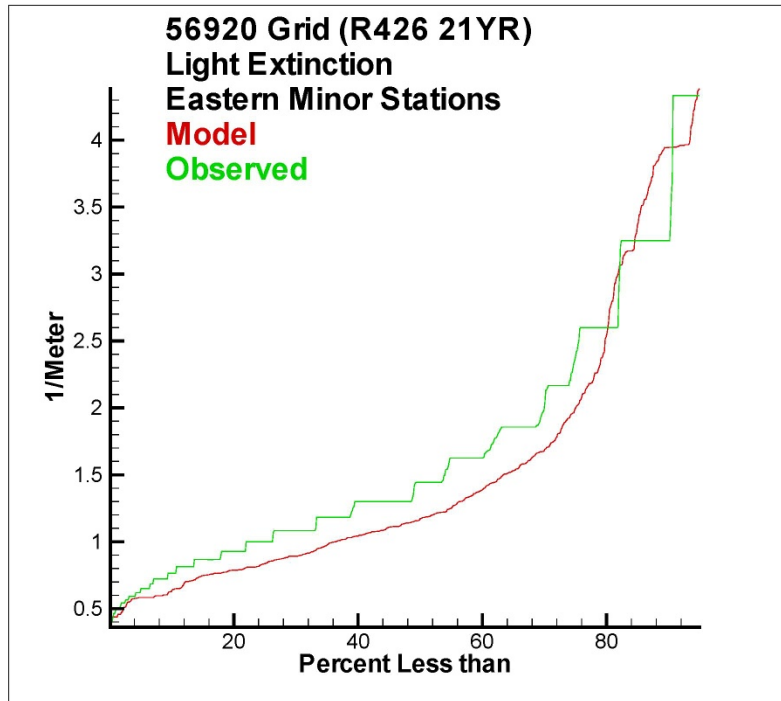
Figure 27. Cumulative distribution plot for observed and computed light attenuation in the eastern shore tributaries.
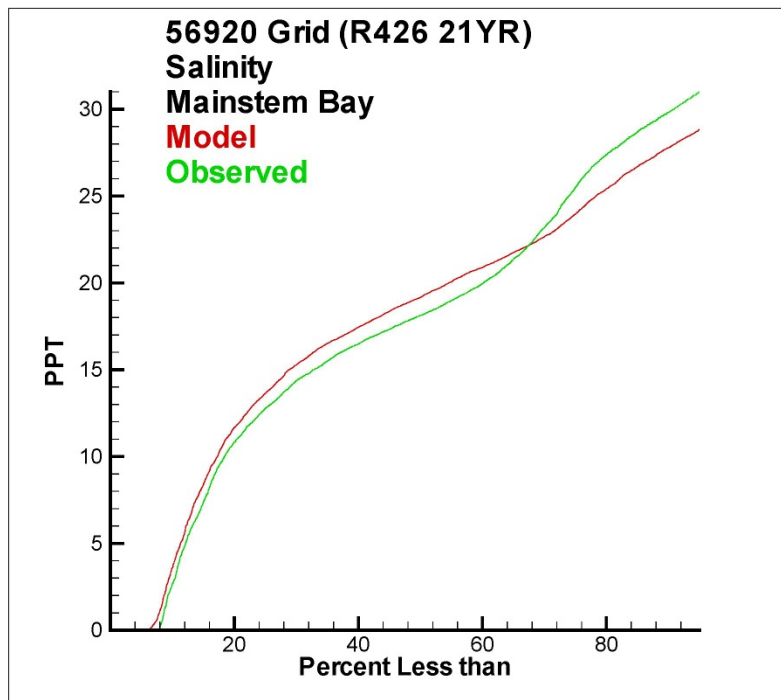

Figure 28. Cumulative distribution plot for observed and computed salinity in the mainstem bay.
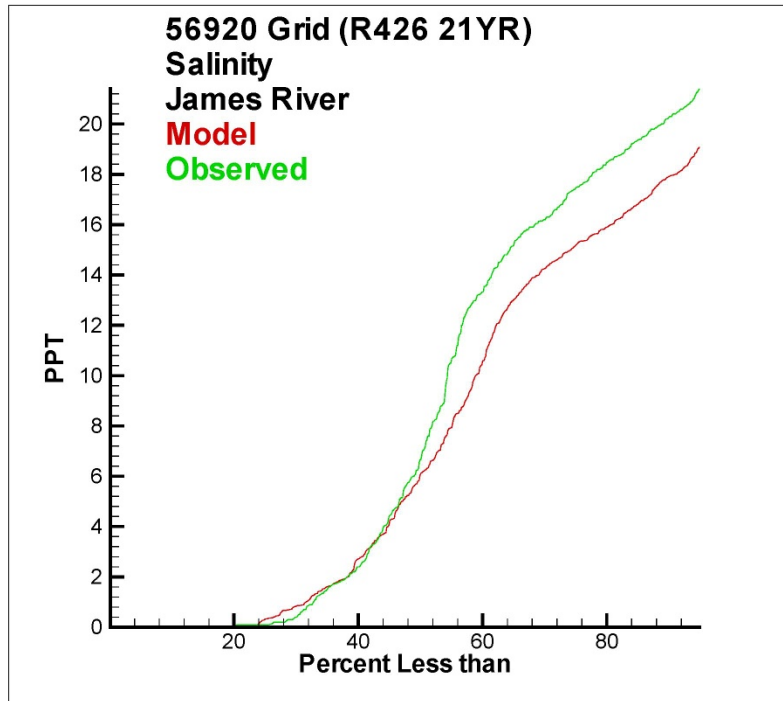
**Figure 29. Cumulative distribution plot for observed and computed salinity in the James River.**
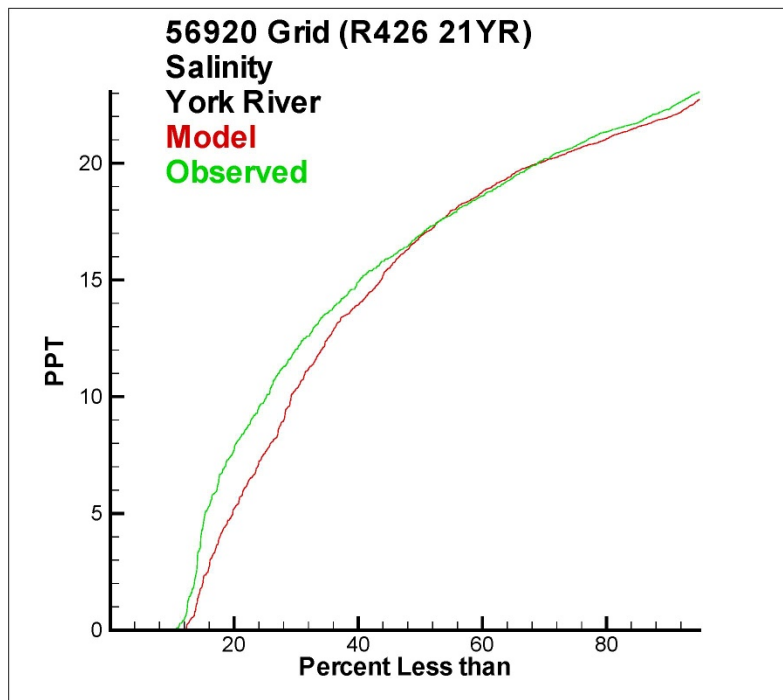
**Figure 30. Cumulative distribution plot for observed and computed salinity in the York River.**
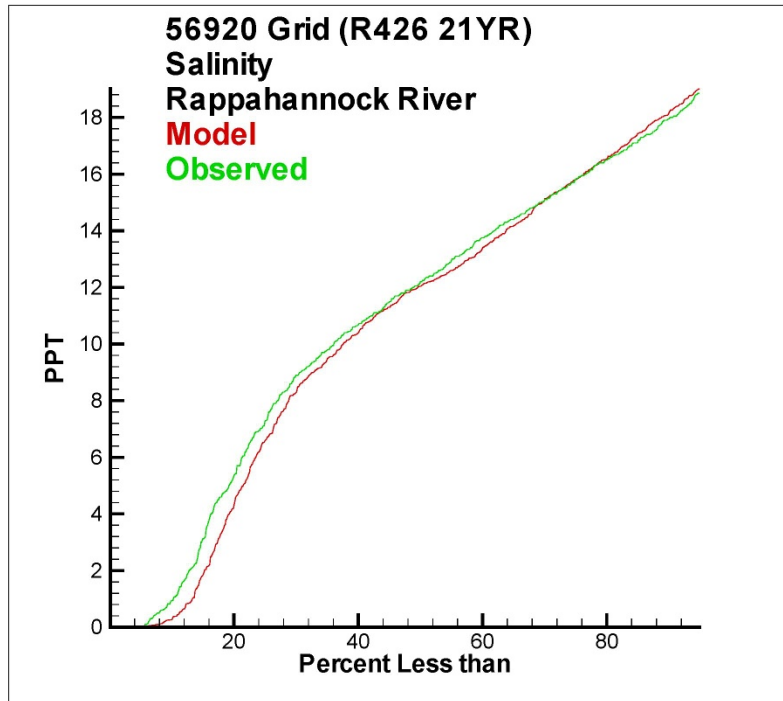
Figure 31. Cumulative distribution plot for observed and computed salinity in the Rappahannock River.
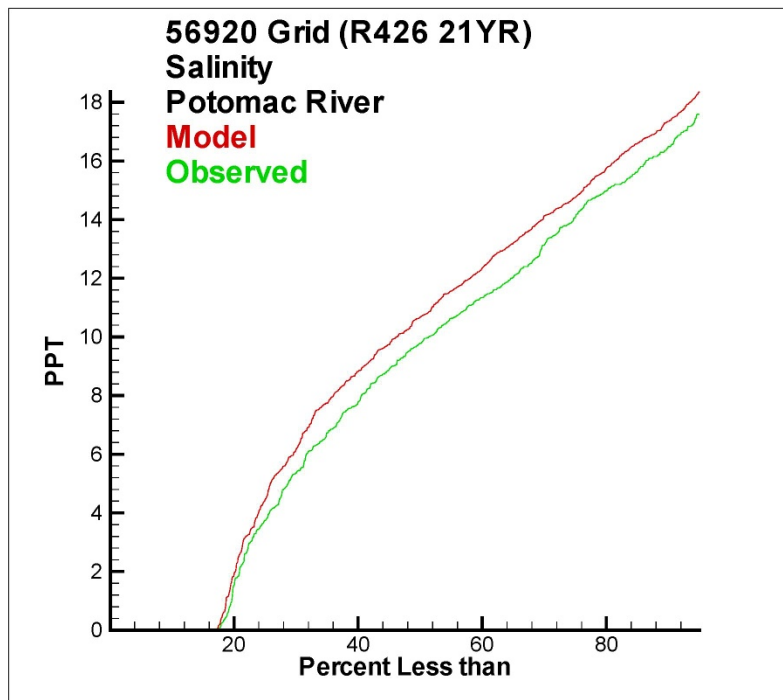
**Figure 32. Cumulative distribution plot for observed and computed salinity in the Potomac River.**
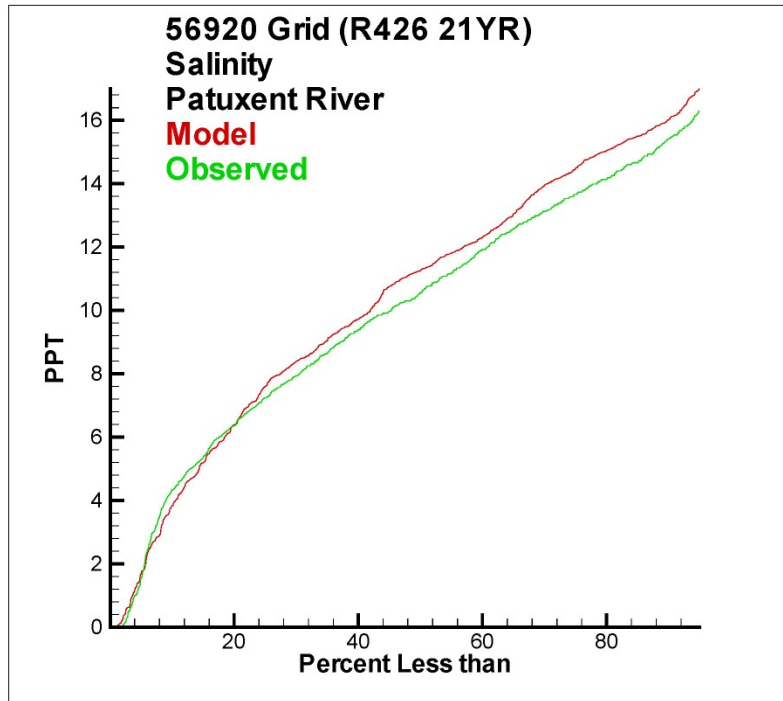
Figure 33. Cumulative distribution plot for observed and computed salinity in the Patuxent River.
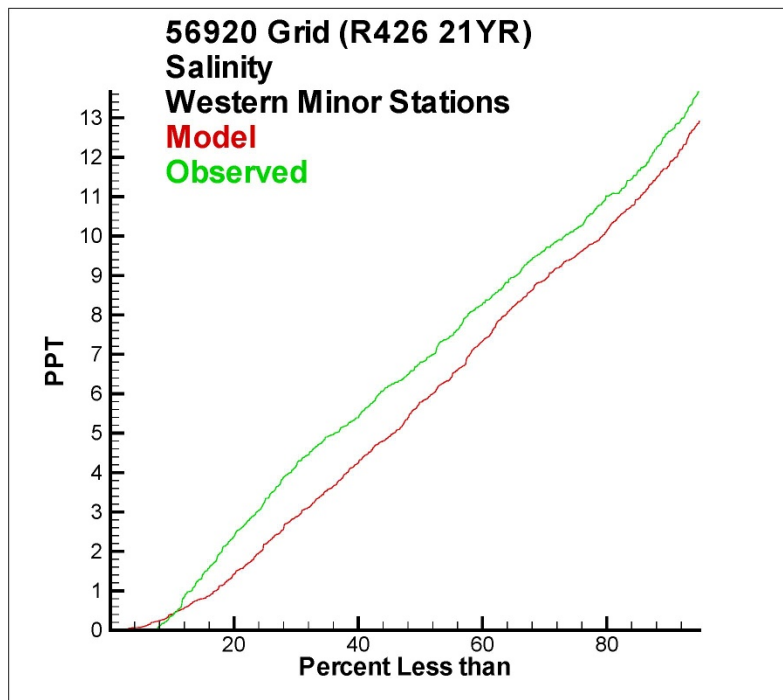
Figure 34. Cumulative distribution plot for observed and computed salinity in the western shore tributaries.
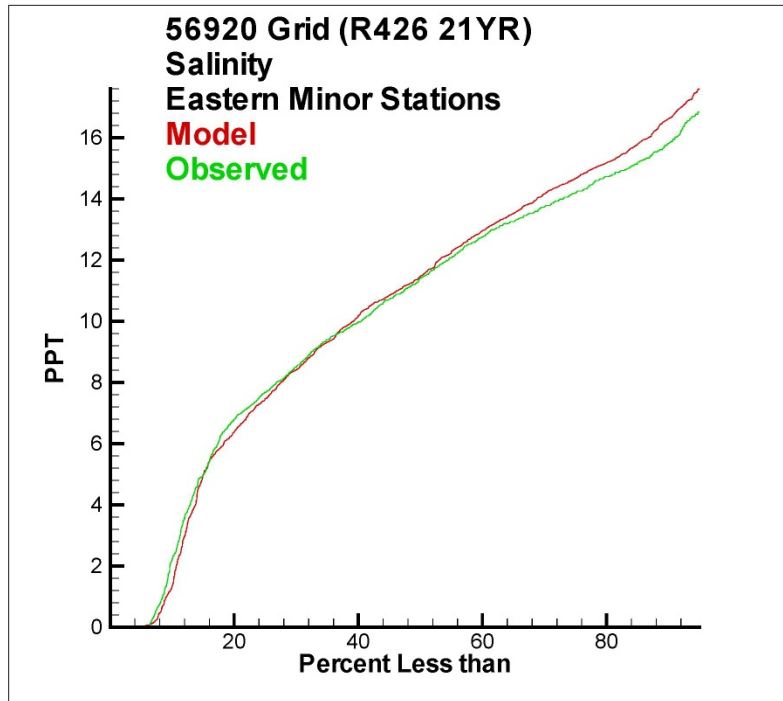
Figure 35. Cumulative distribution plot for observed and computed salinity in the eastern shore tributaries.
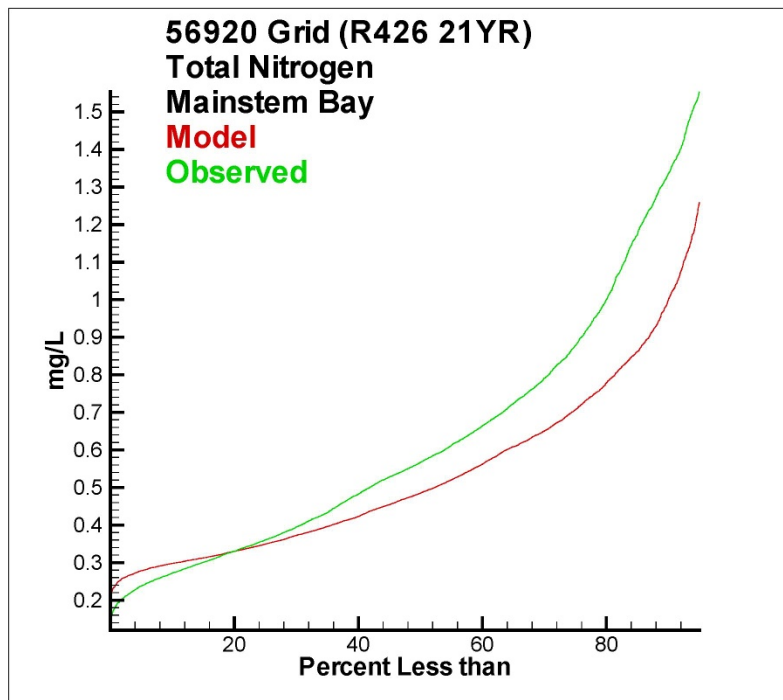
Figure 36. Cumulative distribution plot for observed and computed total nitrogen in the mainstem bay.
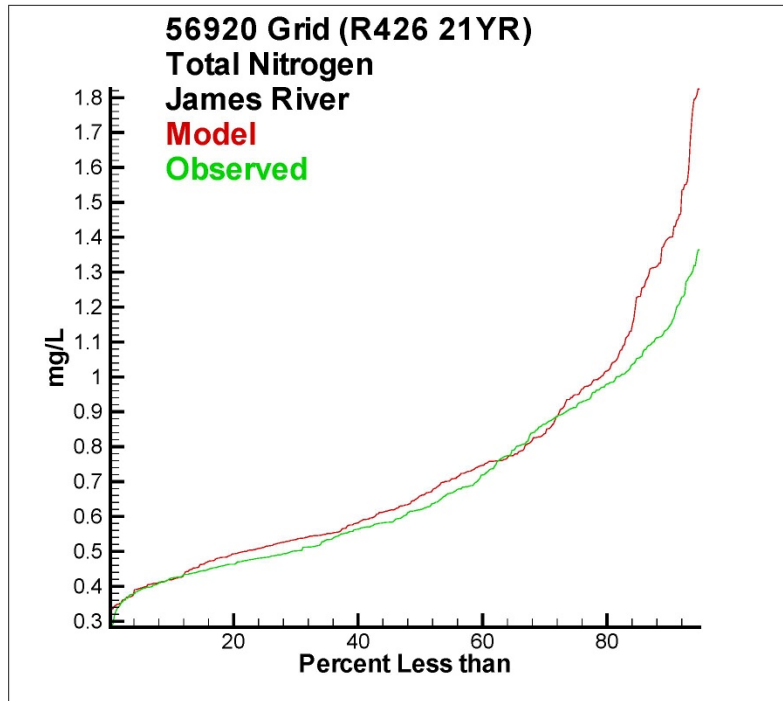
Figure 37. Cumulative distribution plot for observed and computed total nitrogen in the James River.
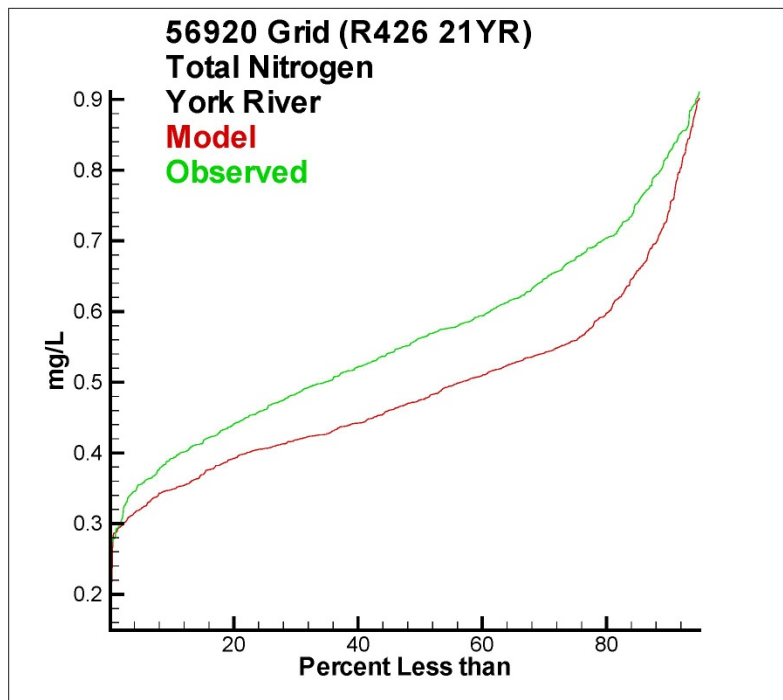
Figure 38. Cumulative distribution plot for observed and computed total nitrogen in the York River.
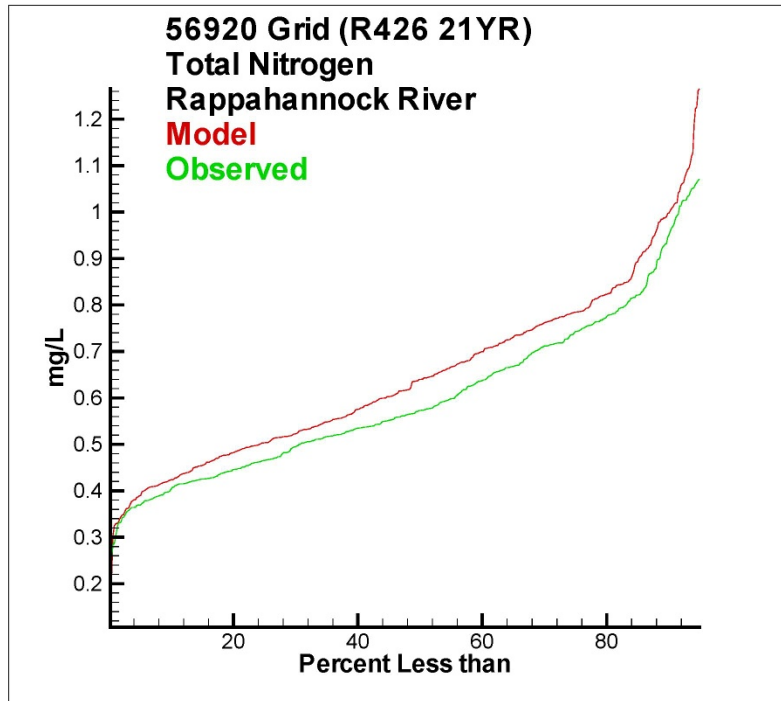
Figure 39. Cumulative distribution plot for observed and computed total nitrogen in the Rappahannock River.
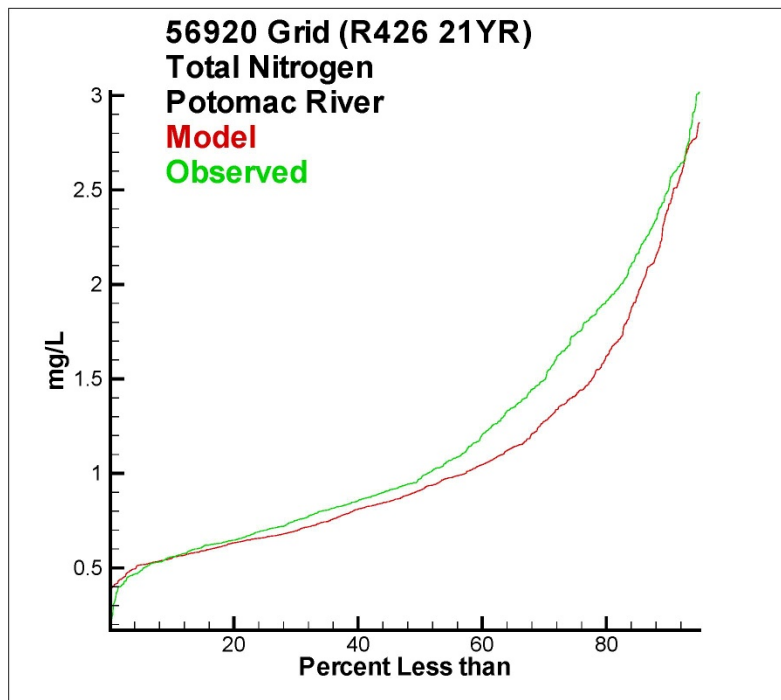
Figure 40. Cumulative distribution plot for observed and computed total nitrogen in the Potomac River.
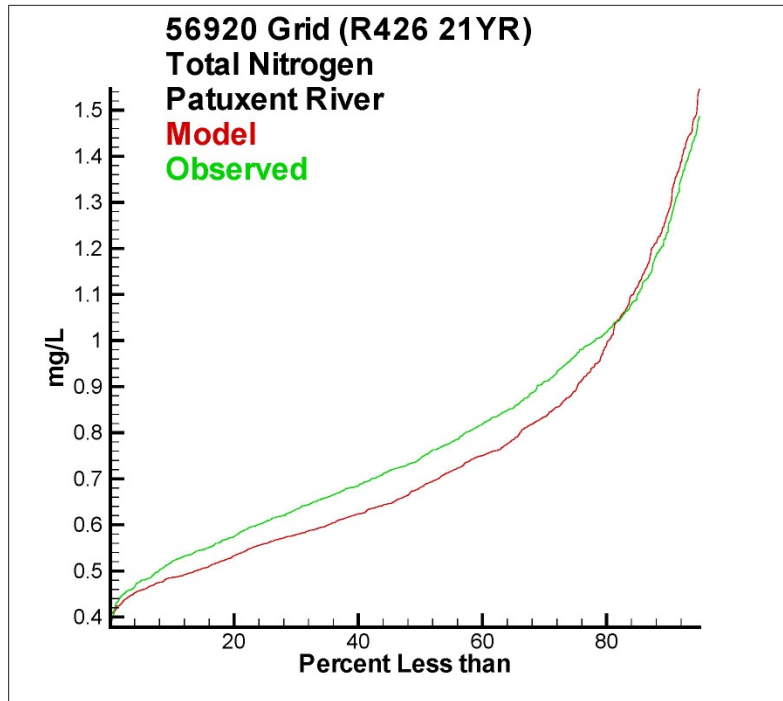
Figure 41. Cumulative distribution plot for observed and computed total nitrogen in the Patuxent River.
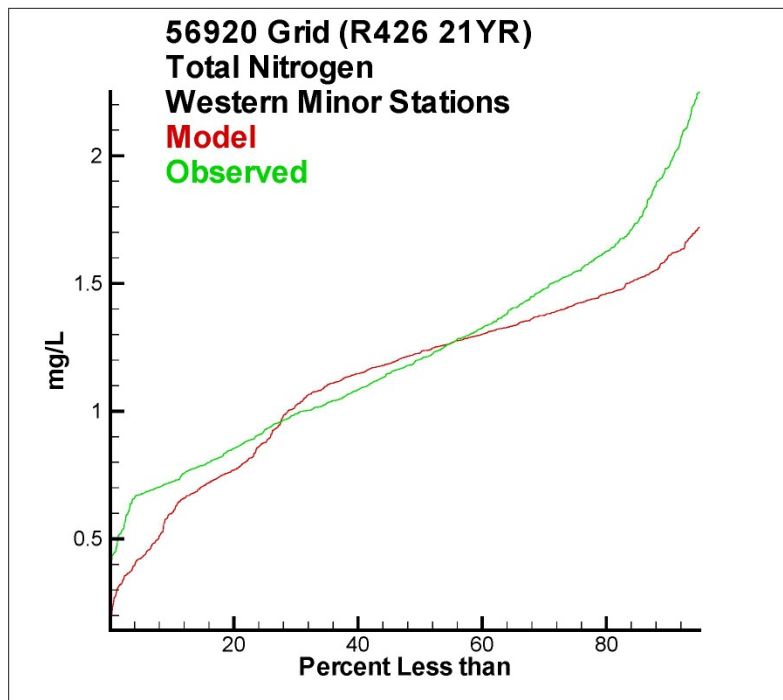
Figure 42. Cumulative distribution plot for observed and computed total nitrogen in the western shore tributaries.
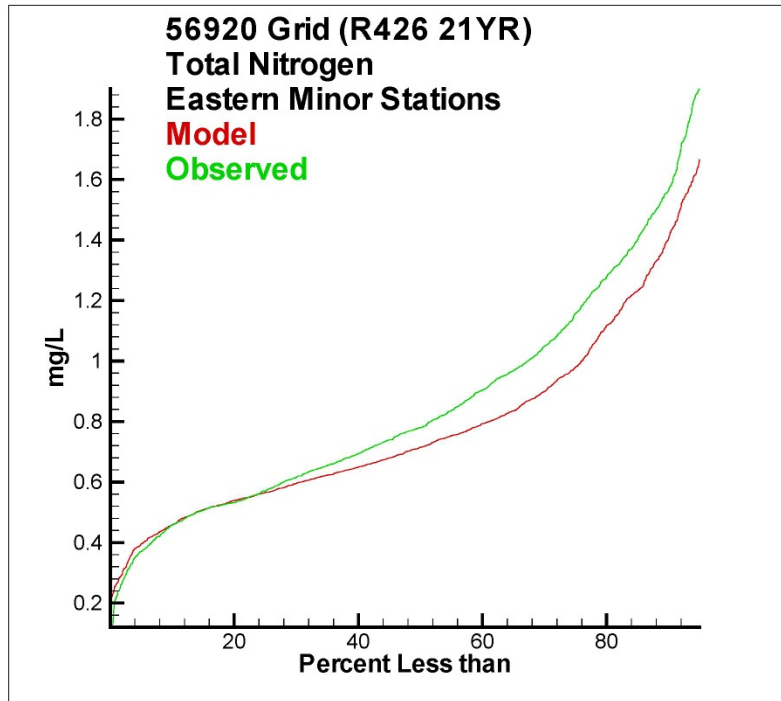
Figure 43. Cumulative distribution plot for observed and computed total nitrogen in the eastern shore tributaries.
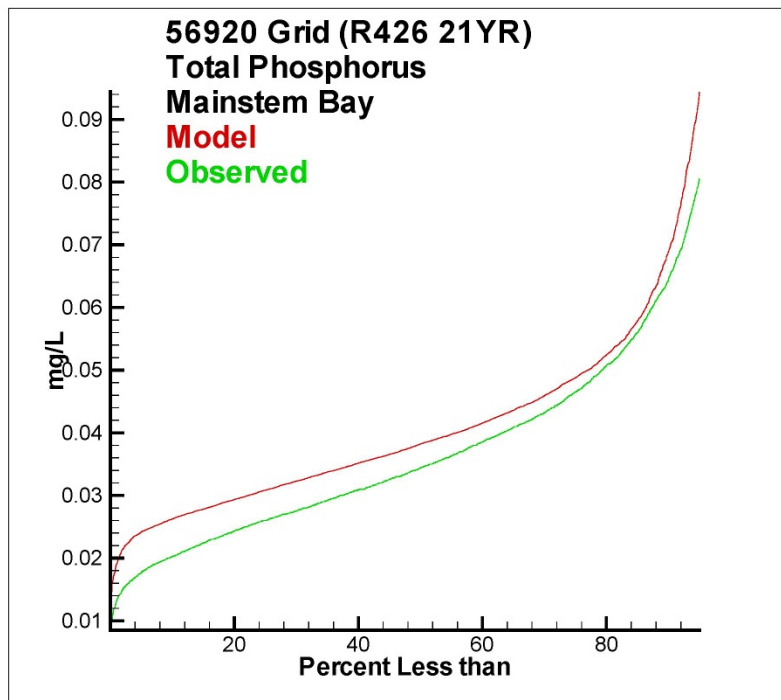

**Figure 44. Cumulative distribution plot for observed and computed total phosphorus in the mainstem bay.**
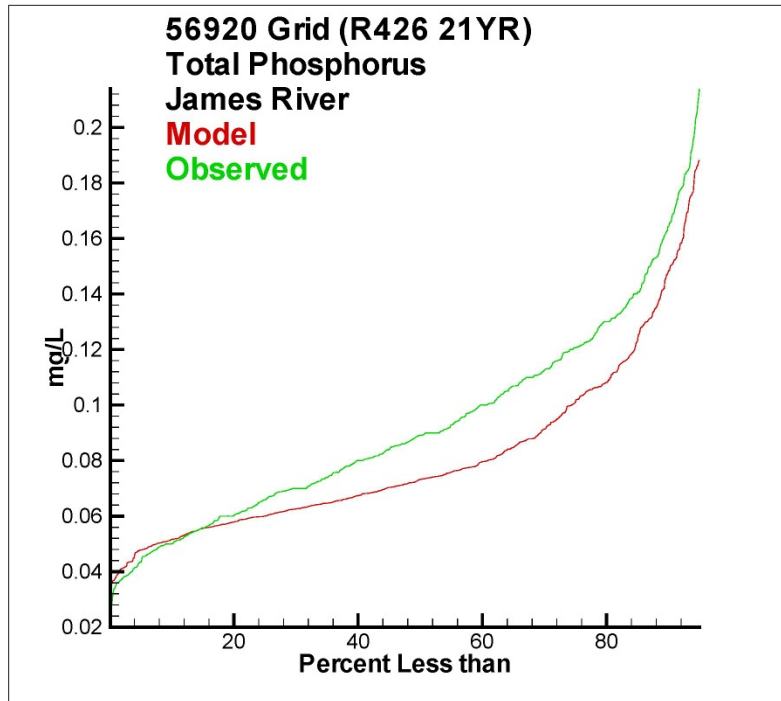
Figure 45. Cumulative distribution plot for observed and computed total phosphorus in the James River.
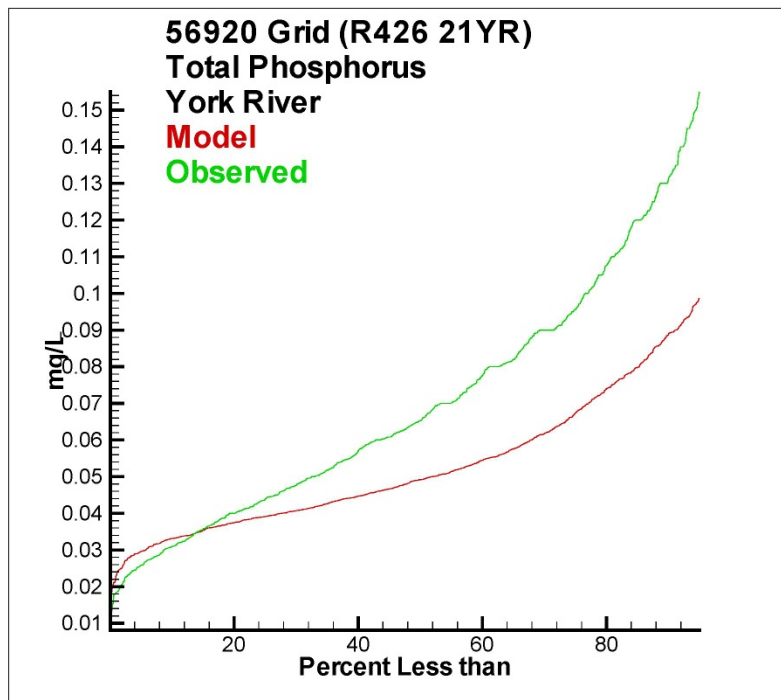
Figure 46. Cumulative distribution plot for observed and computed total phosphorus in the York River.
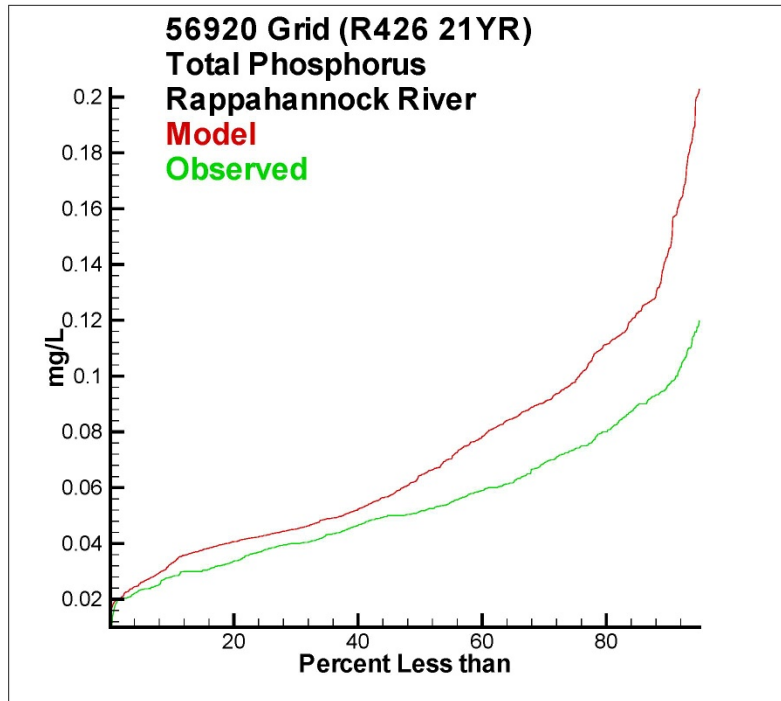
Figure 47. Cumulative distribution plot for observed and computed total phosphorus in the Rappahannock River.
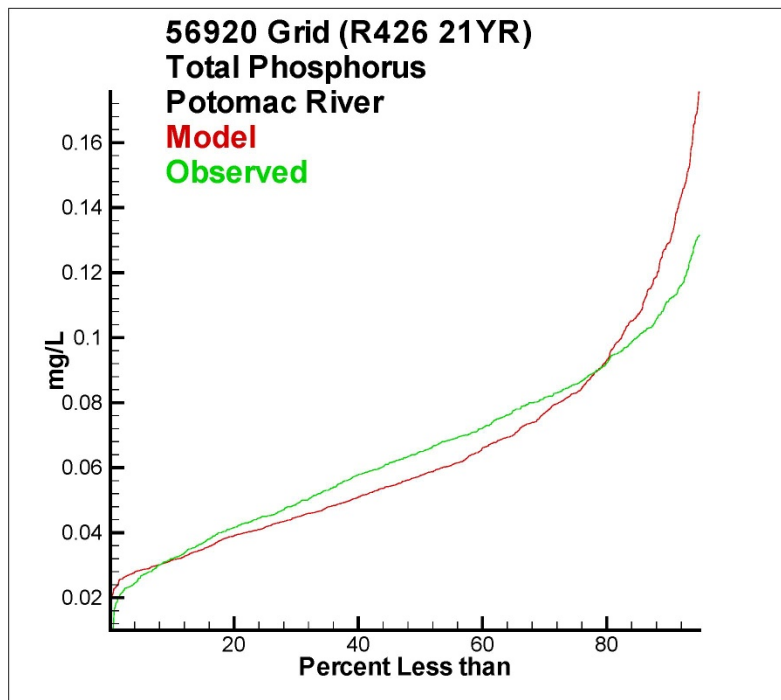

Figure 48. Cumulative distribution plot for observed and computed total phosphorus in the Potomac River.
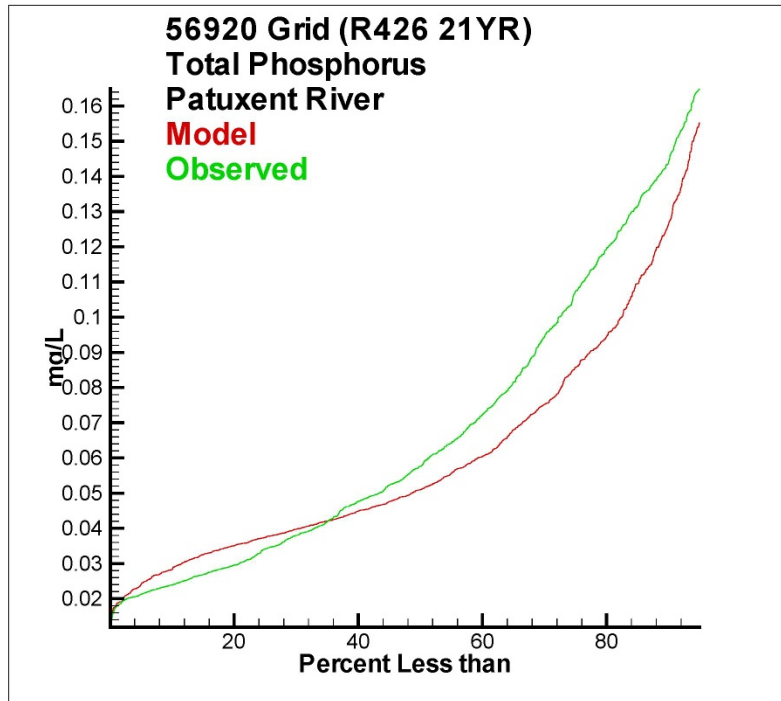
Figure 49. Cumulative distribution plot for observed and computed total phosphorus in the Patuxent River.
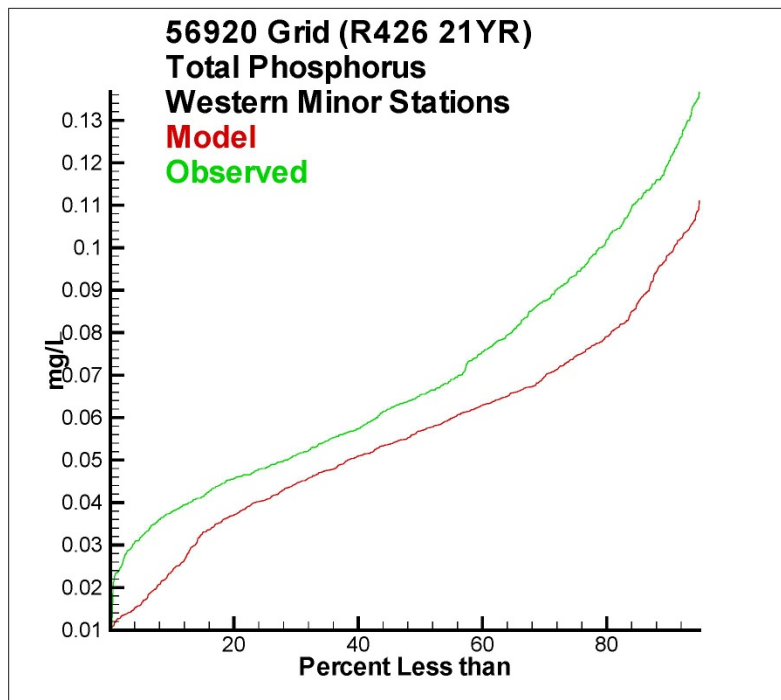
Figure 50. Cumulative distribution plot for observed and computed total phosphorus in the western shore tributaries.
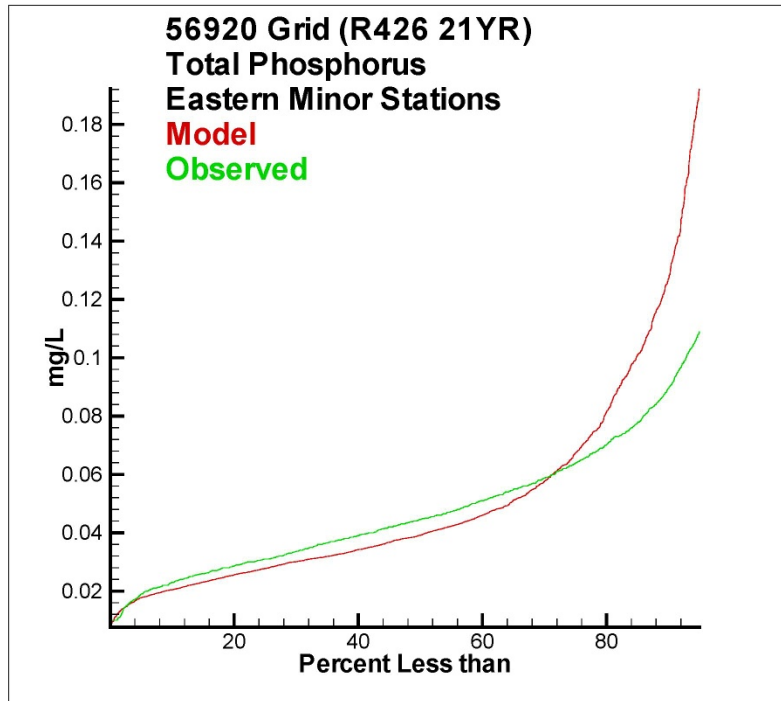
Figure 51. Cumulative distribution plot for observed and computed total phosphorus in the eastern shore tributaries.
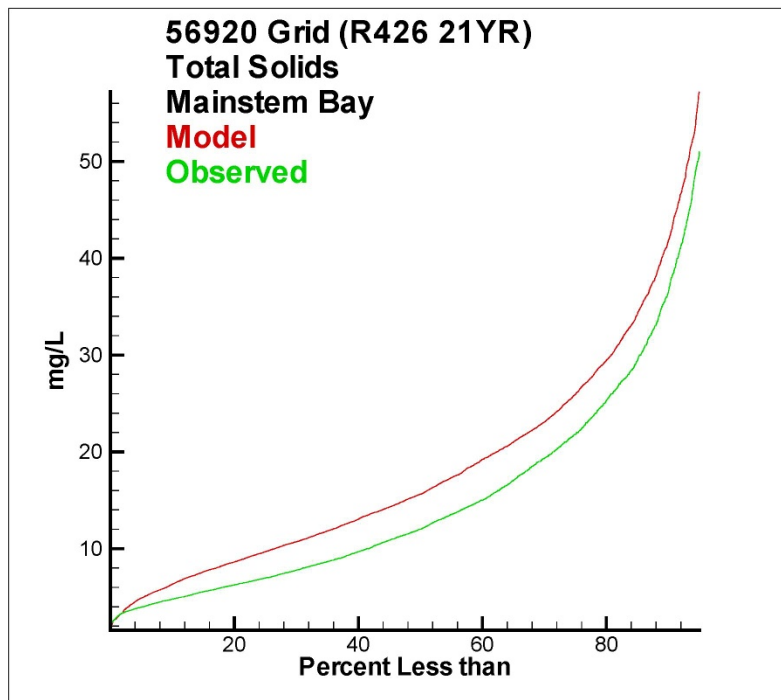
Figure 52. Cumulative distribution plot for observed and computed total suspended solids in the mainstem bay.
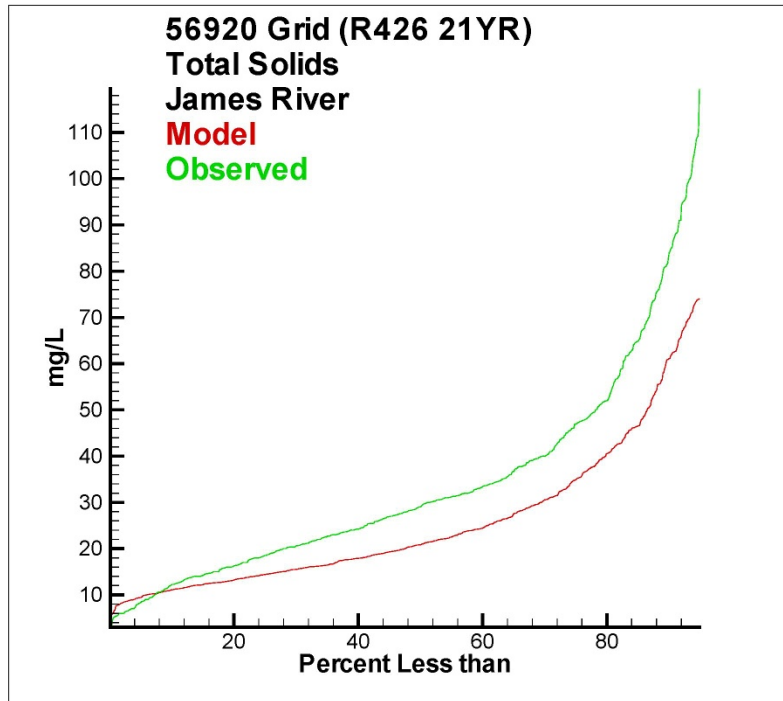
Figure 53. Cumulative distribution plot for observed and computed total suspended solids in the James River.
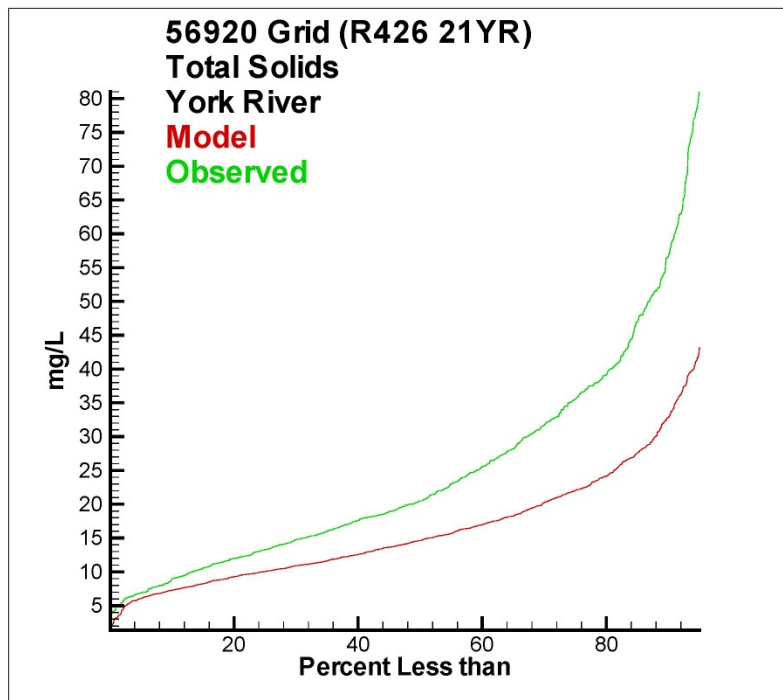
**Figure 54. Cumulative distribution plot for observed and computed total suspended solids in the York River.**
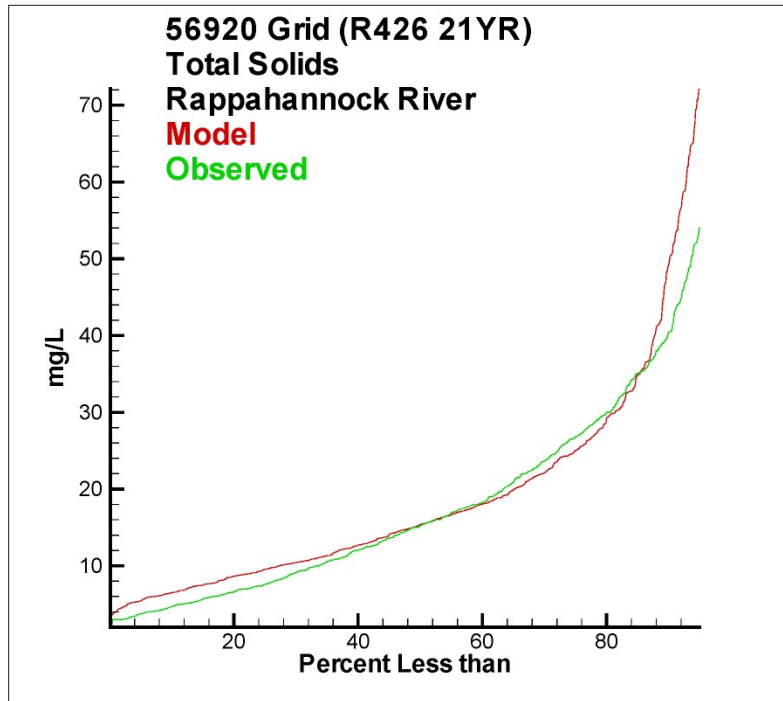
Figure 55. Cumulative distribution plot for observed and computed total suspended solids in the Rappahannock River.
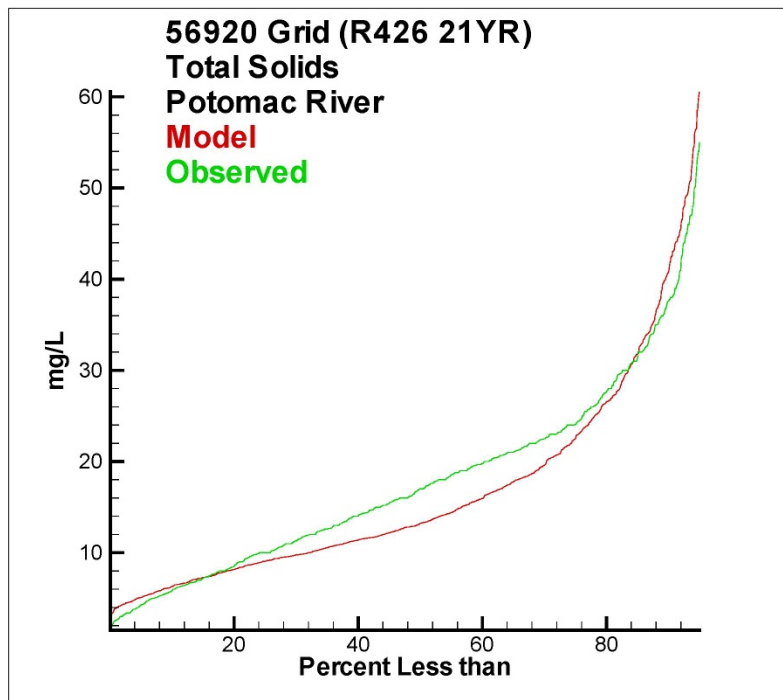

Figure 56. Cumulative distribution plot for observed and computed total suspended solids in the Potomac River.
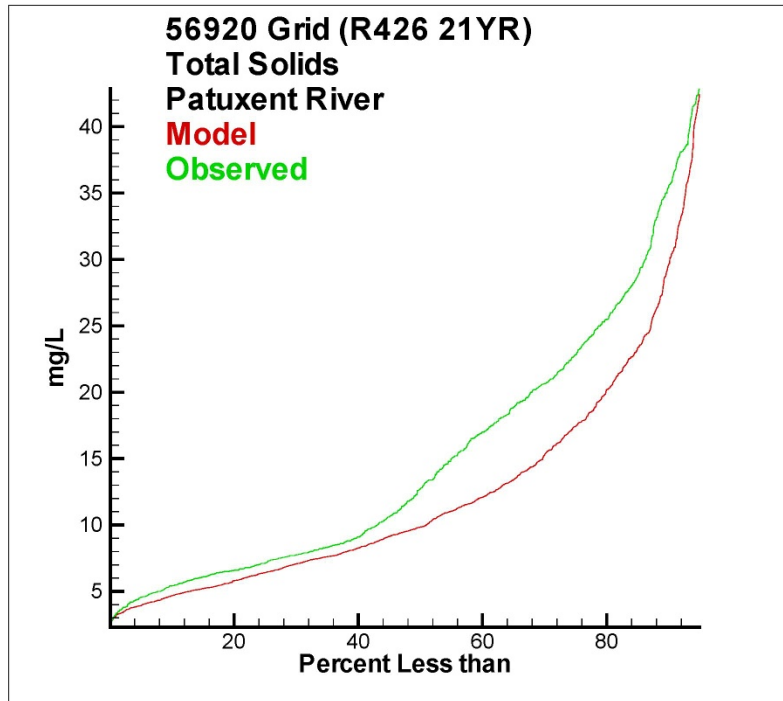
Figure 57. Cumulative distribution plot for observed and computed total suspended solids in the Patuxent River.
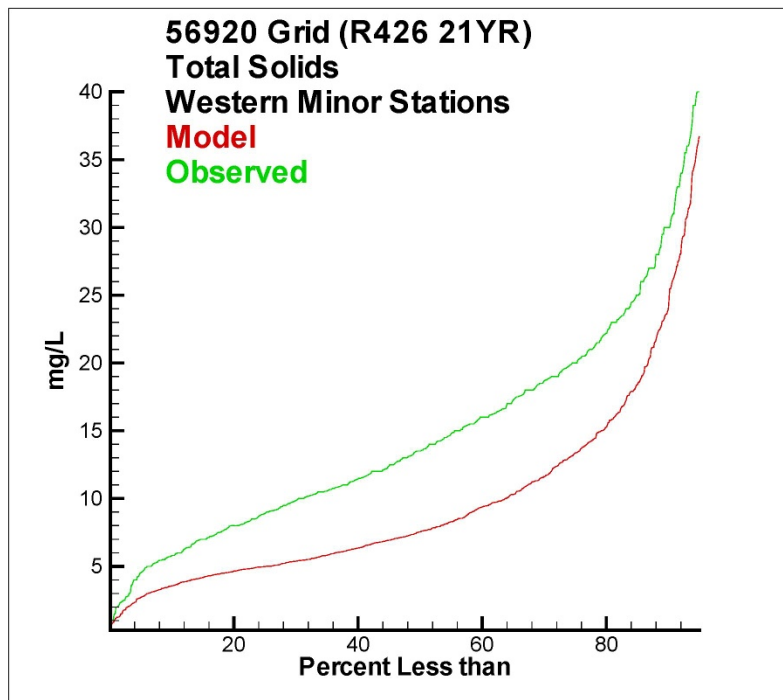

Figure 58. Cumulative distribution plot for observed and computed total suspended solids in the western shore tributaries.
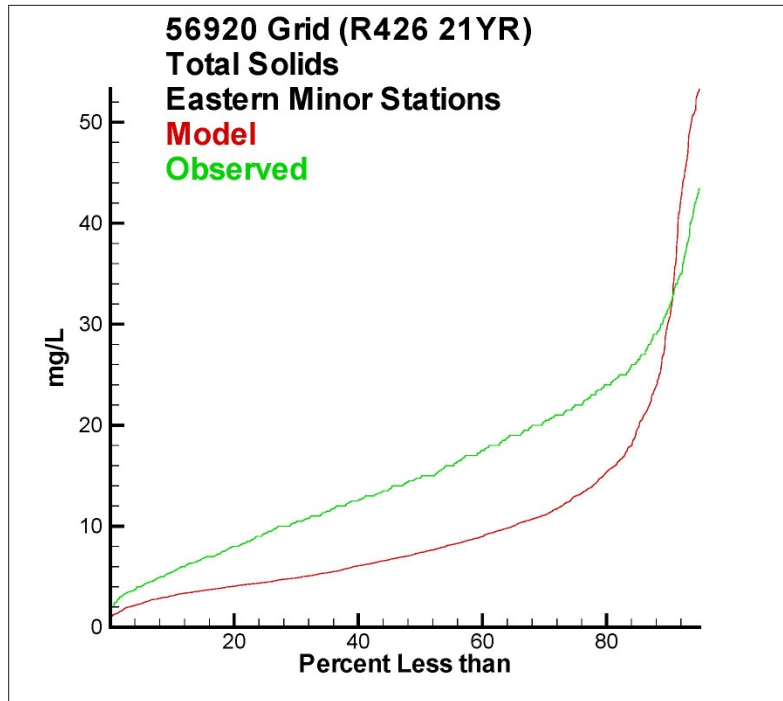
Figure 59. Cumulative distribution plot for observed and computed total suspended solids in the eastern shore tributaries.